Evaluation of Flow Diverter Design and Efficacy of Flow Diversion through Angiographic and CFD Analysis

A Dissertation Presented

by

Ronak Jashwant Dholakia

to

The Graduate School

in Partial Fulfillment of the

Requirements

for the Degree of

Doctor of Philosophy

in

Biomedical Engineering

Stony Brook University

December 2015

Stony Brook University

The Graduate School

Ronak Jashwant Dholakia

We, the dissertation committee for the above candidate for the

Doctor of Philosophy degree, hereby recommend

acceptance of this dissertation.

Baruch Barry Lieber, Ph. D. – Dissertation Advisor
Professor of Neurological Surgery and Biomedical Engineering

Danny Bluestein, Ph.D. - Chairperson of Defense Committee
Professor of Biomedical Engineering

Yi-Xian Qin, Ph. D.,
Professor of Biomedical Engineering

David Fiorella, M.D., Ph. D.,
Professor of Neurological Surgery

This dissertation is accepted by the Graduate School

Charles Taber
Dean of the Graduate School

Abstract of the Dissertation

Evaluation of Flow Diverter Design and Efficacy of Flow Diversion through Angiographic and CFD Analysis

by

Ronak Jashwant Dholakia

Doctor of Philosophy

in

Biomedical Engineering

Stony Brook University

2015

Nearly five percent of all strokes occur due to subarachnoid hemorrhage mostly due to the rupture of brain aneurysms. Treatment options of brain aneurysms include surgical clipping and endovascular embolization by deployment of intrasaccular coils to exclude the aneurysm from the circulation. Complicated fusiform, wide-necked, and large aneurysms are not amenable to surgical clipping or endovascular coiling. Flow diversion devices have evolved as an alternative treatment for such challenging cerebrovascular aneurysm.

At Present, quantitative assessment of the efficacy of flow diversion at the time of treatment is not available. Clinicians estimate adequacy of treatment by visual inspection of contrast transport and its residence time within the aneurysm immediately post implantation. Quantitative parameters of contrast transport dynamics through the rabbit model of human brain aneurysm have shown correlation with long term treatment efficacy of flow diversion. Computational fluid dynamic simulations were employed in attempt to relate contrast transport to blood flow for medical device evaluation.

This study evaluates flow diversion in idealized and patient based aneurysm geometries, in-vitro, in the rabbit aneurysm model as well as in human patients. In the rabbit model mathematical analysis of contrast washout and its correlation to the efficacy of flow diversion was conducted. Statistical analysis suggests that the analyzed parameters correlate with aneurysm occlusion however, significance was not reached due to a low sample size. Intra-aneurysmal hemodynamics CFD analysis was conducted in vitro through flow diverting devices flows as well as in 3 patients in addition to angiographic washout analysis in a larger cohort of patients that underwent flow diversion. Washout parameters such as contrast concentration decay time coefficient were in sync with intra-aneurysmal kinetic energy. Correlation of CFD analysis on the three patients to angiographic contrast washout indicate encouraging trend. This work also applied CFD and angiographic analysis to five commercially available neurovascular devices (not compared before). Geometry of the implanted devices in idealized brain aneurysm models was reconstructed from microCT images and applied to CFD analysis. The combination of experimental and computational approach provides initial data towards device inter-device evaluation of the efficacy of flow diverters for treatment of brain aneurysms.

Table of Contents

LIST OF FIGURES……………………………………………………………………VII

LIST OF TABLES…………………………………………………………………..XIV

ACKNOWLEDGEMENTS…………………………………………………………XV

CHAPTER 1: INTRODUCTION……………………………………………………..1

BACKGROUND AND CLINICAL SIGNIFICANCE………………………….1

TREATMENT OF BRAIN ANEURYSMS……………………………………...3

CLINICAL PROBLEM: EFFICACY OF FLOW DIVERSION………………6

HYPOTHESIS AND SPECIFIC AIMS…………………………………………10

CHAPTER 2: VALIDATION OF CFD SIMULATIONS………………………………13

ANALYTICAL VALIDATION…………………………………………………13
Poiseuille solution for steady flow…………………………………………………14
Womersley solution for pulsatile flow……………………………………………..16

EXPERIMENTAL VALIDATION……………………………………………...19
Methods……………………………………………………………………………19
Results……………………………………………………………………………...23

CHAPTER 3: ANGIOGRAPHIC AND CFD COMPARISON OF FIVE COMMERCIAL NEUROVASCULAR STENTS/FLOW DIVERSION DEVICES……………………..29

INTRODUCTION……………………………………………………………...29

METHODS……………………………………………………………………...29
Model fabrication…………………………………………………………………..30
Experimental setup and angiographic data acquisition……………………………32
Mathematical model………………………………………………………………..36
MicroCT imaging…………………………………………………………………..37
CFD model construction……………………………………………………………38
Meshing and boundary conditions………………………………………………….40

RESULTS………………………………………………………………………….43
Angiographic data…………………………………………………………………..43
CFD data…………………………………………………………………………….47
Angiographic vs CFD results……………………………………………………….53

DISCUSSION……………………………………………………………………...54

CHAPTER 4: EXPERIMENTAL EVALUATION OF FLOW DIVERSION EFFICACY THROUGH ANGIOGRAPHIC WASHOUT ANALYSIS IN THE RABBIT MODEL……………………………………………………………………………..60

INTRODUCTION……………………………………………………………..60

METHODS…………………………………………………………………......60
Creation of experimental aneurysms……………………………………………...60
Flow diversion treatment of aneurysms and experimental data acquisition……....62
Venous and breathing artifact correction……………………………………… 63
Mathematical model…………………………………………………………….....65
Experimental design and statistical analysis………………………………………66

RESULTS……………………………………………………………………..67

DISCUSSION…………………………………………………………………78

CHAPTER 5: CLINICAL ANGIOGRAPHIC WASHOUT ANALYSIS……………81

METHODS……………………………………………………………………81
Clinical data acquisition…………………………………………………………..81
Angiographic image analysis……………………………………………….......86
Image artifact correction – signal processing…………………………………….87
Mathematical modeling…………………………………………………………..92
Data analysis……………………………………………………………………...92
Experimental design and statistical analysis……………………………………...93

RESULTS……………………………………………………………………..94

DISCUSSIONS………………………………………………………………106

CHAPTER 6: PATIENT SPECIFIC CFD MODELING……………………………114

METHODS……………………………………………………………………114
CFD model construction………………………………………………………....114
Patient specific flow diverter construction………………………………………116
Boundary conditions and numerical analysis……………………………………117

RESULTS……………………………………………………………………..121

DISCUSSION…………………………………………………………………127
Clinical CFD and angiographic contrast washout correlation……………………129

CHAPTER 7: CONCLUSION AND RECOMMENDATIONS………………………133

REFERENCES…………………………………………………………………………..138

APPENDIX A: RABBIT DATA…………………………………………………...147

APPENDIX B: CLINICAL DATA………………………………………………...165

List of Figures

Figure 1: Schematic of locations and prevalence of aneurysms in the cerebral circulation (adapted from[1])……………………………………………………………………………….3

Figure 2: Schematic demonstrating treatment options for brain aneurysm including surgical clipping (left) and endovascular coiling (middle and right) (adapted from [1])……………...4

Figure 3: Angiogram of a PComA aneurysm (A) treated with endovascular coiling (B). Recanalization was observed at 8 month follow up (C) and the patient subsequently was re-treated (D)[19]……………………………………………………………………………….. 5

Figure 4: Images of Pipeline embolization device in expanded form (left) and schematic deployment in giant wide necked aneurysm (center); Giant aneurysm before Pipeline treatment and at follow up showing aneurysm excluded from circulation (right)…………………….6

Figure 5: Dye concentration intensity levels following injection in different blood vessels (adapted from[55])……………………………………………………………………………7

Figure 6: Experimentally recorded blood flow waveform (left panel) and pressure (right panel) in the canine femoral artery adapted from[96]…………………………………………………16

Figure 7: Comparison of CFD axial velocity profile (two different mesh sizes in green and blue) with Womersley analytical solution (red) at 7 different time points in the cardiac cycle….18

Figure 8: Pulsatile inflow waveform imposed at the inlet of the idealized sidewall aneurysm model (top left panel); helical stent constructed in SolidWorks (bottom left panel) and Boolean subtraction to obtain the stented model of reference……………………………………….19

Figure 9: Location of cross section for extraction of axial velocity profiles (A) and comparison between PIV and CFD results (B) at four different time points in the cardiac cycle[49]…….23

Figure 10: Direct comparison of intra-aneurysmal velocity profiles during acceleration (top), peak systole (middle) and deceleration (bottom) between CFD (left) and PIV (right)[1]……24

Figure 11: Intra-aneurysmal velocity in the control and the stented aneurysms during peak systole (top) and deceleration (bottom)……………………………………………………..25

Figure 12: Temporal evolution of pressure gradient in the control and the three device cases (left); and mean pressure gradient comparison between the control and the stented models………………………………………………………………………………….25

Figure 13: Temporal waveforms of intra aneurysmal circulation obtained in the Control, stent 1, stent 2, and stent 3 cases [49]……………………………………………………………….27

Figure 14: Mean hydrodynamic circulation comparison between PIV and CFD[49]………...27

Figure 15: Temporal and mean kinetic energy comparison between the control and stented cases..28

Figure 16: Schematic of the sidewall aneurysm model (left) and the silicone model fabrication process. The 3D printed ABS model is dip coated to obtain a clear silicone model into which the device is implanted…………………………………………………………………….31

Figure 17: Five panels showing each a photo and a fluoroscopic image side by side of the 5 devices
tested………………………………………………………..…………………32

Figure 18: Schematic of the experimental apparatus for high speed angiography data acquisition in the aneurysm models…………………………………………………..………………34

Figure 19: Segmented (red) aneurysm region of interest (ROI) (left) and corresponding contrast concentration-time curve obtained by image processing (right)……………………………35

Figure 20: MicroCT slice of pipeline in the aneurysm model (left) and the same slice after segmentation with the device wires cropped (right)……………………………………...37

Figure 21: CAD model for Pipeline in position across the aneurysm neck (top), and expanded view of the anisotropic tetrahedral mesh generated using meshing tools available within ADINA for the Pipeline CAD model (bottom)…………………………………………………...40

Figure 22: CAD model for FRED in position across the aneurysm neck (top), and expanded view of the anisotropic tetrahedral mesh generated using the meshing tools available within ADINA for the FRED CAD model (bottom)……………………………………………………..42

Figure 23: Representative concentration time curves (with gray scale intensity averaged over the region of interest) for the control in the sidewall aneurysm model and the five devices tested..43

Figure 24: Comparison of averaged grayscale intensity amplitude in the ROI for the control and the five devices tested with * indicating statistically significance at p<0.05, ** indicates p <0.01, *** indicates p<0.001……………………………………………………………………44

Figure 25: Normalized washout curve (red) fitted to the mathematical model to delineate the optimized washout curve (blue). The convective (green) and diffusive (cyan) proportions are also shown……………………………………………………………………………………..45

Figure 26: Comparison of convective decay time constant of the control and the five devices with * indicating statistical significance at the p <0.05 level, ** indicates p<0.01, and *** indicates p<0.001……………………………………………………………………....46

Figure 27: Peak systolic speed distribution in the aneurysm (left) and velocity vector map (right) for A) control, B) Neuroform, C) Enterprise, D) LVIS, E) FRED, and F) Pipeline………...48

Figure 28: Temporal comparison of intra-aneurysmal kinetic energy results among the five commercial neurovascular devices deployed in the CFD model…………………………….51

Figure 29: Comparison of intra-aneurysmal mean kinetic energy among the five commercial devices……………………………………………………………………………….....51

Figure 30: Comparison of the percentage reduction in the intra-aneurysmal mean kinetic energy among five commercial neurovascular devices…………………………………………..52

Figure 31: Convection time coefficient obtained from mathematical modeling of the angiographic data plotted against the mean kinetic energy from CFD simulations……….. 53

Figure 32: Geometrical configuration of Pipeline following the original deployment (A).The drag force shifted configuration (B), and the compacted configuration of (C)…………………..56

Figure 33: geometric configuration of the Pipeline device implanted within the same sidewall aneurysm model in 2015 (A) and a device implanted one year earlier (B)………………….58

Figure 34: Schematic of the endovascular procedure for creation of elastase induced aneurysms in rabbits[64]……………………………………………………………………………61

Figure 35: ROI segmentation pre (left) and post (right) flow diverter right implantation and washout curves obtained for the aneurysm (blue: pre-device, red: post-device)…………....63

Figure 36: Rabbit aneurysm washout curve with breathing artifact corrected through notch filter to obtain corrected washout curve[53, 54, 57]……………………………………………………64

Figure 37: Correction for venous overlay on angiographic washout. Top row left to right: pre device angiographic segmentation; washout curve with venous overlay and breathing artifact (center); breathing artifact corrected washout curve (red) and the venous as well as breathing artifact corrected curve (blue). Bottom row left to right: post device angiographic segmentation; washout curve with breathing artifact; breathing artifact corrected washout curve. Image on the right demonstrates segmentation of the aneurysm (red) and venous region (blue) to calculate the average venous contrast concentration……………………………………………………64

Figure 38: Sample aneurysmal washout curve (red) pre (left) and post (right) that is normalized and fit with a mathematical model (blue) that is able to separate the contrast transport mechanics into convection (green) and diffusion (cyan); the final model (blue) is the sum of the convection and diffusion components……………………………………………………………....66

Figure 39: Angiographic image analysis for rabbit R11-007. Top panel shows snapshots of angiographic image data pre device (left), post device implantation (center), and at 6month follow up time point (right). Bottom panel demonstrates the normalized washout curves obtained pre and post flow diverter implantation in red. The mathematical model fitted onto the washout curve is in blue. The fitted mathematical model is distributed into the convective (green) and diffusive (cyan) components of contrast transport mechanics………………………………70

Figure 40: Angiographic image analysis for rabbit R13-197. Top panel shows snapshots of angiographic image data pre device (left), post device implantation (center), and at 6month follow up time point (right). Bottom panel demonstrates the normalized washout curves obtained pre and post flow diverter implantation in red. The mathematical model fitted onto the washout curve is in blue. The fitted mathematical model is distributed into the convective (green) and diffusive (cyan) components of contrast transport mechanics………………………………71

Figure 41: Angiographic image analysis for rabbit R13-198. Top panel shows snapshots of angiographic image data pre device (left), post device implantation (center), and at 6month follow up time point (right). Bottom panel demonstrates the normalized washout curves obtained pre and post flow diverter implantation in red. The mathematical model fitted onto the washout curve is in blue. The fitted mathematical model is distributed into the convective (green) and diffusive (cyan) components of contrast transport mechanics……………………………… 72

Figure 42: Comparison of washout curve amplitude pre and post flow diverter implantation…74

Figure 43: Comparison of washout curve averaged amplitude (angiographic intensity normalized by total number of pixels in region of interest for each aneurysm) pre and post flow diverter implantation…………………………………………………………………………....74

Figure 44: Comparison of convection decay time coefficient pre and post flow diverter implantation……………………………………………………………………………75

Figure 45: Comparison of diffusion decay time coefficient pre and post flow diverter implantation……………………………………………………………………………75

Figure 46: Comparison of washout curve convective component amplitude pre and post flow diverter implantation…………………………………………………………………...76

Figure 47: Comparison of washout curve diffusive component amplitude pre and post flow diverter implantation…………………………………………………………………...76

Figure 48: Comparison of the washout coefficient parameter between the non-occluded and the occluded groups……………………………………………………………………..77

Figure 49: Scatter plot comparison of the washout coefficient values between the non-occluded and occluded groups…………………………………………………………………...78

Figure 50: Top: ROI segmentation pre (left) and post (right) in patient CM021 and quantified washout curves pre and post (center) Bottom: ROI segmentation pre (left) and post (right) in patient LM025 and quantified washout curves pre and post (center)……………………….86

Figure 51: Example of venous overlay correction in patient DW032. Top panel represents the pre device data and bottom panel represents the post device data. Left image represents aneurysm ROI segmentation in red. Center left represents segmentation of venous ROI overlaying the aneurysm in blue and center right represents the venous ROI marked to calculate the average venous contrast drainage. Plots on the right represent the washout curves prior to correction (red) and post venous overlay correction (blue)………………………………………………….88

Figure 52: Venous overlay correction in patient MA031. Top panel represents the pre device data and bottom panel represents the post device data. Left image represents aneurysm ROI segmentation in red. Center left represents segmentation of venous ROI overlaying the aneurysm in blue and center right represents the venous ROI marked to calculate the average venous contrast drainage. Plots on the right represent the washout curves prior to correction (red) and post venous overlay correction (blue)…………………………………………………….89

Figure 53: Application of notch filter to eliminate the contrast leakage signal from the concentration time curves for large (top panel) and giant (bottom panel) patient aneurysms respectively pre and post flow diverter implantation (effect of contrast leakage on the amplitude of ripples in the curve dampened following device deployment……………………………91

Figure 54: Lower envelope filter applied on raw concentration time curve obtained from patient LC006. The raw unfiltered concentration time curve is in blue and the lower enveloped filtered curve is in red……………………………………………………………………………..92

Figure 55: Angiographic image analysis for patient CM021. Top panel represents the aneurysm ROI segmented pre and post device angiographic images and 6month follow up angiogram showing minimal residual filling. Bottom panel shows the mathematical model fitted on the washout curves obtained from angiographic image analysis………………………………..97

Figure 56: Angiographic image analysis for patient LM025. Top panel represents the aneurysm ROI segmented pre and post device angiographic images and 6month follow up angiogram showing complete occlusion of the aneurysm. Bottom panel shows the mathematical model fitted on the washout curves obtained from angiographic image analysis………………………...98

Figure 57: Angiographic image analysis for patient RG022. Top panel represents the aneurysm ROI segmented pre and post device angiographic images and 6month follow up angiogram showing complete occlusion of the aneurysm. Bottom panel shows the mathematical model fitted on the washout curves obtained from angiographic image analysis………………………...99

Figure 58: Angiographic image analysis for patient FC005. Top panel represents the aneurysm ROI segmented pre and post device angiographic images and 6month follow up angiogram showing aneurysm filling. Bottom panel shows the mathematical model fitted on the washout curves obtained from angiographic image analysis………………………………………100

Figure 59: Comparison of the contrast concentration washout mean amplitude pre and post flow diverter implantation (p=0.0016)…………………………………………………………102

Figure 60: Comparison of mean transit time obtained from the contrast concentration time curves pre and post flow diverter implantation (p = 0.0001)…………………………………......102

Figure 61: Comparison of mean convective time coefficient obtained from mathematical model fitting of the contrast concentration time curves pre and post flow diverter implantation (p<0.0001)………………………………………………………………………………103

Figure 62: Scatter plot comparison of convective decay time coefficient obtained from mathematical model fitting on the contrast concentration time curves among the occluded and non-occluded aneurysm groups pre and post flow diversion……………………………...104

Figure 63: Scatter plot comparison of the washout amplitude among the occluded and non-occluded aneurysm groups pre and post flow diversion…………………………………..105

Figure 64: Scatter plot comparison of mean transit time obtained from the contrast concentration time curves among the occluded and non-occluded aneurysm groups pre and post flow diversion…………………………………………………………………………………106

Figure 65: Top Left: Patient specific geometric model construction for CFD simulations through import of axial slice volume and 2D level set segmentation in SimVascular; Bottom Left: import of 2D artery contours to Rhinoceros for lofting to form a solid body; Top Right: Volumetric reconstruction from patient's Rotational Angiography scan; Bottom Right: corresponding CFD model………………………………………………………………………………………..115

Figure 66: Parent artery boundary used to obtain lumen centerlines and cross sections of the boundary going orthogonal to the centerline used to calculate the flow diverter wire centerline configurations in the patient geometry specific implanted format………………………….116

Figure 67: Flow diverter wire centerlines were intersected with the aneurysm boundary (left) to crop the wires (center) and restrict the device to be just sufficient to provide neck coverage; (right) Flow diverter solid model generated by lofting a circular cross section along the wire centerlines; the flow diverter is positioned inside the patient specific model………………117

Figure 68: Reconstructed volume body model for patient 1(CM021)imported in ADINA along with the flow diverter and discretized into tetrahedral mesh; inlet nodal coordinates extracted and imposed with a pulsatile flow waveform in the form of a fully developed Womersley velocity profile…………………………………………………………………………………………119

Figure 69: Reconstructed computational model for patient 2 (LM025) with flow diverters virtually deployed in position across the aneurysm (left), and the finite element mesh generated in ADINA with the cropped flow diverter virtually deployed in position (center) and expanded view on the right……………………………………………………………………………120

Figure 70: Patient 3 (RG022) modeling; volumetric reconstruction of CTA slices (left), reconstructed CFD model with flow diverter virtually implanted (center), and ADINA finite element mesh of the model with cropped flow diverter implanted…………………………..120

Figure 71: CFD model construction for DF023, a 75 year old female patient with a giant partially thrombosed aneurysm on the cavernous segment of LICA; rotational angiographic volume (left); parametric CAD model of patient geometry (center left); simulated flow diverter (center right); Pipeline device virtually implanted in the patient's parent artery (right)…………………….....121

Figure 72: Spatial maps of peak systolic velocity for Patient 1 (CM021) before (left) and after (right) flow diverter implantation obtained from CFD results demonstrating reduction in the velocity magnitude post flow diversion…………………………………………………...122

Figure 73: Spatial maps of peak systolic velocity for Patient 2 (LM025) before (left) and after (right) flow diverter implantation obtained from CFD results demonstrating reduction in the velocity magnitude post flow diversion………………………………………………….123

Figure 74: Spatial maps of peak systolic velocity for Patient 3 (RG022) before (left) and after (right) flow diverter implantation obtained from CFD results demonstrating reduction in the velocity magnitude post flow diversion………………………………………………….123

Figure 75: Spatially averaged intra-aneurysmal temporal kinetic energy plots for Patient 1-CM021(top), Patient 2-LM025(middle) and Patient 3-RG022 (bottom) obtained from velocity

vector results of CFD simulations; pre (blue) and post (red) device implantation plots are shown………………………………………………………………………………………..125

Figure 76: Mean spatially averaged kinetic energy results pre and post flow diverter implantation for the three patients derived from CFD simulations………………………………………..126

Figure 77: Percentage reduction in mean spatially averaged kinetic energy post flow diverter implantation for the three patients………………………………………………………..127

Figure 78: Angiographic parameters and kinetic energy results for Patient 1………………129

Figure 79: Angiographic parameters and kinetic energy results for Patient 2………………130

Figure 80: Angiographic parameters and kinetic energy results for Patient 3………………130

Figure 81: Percentage change in the convective decay time constant vs percentage change in mean kinetic energy with a trendline indicating weak correlation (p=0.54)………………..131

Figure 82: Percentage change in the average slope of angiographic wash-in vs percentage change in mean kinetic energy with a trendline indicating weak correlation (p=0.423)……………131

Figure 83: Percentage change in the average slope of angiographic wash-out vs percentage change in mean kinetic energy with a trend line indicating weak correlation (p=0.382)……132

List of Tables

Table 1: Design parameters for the three experimental helical stents for CFD validation.………………………………………………………………………….…..20

Table 2: Dimensions of the aneurysms induced in the 18 rabbits analyzed in this work ….68

Table 3: Details of aneurysm location, aneurysm dimensions, and morphology for the clinical cases analyzed………………………………………………………………………………82

Table 4: Number of flow diverters implanted at treatment procedure……………………..83

Table 5: Treatment outcome at 6 month follow up, and repeat treatment information for each patient (TBD-to be determined)……………………………………………………………95

Table 6: Washout parameter results derived from concentration time curves pre and post flow diverter treatment (* indicates statistically significant)……………………………………101

Table 7: Occluded vs Non occluded comparison of washout parameters pre and post flow diversion (* indicates statistical significance)……………………………………………...104

Acknowledgments

I would like to thank my advisor Dr Barry Lieber for the opportunity to pursue a doctoral degree under his guidance in his lab. His guidance is paramount to the successful completion of this work. I thank him for the continued financial support during the years of my doctoral study. He has always been there to show the way, especially when I could not see light at the end of the tunnel. I thank him for providing with all the resources required to complete this work.

I sincerely appreciate the mentorship, guidance and friendship from Dr Chander Sadasivan. He has been a role model and a constant source of inspiration.

I would like to thank Dr Danny Bluestein and Dr Yi-Xian Qin for their time and guidance and being on my doctoral dissertation committee.

I thank Dr Henry Woo and Dr David Fiorella for their guidance. Their mentorship helped me develop a clinical and translational focus to solve the problems in this work. I appreciate them devoting their valuable time towards research despite their busy clinical practice. The partnership of Drs Henry Woo, David Fiorella, Barry Lieber and Chander Sadasivan established a world class basic science research program for neurovascular pathologies and I was fortunate to receive their collaborative guidance at the cerebrovascular research lab, within department of neurological surgery at Stony Brook University. I also thank Dr Lissa Peeling, my colleague and mentor during the early years of my dissertation. I sincerely appreciate the clinical education I received during the course of this study and will strive to translate it.

I appreciate the guidance and assistance from the clinical research, radiology, and nursing staff at the cerebrovascular center for collecting and providing patient data for the clinical aspect

of this work. Special thanks to Marlene Baumeister, Dawn Madigan, and Christine Giunta for their assistance with patient enrollment and data acquisition for the clinical study.

I would like thank the DLAR staff including Dr Tom Zimmerman, Nicole Steinhauff, Joan Dejesus and Jean Rooney at Stony Brook University for their assistance during the animal studies conducted for this work.

I thank the current and past members of the cerebrovascular lab including Vasantha Rupasinghe, Julia Fu, Andrew Pagano, Joe Santore, Ari Kappell. I appreciate the guidance from Dr Yared Alemu and Dr Mike Xenos of the Biofluids lab for the finite element simulations. I thank the colleagues from the Biofluids lab including Jawaad Sheriff, Matteo Bianchi, Philip Chiu, Chao Gao, Gil Marom, Peng Zhang, Xuan Liang, and Dinesh Peter for their friendship. I would like to thank the students from department of biomedical engineering.

I thank Betty Bosler, Priscilla Munoz, Marlene Baumeister and Susan Fiore at the department of neurological surgery at Stony Brook University for their assistance with administrative matters and allocating funds for financial support.

This work is dedicated to my parents Dr. Jashwant Dholakia and Mrs. Nalini Dholakia. I am deeply indebted to them for all their sacrifices they made to provide me with the best education. I am thankful for their love, continuous support and encouragement throughout the duration of the doctoral program. I thank my brother Yash for the motivation to pursue the doctoral program.

CHAPTER 1: INTRODUCTION

Background and Clinical significance

Statistics published in 2014 by the American heart association show that stroke is the leading cause of disability in adults as well as the third leading cause of deaths [2]. Annually about 795,000 people (370,000 males and 425,000 females) in the US suffer a stroke 600,000 of which are a first time stroke while the remainder are recurrent ones. In 2010, fatal stroke amounted to 129,476 cases in the US (52,367 males (40.4%), 77,109 females (59.6%)). Including stroke survivors, 6.8 million people (2.8% of the total population) were affected by stroke in the US. The annual direct and indirect cost burden of stroke in the US was $36.5 billion. The projected total cost burden of stroke is expected to reach $95 billion in 2015 and $185 billion by 2030[2]. Smoking, hypertension, and obesity are among the leading factors correlated to the occurrence of stroke [3].

The majority of strokes, about 81%, are ischemic strokes which occur due to blockage of blood supply to a particular area of the brain[2, 4]. This blockage may result from an embolus that may originate from the heart as a result of atrial or ventricular fibrillations. The embolus can travel and lodge in distal cerebral vessels. Ischemic stroke may also occur due to atherosclerotic intracranial arterial disease.

Hemorrhagic stroke occurs in 19% of all strokes due to rupture of arteries inside the brain. Intracranial hemorrhage induces swelling of brain tissue as well as increase of intracranial pressure resulting in vasospasm of cerebral arteries. Intracerebral hemorrhage occurred in approximately 14.5% of all strokes and 4.8% present with subarachnoid hemorrhage[5-18].

Intracerebral hemorrhage results from rupture of blood vessels inside the head due to vascular malformations, aneurysms, hypertension, or trauma. Subarachnoid hemorrhage occurs due to bleeding in the subarachnoid space between the pia matter and the grey matter resulting from aneurysm rupture or head trauma[5, 19]. Rupture of brain aneurysms is the cause of approximately 5% of all stroke cases[5, 19]. Brain aneurysms are abnormal ballooning or dilations of intracranial arteries which when left untreated may rupture leading to fatal outcome for the patients.

The causes of brain aneurysms are not clear, however, they are more prevalent among the older populations[2, 13, 18, 20]. The blood flow to the brain is supplied by the left and right internal carotid and vertebral arteries. The internal carotid arteries bifurcate to into the anterior and middle cerebral arteries. The left and right vertebral arteries (VA) join to form the basilar artery (BA) which then bifurcates into the posterior cerebral arteries [4]. The posterior cerebral arteries (PCA) along with the posterior communicating arteries (PComA), the internal carotid arteries (ICA), middle cerebral arteries (MCA), anterior cerebral arteries (ACA) along with the anterior communicating artery (AComA) form the circle of Willis at the base of the brain [4] (Figure 1). As a result of the communication between the anterior and posterior circulation, collateral flow is established in case of blockage of one of the major arteries supplying the brain. About 90% of all brain aneurysms occur at one of the locations on the circle of Willis. The most common location of ruptured aneurysms is the ACA followed by the MCA and then the BA [4, 11, 20-24] as see in Figure 1. Brain aneurysms mainly occur at bifurcations or branching of arteries, although, around 10% of giant aneurysms (>25 mm diameter) are seen in the cavernous segment of the internal carotid artery [4].

Treatment of brain aneurysms

The treatment of brain aneurysms is dependent on their anatomic and geometric features. Based on their shape or anatomy, brain aneurysms could be categorized as saccular or fusiform. Saccular aneurysms are spherical in shape and do not engulf the entire vessel circumference[9, 10, 25, 26]. Fusiform aneurysms are spindle like aneurysms which engulf the parent artery rather than emanating only from the sidewall[4, 9, 10, 25, 26].

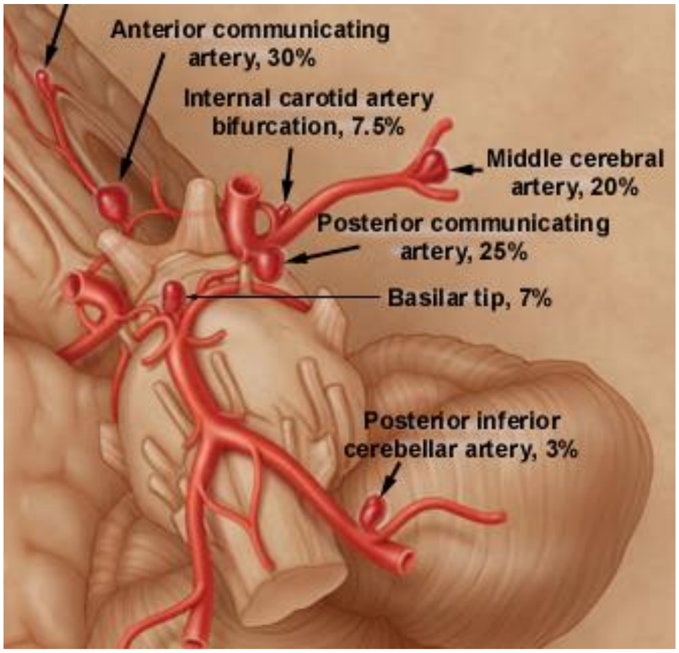

Figure 1: Schematic of locations and prevalence of aneurysms in the cerebral circulation (adapted from [20])

Historically, intracranial aneurysms have been treated surgically by clipping off the aneurysms at the neck to exclude them from the circulation[4, 20, 27] (figure 2). However, surgical treatment of an aneurysm is a highly invasive procedure and involves risk of morbidity to the patients and also longer recovery times[27-29].

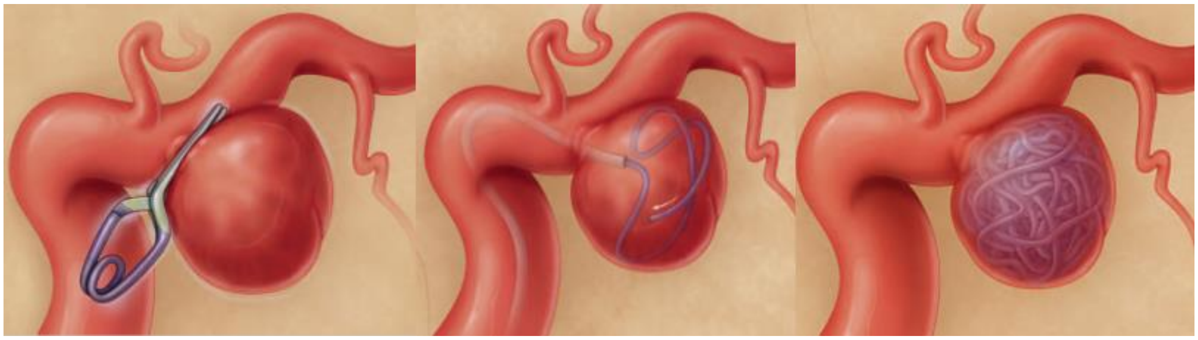

Figure 2: Schematic demonstrating treatment options for brain aneurysm including surgical clipping (left) and endovascular coiling (middle and right) (adapted from [20])

The advent of medical imaging and increasing availability of endovascular devices steadily increased the use of fluoroscopically guided endovascular treatment methods due to their minimally invasive nature[30-33]. Briefly, an introducer sheath is inserted into the femoral artery of the patient to gain entry into the arterial system. Diagnostic catheters are then inserted through the introducer sheaths and angiograms are obtained by injecting radio opaque contrast containing iodine to delineate the lumen of the arteries. Treatment choices are then made after the precise configuration of the aneurysm is elucidated by the angiograms. The current gold standard treatment choice is intrasaccular aneurysm coiling. Coiling was the first FDA approved endovascular treatment of sidewall aneurysms in 1995[32, 34]. Bare metal platinum or hygroscopic coils are packed into the aneurysm to achieve embolization and subsequent elimination of the aneurysm from the circulation[4, 33, 35-38] (figure 2). Coiling is only possible for narrow neck aneurysms where the coils are likely to stay within the aneurysm and not herniate into the parent vessel. For wide necked sidewall aneurysms as well as large to giant aneurysms, which may be either fusiform or saccular in nature, coiling is not practical and/or difficult to implement. Coils have associated shortcomings even when implanted in narrow neck aneurysms. Coil compaction (Figure 3) and aneurysm recanalization are the most common shortcomings that require follow ups to ensure complete cure.

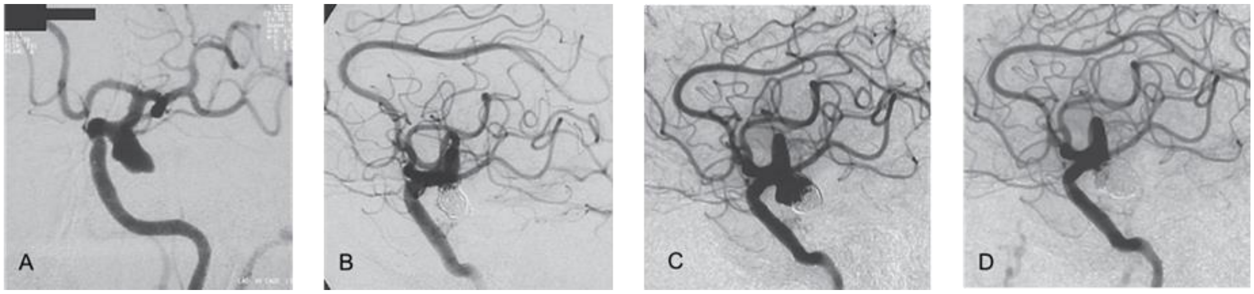

Figure 3: Angiogram of a PComA aneurysm (A) treated with endovascular coiling (B). Recanalization was observed at 8 month follow up (C) and the patient subsequently was re-treated (D)[20].

In the last two decades flow diversion emerged as an endovascular treatment option for complicated aneurysm such as wide necked, giant, and fusiform aneurysms that are not amenable to coiling[39-46]. Early experience with flow diversion was through deployment of coronary or carotid stents[40, 41, 47] that later evolved into porous fine wire braided self-expanding devices. Flow diverting devices are deployed across the neck of the aneurysm to impede flow inside the aneurysm and provide a scaffold for cellular proliferation and development of a layer of endothelium over it. The process of parent vessel remodeling[41, 46, 48] and establishment of a neointima excludes the aneurysm from the circulation. In 2011, FDA approved a highly porous fine wire braided device called Pipeline Embolization Device (Chestnut Medical-ev3-Covidien-Medtronic) following successful clinical trials [39, 42-45] (Figure 4). It is however, unclear how many devices per aneurysm were required to be implanted concentrically to occlude the flow into the aneurysm.

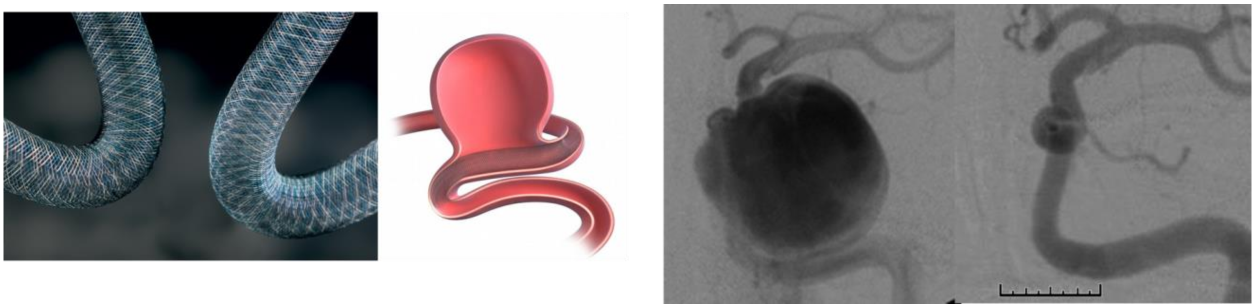

Figure 4 Images of Pipeline embolization device in expanded form (left) and schematic deployment in giant wide necked aneurysm (center); Giant aneurysm before Pipeline treatment and at follow up showing aneurysm excluded from circulation (right).

Clinical problem: Efficacy of flow diversion

Efficacy of flow diverters depends on porosity and pore density, or permeability, of the device as well as the anatomic configuration of the aneurysm and its positioning relative to the oncoming flow as well as the flow rate in the parent artery [1, 41, 47-54]. Fusiform aneurysms require a lower porosity device, or more devices to be deployed concentrically, as compared to a wide necked sidewall aneurysm. Adequacy of the flow diversion effect following deployment of the first device is based on qualitative angiographic assessment of contrast transport into and out of the aneurysm. Increase in contrast residence time in the aneurysm may be assessed based on the recirculation or a slower washout of contrast from the aneurysm compared to contrast washout time prior to the implantation of devices. If needed, more devices can be deployed until contrast residence time is in the aneurysm is deemed to be sufficient to occlude the aneurysm within six months which needs to be confirmed by follow up examination. In case the aneurysm is not completely occluded by then, further treatment options can be decided upon at that time[39, 42].

The mathematical modeling of transport of a dye flowing through blood vessels can be traced back to the observation made by Bassingthwaigthe (Figure 5) that dispersion of the dye was a lagged normal process [55]. In angiography estimation of blood flow rates was attempted based on time to peak concentration of contrast or half time to peak values at different points along the length of an artery. However, such estimations while simple to obtain are not accurate and use only a small part of the information contained in the concentration time curve. Thus, the lagged normal distribution function was also applied to the contrast concentration time curves or washout curves to study the flow in straight tubes or arteries [56].

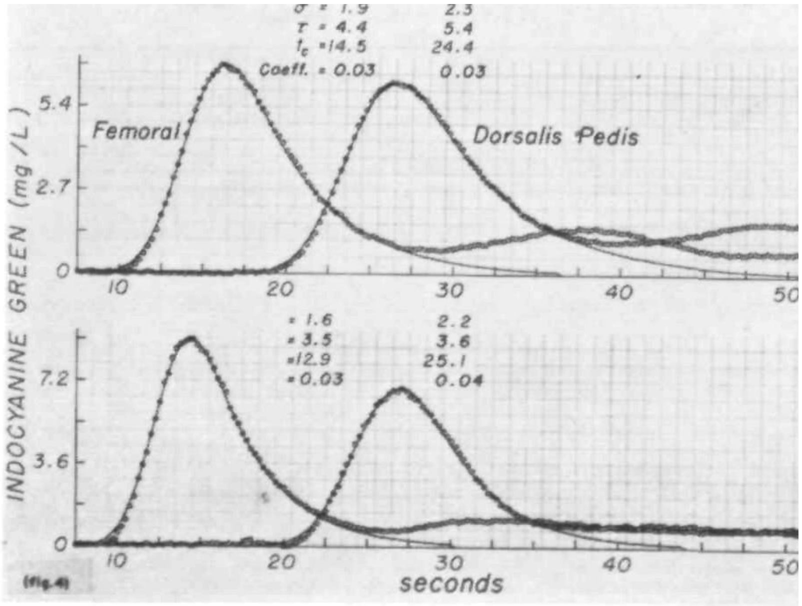

Figure 5: Dye concentration intensity levels following injection in different blood vessels (adapted from [55])

The rabbit elastase induced aneurysm is a widely used model for investigating the biological response to the implantation of endovascular implants such as coils and flow diverters[54, 57-65]. One method to obtain information on the efficacy of flow diverters in the live animal prior to sacrifice and examination of histology is to apply the mathematical model that has been described previously. That model is based on the lagged normal model developed earlier but it further divides the angiographic washout from the aneurysm into convective and diffusive components of mass transport [46, 53, 54, 57, 66]. The first term of the model represent the advective contrast transport that is described by the convolution of a lagged normal and an exponential decay. The second term of the model represents the diffusive process of contrast transport out of the aneurysm. This model has been utilized to compare various designs of flow diverters as well as prediction of their treatment efficacy. However, a statistical confidence level of 95% has not been reached yet using previously available data and it remains unclear which components of the washout curves more directly relates to rates of aneurysm occlusion. A larger sample size can help to elucidate the salient washout component that will help to predict aneurysm occlusion[53, 56, 57].

To the best of our knowledge this is the first pilot study that uses high speed angiography to obtain the intra-aneurysmal contrast concentration data in humans. Previous investigations have been using angiograms that were acquired at low frame rates yielding low resolution washout curves and consequently poor model fits to the data[66]. High speed angiography of contrast washout from human brain aneurysms will help to develop a washout index from the pertinent convection and diffusion coefficients.

Cerebral aneurysm hemodynamics and changes thereof as a result of implantation of various devices was investigated both experimentally and with computational fluid dynamics[49, 67-82]. As computer power increased so did the resolution of the computational simulations. Nevertheless, most CFD studies seem to be content with reporting qualitative results in the form of color or vector maps rather than reduce a tremendous amount of information produced by the simulations to quantifiable indices that can provide a quantitative discriminant among similar results. Another pitfall in using such simulations is the lack of critical validation of many CFD studies against experimental data[83-87]. Unless validated, the simulation should be viewed with caution particularly if attempts are made to apply them to clinical decision making or for device evaluation. Xu *et al* in a recent study compared the effects of using idealized configurations of flow diverters with microCT image based flow diverter geometries on the intra-aneurysmal hemodynamics in the rabbit elastase-induced aneurysm model and they found significant differences [88]. Flow Diverter wires do not maintain uniform isotropic orientation when expanded into an artery across the aneurysm. The tortuosity of the confounding cerebral vessels result in device wires slipping over each other to establish new configurations. Current CFD studies with flow diverters in cerebral aneurysm models use more realistic wire configurations in the models. The local changes in porosity and pore density across the aneurysm neck can help produce more accurate representation of the flow inside the aneurysms past the diverter struts [80, 81].

A computational approach which relies on existing theoretical solution to simplified problems and on more complicated problems that were investigated experimentally can serve as a basis for computations on further complicated domains. Such an approach would provide computational results with higher degree of confidence in accuracy when applied to clinically relevant problems. High resolution computational flow simulations can provide detailed flow information on a local scale that is otherwise unavailable. The inherently 4 dimensional nature of CFD calculations can supplement experimental information such as CT or angiography. [1, 47, 48, 50-52, 56, 66, 89]. A recent study using particle image velocimetry (PIV) demonstrated that the magnitude of the velocity inside the aneurysm reduced significantly after deployment of flow diverter as compared to control [90] and showed a correlation between hydrodynamic parameters of flow and the coefficients of the contrast transport equation [50] . CFD calculations can produce the hydrodynamic flow parameters with a higher level of detail and these can be better related to the angiographic washout parameters. Thus, CFD can underpin the calculations of angiographic contrast concentration curves or complement PIV measurements *in vitro*.

The goal of this work was first to validate CFD simulations against prior PIV data. Second, apply angiographic washout analysis to intra-aneurysmal hemodynamics post flow diversion in a simplified bench-top model and compare the results to kinetic energy calculation inside the aneurysm using CFD. Third, compare washout calculations to kinetic energy analysis in the rabbit Elastase aneurysm model and extend the analysis to data obtained from human patients. The overall goal was to develop predictive indices to determine the efficacy of flow diverter treatment of cerebral aneurysms while the patient is still undergoing the procedure.

This work was conducted in the form of the following hypothesis and specific aims developed and implemented to test the hypothesis.

Hypothesis and specific aims

The primary hypothesis of this work was that parameters obtained from angiographic and computational fluid dynamics analysis can predict the long-term outcome of flow diversion treatment for cerebral aneurysms.

The above hypothesis was tested through the following specific aims.

Specific Aim1: Evaluate and compare intra-aneurysmal hemodynamics in idealized sidewall aneurysm models before and after implantation of 5 commercial neurovascular stents using angiographic analysis and CFD simulations.

Five commercially available neurovascular stents/flow diverter devices including Pipeline embolization device (PED), flow redirection endoluminal device (FRED), Low-profile Visualized Intraluminal Support (LVIS) device, Enterprise, and Neuroform will be implanted in silicone sidewall aneurysm models. Experimental flow characteristics will be captured through high speed angiography. The exact implanted position and geometry of the devices will be obtained through microCT scanning of the models. Flow diversion properties of the devices will be evaluated and compared through contrast washout analysis and microCT image based CFD model analysis. Experimental and numerical data will be correlated.

Specific Aim 2: Establish and verify washout parameters in the flow-diverted rabbit elastase aneurysm model that correlate to treatment outcome.

The rabbit elastase induced aneurysm model will be used for evaluation of flow diversion. High speed angiographic data acquired pre and post flow diverter implantation in 22 rabbits will be analyzed to obtain the intra-aneurysmal washout curves. Outcome of treatment will be recorded based on angiographic follow up at 3 weeks, 12 weeks, and 24 weeks. Washout curves will be fit to mathematical models to obtain the convective and diffusive components of contrast transport. Coefficients of convective and diffusive contrast transport will be evaluated as predictive indices of aneurysm occlusion. Correlation analysis between washout parameters and treatment outcome of aneurysm occlusion will be performed. Washout parameter that predicts flow diverter treatment outcome will be established

Specific Aim 3: Establish and correlate hemodynamics parameters in patients undergoing aneurysm flow diverter treatment to outcome using angiographic contrast washout and CFD analysis.

High speed angiograms will be obtained pre and post Pipeline implantation in brain aneurysm patients (n=40). Angiographic follow up will be performed at 6 months to record the outcome of treatment. Clinical washout curves will be obtained from angiographic data acquired during treatment. Coefficients of convective and diffusive contrast transport will be calculated following fitting of washout curves to a mathematical model and correlated to treatment outcome. For CFD analysis, geometric models of aneurysms will be constructed from rotational angiograms. Deployed configuration of the Pipeline devices will be virtually implanted in the CFD models. CFD analysis will be conducted in ADINA (Watertown, MA) and hydrodynamic parameters calculated from the results will be correlated to washout parameters. We will test whether efficacy of flow diversion can be predicted prospectively through retrospective correlation of the treatment outcome with angiographic and CFD analysis.

CHAPTER 2: VALIDATION OF CFD SIMULATIONS

ANALYTICAL VALIDATION

It is customary to use the conservation of mass and fluid momentum equations for computational fluid dynamics simulations of hemodynamics.[91-95]. Conservation of mass (continuity) equation is generally expressed as:

[*rate of mass accumulation in a control volume*] = [*rate of mass in*]-[*rate of mass out*]. 1

Equation 1 can be expressed mathematically as:

$$\frac{\partial \rho}{\partial t} + \frac{\partial(\rho u)}{\partial x} + \frac{\partial(\rho v)}{\partial y} + \frac{\partial(\rho w)}{\partial z} = 0 \qquad 2$$

where ρ is the density of fluid, and u, v and w are the x, y and z components of the velocity vectors u, v and w, respectively.

The Navier-Stokes equations express the second law of Newton for the motion of an incompressible fluid and incorporate conservation of mass and linear momentum [92, 94, 95]. These are non-linear partial differential equations are:

$$\rho\left(\frac{\partial u}{\partial t} + u\frac{\partial u}{\partial x} + v\frac{\partial u}{\partial y} + w\frac{\partial u}{\partial z}\right) = -\frac{\partial \rho}{\partial x} + \rho g_x + \mu\left(\frac{\partial^2 u}{\partial x^2} + \frac{\partial^2 u}{\partial y^2} + \frac{\partial^2 u}{\partial z^2}\right) \qquad 3$$

$$\rho\left(\frac{\partial v}{\partial t} + u\frac{\partial v}{\partial x} + v\frac{\partial v}{\partial y} + w\frac{\partial v}{\partial z}\right) = -\frac{\partial \rho}{\partial y} + \rho g_y + \mu\left(\frac{\partial^2 v}{\partial x^2} + \frac{\partial^2 v}{\partial y^2} + \frac{\partial^2 v}{\partial z^2}\right) \qquad 4$$

$$\rho\left(\frac{\partial w}{\partial t}+u\frac{\partial w}{\partial x}+v\frac{\partial w}{\partial y}+w\frac{\partial w}{\partial z}\right)=-\frac{\partial \rho}{\partial z}+\rho g_z+\mu\left(\frac{\partial^2 w}{\partial x^2}+\frac{\partial^2 w}{\partial y^2}+\frac{\partial^2 w}{\partial z^2}\right) \tag{5}$$

Where, *g* is an external force such as the gravitational acceleration given in the *x*, *y* and *z* directions.

Poiseuille solution for steady flow:

An analytical solution for steady fluid flow in a straight tube, known as the Hagen-Poiseuille equation, is derived by simplifying the Navier-Stokes equations and applying the boundary conditions [93, 94]. It is a useful solution for simple initial validation of numerical simulations of blood flow in simplified models of arteries.

The Poiseuille solution for the velocity profile of steady flow in a straight tube is shown in equation 6.

$$u_z = -\frac{1}{4\mu}\frac{\partial p}{\partial z}(R^2 - r^2). \tag{6}$$

The pressure gradient along the length to the straight tubel can be derived directly from the Poiseuille equation and is given as:

$$\Delta P = \frac{32\mu L\, u_{z\,\mathrm{avg}}}{D^2}. \tag{7}$$

Analytical validation of CFD simulations was first conducted on an idealized straight tube model that was constructed based on the canine femoral artery diameter in previous experiment [96]. The radius was kept at 2.28 mm and length of the tube at 10 cm to provide sufficient length for the flow to fully develop. Boundary conditions were applied based on the measured blood flow and pressure values [Figure 6] [96].

All simulations were performed using a upwinding stabilized finite element method in Galerkin formulation to solve the governing equations of fluid flow for conservation of mass (continuity) and balance of fluid momentum (Navier-Stokes) equations [92] using a commercial finite element software package ADINA 9.0 (ADINA R&D, Watertown, MA). Steady flow simulations were run on the straight tube model with a mean flow rate of 1.41ml/sec imposed at the inlet and mean pressure of 110 mmHg applied at the outlet face. The steady flow was imposed on the inlet boundary condition in the form of a fully developed parabolic flow profile while on the outlet mean pressure was applied in the form of normal traction to act as resistance to blood flow. Rigid wall assumption was made with no-slip boundary condition applied at the walls. Blood was modeled as a Newtonian fluid having a constant viscosity of 4 cP and density of 1.05 gm/cm^3.

In order to test mesh independent results the simulations were performed for grids with an average tetrahedral element size 0.45mm, 0.4mm, 0.35mm, and 0.3mm. The simulation results were then compared with the analytical Poiseuille equations for pressure gradient and velocity profiles. Steady flow CFD results from ADINA were successfully validated against the analytical solution with errors of less than 10%. The simulation results were mesh independent beyond mesh element size of 0.35 mm.

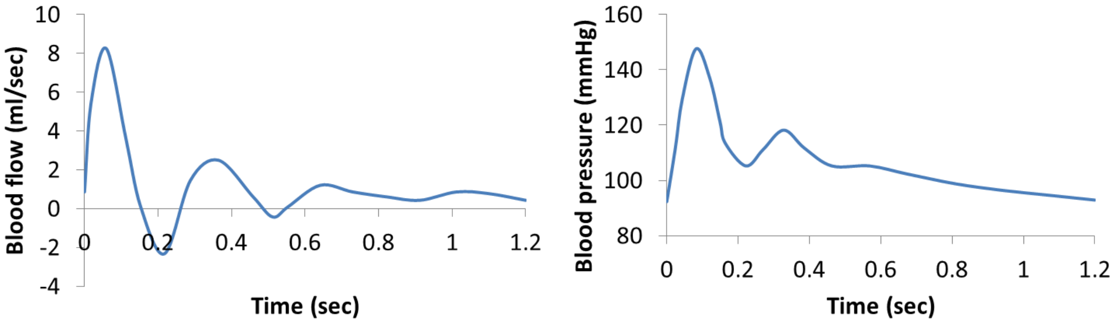

Figure 6: Experimentally recorded blood flow waveform (left panel) and pressure (right panel) in the canine femoral artery adapted from [96].

Womersley solution for pulsatile flow:

Womersley's theoretical analysis of pulsatile blood flow through arteries was published in 1955 [97]. The model considers unsteady (pulsatile) flow of a viscous Newtonian fluid in a tube of circular cross-section under a sinusoidal pressure gradient. The flow is considered incompressible, laminar and fully developed. The pulsatile pressure gradient (Equation 8) can be decomposed into harmonically related sinusoids of a Fourier series and each term treated separately. Assuming that superposition holds, the individual solutions can then be assembled into the final solution.

$$\frac{dp}{dz} = P \cdot e^{i\omega t} \qquad 8$$

The axial velocity profile for the pulsatile flow can be obtained by solving each harmonic and by summation of the obtained solutions. The velocity profile for each harmonic is expressed as a Bessel function:

$$u_z = \mathrm{Re}\left\{ \frac{AR^2}{i\mu\alpha^2} \left[\frac{1 - J_0\left(y i^{3/2}\alpha\right)}{J_0\left(i^{3/2}\alpha\right)} \right] e^{-i\omega t} \right\} \qquad 9$$

Where, Re represents the real component; R is the radius of the tube; μ is the fluid viscosity; $J_0$the zero order Bessel function, y = r/R is the ratio of the radial location to the vessel radius. The pulsatile nature of blood flow in arteries is characterized by a dimensionless parameter called the Womersley number [93-95]. The Womersley number, α, is defined as the ratio of the unsteady inertia forces to the viscous forces in the fluid and is given as:

$$\alpha = R\sqrt{\frac{\omega\rho}{\mu}} \qquad 10$$

Where ω is the angular frequency of the fluid motion and ρ is the fluid density.

An increase in α indicating that unsteady inertia dominates the flow with flatter flow profile and reduction in α indicates that viscous forces dominate the flow and result in a flow profile closer to the parabolic shape of steady flow[93-95]. The Reynolds number[93-95], Re, is used to characterizes steady flow and is useful in characterizing the transition of flow from laminar to turbulent. It is based on density and viscosity of the fluid, velocity of the flowing fluid as well as the diameter of the cylindrical pipe. Re is given as:

$$\mathrm{Re} = \frac{\rho V D}{\mu} \qquad 11$$

The Reynolds number Re is the ratio of steady inertial to viscous forces in the fluid.

Pulsatile flow simulations of blood flow in the same idealized straight tube model of the canine femoral artery were validated against Womersley solution described above. Time varying blood flow and pressure waveforms recorded in the canine femoral artery were applied as boundary conditions at the inlet and outlet, respectively (figure 5). At the inlet face the pulsatile waveform was imposed in the form a fully developed velocity profile obtained by Womersley's solution. The CFD simulations were performed for three cardiac cycles to diminish initial transience and ensure repeatability using ADINA on an in house 16 core serial server with 64 GB of RAM available (King Star supercomputer, Sunnyvale, CA). To test for mesh independence results free-form isotropic meshes were constructed in ADINA using Delaunay triangulation and boundary smoothing method with element average size of 0.35 mm and 0.3 mm.

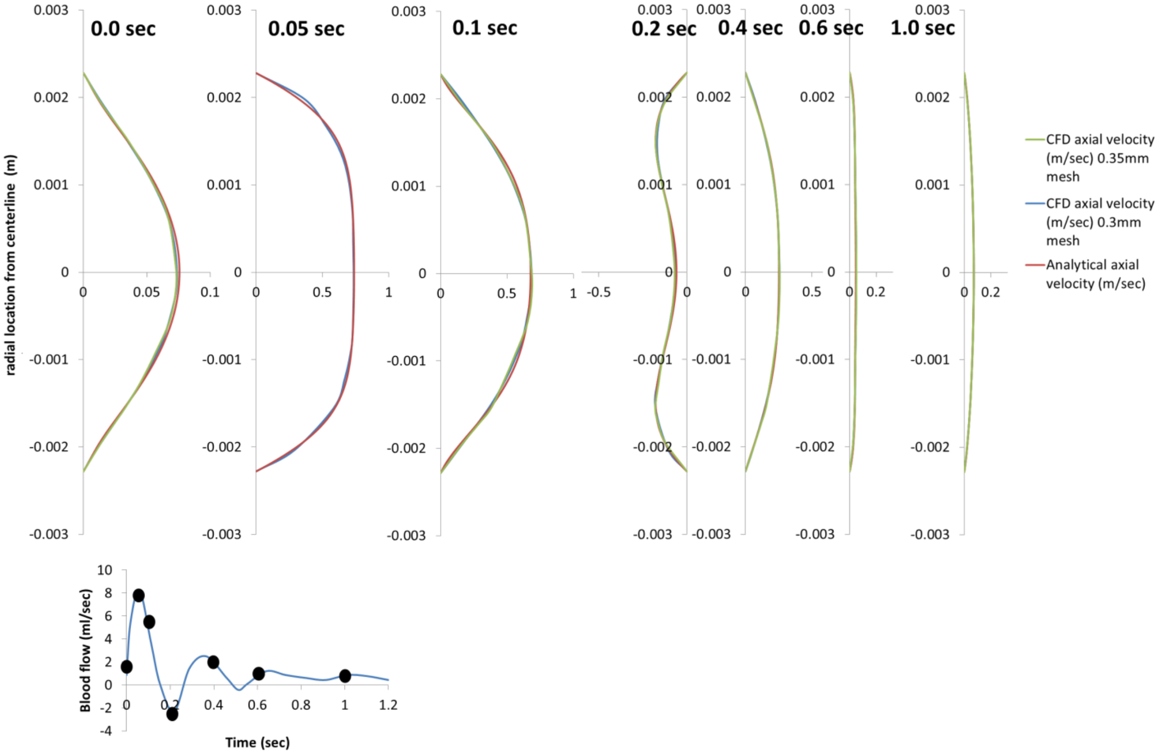

Figure 7: Comparison of CFD axial velocity profile (two different mesh sizes in green and blue) with Womersley analytical solution (red) at 7 different time points in the cardiac cycle.

Results from pulsatile CFD simulations in ADINA were successfully validated against the Womersley analytical solution. Mesh independence test indicated repeatability for isotropic meshes with 0.3 mm average element edge size (Figure 7). Validation of the analytical solution for steady and pulsatile laminar flow results indicates that the Galerkin finite element formulation with average element edge size of 0.3 mm is appropriate for flow simulations on more complicated geometries during the experimental validation part of the study.

EXPERIMENTAL VALIDATION

Methods:

Following analytical validation, experimental validation of CFD simulations in ADINA was performed against in vitro PIV data from idealized sidewall model experiments.

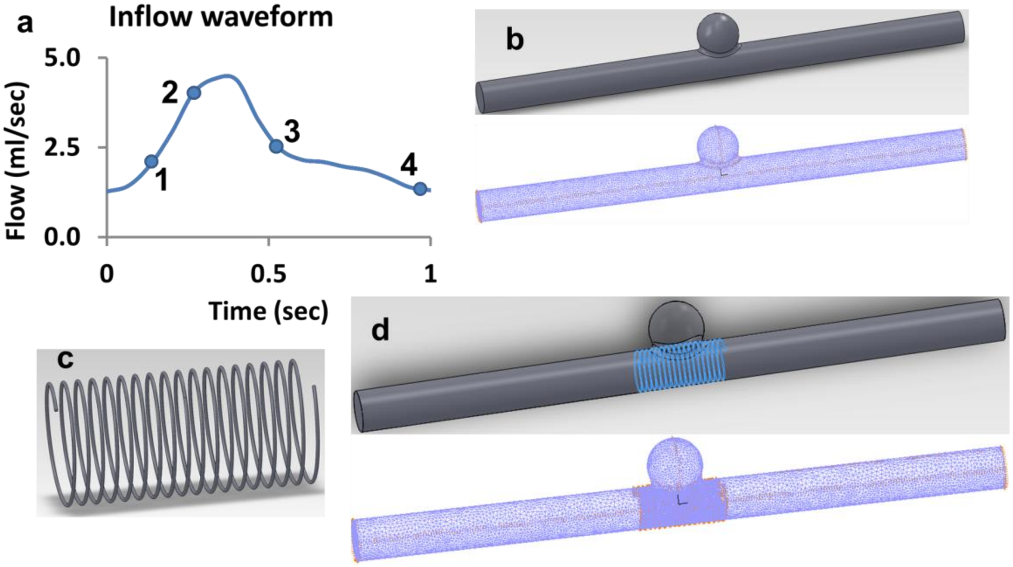

Figure 8: Pulsatile inflow waveform imposed at the inlet of the idealized sidewall aneurysm model (top left panel); helical stent constructed in SolidWorks (bottom left panel) and Boolean subtraction to obtain the stented model of reference.

For the experimental validation, CFD simulations were conducted retaining the geometry and boundary conditions of the experimental study. The flow waveforms used as the inlet boundary conditions for the experimental study were generated by varying the Womersley number α and the Reynolds number Re to generate different mean flow rates as well as vary the transient nature of flow [1, 66]. An idealized model of a side-wall saccular spherical aneurysm was created using a computer aided design (CAD) package SolidWorks 2011 (Dassault Systems, Waltham, MA).

Table 1: Design parameters for the three experimental helical stents for CFD validation.

Design parameter	Stent 1	Stent 2	Stent 3
Wire diameter (mm)	0.178	0.153	0.127
No of loops across the aneurysm	12	15	17
Porosity (%)	76	76	76

The dimensions of the computational model geometry were derived from the dimensions of the *in vitro* model (figure 8). The parent vessel diameter and the aneurysm diameter for the computational model were 6.35 mm and 8.45 mm, respectively. Spiral wires that served as flow diverters were deployed across the neck of the aneurysm (Figure 8d). Based on wire diameter and pitch, three devices of different number of loops across the neck were constructed using SolidWorks while maintaining a constant porosity of 76%. Stents #'s 1, 2, and 3 had wire diameters of 178, 153, and 127 μm; and 12, 15, and 17 spiral loops across the neck of the aneurysm, respectively, as given in Table 1. After positioning the stent across the neck of the aneurysm, the stented lumen models were obtained through Boolean subtraction of the stent from the vessel lumen [98].

CFD simulations for conservation of mass and momentum were performed in stabilized Galerkin finite element formulation using the commercial package ADINA 8.7 (ADINA R&D, Watertown, MA). For our pilot study, a pulsatile waveform with Womersley number 2.54, mean flow of 145.2 ml/min and cardiac cycle of 1 second in duration was mapped on to the inlet face nodes of the models in the form of a fully developed Womersley velocity profile. The vessel wall and the stent surface were assumed to be rigid and no-slip boundary conditions were applied. Flow in the models was assumed to be incompressible and laminar. A Newtonian fluid was assumed with a constant viscosity of 11.42 cP and a density of 1.1475 gm/ml consistent with experiments.

Automated Delaunay meshing scheme in ADINA was used for discretizing the domain. A sidewall aneurysm model with no stent deployed (serving as control) was meshed to 316,931 tetrahedral elements whereas the stented models contained between 2 to 3 million tetrahedral elements in highly anisotropic meshes (Figure 8). The mesh density was higher around the stent wire surfaces as compared to the vessel walls in the model. After an initial flow ramp reaching the diastolic conditions, all simulations were allowed to run for 3 cardiac cycles. The results obtained from the last cardiac cycle were used to calculate hemodynamic parameters and for flow pulsatile flow.

Flow quantification

Results obtained from the simulations are in the form of velocity vectors and pressure distribution. Comparing velocity profiles visually would be a qualitative assessment of the intra aneurysmal hemodynamics. Therefore, hemodynamic indices of vorticity, hydrodynamic circulation, and kinetic energy were derived from the velocity vector field using in house programs to compare these parameters of the intra-aneurysmal flow to the experimental PIV data.

Vorticity describes the rotational nature of the fluid elements. Mathematically, vorticity (ζ) is defined as the curl of the velocity vector or twice the angular velocity of the fluid element.

$$\vec{\zeta} = \nabla \times \vec{V} \qquad 12$$

$$\vec{\zeta} = (\frac{\partial w}{\partial y} - \frac{\partial v}{\partial z}) \cdot \vec{i} + (\frac{\partial u}{\partial z} - \frac{\partial w}{\partial x}) \cdot \vec{j} + (\frac{\partial v}{\partial x} - \frac{\partial u}{\partial y}) \cdot \vec{k} \qquad 13$$

Hydrodynamic circulation is a obtained from the vorticity and it describs the overall rotational nature of the fluid domain in the area of interest [91]. Circulation, Γ, is defined as the line integral of fluid velocity around a closed path.

$$\Gamma = \oint \vec{V} \cdot d\vec{l} \qquad 14$$

Using Stoke’s theorem, circulation can be defined as a surface intergral, and since vorticity is defined as the curl of the velocity vector, we obtain an expression for circulation in terms of the vorticity

$$\Gamma = \iint_A (\nabla \times \vec{V}) \cdot \vec{n} dA = \iint_A \vec{\zeta} \cdot \vec{n} dA \qquad 15$$

Where $\overrightarrow{dl}$ represents an element of the contour, A is the area of the contour elements and $\vec{n}$ is a vector normal to the surface of the contour.

Kinetic energy is a parameter to quantify the bulk flow phenomena inside the aneurysm. For the purpose of studying effects of flow diversion on intra-aneurysmal hemodynamics, kinetic energy can serve as an index characterising the decoupling of aneurysm flow from that in the parent artery. Kinetic energy of a fluid is expressed as:

$$E = \frac{1}{2}\rho V v^2 \qquad 16$$

Assuming that the density of the fluid ρ and volume of the fluid V remain constant, then only the velocity, *v*, is varying and the Kinetic energy can be simplified to $E \propto \sum v_i^2$. Thus kinetic energy inside the aneurysm can be calculated approximately as the summation of the square of the vector field inside the aneurysm. For comparison of CFD with PIV as well inter model comparison of CFD results, the velocity vector field needs to be interpolated onto a fixed uniform grid considering the anisotropic nature of the CFD meshes.

Results:

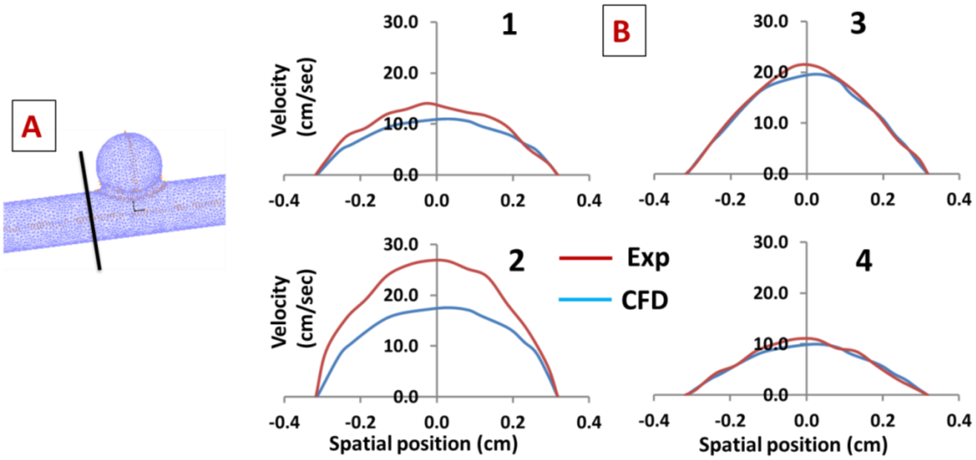

Figure 9: Location of cross section for extraction of axial velocity profiles (A) and comparison between PIV and CFD results (B) at four different time points in the cardiac cycle[1].

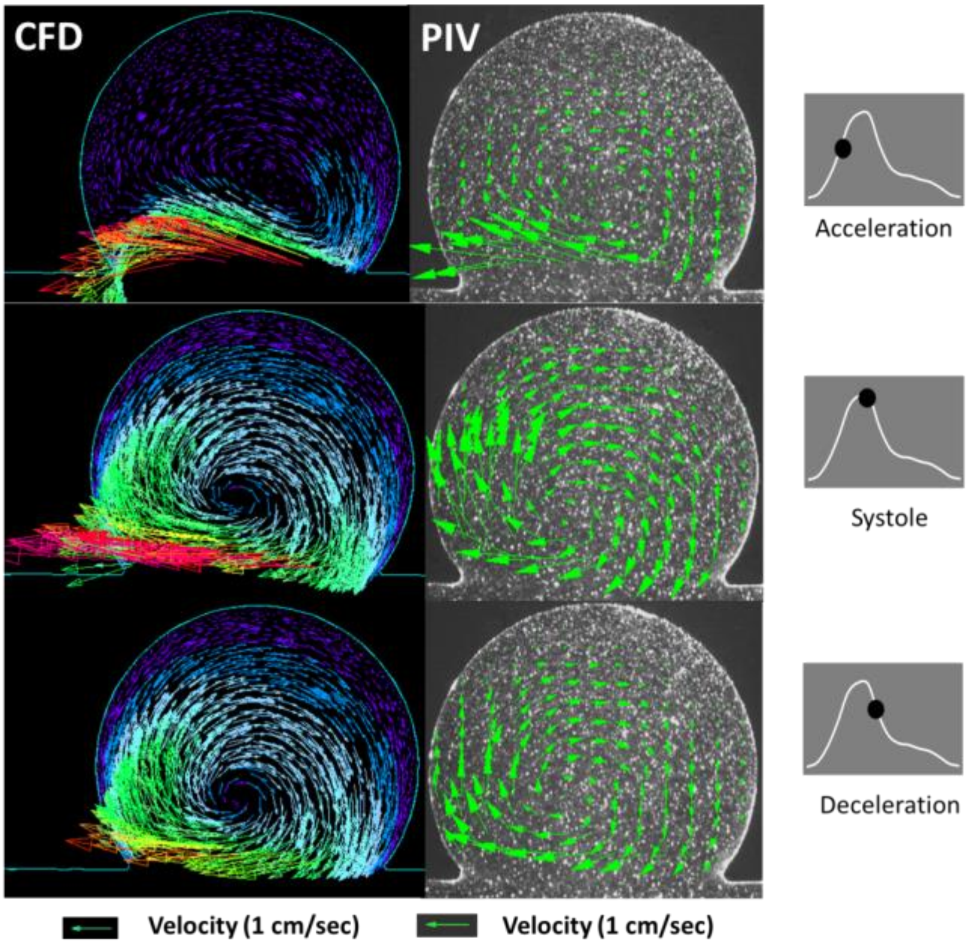

Figure 10: Direct comparison of intra-aneurysmal velocity profiles during acceleration (top), peak systole (middle) and deceleration (bottom) between CFD (left) and PIV (right)[1]

Intra-aneurysmal CFD velocity profiles are shown in figures 9 and 10. They are in good agreement with the PIV results [1]. High density of elements, hence high density of velocity vectors, around the aneurysm necks in comparison with the uniform PIV grid can be seen in Fig 10. For the control case, during early acceleration, fluid enters and exits the aneurysm quickly with anti-clockwise rotation of the velocity vectors near the neck. During the remainder of the cycle, a clockwise vortex develops in the aneurysm with the rotation of velocity vectors being more pronounced during peak systole (Figure 10). Post stenting, the clockwise vortex in the aneurysm was replaced with a continuous anti-clockwise rotation. Importantly, flow inside the aneurysm was reduced after deployment of the flow diverter (Figure 11).

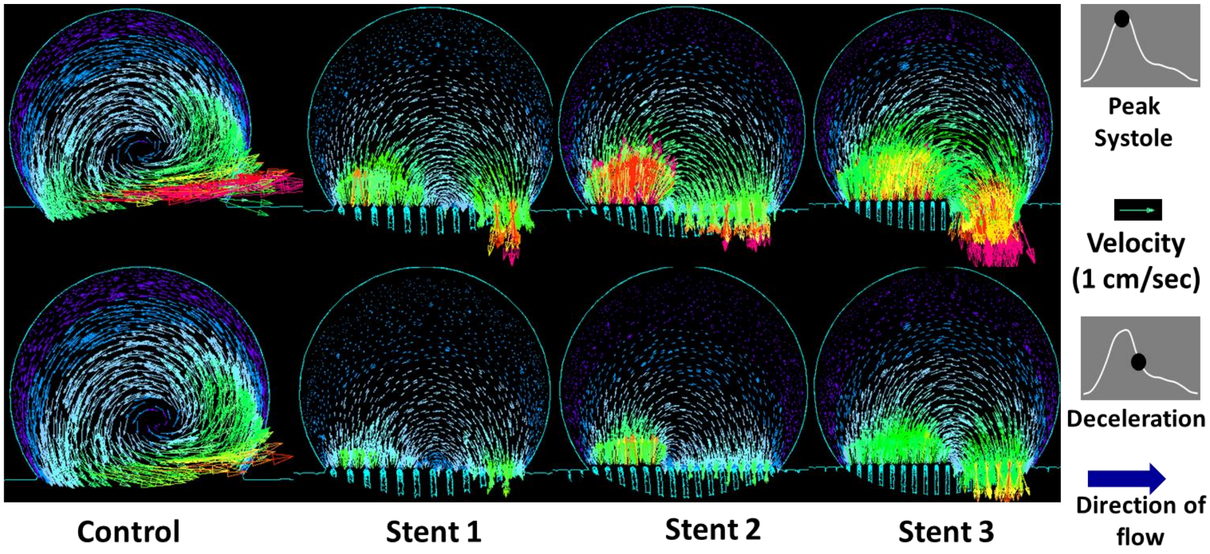

Figure 11: Intra-aneurysmal velocity in the control and the stented aneurysms during peak systole (top) and deceleration (bottom)

Flow activity inside the aneurysm was reduced for all stents compare to control. Flow reduction for stent1 and stent 2 was more than for stent 3 (figure 11). The simulation did not show any appreciable change in intra-aneurysmal pressure before and after stent placement. Furthermore, the pressure gradient between the inlet and outlets of the tube did not change much post stenting (figure 12). The pressure gradient for stent 3 was slightly elevated compare to the other 3 cases as seen in figure 12.

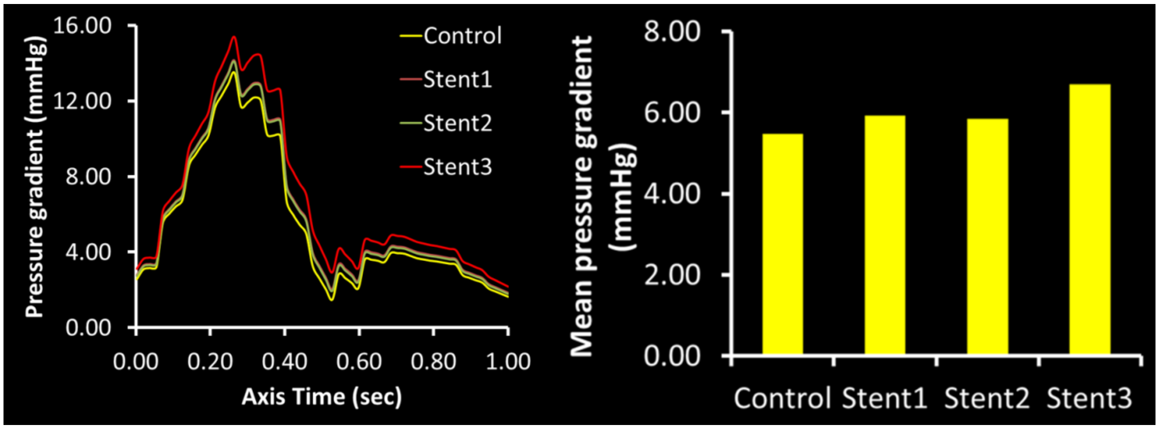

Figure 12: Temporal evolution of pressure gradient in the control and the three device cases (left); and mean pressure gradient comparison between the control and the stented models.

Alteration in intra-aneurysmal vorticity and hydrodynamic circulation in the plane of symmetry were obtained for comparison with PIV. The hydrodynamic circulation over the cardiac cycle is consistent with the PIV results (Figure 13). . In the control, the circulation follows the same pattern with minimal deviation. In the stented cases the circulation follows, in general, the same trend and magnitude as the experimental results but with fewer undulations. These differences may be attributed to the fact that in the experiments the stents were not anchored to the vessel wall, had low radial outward force, and may have fluttered as a result of viscous drag forces of the flow. Such fluctuations were not seen in the computational results. For the control case, peak circulation of 315.2mm^2/sec at 0.34 sec was consistent with the PIV peak value of 316.4 mm^2/sec at 0.34 sec. Among the devices, stent 2 has the lowest peak circulation at 7.7mm^2/sec, while stent 3 has the highest peak circulation at 13.0 mm2/sec (Figure 13). Overall mean circulation over the cardiac cycle is lowest for stent #2 followed by stent #1 and stent #3 (Figure 14).

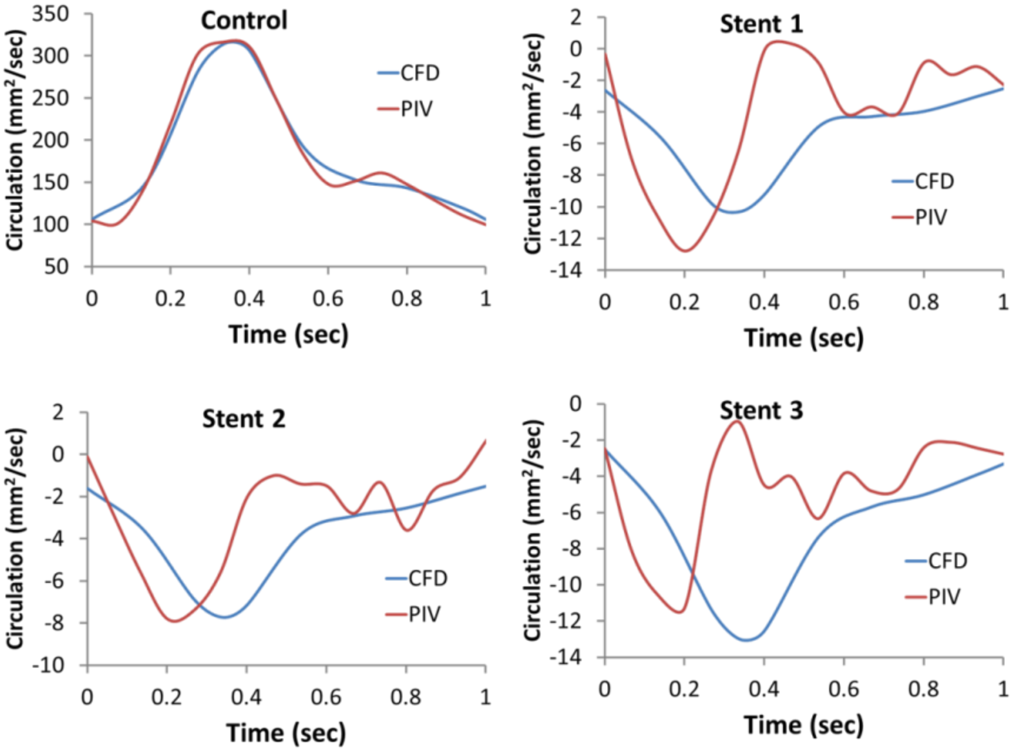

Figure 13: Temporal waveforms of intra aneurysmal circulation obtained in the Control, stent 1, stent 2, and stent 3 cases [1]

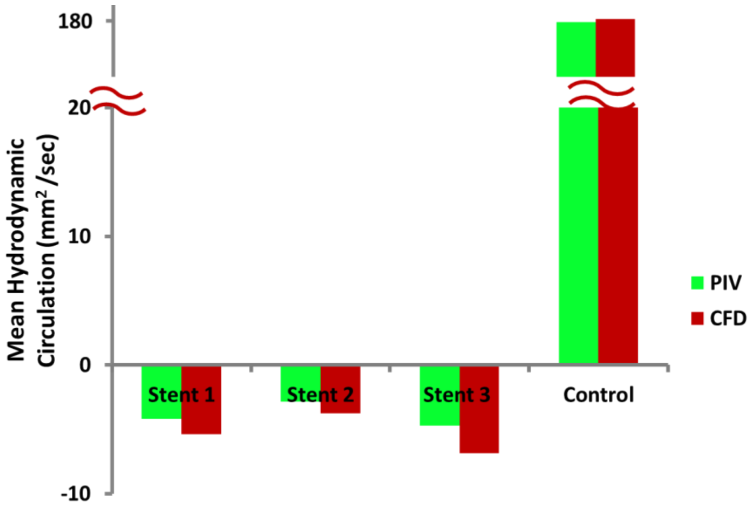

Figure 14: Mean hydrodynamic circulation comparison between PIV and CFD [1]

Kinetic energy inside the aneurysm was quantified as the summation of the square of the velocity vectors inside the aneurysm. Temporal waveforms of kinetic energy did not demonstrate much difference between stents 1 and 2 (Figure 15). However, both stent 1 and 2 appeared to considerably reduce kinetic energy inside the aneurysm as compare to stent 3. That indicates the despite having the same porosity, device pore density and wire diameter may affect the intra-aneurysmal hemodynamics significantly and determine the amount of reduction in flow entering the aneurysm. Overall, mean kinetic energy results were in line with the temporal results (Figure 15). Furthermore, every device reduced the kinetic energy by an order of magnitude when compared to the control.

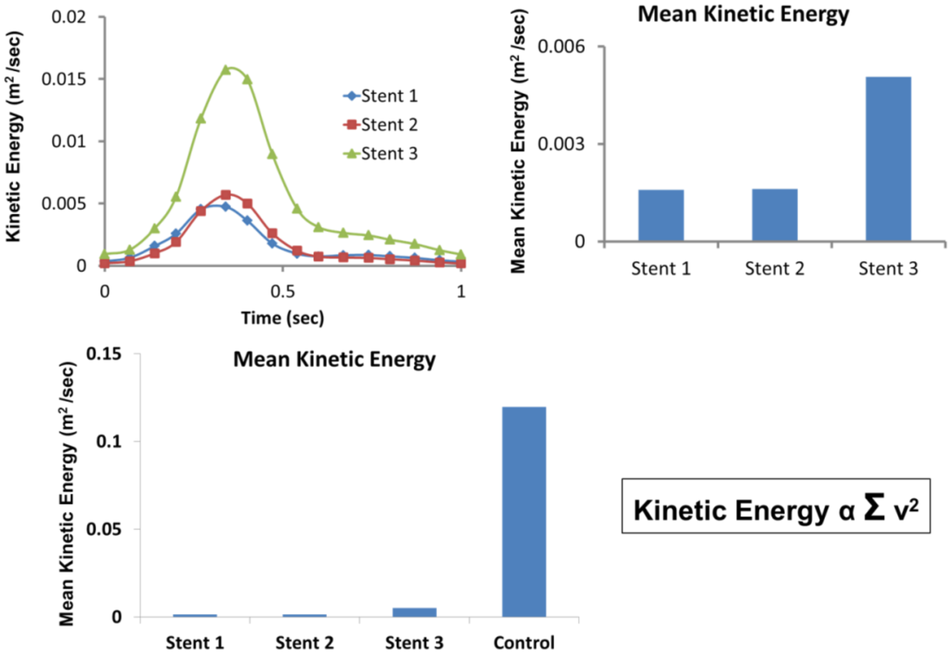

Figure 15: Temporal and mean kinetic energy comparison between the control and stented cases.

In summary, the CFD circulation results were in good agreement with the PIV results. By validation of the results against experimental data, this study can serve as a basis for CFD simulations of flow diversion in more complicated patient derived vascular beds. Additionally, evaluation for other complicated device designs could be tested in this sidewall aneurysm model.

CHAPTER 3: ANGIOGRAPHIC AND CFD COMPARISON OF FIVE COMMERCIAL NEUROVASCULAR STENTS/FLOW DIVERSION DEVICES

INTRODUCTION

Treatment with flow diverters (low porosity, fine-mesh stents) is used for complicated aneurysm geometries not amenable to coiling. Angiographic analysis and mathematical modeling was applied for comparing different designs of stents for brain arteries as well as flow diverters to compare and predict their flow diversion efficacy [1]. High resolution computational fluid dynamics (CFD) was also used to obtain more detailed localized alterations in hemodynamics due to different devices. Virtually all published CFD studies with flow diverters in cerebral aneurysm models do not use the real wire configurations of the deployed devices in the models and the fine differences in porosity and pore density across the aneurysm neck might produce inaccurate results. The proposed study aims to test five commercially available neurovascular devices that have not been compared before through angiographic washout analysis, microCT-based mesh reconstruction of the devices and CFD analysis in idealized sidewall aneurysm models.

METHODS

The devices being tested in this study are either available commercially in the US or are undergoing clinical trials. Pipeline was the first flow diverter to receive the pre-market approval (PMA) in the US in 2011. The device used in this study is second generation Pipeline. Other second generation flow diversion device included in the study is FRED (MicroVention). In addition 3 commercially available neurovascular devices that were tested are Enterprise (Codman J&J), Neuroform (Stryker), and LVIS (MicroVention). Two separate deployed configurations of Pipeline were used and these will be treated as two separate samples for the purpose of this study. Configuration 1 is a highly compacted device with lower porosity than configuration two. The pore density is also much higher in case of configuration 1 as compared to configuration 2. Hence the 6 devices were deployed in 6 idealized experimental sidewall aneurysm silicone tubes. For the purpose of computational modeling of the deployed devices in the experimental models, the Pipeline model is based on a device configuration not involved in the experimental study. This was because the microCT image of the device did not have the same wire orientation as during experiments due to manual manipulation. It is worthwhile noting that over the aneurysm neck the CFD pore density and porosity of the device ly between the two experimental configurations.

Following the experimental comparison study, the computational fluid dynamic analysis study was carried out. The computational modeling involved microCT scanning of the devices to obtain their geometric orientation in order to implement them in the CFD simulations. Following completion of angiographic washout analysis and CFD simulations, correlation of the hemodynamics parameters between the experiments and the simulations are explored.

Model fabrication

Silicone models of the idealized sidewall aneurysm were fabricated in house using a 3D printer followed by a dip coating method described in detail elsewhere [99]. After creation of the vessel lumen using computer aided design, the constructed model was sent to a 3D printer (Dimension Elite, Stratasys, Eden Prairie, MN). The smoothed and processed solid Acrylonitrile butadiene styrene (ABS) model of the lumen was then dip coated in silicone (Figure 16). The silicone coated models were then mounted on a shaft, spun and rotated simultaneously for a period of 10 minutes. This process was repeated three times. The spinning was done to ensure even silicone coating and avoid any bubbles that can affect the transparency of the silicone models. The silicone was then allowed to cure for up to 48 hours and then submerged in a xylene acetone solution to dissolve the ABS core and obtain the transparent silicone model.

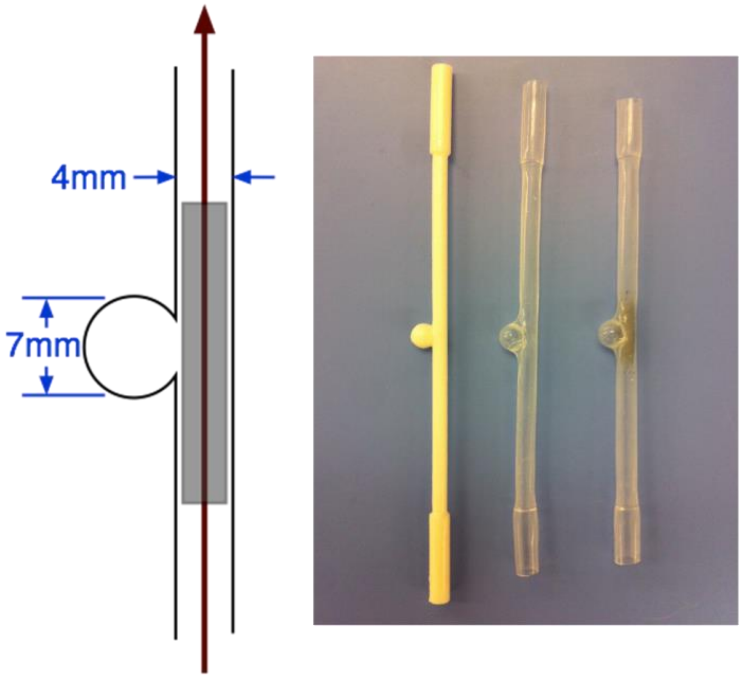

Figure 16: Schematic of the sidewall aneurysm model (left) and the silicone model fabrication process. The 3D printed ABS model is dip coated to obtain a clear silicone model into which the device is implanted.

Under fluoroscopic guidance and assistance of a neurointerventionalist, the five devices were implanted in five separate models across the neck of the aneurysm. Snapshots of the silicone models with the devices implanted and fluoroscopic images are demonstrated in Figure 17. The device specifications are Neuroform 4x20mm, Enterprise 4.5x28, LVIS 4.5x34, Pipeline (4.5x20) and FRED 4x23/17.

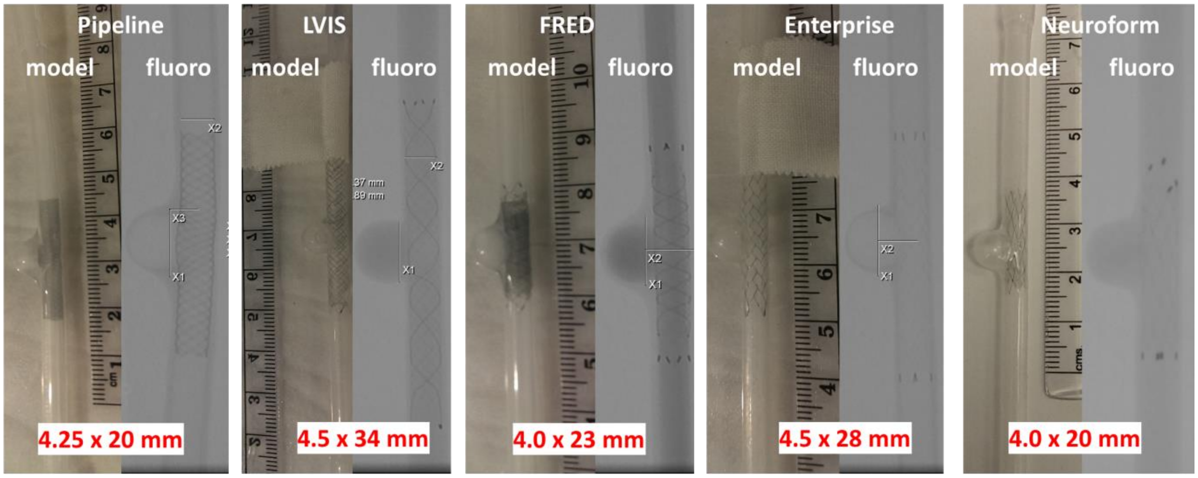

Figure 17: Five panels showing each a photo and a fluoroscopic image side by side of the 5 devices tested.

Experimental setup and angiographic data acquisition

The experimental setup is schematically shown in Figure 18. The flow rig was designed for repeatability in high speed angiograms and better mathematical modeling of the high data density of the gray scale curve. To ensure good mixing of the contrast with the carrying fluid as well as to avoid reflux from the injection catheter, a Starling resistor was introduced into the flow circuit distal to the aneurysm model. The Starling resistor was set at 80 mmHg. The pressure value selected was the lowest for which fluctuations in contrast mixing were minimized due to pressurization of the flow loop.

Flow data was acquired using Transonic in line (cannulated) flow transducer (ME6PXN Transonic, Ithaca, NY) with an inner diameter of 6.4mm connected to a Transonic flow meter (TS410, Transonic, Ithaca, NY) and a LabChart 8 data acquisition system (ADInstruments, Colorado Springs, CO). A peristaltic pump (Masterflex Cole-Parmer, Vernon Hills, IL) was used to drive the fluid through the flow apparatus. The flow rate was set to approximately 4 ml/sec. A 50%/50% glycerol aqueous solution was used as a blood analog fluid with a viscosity of 4cP at 37^0C. The Glycerol solution was stored in a water bath to control its temperature, which also served as the fluid input reservoir to the flow apparatus. To avoid damage to the silicone models from abrupt pressure rises a bypass was introduced into the flow channel with a Starling resistor acting as a pressure limiting relief valve.

We used Ultravist 370mgI for the contrast injections during the angiograms. The specific gravity of the contrast was adjusted to be similar to that of the working fluid by using 50% of contrast solution in distilled water for optimal mixing with the working fluid. Contrast was pumped during preliminary experiments through a 4Fr catheter, however, during the initial experiments it became apparent that the positioning of the tip of the catheter was extremely crucial in affecting the mixing of contrast. Hence, to avoid any such variability catheter injection was discarded and data was acquired by injecting contrast directly into the flow circuit through pressure tubing. The pressure tubing was connected to a 150ml syringe mounted on a Medrad power injector (Medrad® Mark V ProVis®, Bayer Healthcare, Whippany, NJ). A Siemens angiography system (Artis Zeego, Erlangen, Germany) was used to acquire digitally subtracted angiograms. The imaging plane as well as magnification factor were maintained constant to ensure repeatability in the image resolution of the acquired data. High speed angiograms were acquired in all models at 15frames/sec during a one pass steady flow of 4 ml/sec through the model.

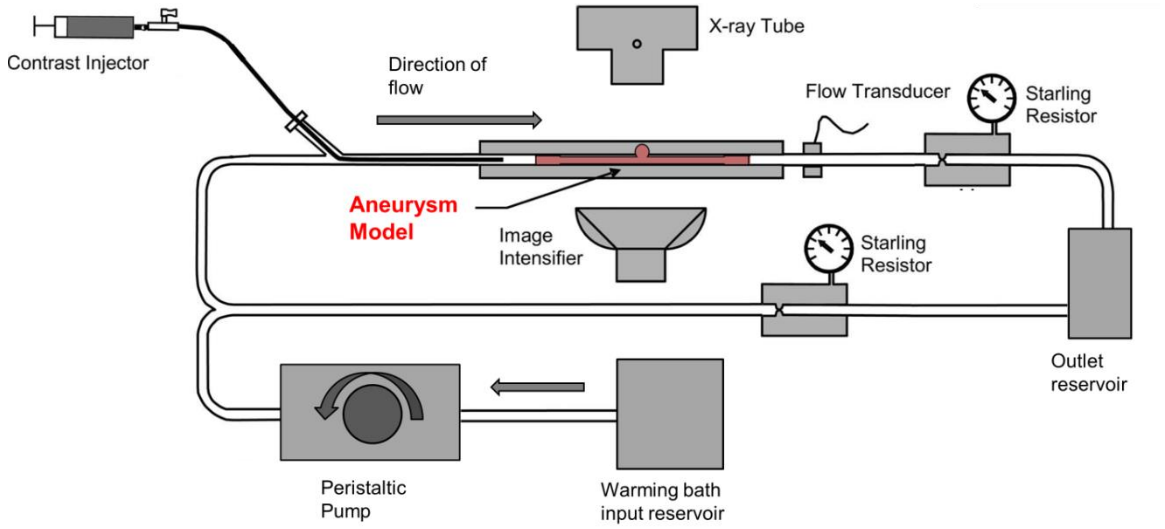

Figure 18: Schematic of the experimental apparatus for high speed angiography data acquisition in the aneurysm models.

The silicone model was positioned in the flow loop and immobilized while acquiring the images. The contrast was injected into the flow about 50 cm upstream (approximately 80 diameters) of the region of interest, a sufficient length for contrast mixing with the working fluid. Contrast was injected using the power injector at 2.5 ml/sec for 2 seconds with a 2 second triggering delay in injections to allow the angiographic unit to acquire the mask for the angiogram.

Angiograms were acquired six times for each model to test repeatability of the data. The six runs were not acquired in a consecutive fashion. Instead they were acquired on different days to account for variability that may be introduced by attaching detaching and reattaching the model to the flow loop. Aneurysm orientation is crucial for contrast transport into the aneurysm. If the aneurysm is positioned towards the bottom, more contrast was observed to enter the model, recirculate, and not washing out quickly. Hence we maintained the position of the aneurysm horizontal (sideways) rather than up or down. However, the precise roll position of the aneurysm cannot be guaranteed after reattachment. To account for such variations 3 runs were acquired at one time for each model and repeated following detachment and reattachment of the model to the flow loop.

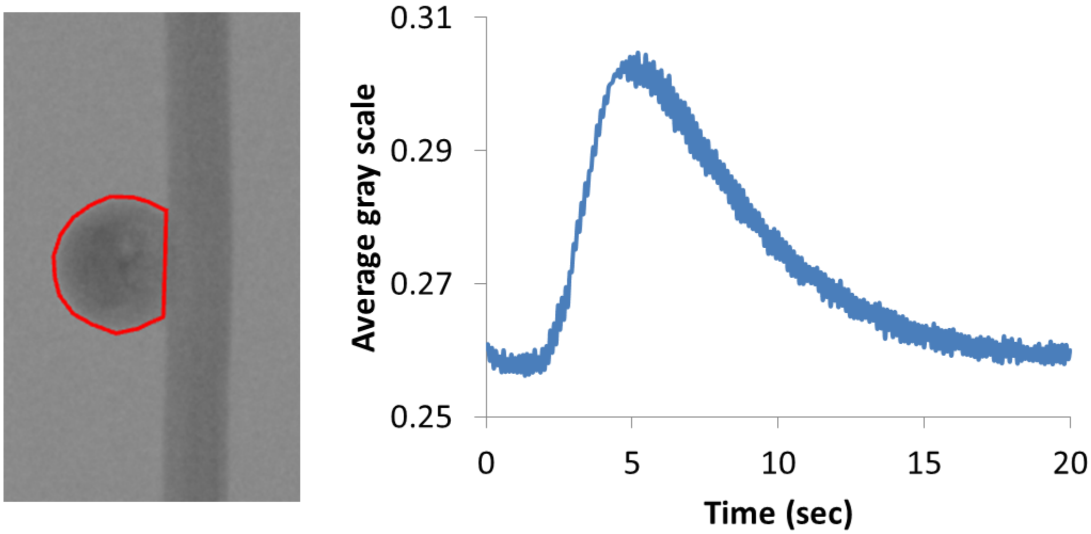

Figure 19: Segmented (red) aneurysm region of interest (ROI) (left) and corresponding contrast concentration-time curve obtained by image processing (right).

The angiograms in DICOM format were transferred from the Artis zeego to the LEO workstation (X-LEONARDO, Siemens, Erlangen, Germany) for analysis. The data was analyzed using the image processing toolbox in MATLAB (MATLAB 2015, Mathworks, Natick, MA). The region of interest containing the aneurysm was segmented in the images to calculate the total gray scale intensity in the aneurysm at every time point in the sequence to yield the contrast concentration-time or washout curves (Figure 19). The total gray scale intensity was divided by the number of pixels to obtain the aneurysm averaged contrast concentration time curve for each model. The contrast concentration-time curves (washout curves) were then fitted to a mathematical model (discussed briefly in the next section) using a least squares approach[53, 57, 66].

Mathematical model:

The amplitude of the aneurysm washout curve (δ) obtained as described in the Preliminary Studies section is one of the parameters used to construct a global washout coefficient for comparison. After the amplitude was recorded the washout curve are normalized and fit to the following mathematical model[53, 54, 56, 57, 66]. The model was fit to the data using minimization of sums of squares differences between the data and the model using a library function available within the optimization toolbox in MATLAB.

$$\begin{aligned} f(t) &= \rho_{conv}\int_0^t \frac{1}{\sigma\sqrt{2\pi}}e^{-\frac{(\eta-\mu)^2}{2\sigma^2}}\times\frac{1}{\tau_{conv}}e^{-\frac{t-\eta}{\tau_{conv}}}d\eta \\ &+\rho_{diff}\left[\int_0^t \frac{1}{\sigma\sqrt{2\pi}}e^{-\frac{(\eta-\mu)^2}{2\sigma^2}}d\eta-(1-e^{-\frac{t}{\tau_{diff}}})\right] \end{aligned} \tag{17}$$

The model has six parameters which describe the physics of contrast transport between the parent vessel and the aneurysm:

1. ρ_{conv} and ρ_{diff}: represent the proportions of convective and diffusive transport, respectively. The deployment of a flow diverter is expected to increase the diffusive proportion. Therefore, the value of ρ_{diff} can be expected to increase after device implantation, whereas the value of ρ_{conv} should decrease.
2. τ_{conv} and τ_{diff}: are the convection and the diffusion time constants, respectively. The residence time of angiographic contrast (and therefore blood) is expected to show an increase due to the deployment of a flow diverter. This increase in residence time

should, therefore, be reflected in increases in the time constants, especially τ_{diff}, after treatment.

3. σ and μ : are related to the method and profile of contrast injection (rate of injection, period of injection, variations in these parameters due to manual injection, etc.) and do not, in general, represent alterations in flow exchange due to flow diverter implantation.

MicroCT imaging:

To obtain the exact geometry of the device in the implanted position inside the silicone model, each model was imaged in a microCT (uCT50 Scanco Medical, Bruttisellen, Switzerland). All models except FRED were scanned at a resolution of 12 microns except FRED that was scanned at a resolution of 6 microns.

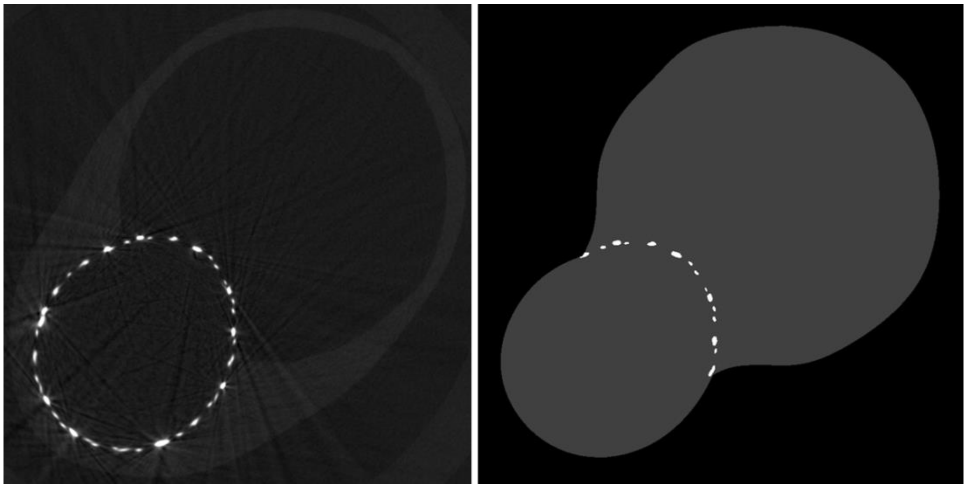

Figure 20: MicroCT slice of pipeline in the aneurysm model (left) and the same slice after segmentation with the device wires cropped (right).

Mimics (Materialise, Leuven, Belgium) software was used to perform image segmentation on the microCT data. The segmentation was applied mainly to delineate the device wires/struts. During segmentation the device was cropped to only retain the portion covering to the neck of the aneurysm (Figure 20).

CFD model construction

Following segmentation, the microCT slices were exported in a binary format using Mimics. The segmented binary images of the stent struts/wires were imported into MATLAB and analyzed using custom functions to obtain the centroids for each section. The centroids from all slices for each device were extracted and combined into a single data file. The centroid data was imported into SolidWorks. Through a semi-automated procedure, the imported points were joined to form continuous centerlines under guidance from segmented 3D volume of each device. These centerlines were in fact 3D splines fitted onto the selected points. The constructed centerlines provide a framework for each device. Next step was to determine the exact cross section for the device wires/stent struts and sweep across the device centerlines.

The microCT images delineated the stent strut cross section as circular. In the case of braided devices including LVIS, FRED and Pipeline the devices are braided from wires with a circular cross section. However, the laser cut stents Enterprise and Neuroform have a rectangular cross section. To determine the correct cross sectional dimensions of the Enterprise and Neuroform stents, the devices were embedded in epoxy and sectioned multiple times. The cross sectional strut width and thickness were measured on microscopy images obtained from the device sections. The dimensions were confirmed with the literature data[100]. For Enterprise, the strut width was 0.078mm and strut thickness was 0.042mm. For Neuroform, the strut width was 0.067mm and strut thickness was 0.066mm. These values were applied in the subsequent computations.

In case of LVIS the wire diameter was measured to be 0.056mm from segmented microCT images and confirmed with the available data in the literature[101]. Based on clinician input and confirmation with microCT segmented image measurements, wire diameter of 0.03mm was applied to Pipeline (Figure 21). . The FRED device is a dual mesh composed of outer larger diameter 16 wire component (that is the LVIS device) and an inner 48 thin wires braided mesh with flow diversion properties. Since literature data on FRED is not available, the image segmentation for the inner 48 wire braided flow diverter component of FRED was calibrated based on the outer LVIS device with a known wire diameter of 0.056 mm. Based on this an inner wire average diameter of 0.0225mm was obtained, which was applied for the FRED CAD model (Figure 22).

The cross sections were drawn at a plane orthogonal to the centerlines. The stent strut and device wires cross sections were swept across the centerlines to obtain the CAD model for the cropped device. Based on guidance from the microCT and a set of markers the devices were virtually brought into their implanted positions within the SolidWorks assemblies. The individual device CAD models were saved in the parasolid format at the implanted position. The CAD model for the sidewall aneurysm and the devices were imported into ADINA and Boolean subtraction was performed to obtain the stented sidewall aneurysm lumen for CFD simulations

Meshing and boundary conditions

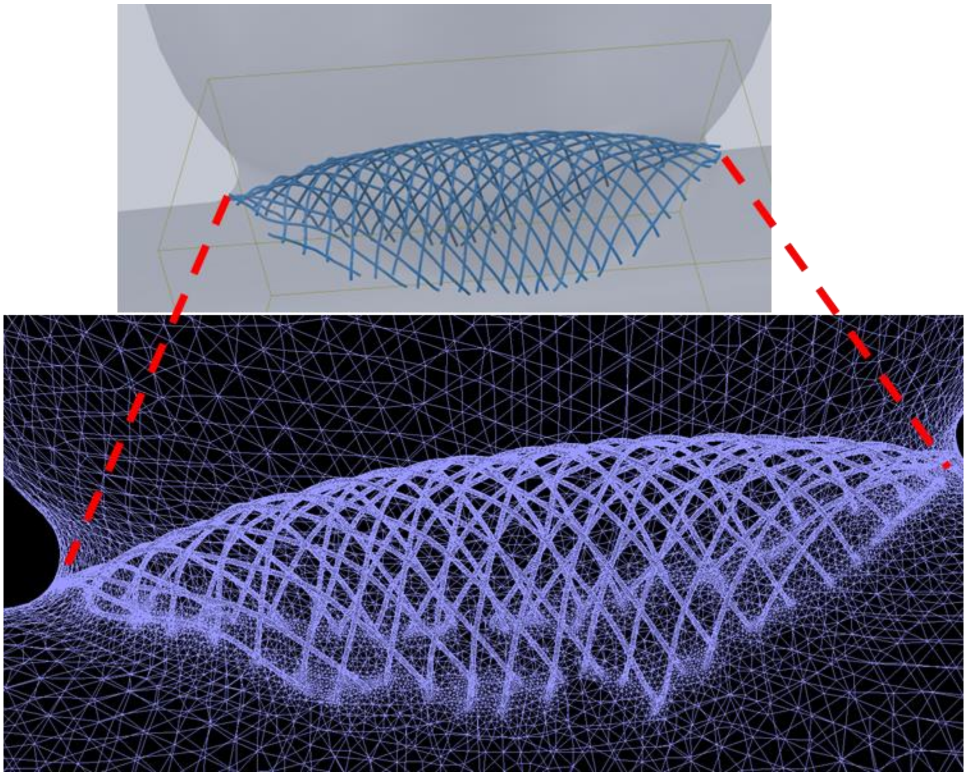

Figure 21: CAD model for Pipeline in position across the aneurysm neck (top), and expanded view of the anisotropic tetrahedral mesh generated using meshing tools available within ADINA for the Pipeline CAD model (bottom).

For all CFD models, meshing was performed using the meshing tools available within ADINA. The ADINA mesher works based on Delaunay triangulation. A free-form meshing scheme comprising of 4-node tetrahedral elements was utilized. The meshing scheme was highly anisotropic in order to adequately resolve the stent strut/device wire faces while maintaining the overall mesh size to be computational solvable through available resources. The global mesh max edge size applied for all models was 0.25mm determined as a good starting point based on previous mesh independence tests. The stent struts for Enterprise and Neuroform devices and the wire faces for the LVIS were resolved through a max edge size of 0.012mm. The mesh was approximately 2 million elements for these three models. In case of Pipeline, the wire faces were resolved through an edge size of 0.012mm. This number was restricted to keep the mesh size computationally feasible for CFD simulations. The highly anisotropic mesh is delineated in Figure 21. The FRED inner wire mesh faces were resolved through an average element edge size of 0.01mm. The restriction to use a lower element edge size was due to the limited computational resources available to solve the CFD problem. The FRED mesh size approached 4 million elements and is demonstrated in Figure 22.

At the inlet of each model, a population averaged internal carotid artery pulsatile flow waveform obtained from literature[102] was applied in the form of a fully developed Womersley flow profile [97] with a detailed technical description given in Chapter 6. The fluid was considered Newtonian and the working fluid viscosity was assumed to be 4cP. No slip boundary conditions were applied on the walls that were also assumed to be rigid and flow was assumed to be laminar.

The CFD simulations were performed under the Galerkin finite element formulation in ADINA [92]. CFD simulations within this formulation were validated against analytical and experimental solutions in chapter 2. The CFD simulations solved for conservation of mass and fluid momentum. Automated time-stepping scheme was utilized to assist in convergence of the simulations. The simulations were performed on an in house 16-core linux server (King Star supercomputer, Sunnyvale, CA) with 64GB available RAM. Additionally simulations were also performed on Blacklight PSC XSEDE national supercomputer (www.xsede.org).

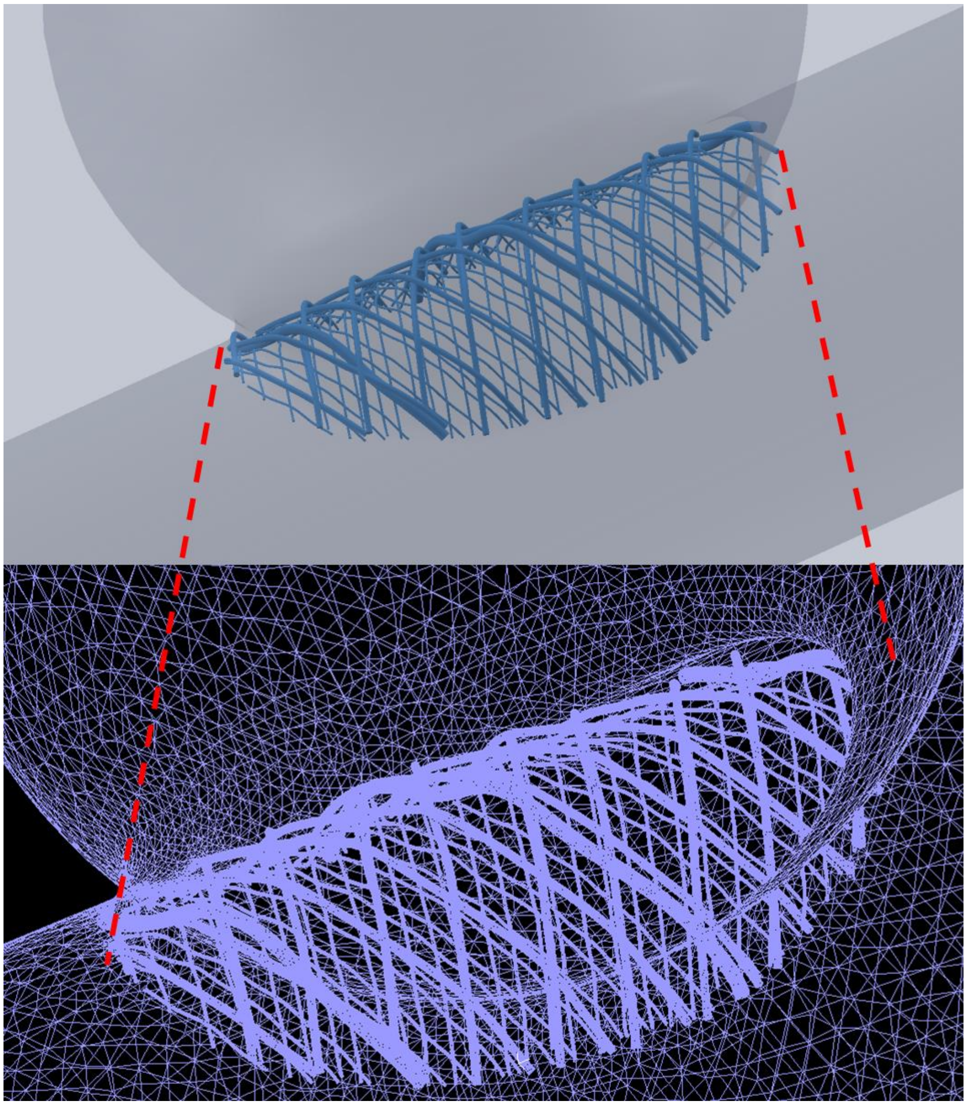

Figure 22: CAD model for FRED in position across the aneurysm neck (top), and expanded view of the anisotropic tetrahedral mesh generated using the meshing tools available within ADINA for the FRED CAD model (bottom).

Post processing of the CFD simulation results was performed in ADINA and the exported nodal velocity vector and nodal pressure data were analyzed in MATLAB. All statistical data analysis was performed in GraphPad Instat (GraphPad, La Jolla, CA). Comparison between the groups was done using one-way analysis of variance (ANOVA) test for parametric or normally distributed data. For non-normal data sets Kruskal-Wallis test was used. In case of significance Tukey-Kramer post-hoc analysis was performed for the parametric data-sets and Dunn post-hoc test for the non-parametric data-sets.

RESULTS

Angiographic data

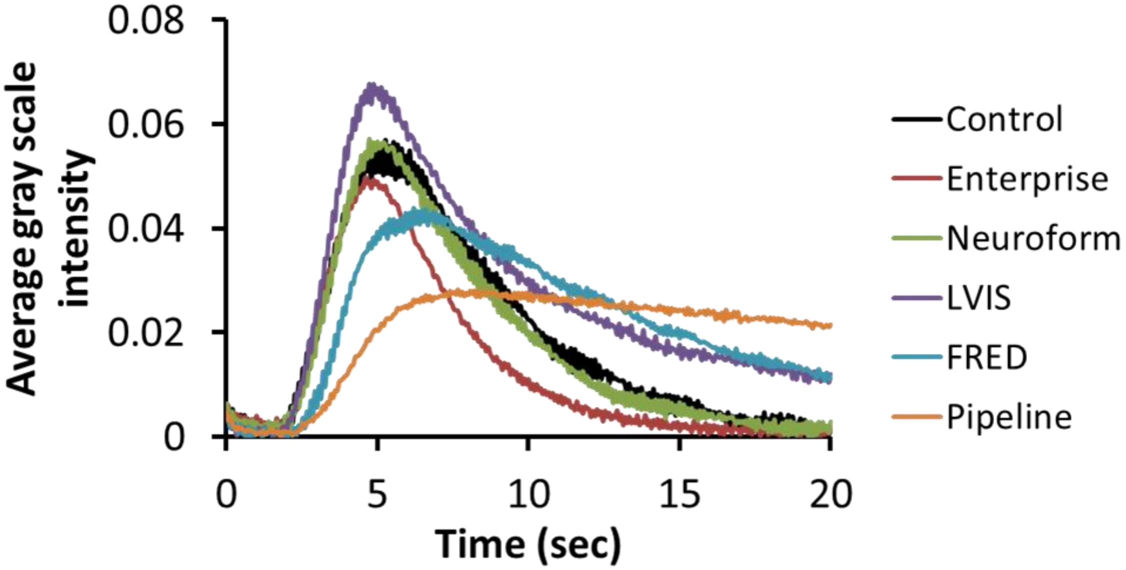

Figure 23: Representative concentration time curves (with gray scale intensity averaged over the region of interest) for the control in the sidewall aneurysm model and the five devices tested.

Representative contrast concentration time curves from the control and the five device groups are plotted for comparison between the devices in Figure 23. As can be observed, the concentration time curves show similar trends for the control and the three high porosity device groups i.e., Neuroform, Enterprise and LVIS. The flow diverters, which are low porosity devices, demonstrated different characteristics of the washout curves where the peak is suppressed and the tail elevated.

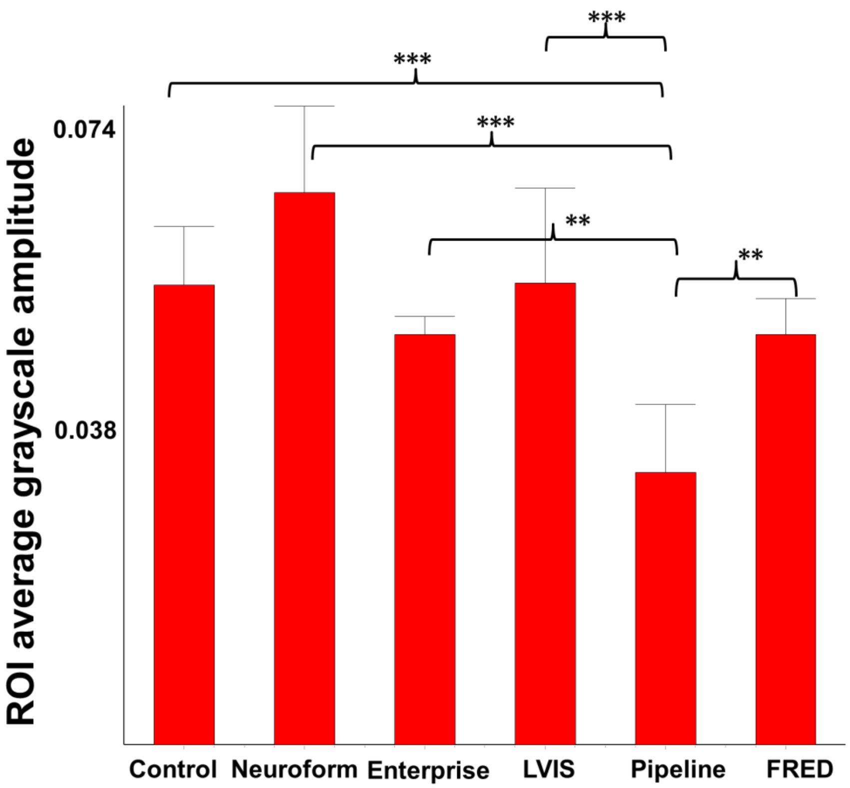

Figure 24: Comparison of averaged grayscale intensity amplitude in the ROI for the control and the five devices tested with * indicating statistically significance at p<0.05, ** indicates p <0.01, * indicates p<0.001.**

Hence, there appears to be a reduction in the contrast influx into the aneurysm and the delayed washout indicating stagnation within the aneurysm. Comparison between the averaged washout curve amplitudes shows statistically significant differences among the devices as demonstrated in Figure 24. The mean amplitude for the Pipeline group (0.0323±0.008) was significantly lower than all other groups. The control group washout amplitude (mean 0.055±0.007) was not statistically different from Neuroform (mean 0.066±0.010), Enterprise (mean 0.0488±0.002), and LVIS (mean 0.055±0.011) where p-values were larger than 0.05. The mean washout amplitude for Pipeline (0.0323±0.008) was lower than FRED (0.0488±0.004) ($p<0.01$). Furthermore, FRED was not statistically different than the control or the four other devices. Pipeline mean amplitude was significantly lower than control ($p<0.001$), Neuroform ($p<0.001$), Enterprise ($p<0.01$), and LVIS ($p<0.001$).

The model fit for the washout curves is illustrated in Figure 25. The modeling demonstrated that for all experimental washout curves the convective component is dominant. The diffusive component was virtually absent in the model fits. Figure 25 demonstrates a flat diffusive component for a representative curve.

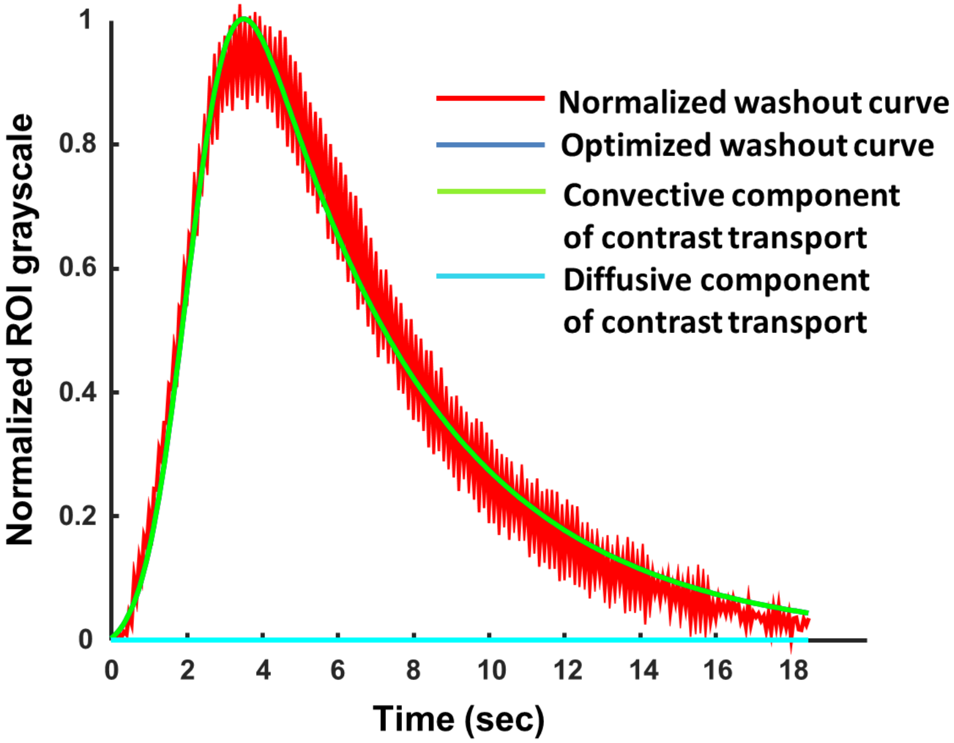

Figure 25: Normalized washout curve (red) fitted to the mathematical model to delineate the optimized washout curve (blue). The convective (green) and diffusive (cyan) proportions are also shown.

The quantitative comparison among the convective time constants for the tested devices is shown in Figure 26. The convective time constant was significantly different between the devices. The mean convective time constant of the control (4.201±0.2078) was not significantly different from Neuroform (4.214±0.643), Enterprise (2.437±0.230), and LVIS (4.243±0.354). Pipeline had a significantly higher convective time constant (18.962±6.267) than all other devices ($p<0.001$). FRED demonstrated significantly smaller time constant (10.534±1.762) ($p<0.001$) compare to Pipeline. Nonetheless, the FRED convective time constant was significantly larger than that of the control and the high porosity devices (Control $p<0.05$, Neuroform $p<0.05$, Enterprise $p<0.01$, and LVIS $p<0.01$).

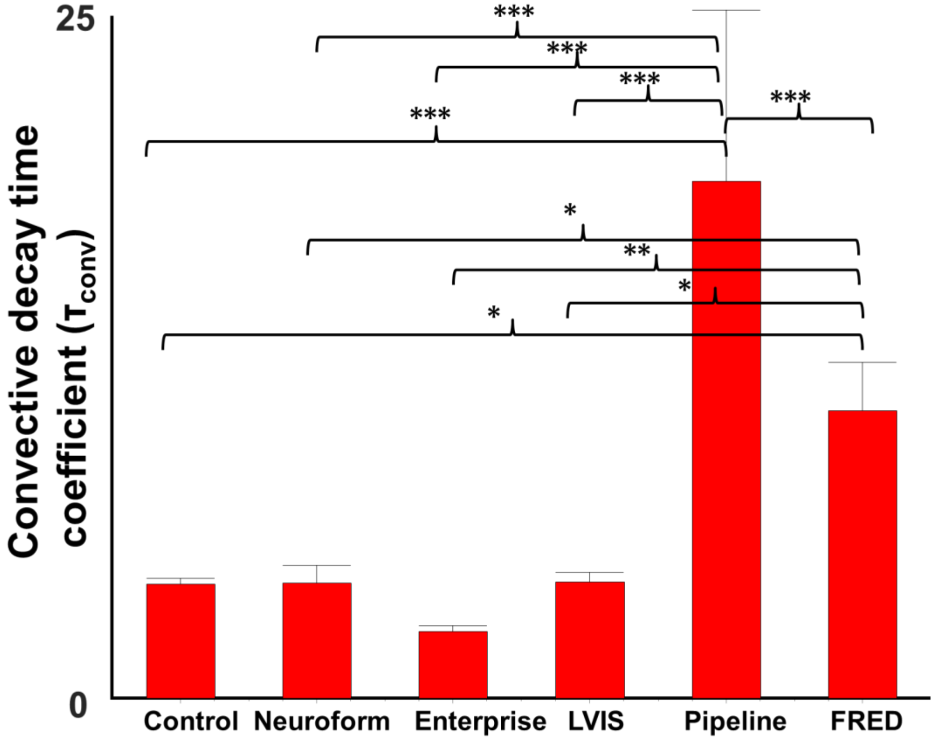

Figure 26: Comparison of convective decay time constant of the control and the five devices with * indicating statistical significance at the $p<0.05$ level, ** indicates $p<0.01$, and * indicates $p<0.001$.**

CFD data

Spatial maps of velocity magnitude and velocity vectors obtained from the CFD simulations for the control and the five devices are presented in Figures 27. Flow patterns inside the aneurysm remain consistent before and after deployment of LVIS, Neuroform, and Enterprise stents whereby a clockwise vortex develops inside the aneurysm after the acceleration phase of systole and persists throughout the cardiac cycle (Figures 27A-D). The flow entry region into the aneurysm was the distal neck area for the control as well as the Neuroform, Enterprise, and LVIS stents as can be seen in Figures 27A-D.

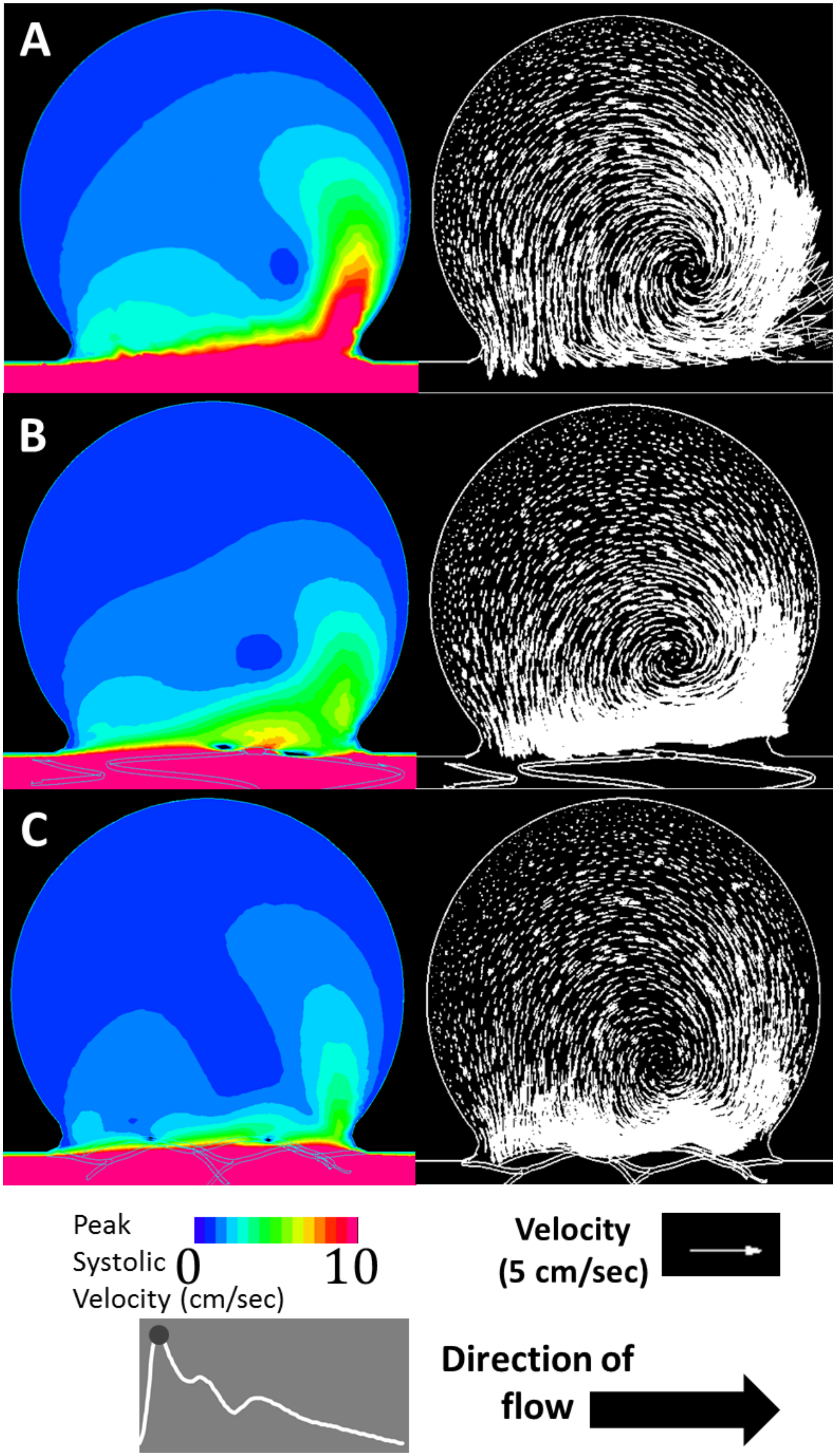
A
B
C
Peak Systolic Velocity (cm/sec)
0
10
Velocity (5 cm/sec)
Direction of flow

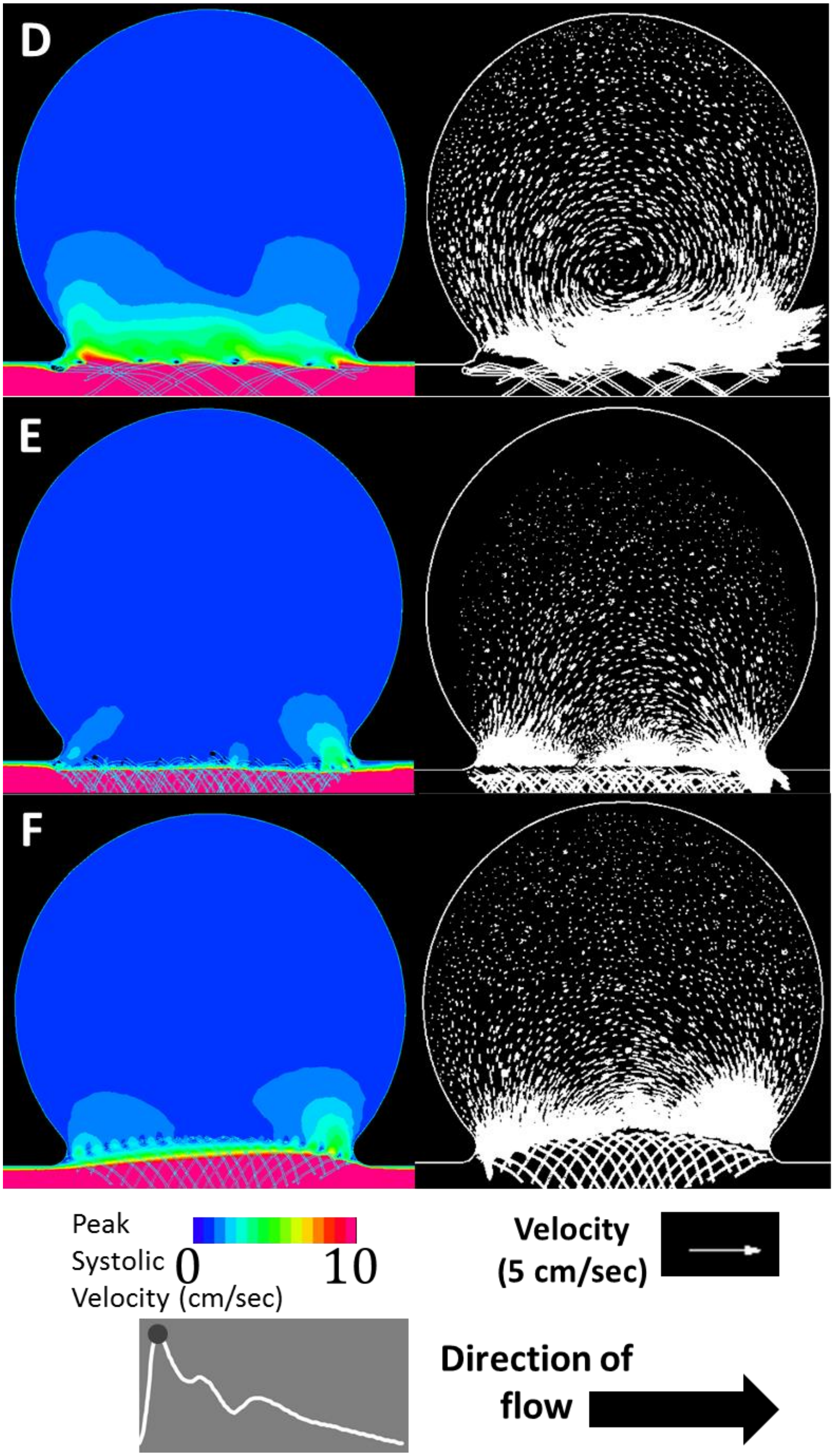
D
E
F
Peak Systolic Velocity (cm/sec)
0
10
Velocity (5 cm/sec)
Direction of flow

Figure 27: Peak systolic speed distribution in the aneurysm (left) and velocity vector map (right) for A) control, B) Neuroform, C) Enterprise, D) LVIS, E) FRED, and F) Pipeline.

Pipeline and FRED (Figure 27E-F) induce a a reversal in intra-aneurysmal flow direction before and after implantation of flow diverters. In case of FRED, the flow inlet region changes from the distal neck to the proximal neck of the aneurysm (Figure 27E). For Pipeline, despite the reduction in velocity magnitude and absence of a vortex in the central region of the aneurysm, the flow entered through the distal region of the neck after the acceleration phase of systole (Figure 27F). For both Pipeline and FRED, the large vortices seen in the control as well as in the high porosity stents were absent. Although the velocity profiles remained similar, the velocity reduce**d** in magnitude following device implantation for the high porosity devices **(**Neuroform, Enterprise, and LVIS**)** as evident in Figures 27.

Differences in intra-aneurysmal velocity were examined through their kinetic energy as discussed earlier (Chapter 2, equation 16). For all CFD models, the kinetic energy was calculated from nodal velocity vector regions for the entire aneurysm. The intra-aneurysmal kinetic energy at various points through the cardiac cycle are presented in Figure 28. The peak kinetic energy was higher for Neuroform, Enterprise, and LVIS in compare to Pipeline and FRED. The Neuroform device had the highest peak kinetic energy among all devices.

The kinetic energy waveforms were then time-averaged to obtain the mean kinetic energy values for each device. Comparison among the mean intra-aneurysmal kinetic energy values for the six CFD models is presented in Figure 29. Following a trend similar to that of the velocity fields, the intra-aneurysmal kinetic energy reduces in magnitude following device implantation for all models.

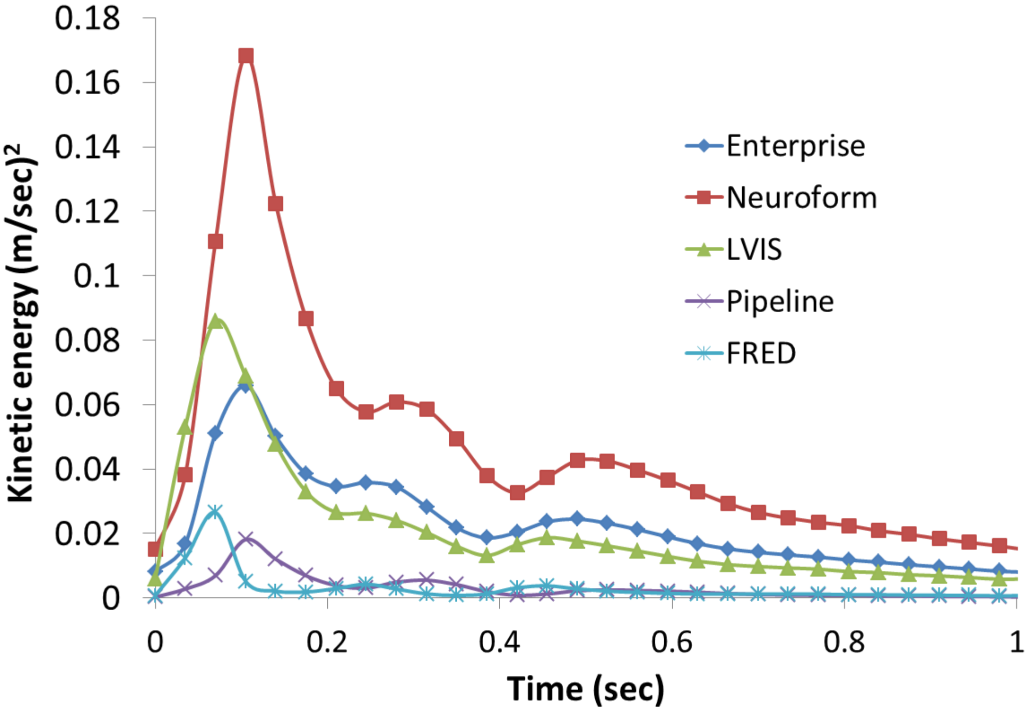

Figure 28: Temporal comparison of intra-aneurysmal kinetic energy results among the five commercial neurovascular devices deployed in the CFD model.

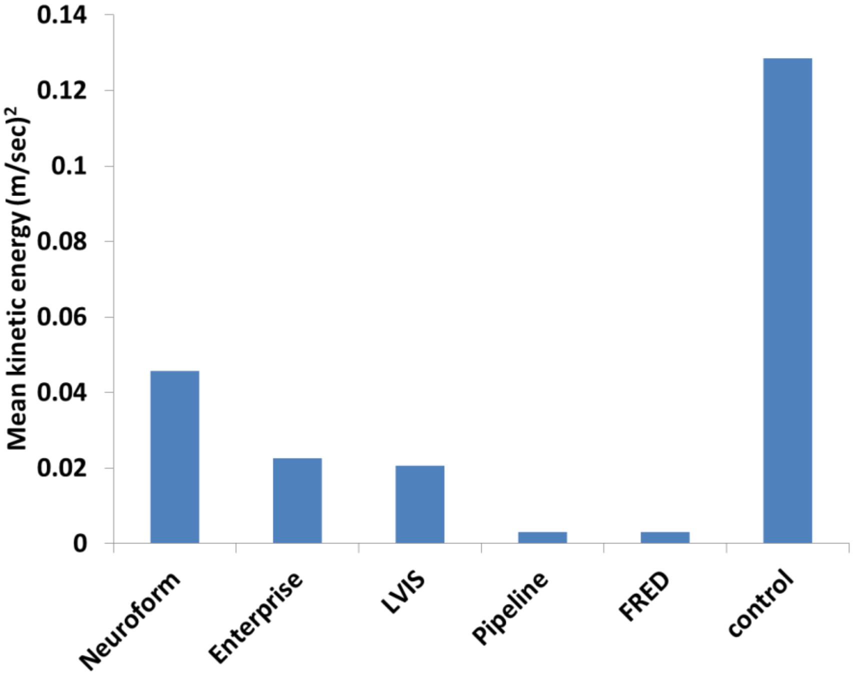

Figure 29: Comparison of intra-aneurysmal mean kinetic energy among the five commercial devices

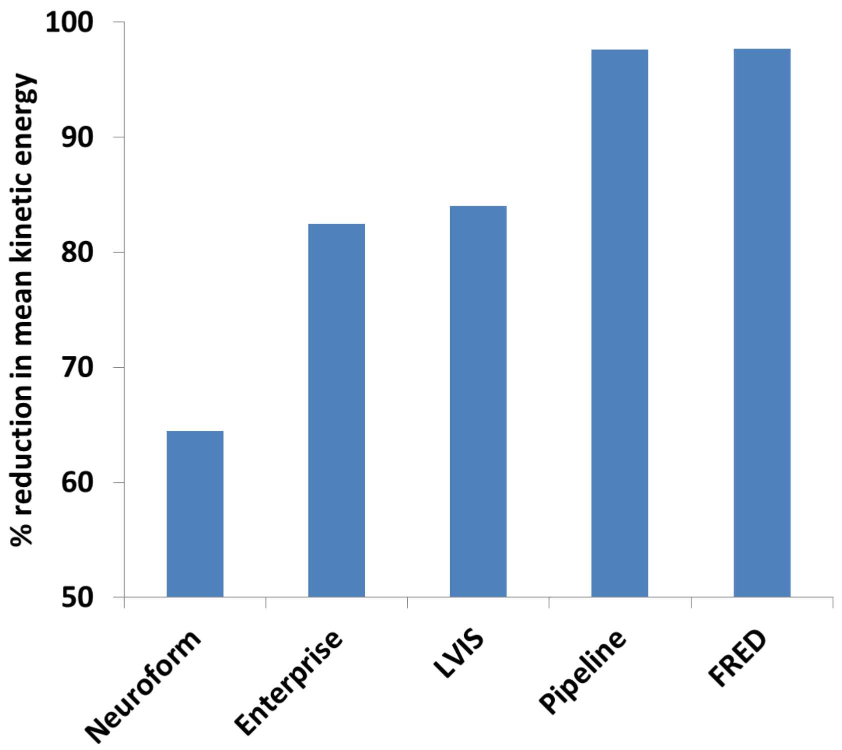

Figure 30: Comparison of the percentage reduction in the intra-aneurysmal mean kinetic energy among five commercial neurovascular devices

To provide a better visual representation of the kinetic energy changes following device implantation, the percentage reduction in the mean intra-aneurysmal kinetic energy was calculated for all devices and the results are presented in figure 30. The highest percent reduction in kinetic energy was imposed by both Pipeline (97.6%) and FRED (97.67%) with little difference between the two. The kinetic energy was also reduced substantially by LVIS (84.01%), Enterprise (82.4%), and Neuroform (64.5%) that imparted the lowest reduction in kinetic energy among all the devices tested.

Angiographic vs CFD results:

While CFD simulations produce a substantial amount of it is not immediately available to be useful in clinical decision making particularly while patients are undergoing a procedure. Therefore, it is useful to seek a correlation between angiograms and CFD results. This can also serve to evaluate potential relation between angiographic washout parameters and hemodynamic parameter such as the hydrodynamic circulation and kinetic energy that can be obtained by CFD simulations. The convective time constant that quantifies the residence time of contrast convected into and out of the aneurysm was plotted against the mean intra-aneurysmal kinetic energy (Figure 31). The comparison shows an inverse relation between the kinetic energy and the convection time constant with a correlation coefficient of 0.54.

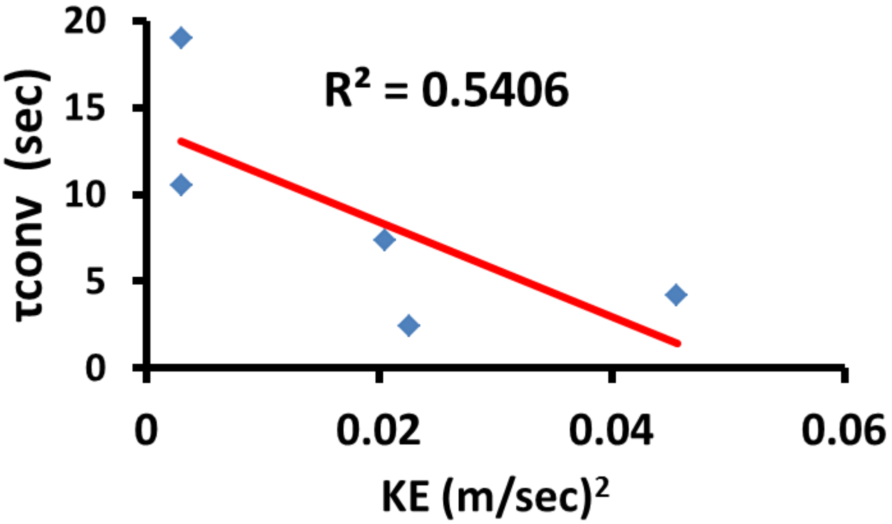

Figure 31: Convection time coefficient obtained from mathematical modeling of the angiographic data plotted against the mean kinetic energy from CFD simulations.

DISCUSSION

To the knowledge of the author, this is the first study performing a detailed experimental and computational analysis of intra-aneurysmal hemodynamics within the same model following implantation of five commercial neurovascular devices. Neuroform and Enterprise stents have been available in the US for stent-assisted coiling treatment for brain aneurysms. The LVIS has been available in US on a humanitarian device exemption (HDE) basis for patients where no other treatment option is possible for stent-assisted coiling. Earlier, we attempted to include LVIS Jr (MicroVention) in this work. However, the largest LVIS Jr has a diameter of 3.5mm which is smaller than our model parent artery of 4mm and hence it was not included in this study. Although the three high porosity devices (Neuroform, Enterprise, and LVIS) are not indicated for flow diversion of aneurysms, this would be valuable information for neurovascular clinicians to know of their potential flow diversion value of any. Pipeline flow diverter has been available in the US market since 2011 and FRED can potentially be the next commercially available flow diverter in US market. Since Pipeline and FRED have not been compared previously, the data generated in this study will be very useful to physicians. Another flow diverter currently in clinical trials in the US is Surpass (Stryker Neurovascular). Surpass was not included in the study due to device unavailability. Solitaire stent from Medtronic is another device currently available in US for stent assisted coiling that was not included for this study and can be part of future experiments.

The experimental angiographic washout and CFD results demonstrate that devices designed to be flow diverters show better performance in modulating the intra-aneurysmal hemodynamics. Flow diverter devices performed better in dissociating aneurysm flow from that of the parent vessel. Experimental results indicated reduced washout amplitude and increased contrast residence time for the flow diverters as compared to the higher porosity stents. CFD simulations demonstrated kinetic energy reductions ranging from 65% to 82% for the high porosity devices. This can be attributed to enhanced flow diversion effect on side wall aneurysm that is perpendicular to the oncoming flow. Our study did not find any significant differences in experimental results between the Neuroform, Enterprise and LVIS stents. Any potential differences would be crucial for a neurointerventionalist in selection for the device when performing stent-assisted coiling[103]. The CFD simulations showed that LVIS and Enterprise performed better in terms of flow diversion when compared to the Neuroform (82% vs 65% reduction in kinetic energy). Interestingly this difference was note picked up in the washout experiments. LVIS is a braided device (Enterprise and Neuroform are laser cut) and therefore provides better wall apposition making it a preferred choice for stent-assisted coiling among clinicians [103]. The open cell stent design of Neuroform (as oppose to Enterprise which is of close cell design) results in the device providing least coverage over the aneurysm and least resistance to flow as seen from the CFD simulation results. During the acceleration phase of systole fluid inertia dominates and flow enters the aneurysm through the proximal neck and exits through the distal neck with minimal penetration into the dome. This trend was also seen in previous experimental studies with simple spiral flow diverting devices as well as braided flow diverters by Lieber et al [1] and Seong et al [52]. The kinetic energy inside the aneurysm in our control is comparable to the kinetic energy within the aneurysm following flow diversion in the rabbit elastase induced aneurysm in-vitro model [52].

Since at present computational simulations cannot be performed in real time while the patient is undergoing the procedure we aimed to correlate clinically available data such as angiograms with CFD both for comparing performance of implanted devices to provide the interventionalist with a tool to predict treatment outcome while the patient is still undergoing the procedure. A 97-98% reduction in volumetric flow at the aneurysm neck post deployment of a 4 mm diameter device in a 4 mm parent vessel of an idealized aneurysm model was observed for inflow conditions similar to our experiments [90]. Our study found a 97.6% reduction in the intra-aneurysmal kinetic energy for the 4 mm aneurysm model with a 4 mm Pipeline device deployed across the neck of the aneurysm. The study by Dennis et al. [90] calculated a Pipeline porosity of 74% with a pore size of 300x300 micron for the 4 mm device and a porosity of 79% with a pore size of 320x340 micron for the 5 mm device. The 5 mm device deployed in a 4 mm parent vessel showed a 85-92% reduction of volumetric flow for inlet velocity of 18-39 cm/sec [90].

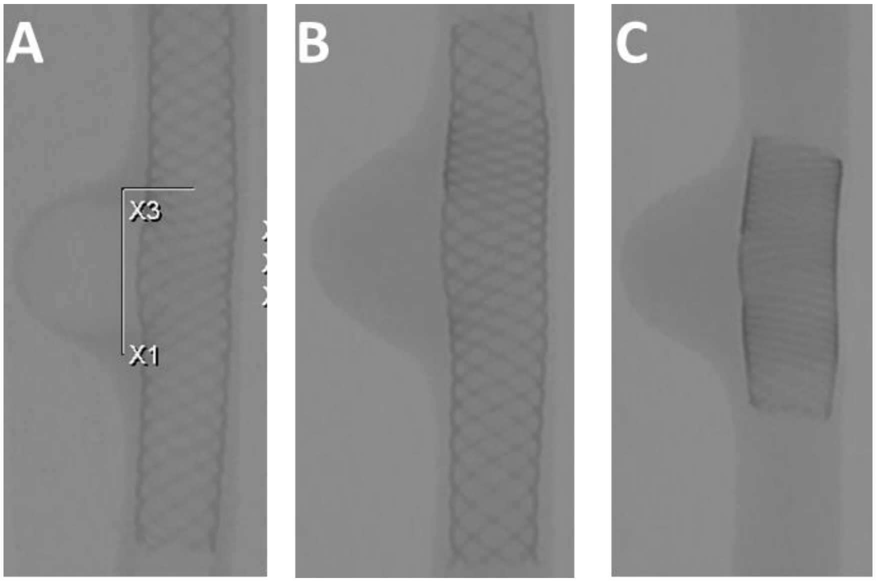

Figure 32: Geometrical configuration of Pipeline following the original deployment (A).The drag force shifted configuration (B), and the compacted configuration of (C).

The microCT data for the Pipeline configuration used in the CFD simulations was different than the configuration available for the washout experiments. The first set of experiments that were performed in 2014 for this study were discarded due to lack of repeatability. The experimental setup was not robust enough and introduced variability mainly in contrast mixing producing inconsistent results. However, the microCT imaging was obtained for all the models after the first set of experiments in 2014. The experimental setup was later modified by introduction of Starling resistors in the circuit and injection of contrast directly into the flow circuit through a connector rather than a catheter. These modifications eliminated variability in contrast mixing due to catheter tip positioning. During the second set of experiments, the Pipeline device configuration changed due to the fact that this device can change its configuration depending on the external forces applied on it at the time of deployment. In addition, the need to remove air bubbles from the system subjects the device to further manipulations. The Pipeline initial configuration seen in Figure 32A was imaged by microCT and applied in the CFD simulations. The modified configuration in Figure 32B appeared slightly more compacted with the wires in the distal end packed closely providing more resistance to contrast entry into the aneurysm, which was reflected in the washout experimental data. The Pipeline device got further deformed to the configuration in Figure 32C where it appears as a highly dense wire mesh. The data collected from these latter configurations is reflected in the washout angiograms. The convective decay time constant for the Pipeline group was significantly higher than the FRED group. The experimental results which reflect device configuration variability were not captured in the CFD simulations where there was little difference in the intra-aneurysmal kinetic energy for FRED and Pipeline.

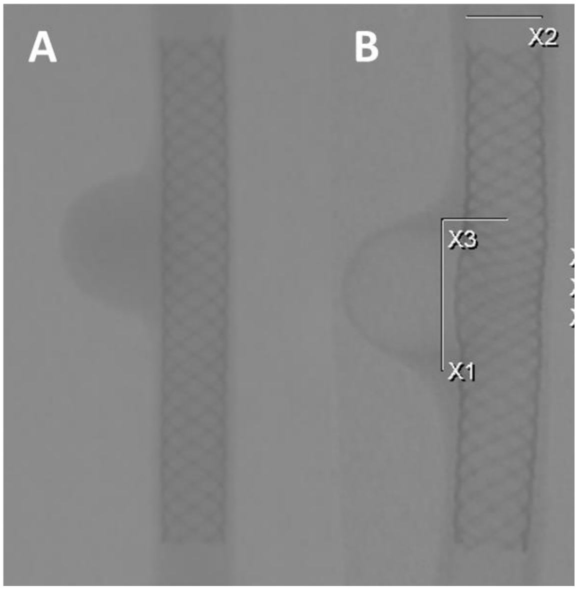

Figure 33: geometric configuration of the Pipeline device implanted within the same sidewall aneurysm model in 2015 (A) and a device implanted one year earlier (B)

Figure 33 shows two Pipeline devices deployed in the same sidewall aneurysm model by the same neurointerventionalist using the same technique. The devices appear slightly different in the angiogram and a more detailed comparison may be obtained by microCT imaging of the new device deployment in Figure 33A. Overall, the unstable configuration of the Pipeline device, is evident in Figures 32 and 33, is the result of a device composed of inadequate number of wires braided at too high of a braiding angle to compensate for the small number of wires. For future studies, microCT imaging is needed for the configuration of the device that will be used for both experiments and simulations.

The self-expanding braided flow diverters require delicate handling. Particularly when performing *in vitro* experiments care must be taken to ensure that wire configurations are not modified by external handling of the silicone vessel. Minor modifications in wire configurations can significantly alter the flow exchange between the parent vessel and the aneurysm. A more robust comparison between commercial flow diverters with different designs will require a larger number of flow samples to eliminate intra-device group variability.

CHAPTER 4: EXPERIMENTAL EVALUATION OF FLOW DIVERSION EFFICACY THROUGH ANGIOGRAPHIC WASHOUT ANALYSIS IN THE RABBIT MODEL

INTRODUCTION

The rabbit elastase-induced aneurysm model is a widely used in-vivo model for testing of neuro-endovascular devices. The rabbit elastase aneurysm model provides a robust and relatively economical in-vivo model with several similarities in size and morphology to human aneurysms. Performance of flow diverters has been evaluated in-vivo through the rabbit elastase induced aneurysm model previously [53, 54, 57, 65, 104, 105]. Specifically, efficacy of flow diversion was investigated in the rabbit elastase aneurysm model[53, 57, 106].

METHODS

Creation of experimental aneurysms:

Creation of the aneurysm in the rabbit has been described in detail elsewhere[64, 65]. The experiments were approved by the IACUC. A schematic of the elastase induced aneurysm induction procedure is described in Figure 35. Briefly, male white New Zealand rabbits were pre-anesthetized through local intramuscular injections of xylazine and ketamine. The rabbits were then intubated and maintained under inhalation anesthesia of 1-2% isoflurane. Following incision, the right common carotid artery (RCCA) was exposed and a 6F introducer sheath was introduced retrograde with a micropuncture access kit. Diagnostic angiogram was performed by contrast injection through the sheath. A 3F balloon was introduced (Fogarty, Baxter Healthcare) through the sheath and positioned at the RCCA ostium. A microcatheter was introduced side by side with the balloon and positioned just distal to (above) the balloon. The distal end of the RCCA was ligated. The balloon was then inflated with a contrast-saline solution to enable visualization of the balloon under fluoroscopy. The balloon sealed the RCCA to provide an isolated vessel segment. Elastase solution comprised of 50% porcine pancreatic elastase (Worthington Biochemical, Lakewood, NJ) and 50% angiographic contrast was then infused into the dead space between the balloon and the introducer sheath and incubated there for 10 to 15 minutes. The elastase solution was then drained and the balloon was deflated. Post incubation diagnostic angiogram was acquired. The incision was sutured, the rabbits were recovered from anesthesia, and the aneurysms allowed to mature for a period of three weeks.

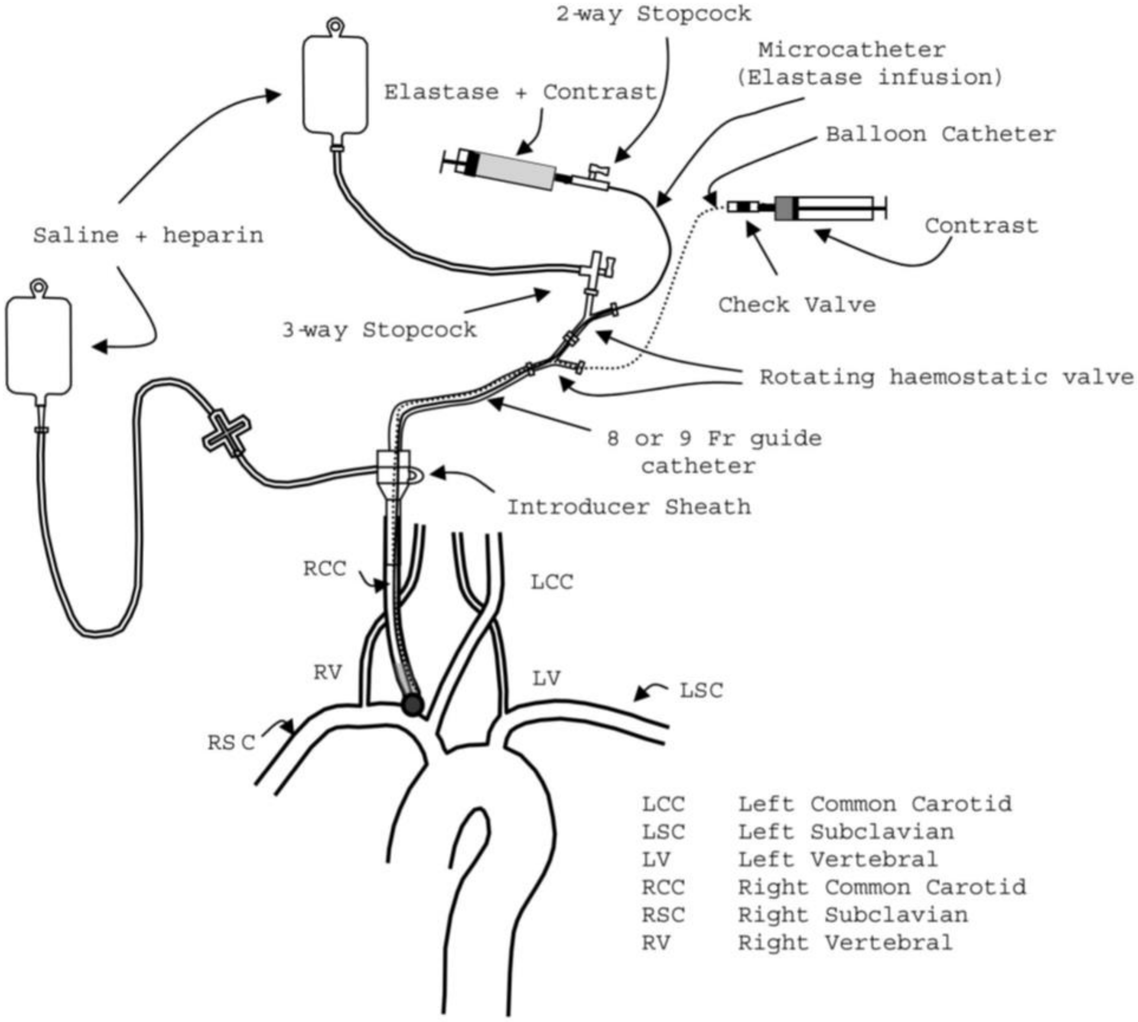

Figure 34: Schematic of the endovascular procedure for creation of elastase induced aneurysms in rabbits [64]

Flow diversion treatment of aneurysms and experimental data acquisition:

Following the three weeks the rabbits were implanted with a flow diverter designed in our own lab (4 mm device diameter, nominal porosity of 70%, and nominal pore density of 18.3pores/mm^2). For the implantation procedure the animals were anesthetized similar to the aneurysm induction procedure. Thereafter, the right femoral artery was exposed by a surgical cut-down and a micro-puncture access kit was used to insert a 4F introducer sheath. A 4F catheter was navigated through the sheath to the aortic arch and a diagnostic angiogram was performed. Under roadmap guidance, the 4F catheter was replaced with a stent delivery system. The flow diverter was then deployed such that the device had equal landing zones proximal and distal to the aneurysm.

High-speed angiograms were acquired at 30frames/sec for 20 seconds just before and immediately after device implantation. Apnea was mechanically induced during the imaging period. The injection parameters were kept the same for all angiograms acquired in this study (5 ml of contrast injected at2.5 cc/s). An injection delay of 2.5 sec was programmed into the power injector to allow acquisition of a mask for digital subtraction angiography (DSA).

The DSA data was imported into MATLAB and the aneurysm region of interest (ROI) was segmented[53, 57, 66] as seen in Figure 35. A contrast concentration-time curve (washout curve) was obtained for each angiogram by taking a sum of the gray scale intensities of all pixels within the ROI (Figure 35).

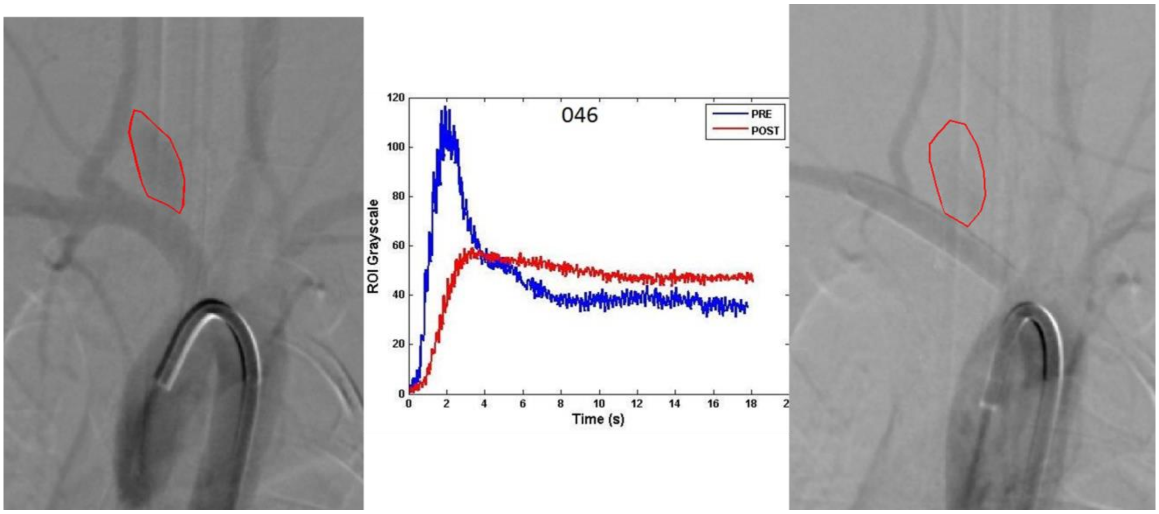

Figure 35: ROI segmentation pre (left) and post (right) flow diverter right implantation and washout curves obtained for the aneurysm (blue: pre-device, red: post-device).

Venous and breathing artifact correction:

In some rabbits high frequency fluctuations were observed in the contrast washout curves. The frequency of these fluctuations showed that these are related to respiratory rate caused by motion artifact of the aneurysmal region of interest when (sufficient) apnea was not induced during contrast injection and imaging. This respiratory artifact was removed, or attenuated, by using a notch filter in MATLAB as demonstrated in Figure 36 [53, 57, 66].

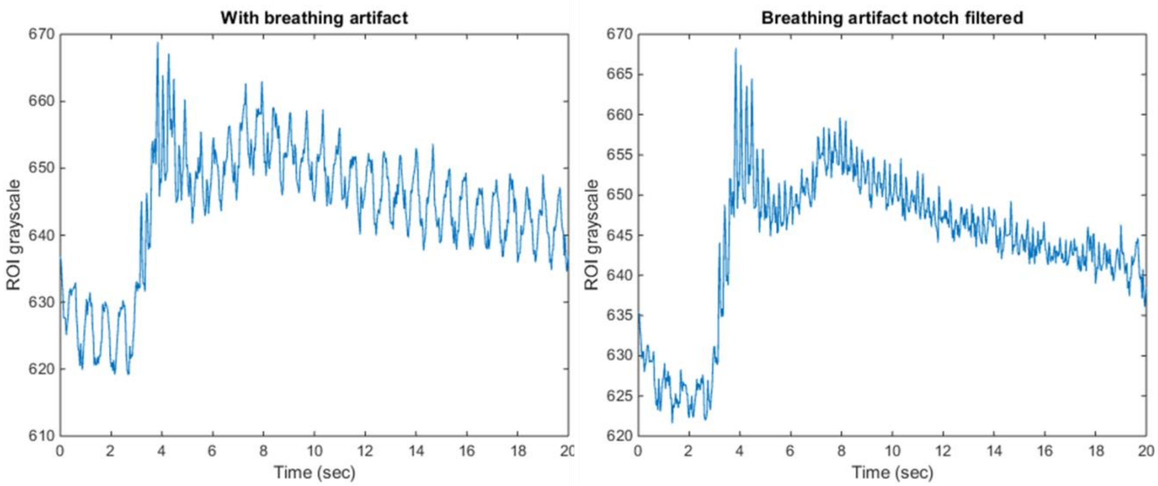

Figure 36: Rabbit aneurysm washout curve with breathing artifact corrected through notch filter to obtain corrected washout curve[53, 54, 57].

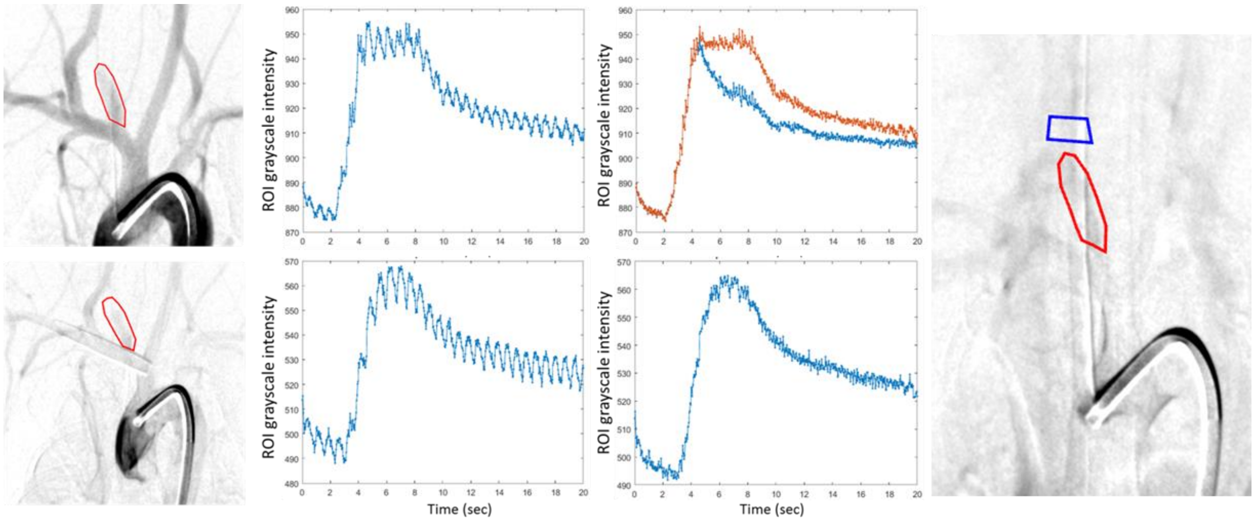

Figure 37: Correction for venous overlay on angiographic washout. Top row left to right: pre device angiographic segmentation; washout curve with venous overlay and breathing artifact (center); breathing artifact corrected washout curve (red) and the venous as well as breathing artifact corrected curve (blue). Bottom row left to right: post device angiographic segmentation; washout curve with breathing artifact; breathing artifact corrected washout curve. Image on the right demonstrates segmentation of the aneurysm (red) and venous region (blue) to calculate the average venous contrast concentration.

Since the mathematical model fit requires long acquisition times, inevitably the contrast that was injected arterially will appear in the veins and there is a high likelihood that one of these veins over/under-lays the aneurysm. Contrast return through veins traversing the ROI will thus introduce artefactual undulations in the washout curves, particularly in the contrast decay portion of the curve. Venous correction was applied by identifying a segment of the vein outside the aneurysm, finding its contrast concentration-time curve and subtracting it from the arterial curve as shown in Figure 37. After the final concentration-time curves (washout curves) within the aneurysm were obtained, the mathematical model described in equation 17 was applied to obtain the optimized parameters of the model [53, 54, 56, 57, 66].

Mathematical model:

The amplitude of the aneurysm washout curve (δ) is one of the parameters used to construct the washout coefficient. The amplitude δ for each washout curve prior to normalization is measured as:

$$\delta = C(t)\max - C(t)\min \qquad 18$$

The final washout curves for each animal pre and post flow diversion were normalized after the amplitude was obtained and these were fitted to the mathematical model described in equation 17 and explained in detail in Chapter 3 [53, 54, 56, 57, 66]. In order to establish a singular parameter that can predict the efficacy of flow diversion, the washout coefficient W was constructed and quantified. The washout coefficient was first described by Sadasivan et al [57] to test the efficacy of flow diversion in the rabbit elastase induced aneurysm model.

$$W = \frac{\delta_{POST}}{\delta_{PRE}} \times \frac{\rho_{diff\,POST}}{\rho_{diff\,PRE}} \times \frac{\tau_{diff\,POST}}{\tau_{diff\,PRE}} \qquad 19$$

The washout coefficient utilizes the washout parameters obtained by the model fit to the washout curve. The washout coefficient is calculated as the multiplication of the post/pre ratios of the washout amplitude, the diffusive component amplitudes, and the diffusive decay time constants. For the rabbit elastase aneurysm morphology, the diffusive component of contrast transport is hypothesized to increase following flow diversion, which is reflected in an increase the washout time constant and thus in the washout coefficient. The washout coefficient is expected to capture the alteration to the washout curve from an aneurysm in response to a flow diverter implantation in a single number and consequently be able to predict aneurysm occlusion. Follow-up angiograms were acquired at 3 months and 6 months post flow diverter implantation to assess aneurysm occlusion status.

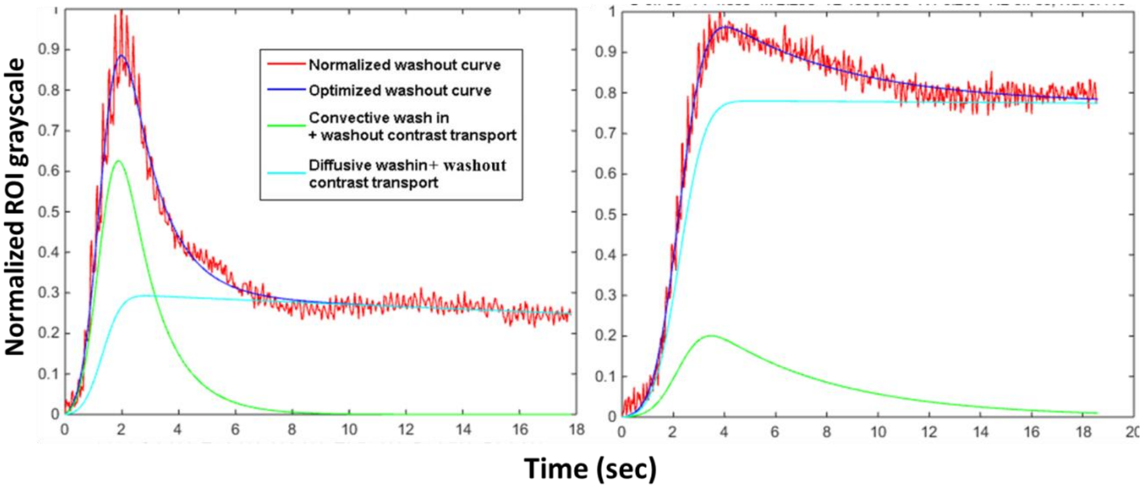

Figure 38: Sample aneurysmal washout curve (red) pre (left) and post (right) that is normalized and fit with a mathematical model (blue) that is able to separate the contrast transport mechanics into convection (green) and diffusion (cyan); the final model (blue) is the sum of the convection and diffusion components.

Experimental design and statistical analysis

In order to correlate the washout parameters in the rabbit elastase induced aneurysm model with the outcome of flow diverter treatment and determine parameter values for predicting efficacy of flow diversion, we had to determine the sample size by the width of the confidence interval of the sensitivity or specificity estimates instead of power analysis. In order to determine the same sample size for the required sensitivity or specificity confidence intervals (~0.9 or close to 1), we used Wilson score method as it provides the best performance for all sample sizes [107, 108]. Assuming an estimate of 90% for specificity (p = 0.9) and alpha = 0.05 and assuming that a lower confidence interval of 70% is acceptable, n = 21 was obtained through Wilson score method for estimating confidence interval. The obtained n is for the number of controls where aneurysm is not occluded required since we estimated specificity. Now estimating 90% sensitivity interval in the same manner, the required number of cases with aneurysm occluded is n = 21. Thus we needed a total of 42. Data was available from n = 22 rabbits from a previous study [54, 57]. Hence for this work, at least n = 20 successful data points were required. The rabbit elastase induced model has a 20% attrition rate [109].

Statistical analysis was performed using Instat (GraphPad Software, La Jolla, CA). Comparison between the washout curve parameters and the parameters obtained from the mathematical model pre and post flow diversion was performed using paired t-test. Comparison between the occluded and non-occluded groups was performed through unpaired t-test. Each data-set went through the normality test and based on the normal or non-normal distribution of the data, parametric or non-parametric tests were selected for comparison. In case of non-parametric data, the Wilcoxon test was selected to perform comparison between the groups. For all statistical tests, a p value of 0.05 or less was considered significant.

RESULTS

Twenty seven aneurysms underwent the flow diversion treatment procedure[53, 54, 57]. Five rabbits died during treatment phase – 1 due to hypervolemic hemodilution from infusion of excess fluids, 1 during anesthesia induction prior to the treatment procedure, 1 due to wire perforation of an abdominal artery resulting in retroperitoneal hemorrhage, 1 due to excessive chewing of the rubber mat in its cage resulting in gastric rupture, and 1 due either to a difficult intubation requiring mask inhalation or hypervolemic hemodilution. Of the remaining 22 animals, 1 rabbit (R11-144) was not included in the analysis because the brachiocephalic artery was found to be completely occluded from its origin at the aortic ostium at 3 month (and 6 month) follow up due to device-induced thrombosis. In two further rabbits R11-026, R11-030 the washout curve was heavily affected by breathing, venous overlay, and a small size aneurysm making the data unamenable to artifact correction. The angiograms of a fourth rabbit (R11-021) were deleted from the angiography computer before the data was backed up. Sixty percent of the net attrition occurred within the first 2 months of this 2½ year study. In 17 of the remaining 18 rabbits that were analyzed, angiograms were taken at 3 and 6 months post flow diversion, however, in the remaining rabbit (R11-142) the final angiogram was taken at 120 days post implant instead of 6 months since the rabbit injured its spine and had to be euthanized at that time point.

Average dimensions of the aneurysms created in this study are: length 7.69 ± 1.3, neck 2.86 ± 0.71, width 3.44 ± 0.66 mm (See Table 2).

Table 2: Dimensions of the aneurysms induced in the 18 rabbits analyzed in this work.

Rabbit ID	Length (mm)	Neck (mm)	Width (mm)
R11-007	5.89	1.92	1.94
R11-008	7.5	2.35	3.5
R11-020	7.88	2.36	4.26
R11-027	7.25	2.81	3.8
R11-028	8.26	4.33	4.05
R11-029	5.27	2.53	3.1
R11-142	8.29	3.35	3.95
R11-145	10.93	3.59	3.96
R12-037	7.38	3.2	3.19
R12-039	9.35	2.57	4.35

R12-040	7.44	3.4	3.2
R12-043	7.43	3.58	3.79
R12-045	8.89	2.72	3.3
R12-046	8.05	3.6	4
R12-047	7.22	2.14	2.34
R12-049	7.92	3.28	2.77
R13-197	7.6	1.9	3.35
R13-198	5.9	1.9	3
Mean±s.d.	7.69 ± 1.3	2.86 ± 0.71	3.44 ± 0.66

. The occluded and non-occluded groups had 9 rabbits each. Based on the angiograms, the aneurysms in rabbits R11-007, R11-028, R11-145, R12-039, R12-040, R12-045, R12-047, R12-049, and R13-198 were not occluded at final follow up. In rabbits R11-145, R12-039, R12-040, R12-049, and R13-198 minimal filling of a minute remnant of the aneurysm was visible. This leads to the speculation that given more time these aneurysms could have possibly gone on to complete occlusion.

Some representative examples of angiograms and washout curves are shown here while the others are given in Appendix A. The first example is rabbit R11-007, which did not occlude at the 6 month follow up time point. The angiographic image segmentation and washout curves fitted with the mathematical model are presented in Figure 39.

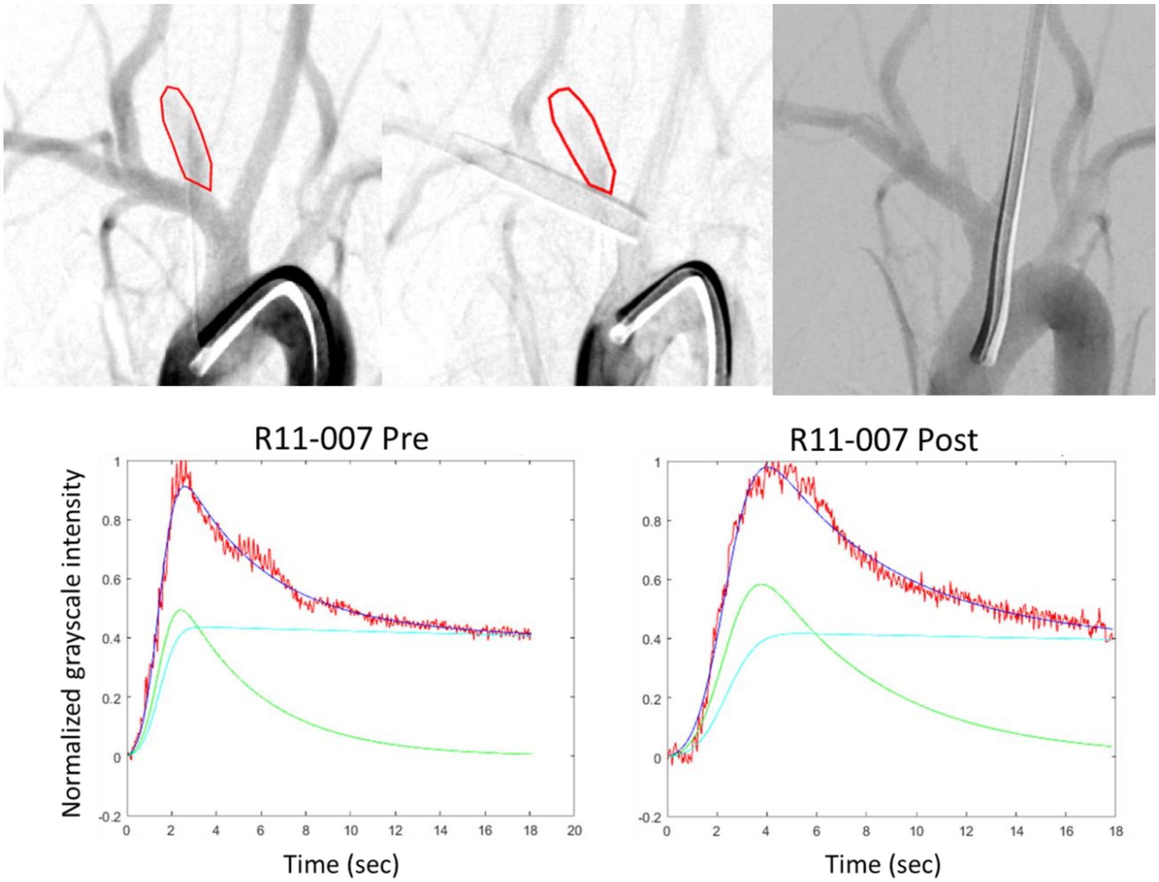

Figure 39: Angiographic image analysis for rabbit R11-007. Top panel shows snapshots of angiographic image data pre device (left), post device implantation (center), and at 6month follow up time point (right). Bottom panel demonstrates the normalized washout curves obtained pre and post flow diverter implantation in red. The mathematical model fitted onto the washout curve is in blue. The fitted mathematical model is distributed into the convective (green) and diffusive (cyan) components of contrast transport mechanics.

In the second example, rabbit R13-197, the aneurysm completely occluded at the 6 month follow up time point (Figure 40).

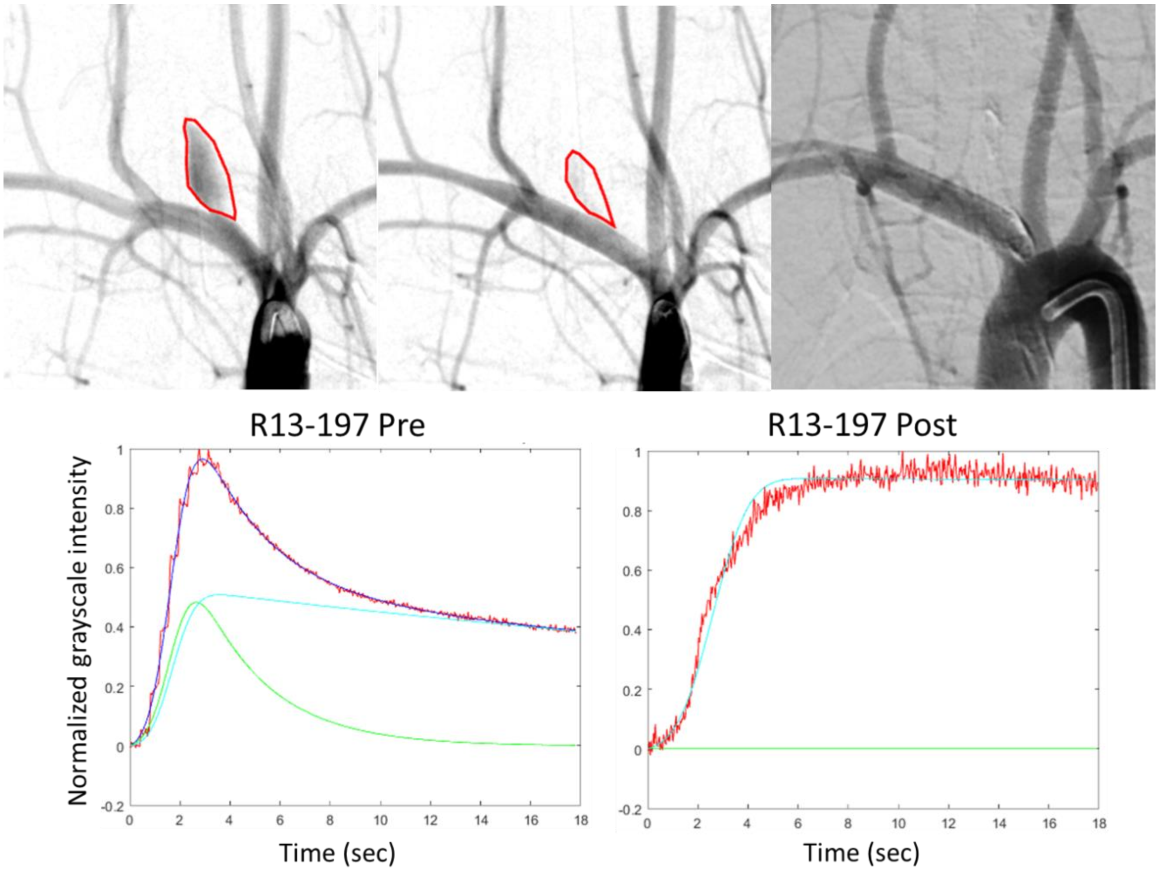

Figure 40: Angiographic image analysis for rabbit R13-197. Top panel shows snapshots of angiographic image data pre device (left), post device implantation (center), and at 6month follow up time point (right). Bottom panel demonstrates the normalized washout curves obtained pre and post flow diverter implantation in red. The mathematical model fitted onto the washout curve is in blue. The fitted mathematical model is distributed into the convective (green) and diffusive (cyan) components of contrast transport mechanics.

The third example presented here that of is rabbit R13-198 in which the aneurysm nearly occluded but still had minor residual filling at 6 month follow up (Figure 41).

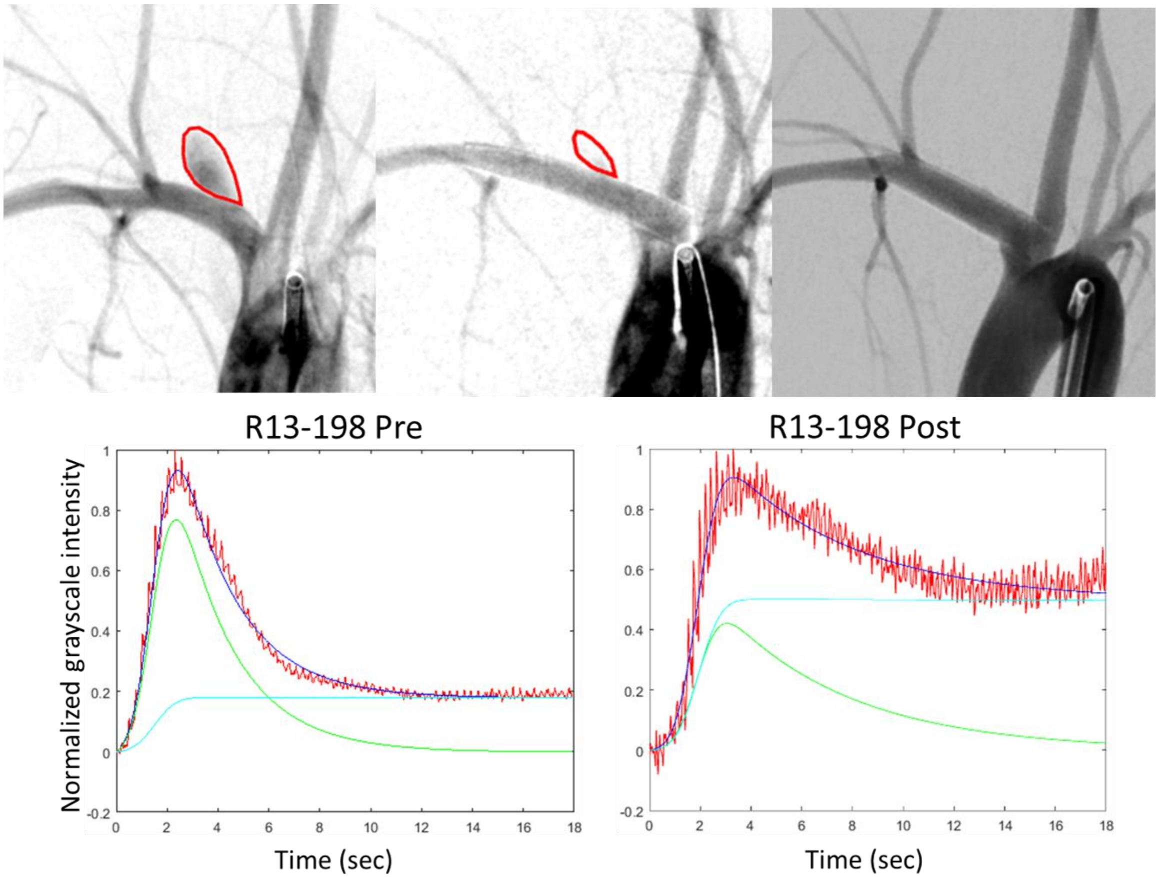

Figure 41: Angiographic image analysis for rabbit R13-198. Top panel shows snapshots of angiographic image data pre device (left), post device implantation (center), and at 6month follow up time point (right). Bottom panel demonstrates the normalized washout curves obtained pre and post flow diverter implantation in red. The mathematical model fitted onto the washout curve is in blue. The fitted mathematical model is distributed into the convective (green) and diffusive (cyan) components of contrast transport mechanics.

The normalized washout curves and model-fits pre and post flow diverter implantation for the 18 rabbits included in the analysis are presented in Appendix A. The magnitude of the washout curves was normalized to enable comparison between the rabbits. The normalized washout curves indicate a shallower slope of contrast wash-in into the aneurysm following flow diverter implantation and prolonged decay of the contrast intensity. Qualitatively the curves indicate an increase in the diffusive component and reduction of the convective component following flow diversion.

Comparison of washout parameters in the 18 rabbits pre and post flow diversion shows significant differences. Washout curve amplitude δ both raw and normalized by number of pixels were significantly lower ($p<0.0001$) post flow diverter implantation (Figures 42, 43). Following normalization of the washout curves comparisons were performed on the other model parameters using paired t-test since they were evaluated pre and post device implantation in the same animal. The convective time constant ($p=0.0003$) as well as the diffusive time constant ($p=0.0016$) were significantly higher post flow diversion (Figures 44, 45). The convective time constant was 1.403±0.84s pre device and 4.613±4.59s post device. The diffusive time constant was 390.75±737.37s pre device and 1419.5±840s post device. This indicates increased residence time of contrast within the aneurysm post flow diversion.

The proportionate amplitudes of the convective and diffusive components were significantly different pre and post flow diversion. The convective component amplitude was significantly lower while the diffusive component was significantly higher post flow diversion. Figures 46 and 47 compare the convective and diffusive component amplitudes pre and post flow diverter implantation, respectively. The pre and post device convective component amplitudes were 0.622±0.122 and 0.377±0.183 ($p<0.0001$), respectively. The pre and post device diffusive component values were 0.313±0.123 and 0.547±0.182 ($p<0.0001$), respectively.

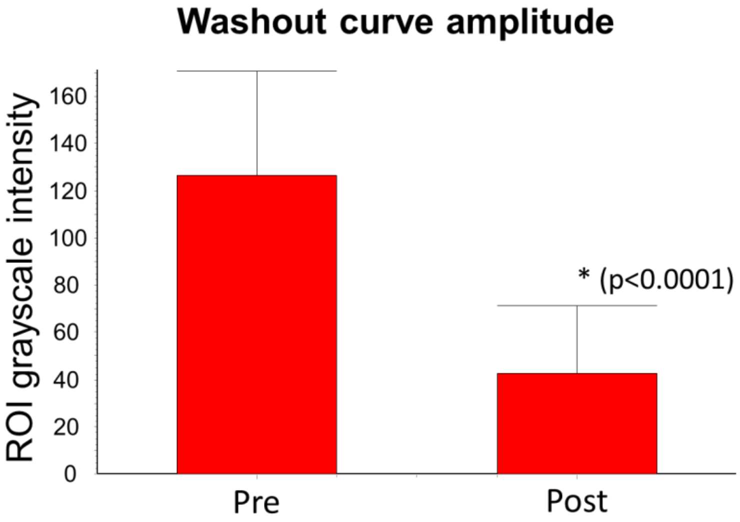

Figure 42: Comparison of washout curve amplitude pre and post flow diverter implantation

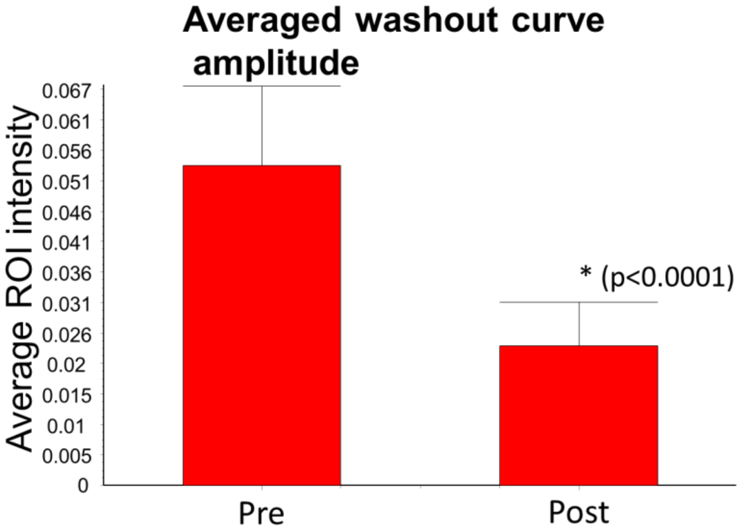

Figure 43: Comparison of washout curve averaged amplitude (angiographic intensity normalized by total number of pixels in region of interest for each aneurysm) pre and post flow diverter implantation

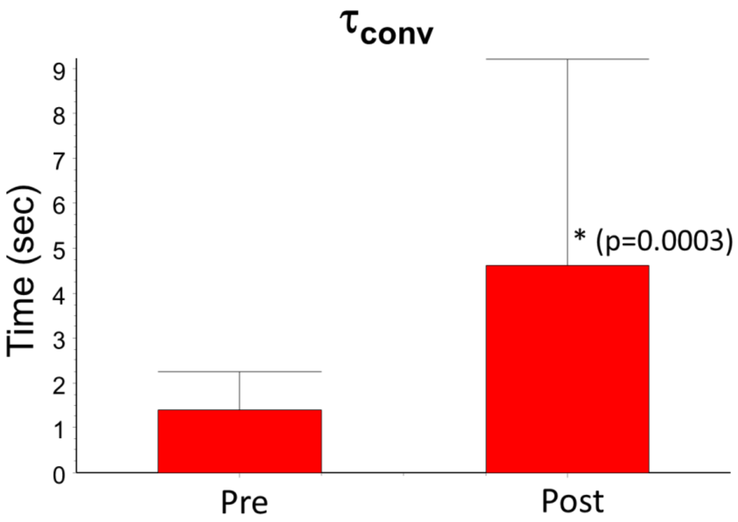

Figure 44: Comparison of convection decay time coefficient pre and post flow diverter implantation

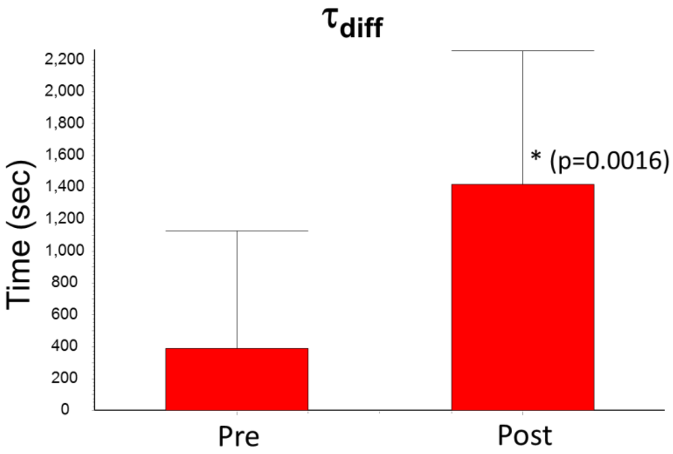

Figure 45: Comparison of diffusion decay time coefficient pre and post flow diverter implantation

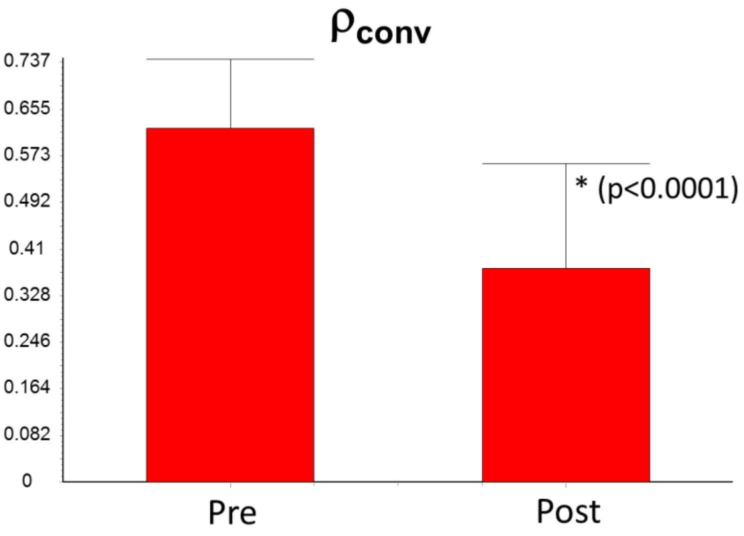

Figure 46: Comparison of washout curve convective component amplitude pre and post flow diverter implantation

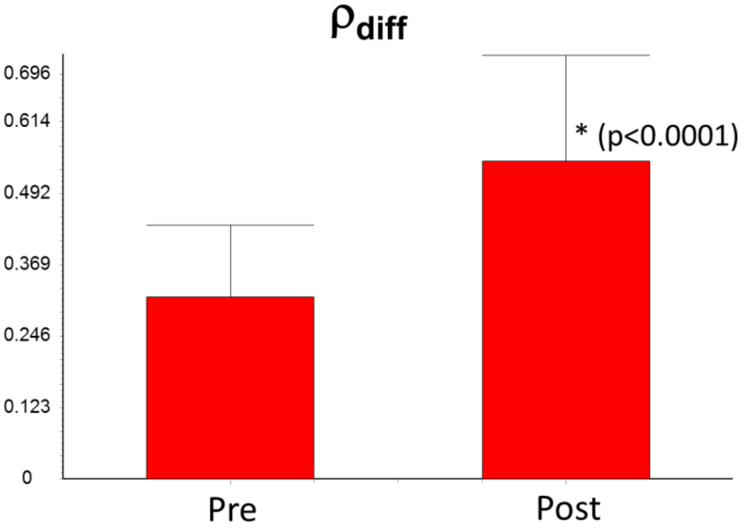

Figure 47: Comparison of washout curve diffusive component amplitude pre and post flow diverter implantation

The average calculated value of the washout coefficients for the occluded and non-occluded groups were not significantly different, (p=0.0625), although the p-value was just above the selected significance value of 0.05 as seen in Figure 48. Therefore, it is possible that the washout coefficient can be further investigated and optimized to achieve a higher significance level.

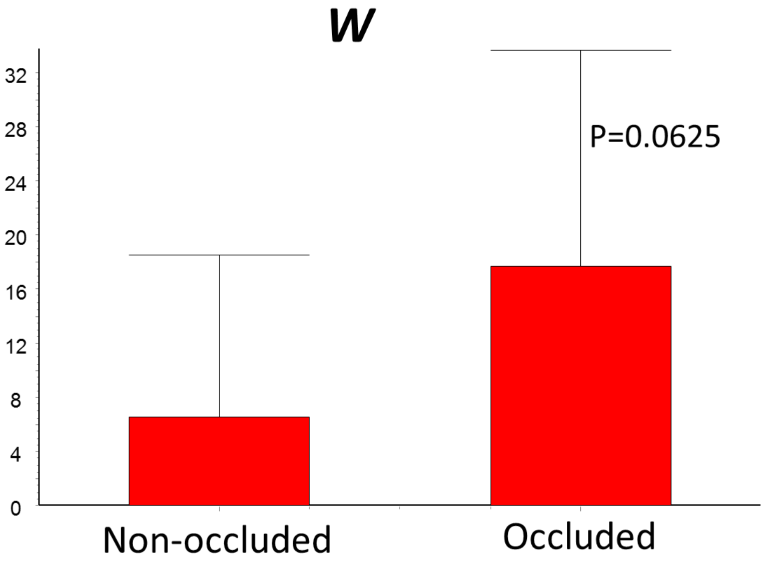

Figure 48: Comparison of the washout coefficient parameter between the non-occluded and the occluded groups

The mean value of the washout coefficient for the occluded group was 17.65 ± 16.01 and for the non-occluded group it was 6.54 ± 12.01. The large standard deviation in both groups shows that there was a high scatter in the data (Figure 49), nevertheless, the overall the trend indicates a higher washout coefficient value for the occluded group (Figure 49).

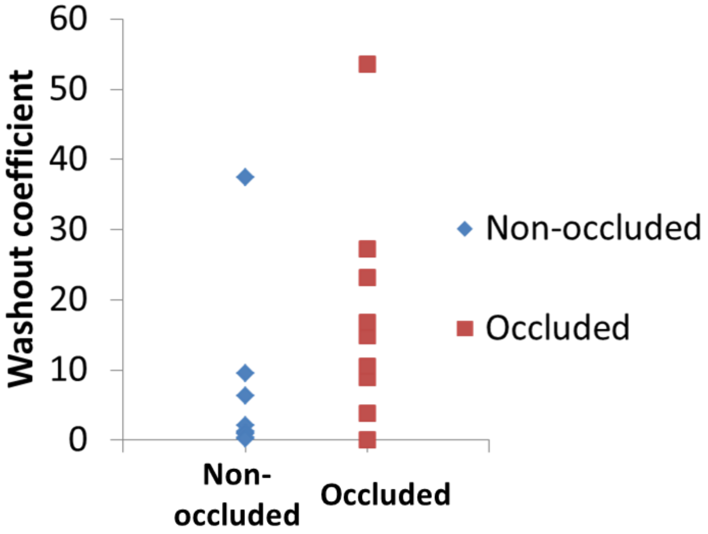

Figure 49: Scatter plot comparison of the washout coefficient values between the non-occluded and occluded groups

DISCUSSION

The mean dimensions of the aneurysms in this study are height 7.69 mm, neck 2.86 mm and width 3.44 mm. A previous study [57] reported mean aneurysm size in 40 rabbits of height 7.9+/-0.3 mm, neck: 4.1+/-0.2 mm, and width 3.7+/-0.1 mm. The average aspect ratio for the aneurysms was 2.1+/-0.1[57]. Onizuka et al. reported mean dimensions of height 10.2+/-2.8, width 4.2+/-1.2, and neck: 3+/-1.5 [58] in the same animal model of 30 rabbits. While the aneurysms in this study are within the range of dimensions of other published studies, they, especially the neck dimension, are at the lower end of the range. During the course of the study, it was noted that identical concentrations of elastase from different vendors can elicit marked variations in animal morbidity and mortality as well as aneurysm dimensions. This effect needs to be investigated further and may be related to the lower range of dimensions found.

This study is a continuation of previous experiments in rabbits to better understand the changes in contrast transport into the aneurysm after implantation of a flow diverter in the parent artery and to develop a methodology through which the long term efficacy of the implant can be predicted by contrast transport analysis. The presence of a flow diverter significantly alters the blood flow dynamics into and out of the aneurysm and such changes are reflected in the changes in the transport of a bolus of contrast into and out of the aneurysm. The mathematical model that was applied to the contrast concentration time curve inside the aneurysm which includes 7 parameters shows that 5 of the parameters that are related to contrast dispersion indeed show significant differences when their values are compared before and after placement of the implant. The increased convective and diffusive time constants signify a decrease in flow activity inside the aneurysm, which is visible in the angiograms as longer time required for the contrast to wash through. In the rabbits, the aneurysms are located on the outer aspect of the bend and therefore contrast transport can be differentiated into the convective (bulk transport) and diffusive components, each of an appreciable proportion. Furthermore, after device implantation there are significant changes in both physical mechanisms, namely, convection and diffusion, which are involved in transport of contrast into and out of the aneurysm. While not surprising, our initial clinical data suggests that in human, naturally occurring, aneurysms most of the contrast transport in and out of the aneurysm is occurring by convection with minimal or lack of the diffusive component. Indeed most human aneurysms tend to occur at flow impingement points where the axis of the aneurysm tends to coincide with the direction of the oncoming flow. In the animal model the choice of the location of the aneurysm is dictated by many other factors and as such, the axis of the aneurysm does not coincide with the direction of the flow accentuating phenomena such as diffusion that may be negligible in the human case.

The mathematical model used in this study has been applied by other groups and successfully delineated the convective and diffusive components of contrast transport. Struffert et al. [106] created elastase induced aneurysms in 16 rabbits with mean height 6.2+/-2.4 mm, width 3.5+/-1 mm, and neck, 3.4+/-1.1 mm. They successfully fitted their time density curves (contrast concentration washout curves) to the mathematical model proposed by Sadasivan et al[57]. Even though their contrast injections were not standardized or automated (hand injections were performed[106]), the study concluded that it is feasible to use the convective-diffusive model to determine flow diversion efficacy.

This study shows significant differences (p=0.0625), although strictly speaking it did not hit the arbitrary significance value of 0.05, between the washout coefficient calculated immediately post flow of aneurysms that eventually went on to occlude at six months vs the ones that did not occlude at the end point. This suggests it may be a potential predictive parameter of long term aneurysm occlusion at the time of treatment. One of the reasons that significance at the 95% value was not attained may be attributed to the small sample size of n = 9 in each group. Another possibility is that a 6 month follow up time is too short, particularly because 5 of the 9 aneurysms in the non-occluded group had only a small remnant at follow up.

Yet another possibility is that the washout coefficient is not the optimal parameter for the task and another parameter may be sought that may yield more definitive results.

CHAPTER 5: CLINICAL ANGIOGRAPHIC WASHOUT ANALYSIS

This chapter describes clinical washout data acquisition and analysis. The need to predict the efficacy of flow diversion has been described in detail in the Introduction. Angiographic image analysis on data acquired at a high frame rate in patients can be used to quantify the alteration in contrast transport mechanics post flow diversion, which in turn can establish a threshold or parameter to predict long term treatment outcomes after flow diversion. The angiographic analysis and mathematical modeling presented in Chapter 4 for the in vivo experiments are utilized for the analysis of clinical data.

METHODS

Clinical angiographic data acquisition

Following IRB approval, consent for high speed angiographic imaging was obtained from patients scheduled for flow diversion treatment. This work aimed to enroll and acquire high speed angiograms in 40 aneurysms. Table 3 shows the aneurysm location, morphology and number of flow diverters deployed for each case. Angiographic data was acquired before and after flow diverter deployment in each patient using a state of the art Artis zee biplane angiography unit (Siemens Medical, Erlangen, Germany). Contrast injections were performed at 6 ml/sec for duration of 1 second and a 2.5 second injection delay through a 5Fr injection catheter with the catheter tip position maintained constant. Contrast injections were performed using a power injector (Medrad, Warrendale, Pennsylvania) as described in chapters 3 and 4. Angiographic data was acquired in either single- or dual-plane as determined by the physician performing the treatment. The selection of the plane was done based on the position of the aneurysm.

Table 3 describes the aneurysm location, size, and morphology information for the patients. The number of flow diverters implanted in patients during treatment and their device specifications are mentioned in Table 4.

Table 3: Details of aneurysm location, aneurysm dimensions, and morphology for the clinical cases analyzed.

Patient number(ID)	**Aneurysm location**	**Aneurysm dimensions**	**Aneurysm morphology**
Patient 1 (RH001)	Basilar artery	Length = 2.5cm, width = 11mm, Total size ~ over 4 cm	Giant partially thrombosed fusiform
Patient 2 (RK002)	Right cavernous segment ICA	2.5x2.3x2.4 cm neck 11mm	Giant bilateral saccular
Patient 3 (LP004)	Left ophthalmic segment ICA	4.3x3.6x3.4 mm	Saccular sidewall
Patient 5 (FC005)	Left cavernous segment ICA	Length = 3.6 cm, Width = 9.6 mm	Giant fusiform
Patient 6 (LC006)	Left ICA terminus	3.8x2.0 mm	Saccular terminus
Patient 7 (RH008)	Left ophthalmic segment ICA	2.8x3.5x3.8 mm Neck 4.1 mm	Saccular
Patient 8 (AA010)	Left vertebral artery	Length 16 mm, Width 11 mm	Large fusiform
Patient 9 (EAM011)	Left PCOM segment ICA	3.6x2.6 mm	Saccular wide-necked sidewall
Patient 10 (DT012)	Right cavernous segment ICA	Length > 4cm (petrous and cavernous segments)	Giant bilateral fusiform
Patient 11 (MN015)	Right ophthalmic segment ICA	10 mm, neck 4mm	Large saccular wide-necked
Patient 12 (PC016)	Right ophthalmic segment ICA	14x12.5x9.9mm, Neck 7mm	Large saccular wide-necked
Patient 13 (LT018)	Left ophthalmic segment ICA	11.5x6.3x6.3 mm, Neck 5.6 mm	Large multi-lobulated saccular wide-necked
Patient 14 (MZ019)	Right ophthalmic segment ICA	10.8x8.2x5.3mm, Neck 6.3 mm	Large saccular wide-necked
Patient 15 (KD020)	Right ophthalmic segment ICA	5.6x3.5x4.3, Neck 4.7 mm	Saccular sidewall wide-necked
Patient 16 (CM021)	Right cavernous segment ICA	16x13 mm, neck 6.5 mm	Large saccular wide-necked
Patient 17 (RG022)	Right ophthalmic	4.2x3.6x3.8 mm	Sidewall saccular

	segment ICA		
Patient 18 (DF023)	Left cavernous segment ICA	2x1.45 cm	Giant partially thrombosed saccular wide-necked
Patient 19 (LM025)	Right superior hypophyseal segment ICA	6.1x5x5.7mm, Neck 3.1mm	Saccular sidewall
Patient 20 (DL026)	Right superior hypophyseal segment ICA	4.9x4.7x.6.3mm, Neck 3.9 mm	Saccular sidewall
Patient 21 (MN027)	Right PCOM segment ICA	3.8x3.3x3.4 mm, Neck 3.5 mm	Saccular sidewall
Patient 22 (VB028)	Left superior hypophyseal segment ICA	4.8x.43 mm Neck 2.6 mm	Saccular sidewall
Patient 23 (VK029)	Left ophthalmic segment ICA	7x7 mm, Neck 4.5 mm	Saccular sidewall wide-necked
Patient 24 (MA031)	Left PCOM segment ICA	6mm	Saccular sidewall wide-necked
Patient 25 (DW032)	Left MCA	1.57x1.2cm	Large fusiform

Table 4: Number of flow diverters implanted at treatment procedure

Patient number(ID)	**No of flow diverters (Pipeline embolization device (PED)) deployed**
Patient 1 (RH001)	3 PEDs (PED1 4.5x35mm, PED2 4.5x20mm, PED3 4.5x16)
Patient 2 (RK002)	5 PEDs (PED1 5x35mm, PED2 5x30mm, PED3 5x30mm, PED4 5x30mm, PED5 5x12mm)
Patient 3 (LP004)	3 PEDs (PED1 4.25x20mm, PED2 4.25x18mm, PED3 4.25x16mm,
Patient 5 (FC005)	7 PEDs (PED1 5x20, PED2 5x20mm, PED3 4.75x20mm, PED4 4.5x20mm,

	PED5 4.25x20mm, PED6 4x20mm, PED7 3.75x20mm)
Patient 6 (LC006)	1 PED 3.75x12mm
Patient 7 (RH008)	3 PEDs (PED1 4.25x14mm, PED2 4x12mm PED3 4x12mm)
Patient 8 (AA010)	4 PEDs, (PED1 4.75x30, PED2 4.75x25mm, PED3 4.75x20mm, PED4 4.75x16mm)
Patient 9 (EAM011)	2 PEDs, (PED1 4.5x20 PED2 4.5x20)
Patient 10 (DT012)	12 PEDs, (PEDs 1-6 5x35mm, PEDs 7-11 5x30mm, PED12 5x25mm)
Patient 11 (MN015)	2 PEDs, (PED 1-2 3.75x18mm)
Patient 12 (PC016)	2 PEDs, (PED 1 4.5x16mm PED 2 4.5x20mm)
Patient 13 (LT018)	2 PEDs, (PED 1 4.25x20mm PED 2 4.00x14mm)
Patient 14 (MZ019)	1 PED 4x20 mm
Patient 15 (KD020)	2 PEDs, (PED 1 3.5x16mm PED 2 3.25x16mm)
Patient 16 (CM021)	1 PED 5x20 mm
Patient 17 (RG022)	2 PEDs, (PED 1 4.25x16mm PED 2 4x14mm)
Patient 18 (DF023)	2 PEDs, (PED 1 5x30mm PED 2 4.75x30mm)
Patient 19 (LM025)	3 PEDs, (PED 1 3.5x16mm PED 2 3.5x16mm PED3 4x20mm)
Patient 20 (DL026)	2 PEDs, (PED 1 3.75x20mm PED 2 3.75x20mm)

Patient 21 (MN027)	1 PED 3.75x18mm
Patient 22 (VB028)	1 PED 4x20mm
Patient 23 (VK029)	2 PEDs, (PED 1 4.25x20mm PED 2 4.25x14mm)
Patient 24 (MA031)	3 PED Flex, (PED 1 4x18mm PED 2 3.5x12mm PED 3 4x18 mm)
Patient 25 (DW032)	2 PED Flex, (PED 1 3.75x16mm PED 2 3.5x20mm)

To address concerns over radiation exposure, a variable frame rate (VFR) protocol was incorporated in collaboration with Siemens. Through VFR the angiograms are acquired efficiently with reduced radiation dosage to the patients where a high frame rate is utilized during the early portion of the run when maximal contrast transport occurs. Hence the rapid wash-in and wash-out phases of contrast transport inside the aneurysm are captured at a good resolution. For the second half of the angiogram when contrast transport in minimal or none, the frame rate is reduced to 7.5frames/sec from 15frames/sec. Follow up imaging was acquired in the patients at 6 months.

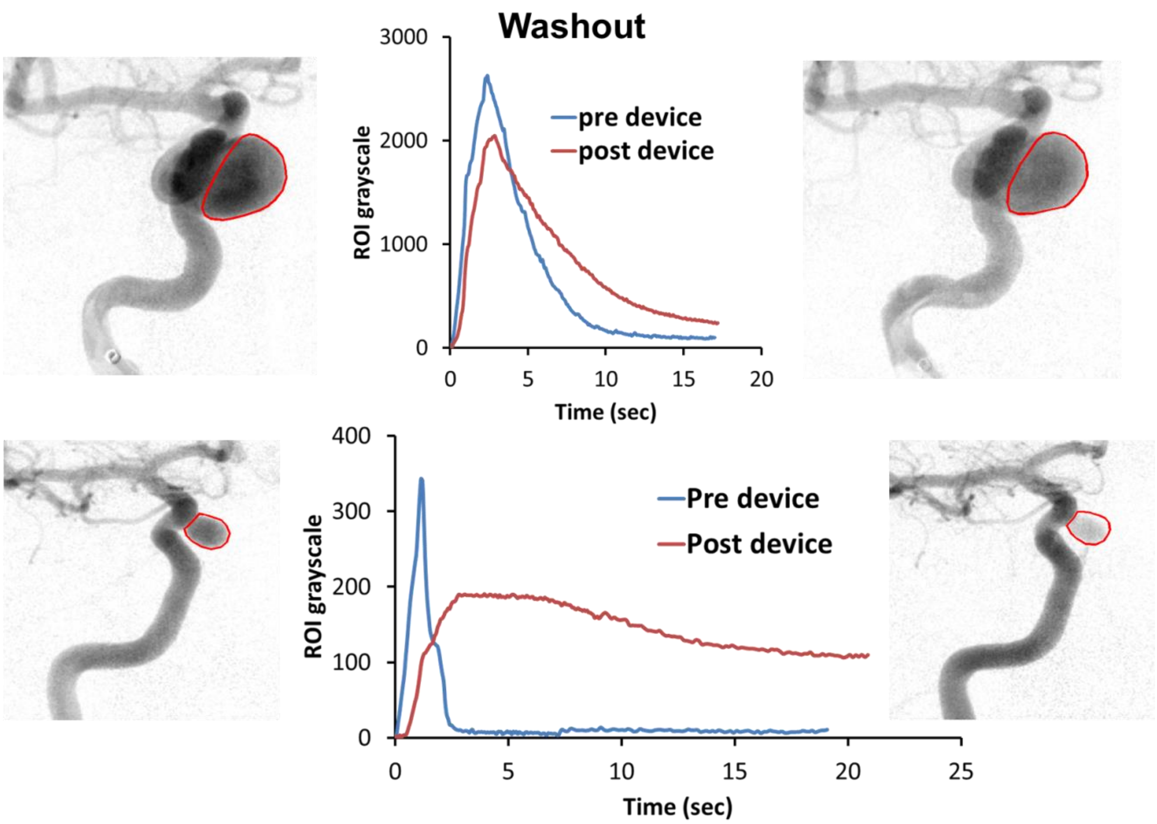

Figure 50: Top: ROI segmentation pre (left) and post (right) in patient CM021 and quantified washout curves pre and post (center) Bottom: ROI segmentation pre (left) and post (right) in patient LM025 and quantified washout curves pre and post (center)

Angiographic image analysis

The angiographic data acquired during the patient treatment was anonymized and exported from the Siemens angiographic machine. The angiographic image analysis was performed in MATLAB as described in detail in Chapters 3 and 4. The aneurysm region of interest was manually segmented and the contrast concentration-time curve within the region of interest was recorded. Angiographic image segmentation and washout curve generation are demonstrated in Figure 50 for two patients.

Image artifact correction – signal processing

Two sources of artifacts were noted on the recorded washout curves – venous overlay and catheter leakage. The corrections used for these artifacts are described below.

Interference into the aneurysm ROI from venous overlay altered the contrast concentration time curves for some of the patients in the study (Figures 51, 52). To correct for the overlay, a ROI was marked on the veins located close to the aneurysm and a venous washout curve was recorded. The average gray scale intensity was calculated by dividing by the number of pixels as:

$$Cavg = \frac{Cvein}{npix_{vein}} \qquad 20$$

Within the aneurysm ROI, the region of interference with the vein was identified and segmented to obtain the number of pixels altering the aneurysm signal (Figure 51, 52). The contrast concentration time curve of venous interference was then calculated by multiplying the average vein gray scale intensity with the number of pixels with interference to obtain Cvi.

$$Cvi = Cavg \times npix_{ROIvenousinterference} \qquad 21$$

Based on careful qualitative evaluation of the high speed angiography data as well as the quantitative washout aneurysm ROI and washout venous ROI curves, start and end points of venous interference were identified (Figures 51, 52). The original altered washout curve was then corrected by subtracting out the venous overlay values within the start and end points as:

$$C_{corrected} = C - Cvi \qquad 22$$

Where, C and Cvi were concentration time curves constraint within the duration of venous overlay on the aneurysm ROI defined by the start point and end point previously identified. The above correction was implemented in MATLAB.

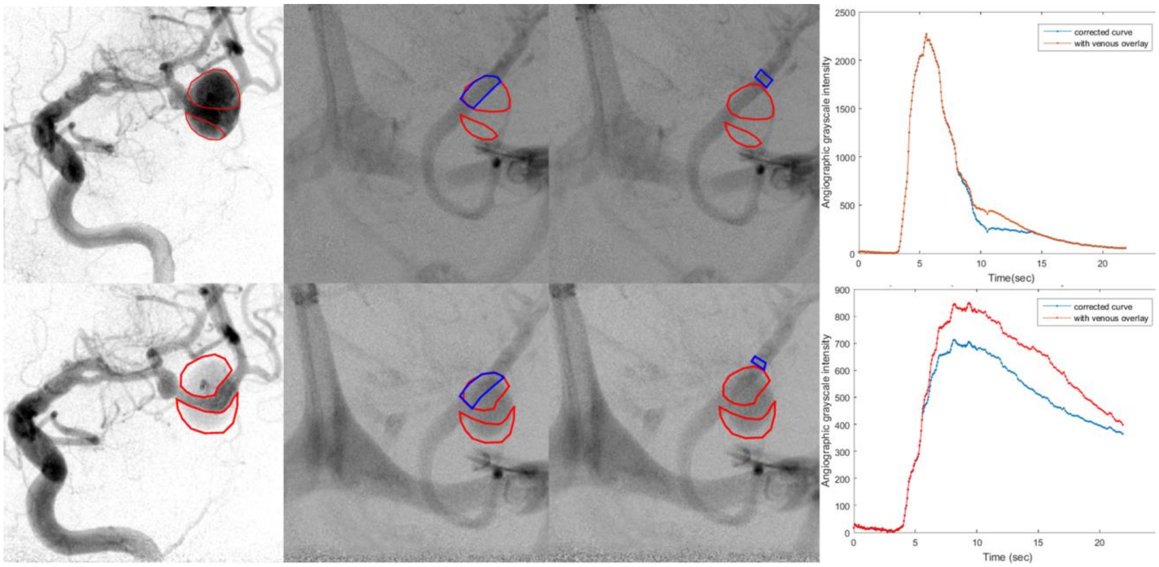

Figure 51: Example of venous overlay correction in patient DW032. Top panel represents the pre device data and bottom panel represents the post device data. Left image represents aneurysm ROI segmentation in red. Center left represents segmentation of venous ROI overlaying the aneurysm in blue and center right represents the venous ROI marked to calculate the average venous contrast drainage. Plots on the right represent the washout curves prior to correction (red) and post venous overlay correction (blue).

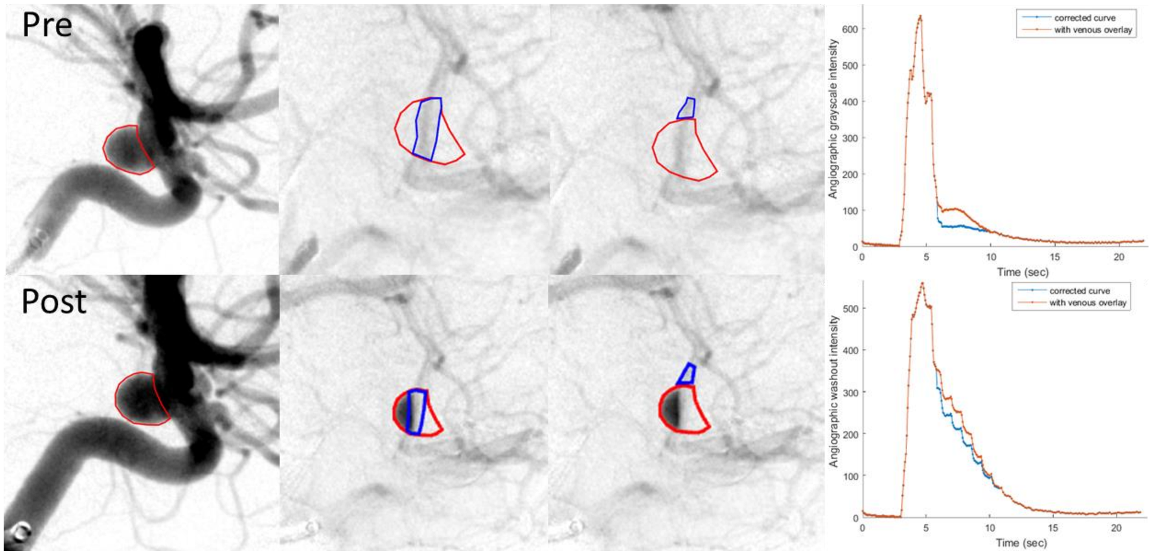

Figure 52: Venous overlay correction in patient MA031. Top panel represents the pre device data and bottom panel represents the post device data. Left image represents aneurysm ROI segmentation in red. Center left represents segmentation of venous ROI overlaying the aneurysm in blue and center right represents the venous ROI marked to calculate the average venous contrast drainage. Plots on the right represent the washout curves prior to correction (red) and post venous overlay correction (blue).

Besides venous washout interference, clinical contrast washout data was affected strongly by the leakage of contrast from the injection catheter following completion of the injection. The contrast continued to be aspirated from the contrast filled 5French injection catheter that was utilized in the patients. This aspiration was because of the fluid forces and the suction generated from the blood flow to the stagnant contrast inside the catheter. Resulting contrast interference was observed with each cardiac cycle and eventually reduced with time within the 20 second high speed angiographic run. Maximum interference was observed within the first few seconds after completion of the injection.

After this problem of contrast leakage from the injection catheter was observed in the data from initial set of patients, a 3-way stopcock was used between power injector tubing connected to the contrast syringe and the 5 Fr injection catheter tip positioned within the patient’s intracranial artery being imaged. The stop cock served as switch that was manually switched off immediately following completion of the contrast injection from the power injector to disconnect the contrast supply.

In several patient data-sets the concentration time curve correction was done through notch filtering. As applied in the previous chapter for rabbit data the notch filter removes a particular frequency from the signal. For persistent leakage of contrast from the catheter tip that arrived with every cardiac cycle a notch filter was applied to eliminate the particular frequency (Figure 53).

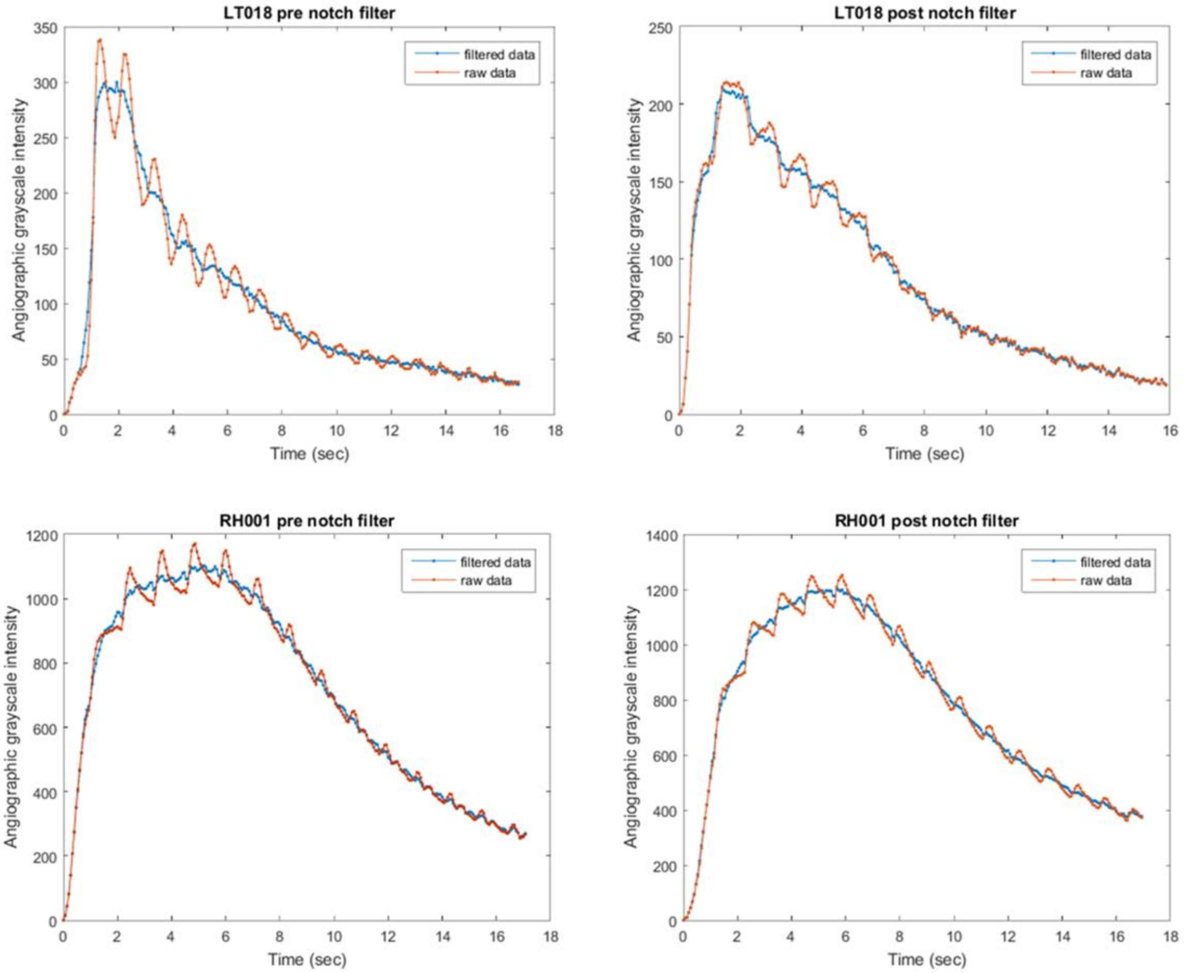

Figure 53: Application of notch filter to eliminate the contrast leakage signal from the concentration time curves for large (top panel) and giant (bottom panel) patient aneurysms respectively pre and post flow diverter implantation (effect of contrast leakage on the amplitude of ripples in the curve dampened following device deployment.

Although the notch filter was found to be suitable for large size aneurysms (Figure 53), in smaller sized aneurysms (<5-6mm), the secondary peak overshoot attributed to the contrast leakage was higher than the primary peak and could not be eliminated through a notch filter. In such cases, the signal was corrected by constructing a lower envelope through the valleys of the washout curve (Figure 54). A previously written envelope function in MATLAB [www.mathworks.com/matlabcentral/fileexchange/24902-envelope] was utilized and the resulting signal was an interpolation between user guided points. This removed what may have been interference in the form of a secondary peak.

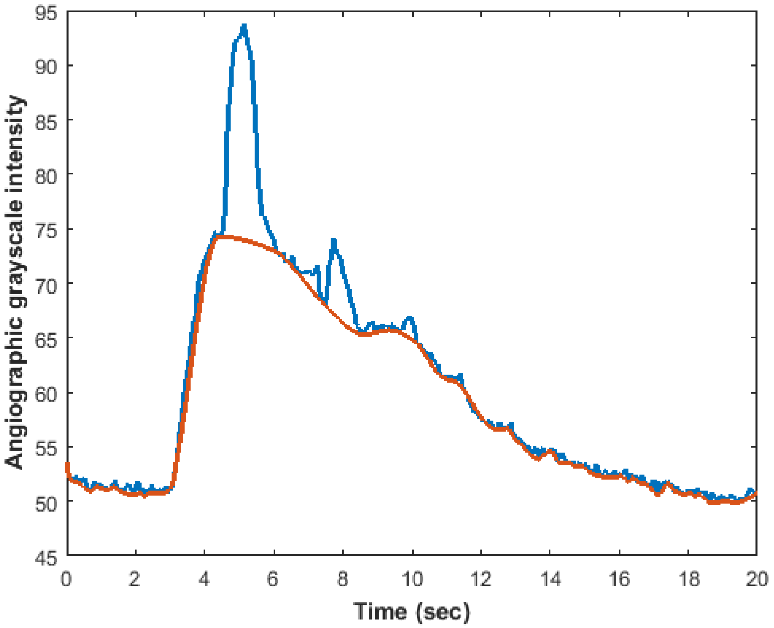

Figure 54: Lower envelope filter applied on raw concentration time curve obtained from patient LC006. The raw unfiltered concentration time curve is in blue and the lower enveloped filtered curve is in red.

Mathematical modeling

The amplitude δ for each washout curve prior to normalization was measured as:

$$\delta = C_{max} - C_{min} \qquad 23$$

The final corrected washout curves for each patient pre and post flow diversion were then normalized. The normalized curves were fitted to the mathematical model is described in detail in chapter 3, equation 17.

Data analysis

To quantify the exposure of contrast inside the aneurysm during the high speed angiographic image acquisition, the parameter Area under curve (AUC) for the final corrected washout curves was calculated as:

$$AUC = \int_0^T C(t)dt \qquad 24$$

Where, C(t) is the concentration time function for the given washout curve going from 0 to end of the acquisition time period, T

Additionally total contrast exposure inside the aneurysm was determined as a quantifiable index given by the area under curve from zero to infinity as:

$$AUCinf = \int_0^\infty C(t)dt \qquad 25$$

The mean transit time of the curves which gives us the median for each contrast injection and corresponding high speed angiogram was quantified as:

$$MTT = \frac{\int_0^T t.C(t)dt}{\int_0^T C(t)dt} \qquad 26$$

Experimental design and statistical analysis

As determined for chapter 4, a sample size of 40 was required for the diagnostic test on outcome of flow diverter treatment in the clinical group through washout analysis.

For each patient the corresponding pre and post washout parameters calculated including the mean transit time, washout curve amplitude, convection time decay coefficient, area under curve, and area under curve zero to infinity were compared using non parametric Wilcoxon matched-pairs signed-rank test in GraphPad InStat.

To establish a quantifiable index or threshold to predict the efficacy of flow diverter treatment in terms of aneurysm occlusion the parameters for the occluded and non-occluded groups were compared using non-parameter Wilcoxon test.

RESULTS:

So far high speed angiographic data has been acquired on 38 aneurysms of 32 patients and the contrast washout has been analyzed. Table 5 presents the imaging follow-up and occlusion status for each patient. Typically flow diversion in patients requires 6 to 12 months to completely occlude the aneurysms following treatment[39, 43].

Total of 33 patients with 38 aneurysms have thus far been enrolled and underwent flow diversion treatment and high speed angiographic imaging. Follow up imaging has been acquired in 32 of the 38 aneurysms enrolled so far. From the 38 aneurysms based on a size threshold in the range of 3-4 mm, 24 aneurysms were selected for this preliminary angiographic analysis. Follow up data at 6 months after treatment was available on 19 of the 24 aneurysms included for the analysis. From these 19 aneurysms with available follow-up treatment outcome, complete occlusion was noted in 11 aneurysms at 6 month follow up (57.9%). The remaining 8 patient aneurysms were found to be filling. From the 8 non occluded aneurysms, 4 aneurysms underwent repeat treatment for the persistent filling observed. The other 4 aneurysms were reported to occlude at a future follow up time point with altered anti-platelet medication regimen prescribed by the physician (Appendix B).

Looking collectively for aneurysms sized 6 mm and smaller enrolled in this study, only 1 aneurysm out of 22 (3.7%) required repeat treatment through flow diversion (96.3% occlusion rates without secondary intervention). Complete occlusion at 6 months was observed for 14 out of 22 aneurysms (63.6%). In comparison all sizes above this group including fusiform aneurysms 4 out of 10 (40%) reported complete occlusion at 6 months. At further follow up 6 out of 10 (60%) were occluded completely (Appendix B). Repeat treatment with Pipeline device implantation was required in 4 out of 10 (40%) patients. All giant aneurysms (3 saccular and 1 fusiform) required repeat treatment.

Table 5: Treatment outcome at 6 month follow up, and repeat treatment information for each patient (TBD-to be determined).

Patient number(ID)	6 month follow up outcome	Repeat PED treatment
Patient 1 (RH001)	Not occluded, residual aneurysm filling	Yes
Patient 2 (RK002)	Not occluded, Persistent filling	Yes
Patient 3 (LP004)	Completely occluded	No
Patient 5 (FC005)	Not occluded, giant residual aneurysm	Yes
Patient 6 (LC006)	Completely occluded	No
Patient 7 (RH008)	Completely occluded	No
Patient 8 (AA010)	Completely occluded	No
Patient 9 (EAM011)	Not occluded, residual filling	No
Patient 10 (DT012)	Not available	TBD
Patient 11 (MN015)	Not occluded, residual filling	No
Patient 12 (PC016)	Completely occluded	No
Patient 13 (LT018)	Completely occluded	No
Patient 14 (MZ019)	Completely occluded	No
Patient 15 (KD020)	Not occluded, residual filling	No
Patient 16	Not occluded, minimal	No

(CM021)	residual filling	
Patient 17 (RG022)	Completely occluded	No
Patient 18 (DF023)	Not occluded, persistent residual filling	Yes
Patient 19 (LM025)	Completely occluded	No
Patient 20 (DL026)	Completely occluded	No
Patient 21 (MN027)		TBD
Patient 22 (VB028)	Completely occluded	No
Patient 23 (VK029)	Scheduled September 2015	TBD
Patient 24 (MA031)	Scheduled Jan 2016	TBD
Patient 25 (DW032)	Scheduled Jan 2016	TBD

Representative examples of the angiographic image analysis and washout curve mathematical model fitting are presented in Figures 55-58. Figures 55, 56, and 57 represent patients CM021, LM025 and RG022. All other cases are presented in Appendix B. Figure 58 represents patient FC005 with a giant fusiform aneurysm that did not occlude at 6 months follow up.

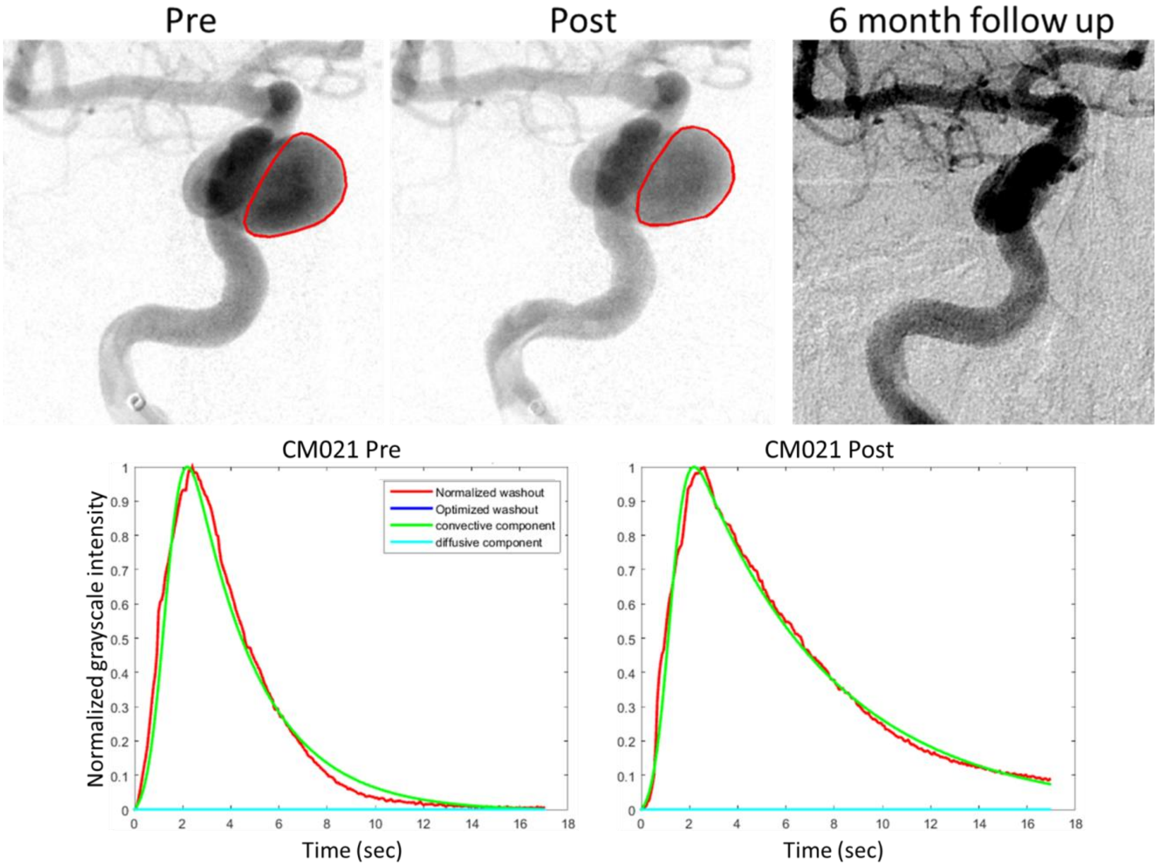

Figure 55: Angiographic image analysis for patient CM021. Top panel represents the aneurysm ROI segmented pre and post device angiographic images and 6month follow up angiogram showing minimal residual filling. Bottom panel shows the mathematical model fitted on the washout curves obtained from angiographic image analysis.

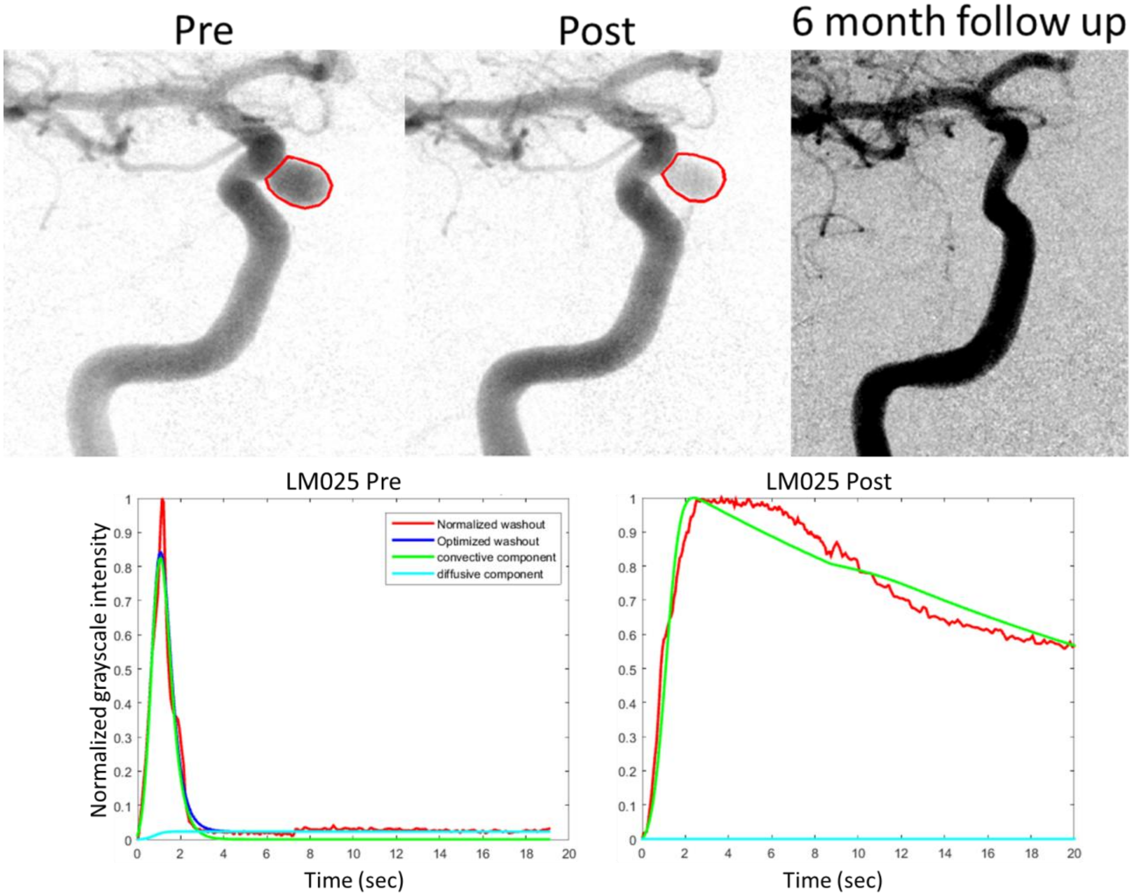

Figure 56: Angiographic image analysis for patient LM025. Top panel represents the aneurysm ROI segmented pre and post device angiographic images and 6month follow up angiogram showing complete occlusion of the aneurysm. Bottom panel shows the mathematical model fitted on the washout curves obtained from angiographic image analysis.

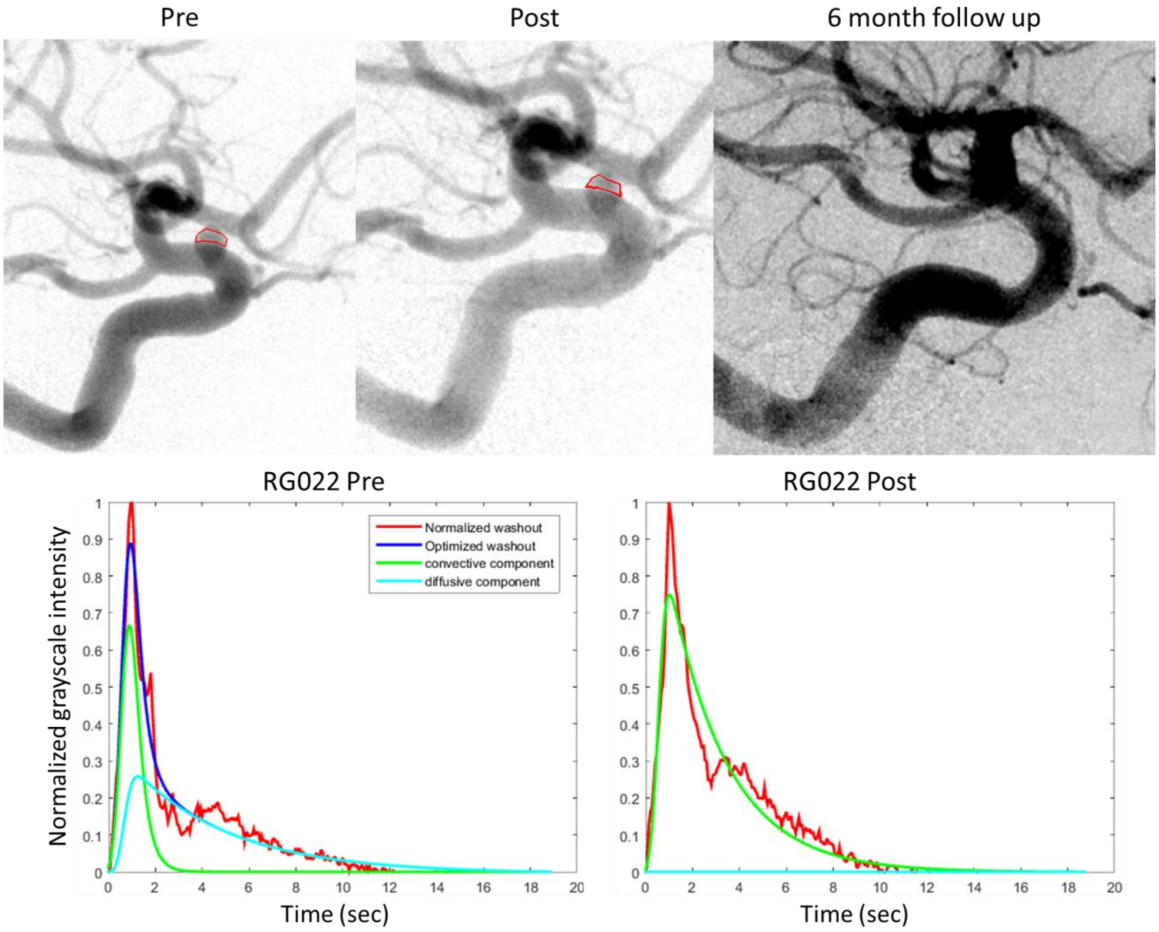

Figure 57: Angiographic image analysis for patient RG022. Top panel represents the aneurysm ROI segmented pre and post device angiographic images and 6month follow up angiogram showing complete occlusion of the aneurysm. Bottom panel shows the mathematical model fitted on the washout curves obtained from angiographic image analysis.

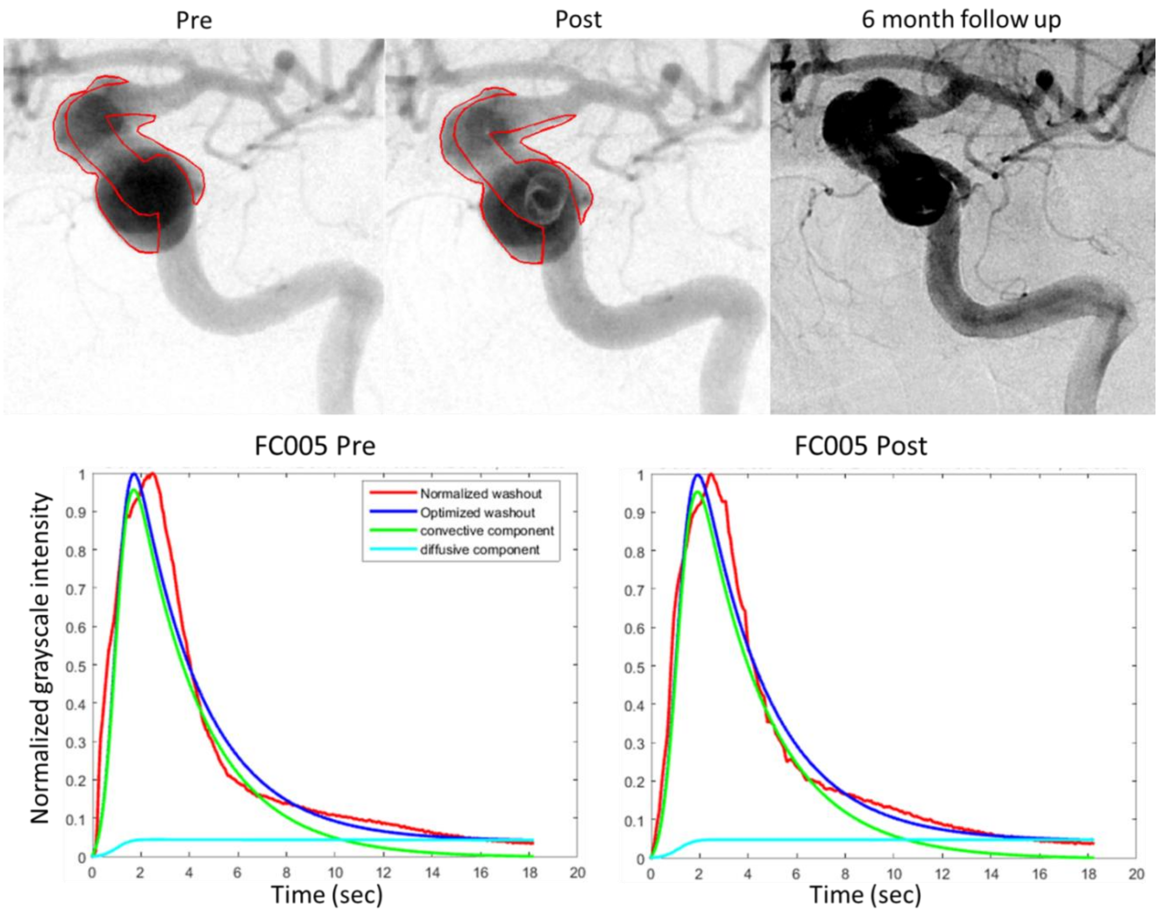

Figure 58: Angiographic image analysis for patient FC005. Top panel represents the aneurysm ROI segmented pre and post device angiographic images and 6month follow up angiogram showing aneurysm filling. Bottom panel shows the mathematical model fitted on the washout curves obtained from angiographic image analysis.

The post flow diversion angiographic washout parameters were significantly different than the pre washout parameters as determined from the paired test comparisons shown in Figures 59-61 and Table 6. The significant differences demonstrate the changes in contrast transport due to flow diverter deployment.

The amplitude of washout curves reduced significantly following flow diversion in the patients (Figure 58) (p=0.0016). Pre device washout amplitude was 1284.4±1939.8 and post device washout amplitude was 899.3±1329.8. Mean transit time (MTT) quantifying the median of contrast transport during each washout was significantly higher post flow diversion in patients (Figure 59) (p=0.0001). The mean MTT pre device for the patient group was 3.9±1.2s and post device was 5.5±2.2s. Results for time to peak (TTP), AUC, average inflow and outflow of contrast within the aneurysm were significantly different post flow diversion.

Table 6: Washout parameter results derived from concentration time curves pre and post flow diverter treatment (* indicates statistically significant)

Parameter	Pre (mean±SD)	Post (mean±SD)	P value
δ	1284.4±1939.8	899.3±1329.8	0.0016*
MTT (sec)	3.9±1.2	5.5±2.2	0.0001*
TTP (sec)	1.78±0.89	2.47±1.32	0.0001*
AUC	4995.2±9248.57	7100.48±14342.87	0.0366*
AUC inf	6496.1±9597.8	11170±20517	0.074
τ_{conv} (sec)	3.0±3.0	7.74±7.1	0.0001*
Inflow	643.67±972.05	303.63±379.04	0.0001*
Outflow	81.18±123.96	49.49±69.565	0.0065*

The stagnation of contrast within the aneurysm represented by intra-aneurysmal contrast transport decay time constant was significantly higher following the treatment of aneurysm through deployment of Pipeline flow diverter (Figure 60) (p<0.0001). Mean contrast transport decay time constant pre device was 3.0±3.0s and post device was 7.74±7.1s. Thus, flow diversion altered intra-aneurysmal contrast transport mechanics which are representative of the hemodynamics. The alteration was in the form of reduction in intensity represented by washout amplitude and increased stagnation represented by increased mean transit time and decay time constant.

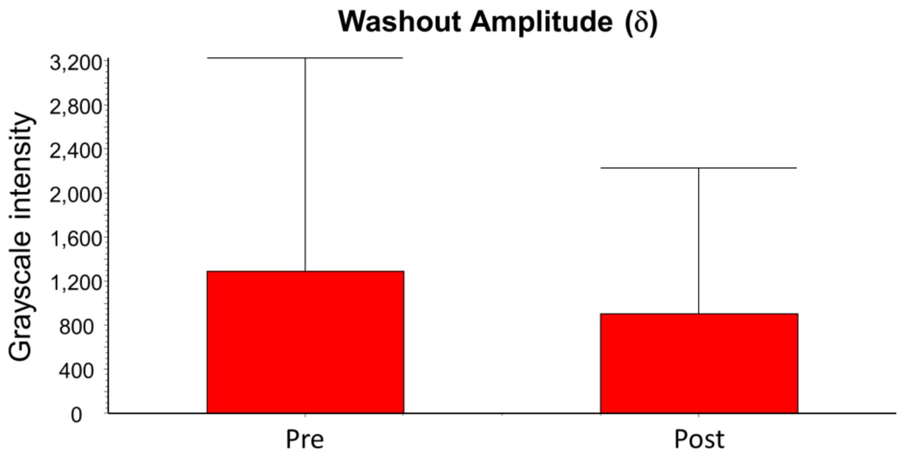

Figure 59: Comparison of the contrast concentration washout mean amplitude pre and post flow diverter implantation (p=0.0016)

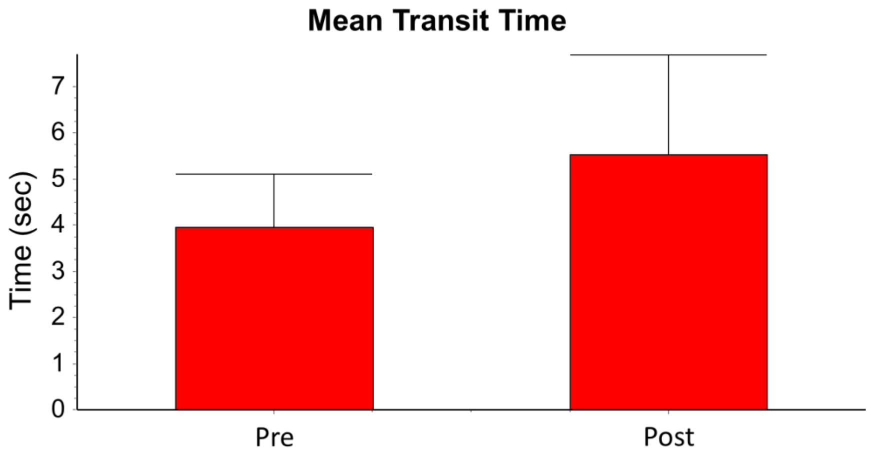

Figure 60: Comparison of mean transit time obtained from the contrast concentration time curves pre and post flow diverter implantation (p = 0.0001)

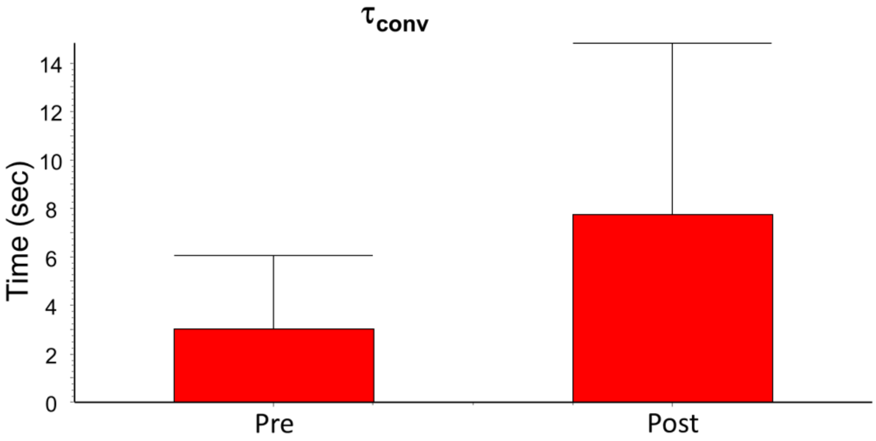

Figure 61: Comparison of mean convective time coefficient obtained from mathematical model fitting of the contrast concentration time curves pre and post flow diverter implantation ($p<0.0001$).

The primary goal of this clinical study has been to identify the parameters of contrast transport that may delineate the differences between occluded and non-occluded groups and thus establish thresholds that may be applicable in a diagnostic test for flow diversion efficacy.

The scatter plots demonstrate similar spread for the pre device values for the patients from both occluded and non-occluded groups (Figures 62-64). No significant differences were found when comparing the washout curve amplitudes between the occluded and non-occluded groups (Figure 63). However the spread appears to reduce the range for the occluded group post occlusion. For mean transit time data, the spread within the scatter plot appears similar for the pre device values for both groups (Figure 64). Post flow diversion scatter for mean transit time show a trend towards a shift in the range (higher) for the occluded and non-occluded groups. Among the occluded aneurysm group, there appears to be an increase in scatter for the results post flow diversion. Despite the range, the MTT results post flow diversion show a trend towards increased values for the occluded group in comparison with the non-occluded group. The mean and standard deviation values for the occluded and non-occluded group comparisons are given in

Table 7.

Table 7: Occluded vs Non occluded comparison of washout parameters pre and post flow diversion (* indicates statistical significance).

Parameter	Non-Occluded	Occluded	P value
δpre	1637.1±1621.7	511.29±846.1	0.075
δpost	1328.3±1127.7	304.21±426.9	0.0328*
MTTpre (sec)	4.20±1.61	3.81±1.01	0556
MTTpost (Sec)	5.75±1.71	5.33±2.42	0.395
τ_{conv}(sec)pre	4.34±4.33	2.58±2.29	0.272
τ_{conv}(sec)post	6.49±4.15	8.50±9.01	0.840

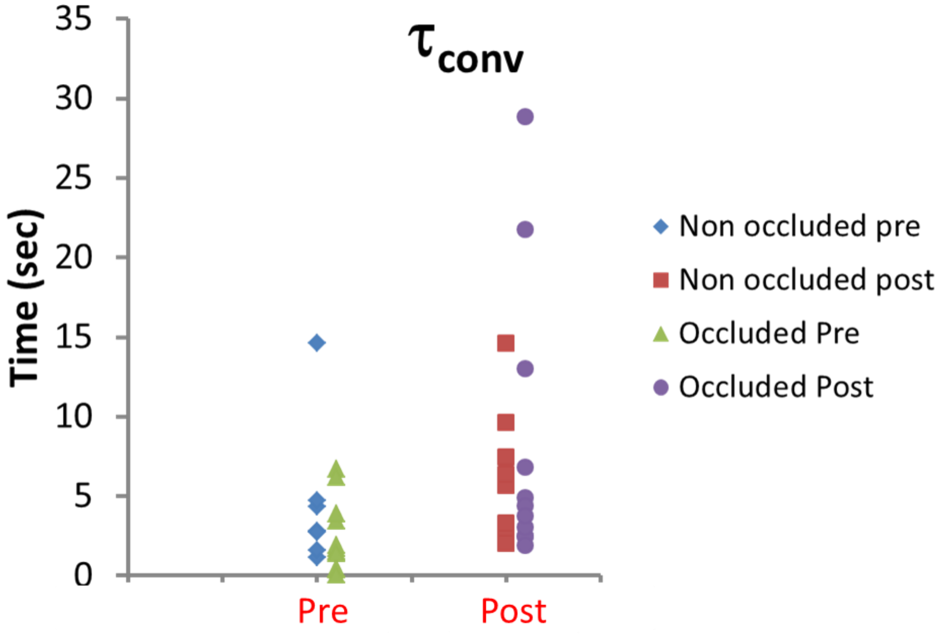

Figure 62: Scatter plot comparison of convective decay time coefficient obtained from mathematical model fitting on the contrast concentration time curves among the occluded and non-occluded aneurysm groups pre and post flow diversion.

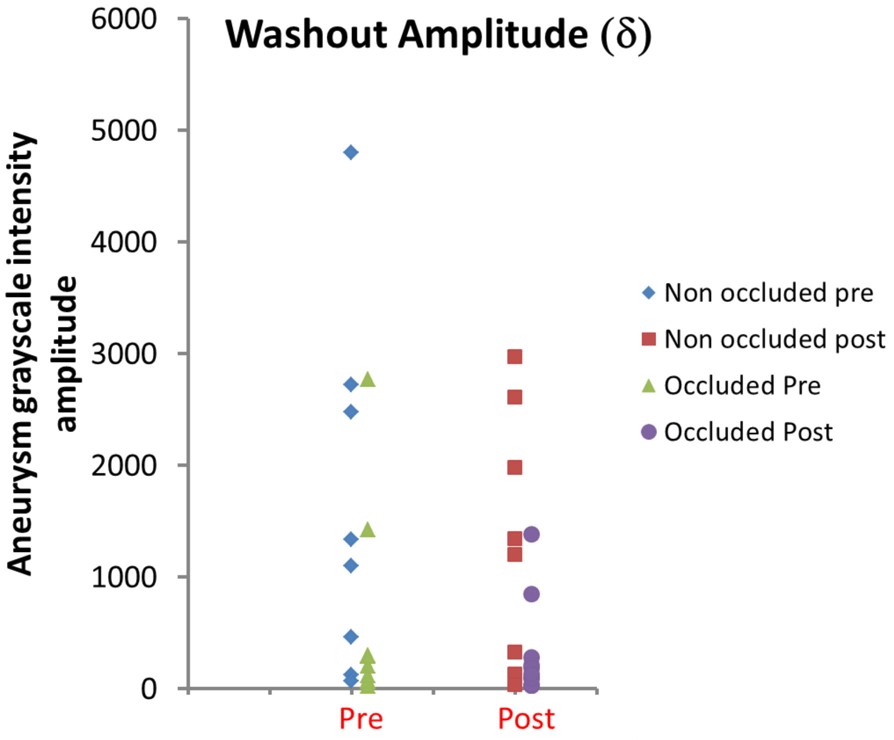

Figure 63: Scatter plot comparison of the washout amplitude among the occluded and non-occluded aneurysm groups pre and post flow diversion.

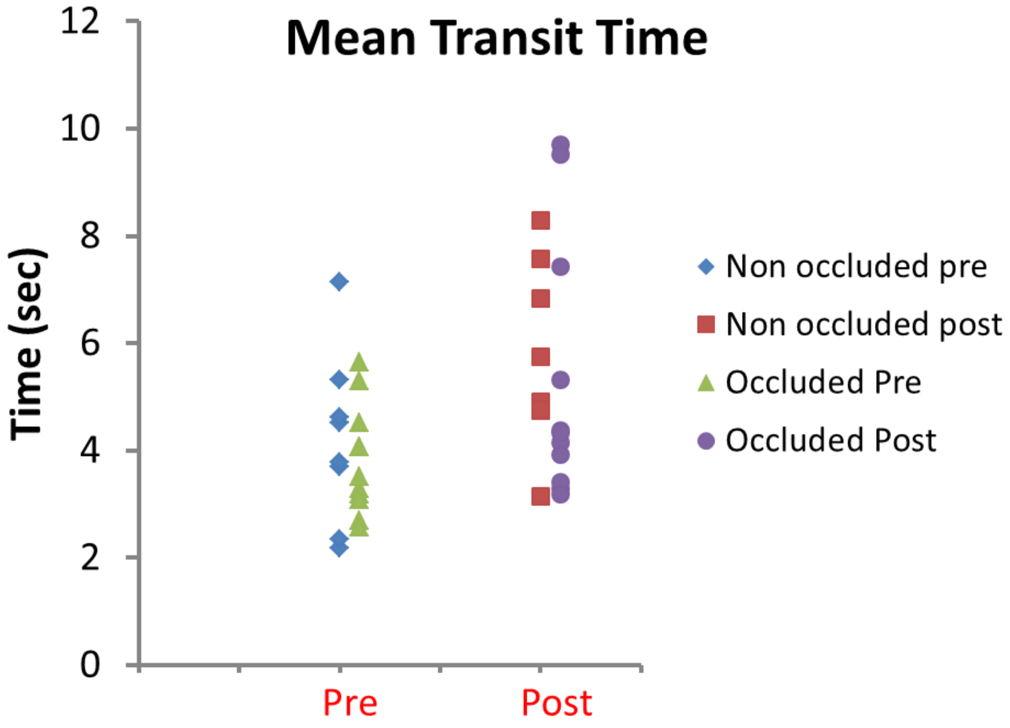

Figure 64: Scatter plot comparison of mean transit time obtained from the contrast concentration time curves among the occluded and non-occluded aneurysm groups pre and post flow diversion.

DISCUSSION:

This is the first study to the knowledge of the author, performing quantitative analysis on intra-aneurysmal hemodynamics based on mathematical modeling of high speed angiography data acquired in patients before and after flow diverter deployment. Angiographic image analysis to study contrast concentration curves has been previously applied to study the alterations in intra-aneurysmal hemodynamics within *in-vivo* and *in-vitro* aneurysm models. Sadasivan *et al* applied the method developed earlier by the same authors on some clinical angiographic image data over a decade ago [66]. However, the acquired angiographic data did not have sufficient temporal resolution to perform mathematical modeling on the washout curves and delineate the components of convection and diffusion. Sadasivan *et al* extensively applied this model for comparing different flow diverter designs deployed in the rabbit elastase induced aneurysm model.

Previously, investigators attempted qualitative approaches through grading scales for the assessment of flow diversion treatment efficacy for brain aneurysms. Based on qualitative visual assessment of angiographic image data, clinicians have attempted to grade and stratify aneurysms based on the contrast washout. These scales were based on the contrast residence within the aneurysm at different stages of an angiogram while the contrast washes out of the arteries, capillaries, veins and beyond to a near permanent or infinite stagnation. These scales may involve some intra-observer variability but provide a quick tool to separate different aneurysm morphologies. However, usage of qualitative data for estimation of treatment efficacy of flow diversion might not provide the most accurate outcome and may involve guesswork.

In 2010, the first grading scale for angiographic assessment of brain aneurysms following flow diversion treatment was proposed by O'Kelly et al., known as the O'Kelly Marotta grading scale [110]. The primary basis for this grading scale was a combination of intra-aneurysmal contrast stasis and angiographic filling. By combining level of stagnation within the aneurysm and area of aneurysm filling, the temporal and spatial aspects of contrast concentration mechanics were evaluated in a qualitative manner.

Grunwald et al. proposed a simplistic 5 point grading system based on qualitative evaluation of the angiographic image data from aneurysms following flow diversion treatment[111]. The scales ranged from 0 to 4 with 0 being the case with convective inflow jet entering the aneurysm following treatment with very little change in pattern, 1 being diffusive flow into the aneurysm, 2 with residual filling of the dome, 3 with residual filling of the neck region and 4 being complete occlusion. Within our study we observed pattern 0 for most small sized aneurysms (<5 mm) and 1 for some sidewall saccular aneurysms and within the large and giant saccular aneurysm. Some aneurysms were a mixture of 0 and 1. Hence, application of such scales is user dependent and qualitative providing only ballpark idea. We mainly observed patterns 3 and 4 at 6 month and further follow ups. We did not observe any residual filling of aneurysm dome in our study.

High speed angiography was first applied for intra-aneurysmal hemodynamic studies by Tenjin *et al*. comparing the contrast concentration time curves for regions of interests within the aneurysm and the parent vessel[112]. The investigators acquired angiographic images at 30frames/sec which may expose the patient to additional radiation. The contrast dye washout curves were fitted to gamma-variate and exponential functions to determine time to peak and mean transit time. The study did not involve any patients treated with flow diverters. But this paved the way for application of functional angiography to study intra-aneurysmal hemodynamics, a tool that clinicians can acquire data for during routine endovascular procedures.

Reduction in the washout curve intensity amplitude levels following flow diversion is indicative of reduced contrast transport intensity which may be a lumped physical analog to kinetic energy of intra-aneurysmal fluid flow. The mean transit time increased significantly post flow diversion in the patients. Longer contrast residence and delay in wash in as well as washout of the contrast are the end results of a flow diverter implanted across the aneurysm. Contrast transport decay time constants increase in magnitude following flow diversion. The combination of these parameters is an effective validation for the intra-aneurysmal contrast transport modeling from high speed angiography image data as a tool to study intra-aneurysmal hemodynamics. The alteration in contrast transport mechanics observed from this set of patients establishes the functionality of flow diversion as a whole.

The mathematical model used in this study was previously developed and applied to the contrast concentration washout curves in the elastase induced aneurysms created in rabbits [53, 54, 57]. These model fitted well to the contrast dye transport mechanics within the rabbit aneurysms with the diffusive components rising following flow diversion and overall increase in the convective and diffusive decay time constants. However in case of the clinical washout data, the contrast transport phenomena was mostly represented by the convective component with very low or no contribution from the diffusive process. Sidewall aneurysms smaller in size with a narrower neck and elliptical morphology represented diffusive components and demonstrated a response similar in rabbit elastase induced aneurysm model. Washout coefficient, a parameter derived using the ratios (post/pre) of diffusive components of contrast transport as well as concentration time curve amplitude was quantified for the rabbit study in Chapter 5. Due to the lack of diffusive component of contrast transport in clinical angiographic data the washout coefficient was not quantified for clinical data.

Other groups have applied the mathematical model used for this clinical study for in vivo rabbit elastase induced aneurysm model acquired high speed angiography data at 30frames/sec[106]. Time to peak, and time to half peak (mean transit time) calculated and discussed in this work were hypothesized to alter following flow diversion. Separately inflow and outflow were calculated as the averaged slope of the fitted mathematical model during wash in and wash out phases of contrast. The same group very recently applied angiographic analysis in clinical patients. This was done through inbuilt tools on the Siemens processing workstation that applied the mathematical model towards calculation of time to peak, inflow and outflow values[113]. The group analyzed 38 aneurysms in 36 patients, and at follow up 26 were completely occluded (68%). Significant increase in time to peak (82%) and reduction in inflow (37%) and outflow (35%) were observed. The study was able to predict occlusion for saccular aneurysms with a sensitivity of 89% and specificity of 82% through thresholds of 15% reduction in inflow and 35% reduction in outflow. Current work found significant differences between pre and post angiographic parameters. Statistical significance was not obtained for the washout parameters obtained through mathematical model fitting between the occluded and non-occluded groups. However, post flow diversion the value for inflow was just significantly lower for the occluded group (128.86±137.58) in comparison with non-occluded group (431.49±356.91) (p=0.041). Showing a similar trend, the outflow slope values were significantly lower (p =0.026) for the occluded group (17.31±22.84) as compared to the non-occluded group (77.263±63.773). There was no significant difference in the inflow and outflow values before flow diverter deployment. The post/pre ratio of the inflow and outflow parameters (important to predict efficacy) was not significantly different between the occluded and non-occluded groups (inflow: p=0.642 and outflow: p = 0.4504). The parameters inflow and outflow as described are based on the change in contrast concentration at specific points at the center of the aneurysms. Our study calculated the contrast concentration time curves over the entire aneurysm and not only at specific points.

Towards the prediction of flow diversion efficacy temporal high speed angiographic data has been transformed into blood flow velocity information. Angiographic image data was acquired at a high frame rate of 60 frames/sec [114]. The data was acquired in 24 patients enrolled in the study and flow was quantified for 21 out of the 24 patients. By applying an approach used in previous studies, the ratio of absolute mean velocity amplitude parameters post to pre was calculated. They found a threshold value of 1.03 (p<0.035) for the mean aneurysm flow amplitude ratio to detect complete thrombosis of aneurysms at 6 to 36 months without additional device intervention. The sensitivity and specificity of this predictive index were 88% and 73% respectively. The essential purpose of flow diverters remains to decouple the aneurysm from the parent vessel and provide a layer or mesh construct for endothelialization and vascular reconstruction. Aneurysm occlusion is not immediately apparent following flow diverter implantation. However, the magnitude and direction of intra-aneurysmal flow velocity vectors are modified causing alterations in flow patterns. The level of alteration of intra-aneurysmal flow is one of the crucial factors that affect endothelialization of the flow diverter construct, thrombosis within the aneurysm and subsequent complete occlusion of the aneurysm. From angiographic image data, washout curve amplitude intensity, mean transit time, and the decay time coefficients are the parameters of contrast concentration mechanics that may be physically equivalent or related to hemodynamic parameters like flow velocity or kinetic energy. The pulsatile flow impingement on the neck of intermediate (5-10mm) and large sized aneurysms (>10) may be higher than smaller aneurysms. The reduction of intra-aneurysmal kinetic energy may have to be at a different level for larger aneurysms than small sized wide necked aneurysms (<5mm) to assist with endothelialization of the aneurysm neck. For example, a smaller wide necked saccular aneurysm may occlude at 6 months with only a 50% reduction in kinetic energy immediately after flow diverter deployment while a larger aneurysm with up to 70-80% reduction in kinetic energy may have residual filling at 6-12 months.

The design of the clinical study was done based on the *in-vivo* washout studies in rabbits. The rabbit elastase induced aneurysm model is a robust model to replicate aneurysms of similar morphology, size, and shape. The injection catheter can also be positioned at a similar location within the ascending aorta to obtain repeatable contrast concentration washout curves pre and post flow diverter treatment. Hence the variance is not very high for the obtained washout curves and the subsequent contrast transport parameters obtained through mathematical model fitting. The data analyzed for this study was from 24 patients with a large range in aneurysm sizes going from 4 mm to fusiform aneurysms with a length dimension of 96 mm. As a result the contrast transport mechanics differ within patients and bring about a wide spread in the data, reducing the statistical power of the study. In comparison to the analysis on washout data from the rabbit study in Chapter 4, more parameters including area under curve, mean transit time and average inflow and outflow slope were quantified for the clinical data. This was done to investigate any possible differences between the occluded and non-occluded groups no apparent for the convective and diffusive components derived from mathematical model fitting. As seen from the scatter plots for occluded and non-occluded aneurysms, there is some visible trend hinting at differences. However, statistical significance could not be obtained at this stage. Washout data from more patients will need to be acquired.

It might be useful to establish data-sharing collaborations with other big cerebrovascular clinical centers where endovascular flow diversion treatment is offered. Within the aneurysm data-sets, fusiform morphologies may need to be analyzed separately from the saccular aneurysm morphologies. Size might need to be considered as well to stratify the aneurysms into groups of large (>10 mm), giant, and small (<5mm), and intermediate (5-10 mm). This data would help understand the contrast mechanics and flow diversion effect for different aneurysm sizes and morphologies resulting in establishment of thresholds separating the occluded and non-occluded groups and formation of more accurate diagnostic tests for groups of aneurysm size and morphologies.

The issue of increased radiation exposure to patients is crucial. Radiation exposure can be minimized through application of single plane angiography for the high speed angiography runs. Application of variable frame rate (VFR) at our institute reduces the number of frames acquired from 300 to 240 for a typical 20 second run. More tests need to be done on in-vitro phantoms to verify if lower frame rates would provide adequate temporal resolution to capture the contrast transport mechanics in an accurate manner.

CHAPTER 6: PATIENT SPECIFIC CFD MODELING

CFD analysis was performed on the data from three patients. Patient 1 (CM021) is a 73 year old female with a large proximal cavernous aneurysm of the right ICA with the aneurysm neck, height, and width of 6.5, 13, and 16 mm, respectively. The patient was treated with 1 PED size 5mm x 20mm (diameter x length). Patient 2 (LM025) is a 50 year old female with superior hypophyseal aneurysm in the paraclinoid segment of the right ICA. The aneurysm neck, height, and width measured 3, 6.1 and 5.7 mm respectively. This patient was treated with 3 PEDs , device 1: 3.5mm x 16 mm, device 2: 3.5mm x 16mm, and device 3: 4mm x 20mm. Devices 2 and 3 were telescoped within device 1 resulting in a denser flow diverter construct. The additional devices were deployed to ensure complete wall apposition of the flow diverter construct within the tortuous segment of the ICA siphon. Patient 3 (RG022) is a 50 year old female with ophthalmic segment aneurysm of the right ICA. The aneurysm neck, height, and width measurements were 4.2 mm, 3.6 mm and 3.8 mm respectively. The patient was treated with 2 PEDs, device 1: 4.25mm x 16 mm and device 2: 4mm x 14mm.

METHODS

CFD model construction:

Flow modeling was performed on geometries derived from rotational angiography data acquired at time of flow diverter treatment using the Siemens Artis Zee biplane angiography unit. The DICOM axial slices were imported in VolView (Kitware, Clifton Park, NY) to create a volume reconstruction in the *.vti format. The volumetric imaging data in the *.vti format were imported into a cardiovascular image based modeling software SimVascular (www.simvascular.org) (Figure 65) [115]. Centerlines were created for the parent and branch vessels using a semi-automatic method to function as a framework for the model[116]. Contours delineating vessel lumen were created using 2D level set segmentation moving orthogonally along the centerlines[115, 116]. The centerline contours were exported from SimVascular. These 2D segments were imported into a commercial CAD package Rhinoceros 5 (McNeel North America, Seattle, WA) to loft them together and obtain volumetric 'NURBS' bodies (Figure 65).

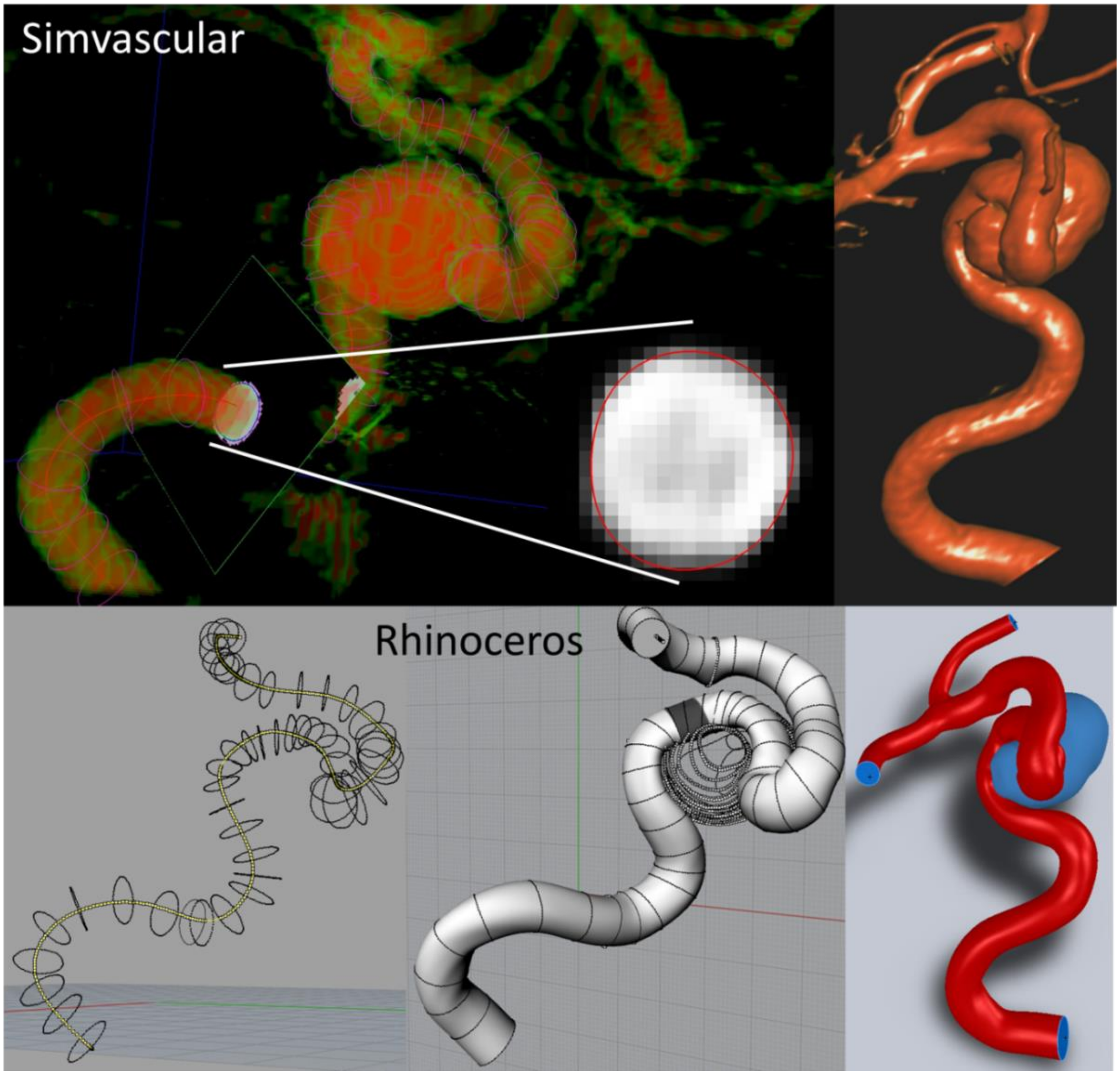

Figure 65: Top Left: Patient specific geometric model construction for CFD simulations through import of axial slice volume and 2D level set segmentation in SimVascular; Bottom Left: import of 2D artery contours to Rhinoceros for lofting to form a solid body; Top Right: Volumetric reconstruction from patient's Rotational Angiography scan; Bottom Right: corresponding CFD model.

Patient specific flow diverter construction

Pipeline embolization devices consisting of 48 wires of 30µm diameter, braiding angle 130 degrees were simulated in their deployed orientation adhering to the vessel wall (US patent application US 13/489,436)[117]. To construct the simulated device in situ first the boundary of the parent artery was obtained. A smoothed centerline for the boundary of the parent artery was determined using an open source program, The Vascular Modeling Toolkit (VMTK) (www.vmtk.org). VMTK software was then utilized to obtain circumferential contours of the parent artery orthogonal to the centerline (Figure 66). Device wire centerlines were calculated using in house algorithms in MATLAB 2013 (MathWorks, Inc. Natick, MA.) to geometrically simulate the implanted device along the artery wall. The centerlines were imported into SolidWorks 2013 (Dassault Systemes, Waltham, MA) and individual wires were swept to obtain the stent geometry in its deployed form.

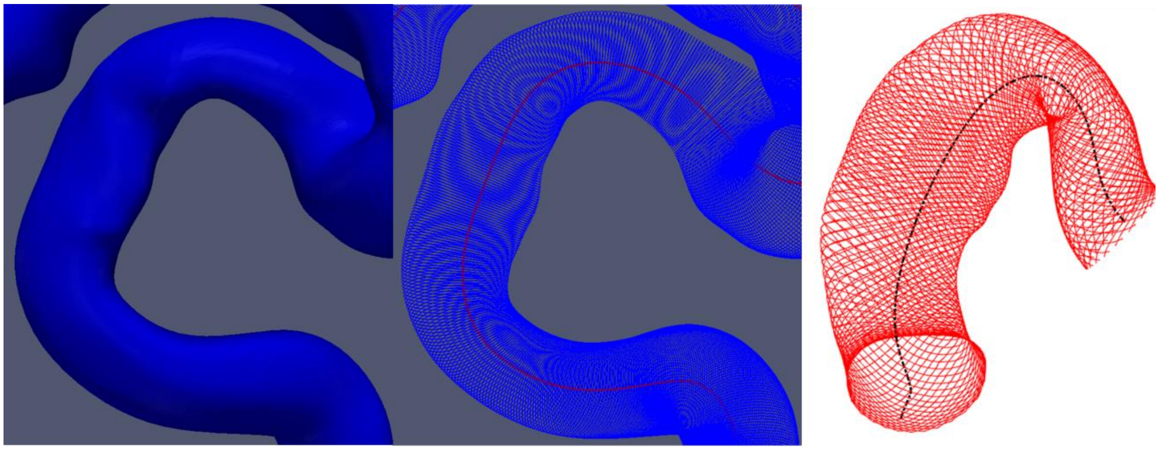

Figure 66: Parent artery boundary used to obtain lumen centerlines and cross sections of the boundary going orthogonal to the centerline used to calculate the flow diverter wire centerline configurations in the patient geometry specific implanted format.

For the purpose of reducing the computational effort in solving the flow field only the diverter wires across the aneurysm neck were used in the modeling. The rest of the device was cropped out as shown in the Figure 67.

.

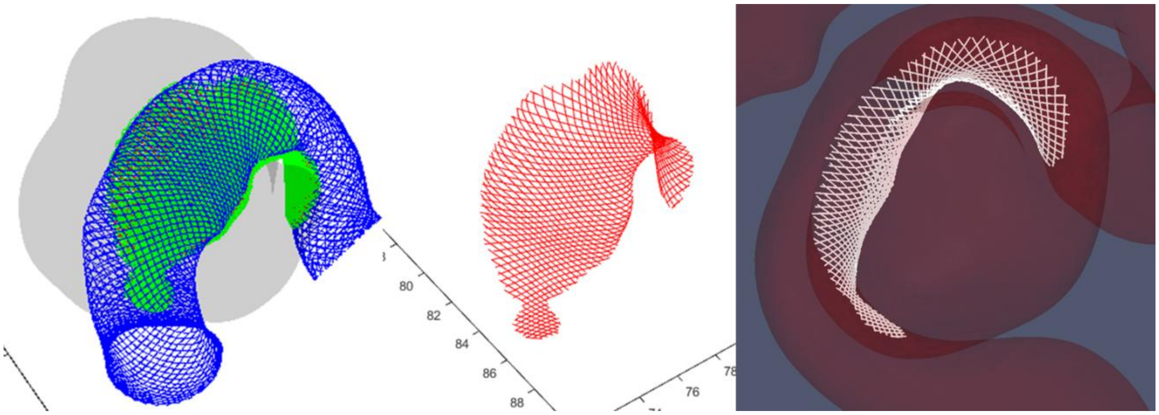

Figure 67: Flow diverter wire centerlines were intersected with the aneurysm boundary (left) to crop the wires (center) and restrict the device to be just sufficient to provide neck coverage; (right) Flow diverter solid model generated by lofting a circular cross section along the wire centerlines; the flow diverter is positioned inside the patient specific model.

Boundary conditions and numerical analysis

Flow was assumed to be laminar and incompressible. No slip boundary conditions were applied as well as rigid walls for all CFD models. The fluid was assumed to be Newtonian with a viscosity of 4.0 cP and a density of 1.05 gm/ml.

Flow simulations employed conservation of mass (continuity) and balance of fluid momentum (Navier-Stokes) using a nodal based finite element method (FEM) discretization scheme with the commercial package ADINA 9.0 (ADINA R&D, Watertown, MA). A Galerkin finite element upwinding scheme was applied. The model geometries (especially the ones including the stents) were discretized using an automated free-form meshing scheme utilizing Delaunay triangulation and surface refinement algorithms with 4-node tetrahedral elements to obtain a highly anisotropic grid with the area around the flow diverter wires more refined than the rest of the fluid domain (Figure 68). Following discretization, nodal coordinates on the inlet face are obtained. Since the geometry is floating in three dimensional space, the inlet nodes are rotated to a two dimensional plane and fully developed Womersley flow profile is imposed on this section. The flow profile was calculated from a population averaged pulsatile flow waveform for the internal carotid artery that was obtained from the literature [102] and interpolated to fit on the rotated nodal points (Figure 68). The time varying waveform of fully developed velocity profiles was then rotated back to the original coordinates and imposed on the nodes in the inlet face (Figure 67). The simulations started from a zero velocity flow field and an initial flow ramp was applied at the inlet to establish a flow field of the same order of velocity that can be expected in the vessel. Thereafter the simulations were run for 3 cardiac cycles using the Womersley inlet profile to ensure that initial transients decayed and the flow field was repeatable.

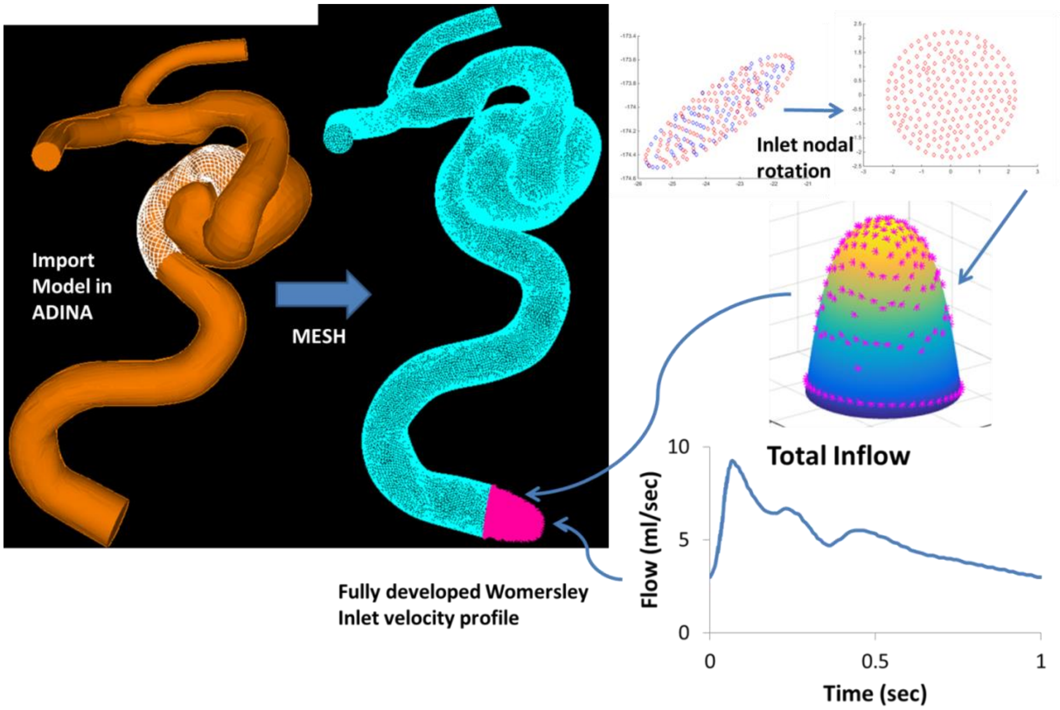

Figure 68: Reconstructed volume body model for patient 1(CM021)imported in ADINA along with the flow diverter and discretized into tetrahedral mesh; inlet nodal coordinates extracted and imposed with a pulsatile flow waveform in the form of a fully developed Womersley velocity profile.

Reconstructed arterial segments with Pipeline flow diverter virtually implanted within patient geometries CM021, LM025 and RG022 are shown in Figures 68, 69, and 70, respectively. Figure 71 shows a CFD model constructed for patient DF023 who had a giant saccular partially thrombosed sidewall aneurysm treated with 2 flow diverters. The extremely complicated vascular geometry and the deployment of two large flow diverters resulted in difficulties obtaining the fluid domain and the final mesh size (exceeding 5 million elements with a coarse resolution for flow diverter wires) was too large to run on the 16core/64GB RAM linux server (KingStar supercomputer, Sunnyvale, CA) dedicated to this study. Simulations were not conducted on this geometry.

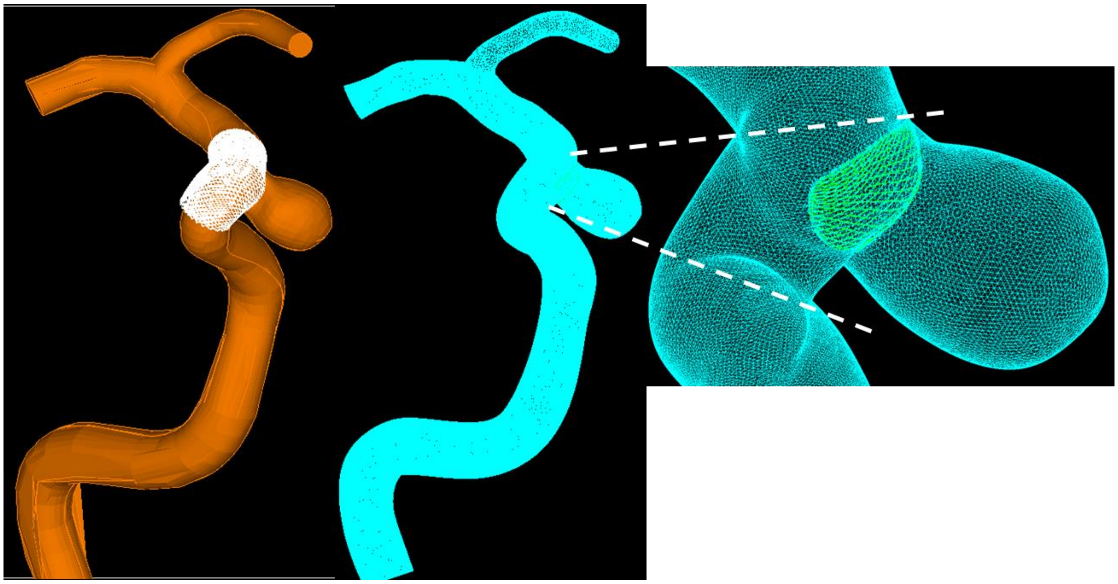

Figure 69: Reconstructed computational model for patient 2 (LM025) with flow diverters virtually deployed in position across the aneurysm (left), and the finite element mesh generated in ADINA with the cropped flow diverter virtually deployed in position (center) and expanded view on the right.

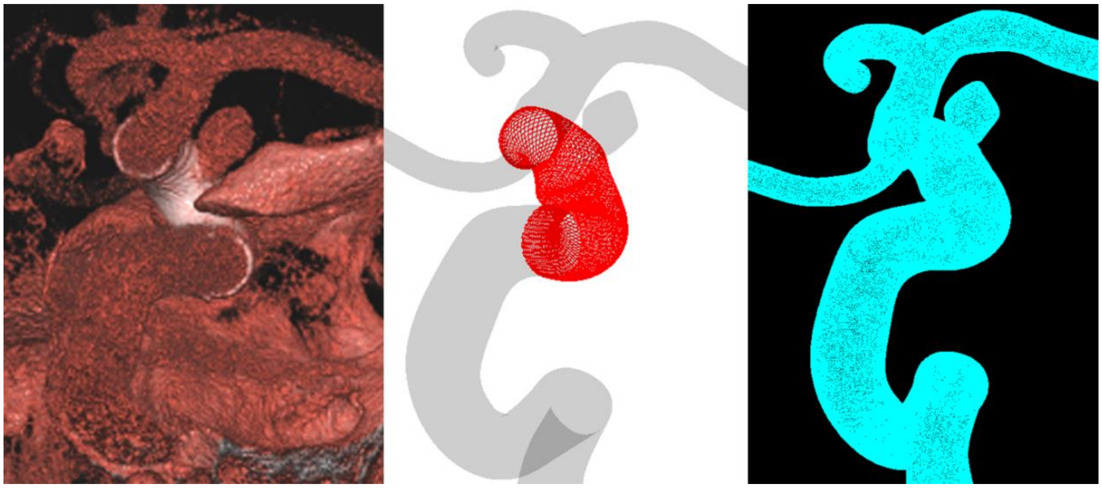

Figure 70: Patient 3 (RG022) modeling; volumetric reconstruction of CTA slices (left), reconstructed CFD model with flow diverter virtually implanted (center), and ADINA finite element mesh of the model with cropped flow diverter implanted.

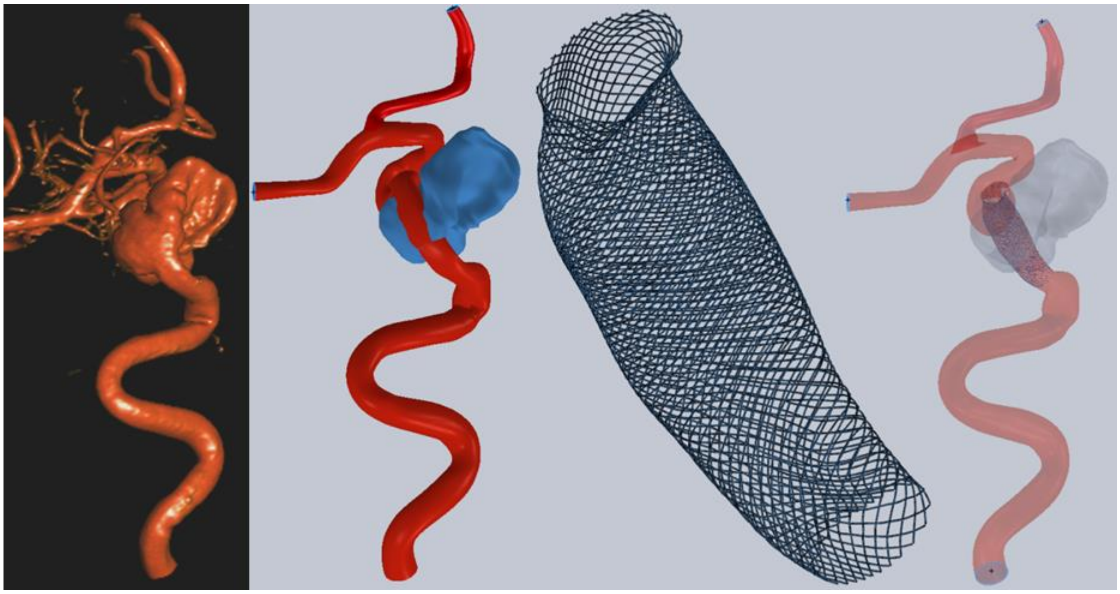

Figure 71: CFD model construction for DF023, a 75 year old female patient with a giant partially thrombosed aneurysm on the cavernous segment of LICA; rotational angiographic volume (left); parametric CAD model of patient geometry (center left); simulated flow diverter (center right); Pipeline device virtually implanted in the patient's parent artery (right).

RESULTS:

Analysis of the computational results shows reduction in flow activity inside the aneurysms post device implantation. The velocity flow fields at peak systole for Patients 1, 2, and 3 are presented in Figures 72, 73, and 74, respectively. Overall, the velocity magnitude within the aneurysm was reduced but the characteristics of the flow, such as direction or location of high velocity spots did not change based on qualitative inspection of velocity maps. The larger aneurysm (Patient 1: CM021) that was treated with a single device demonstrated some stagnation and reduction in flow (Figure 72). Patients 2 and 3 had sidewall aneurysms in which the reduction in intra-aneurysmal flow was more pronounced than for Patient 1 as can be seen in Figures 73 and 74. Flow entered the aneurysm through the distal neck both pre and post device implantation, however, the presence of the flow diverter reduced the impingement on the aneurysm wall.

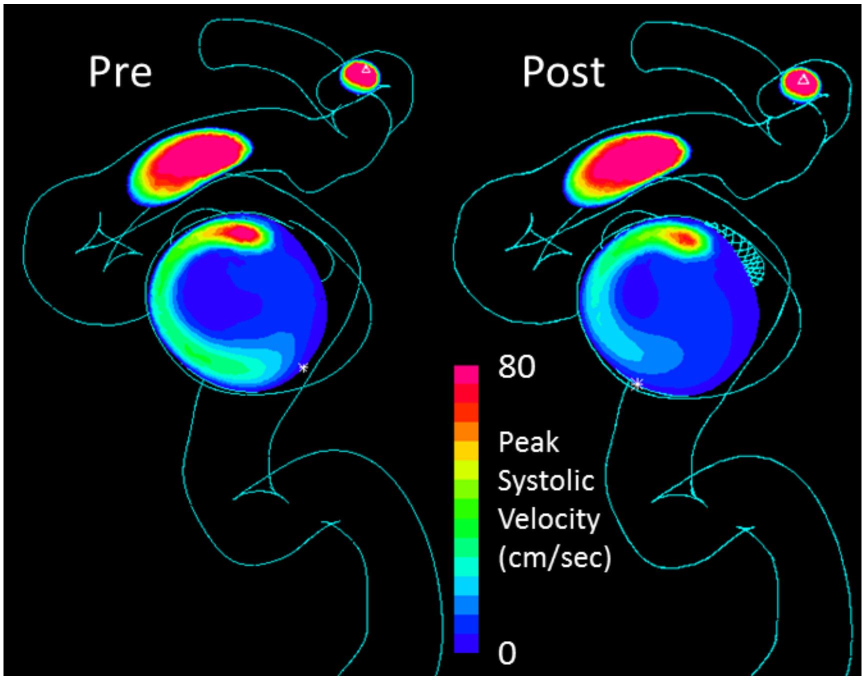

Figure 72: Spatial maps of peak systolic velocity for Patient 1 (CM021) before (left) and after (right) flow diverter implantation obtained from CFD results demonstrating reduction in the velocity magnitude post flow diversion.

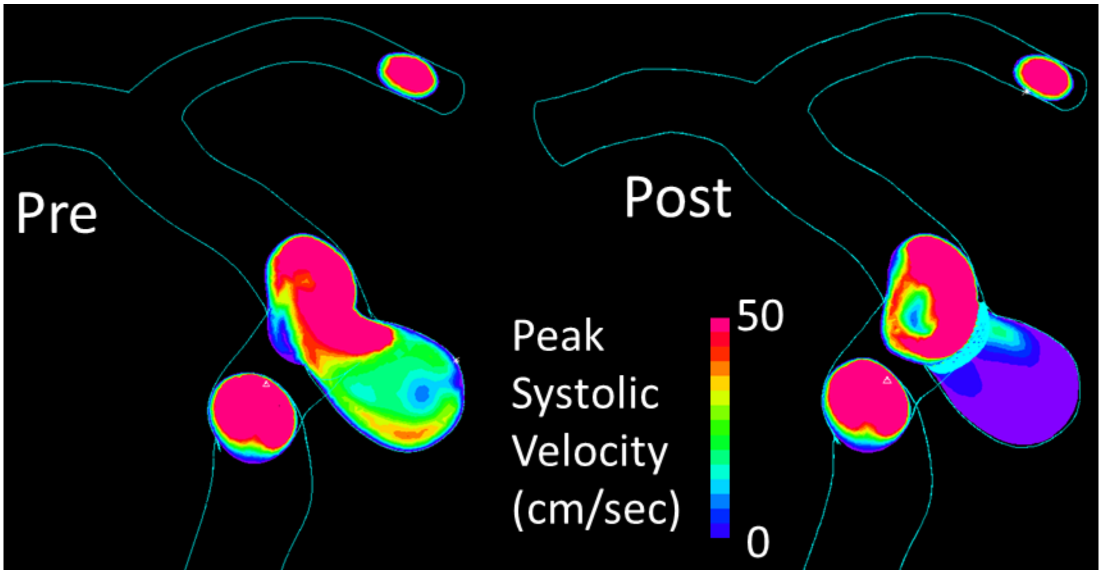

Figure 73: Spatial maps of peak systolic velocity for Patient 2 (LM025) before (left) and after (right) flow diverter implantation obtained from CFD results demonstrating reduction in the velocity magnitude post flow diversion.

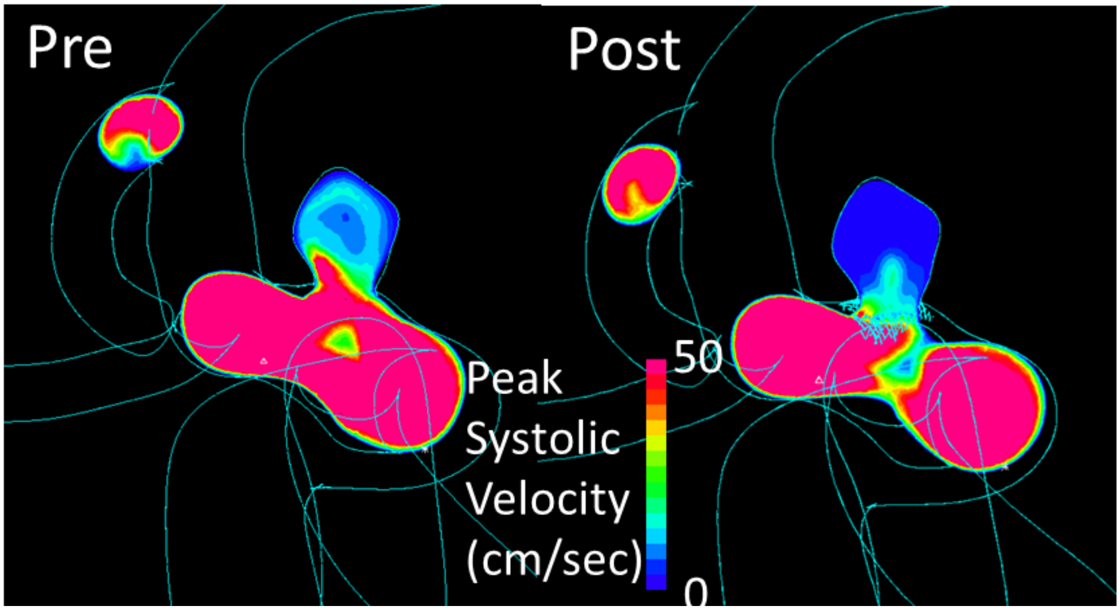

Figure 74: Spatial maps of peak systolic velocity for Patient 3 (RG022) before (left) and after (right) flow diverter implantation obtained from CFD results demonstrating reduction in the velocity magnitude post flow diversion.

Intra-aneurysmal kinetic energy was quantified from nodal velocity vectors within the entire aneurysm volume as described in chapters 2 and 3. The temporal evolution of intra-aneurysmal kinetic energy is shown in Figure 75 for the three patients. Beat averaged kinetic energy for the three cases pre and post flow diversion is shown in Figure 76. The kinetic energy values were spatially averaged to obtain a more objective comparison between aneurysms of different sizes. The beat averaged kinetic energy pre device implantation was highest for patient 2; KE = 284.46 $(cm/sec)^2$. Patient 1 had a mean kinetic energy 112.97 and patient 3 had the lowest kinetic energy of 75.716 $(cm/sec)^2$. Post device implantation, patient 1 had the highest mean kinetic energy at 54.23 $(cm/sec)^2$ while patients 2 and 3 had much lower kinetic energy of 2.99 $(cm/sec)^2$ and 3.26 $(cm/sec)^2$, respectively (Figure 76).The flow diverter induce a marked reduction in kinetic energy within the aneurysm particularly for patient 2 (LM025) where 3 devices were deployed telescopically. The peak kinetic energy during systole before device implantation (Figure 75) as well as the spatially averaged kinetic energy (Figure 76) were the highest for Patient 2 despite being considered a sidewall aneurysm. This is potentially a consequence of the sharp bend in the artery just proximal to the aneurysm that redirects the bulk flow into the aneurysm due to a sharp angle of attack. Percent reduction in intra-aneurysmal kinetic energy post flow diversion, as described in chapter 3, is shown in Figure 77.

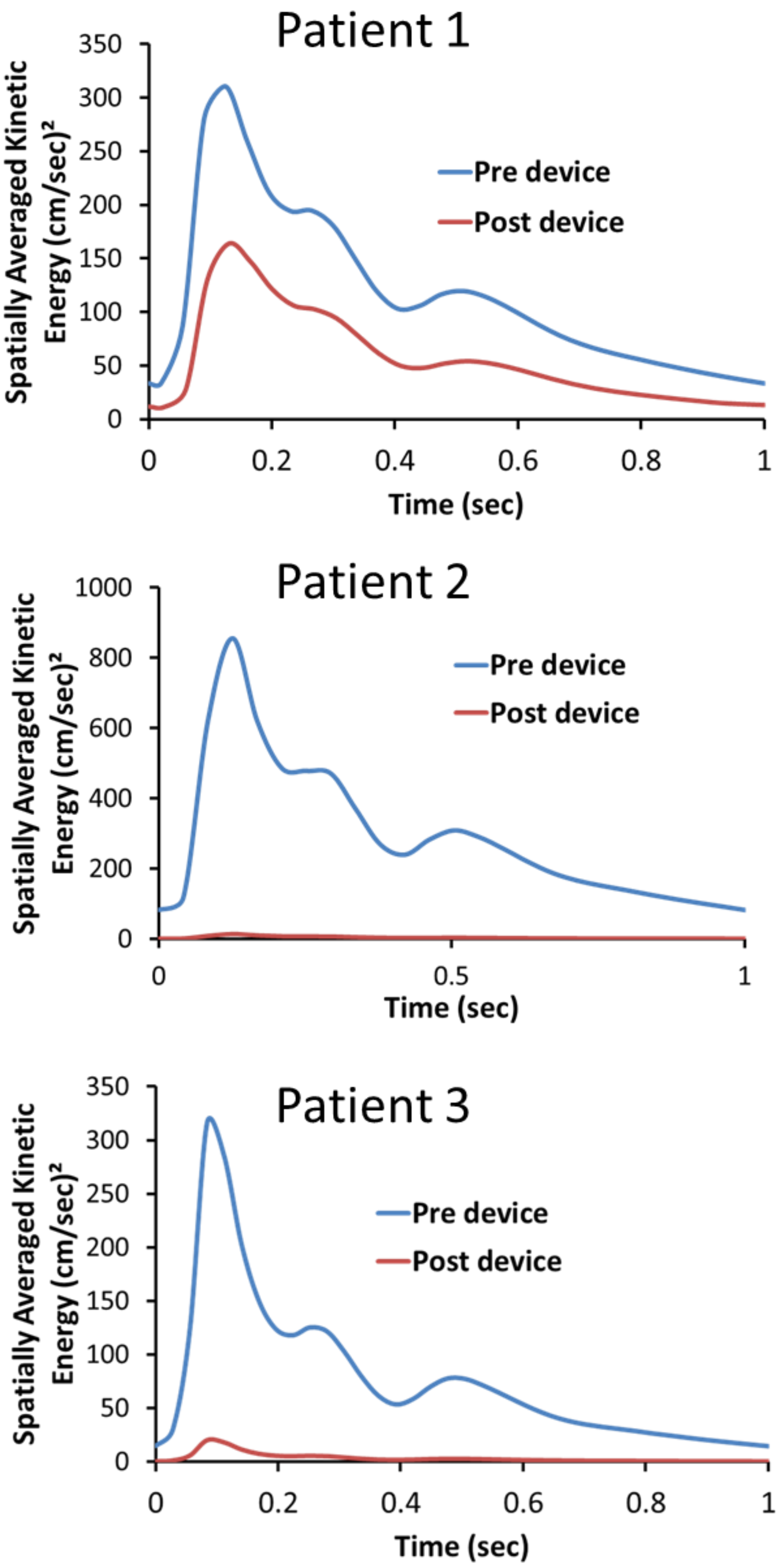

Figure 75: Spatially averaged intra-aneurysmal temporal kinetic energy plots for Patient 1-CM021(top), Patient 2-LM025(middle) and Patient 3-RG022 (bottom) obtained from

velocity vector results of CFD simulations; pre (blue) and post (red) device implantation plots are shown.

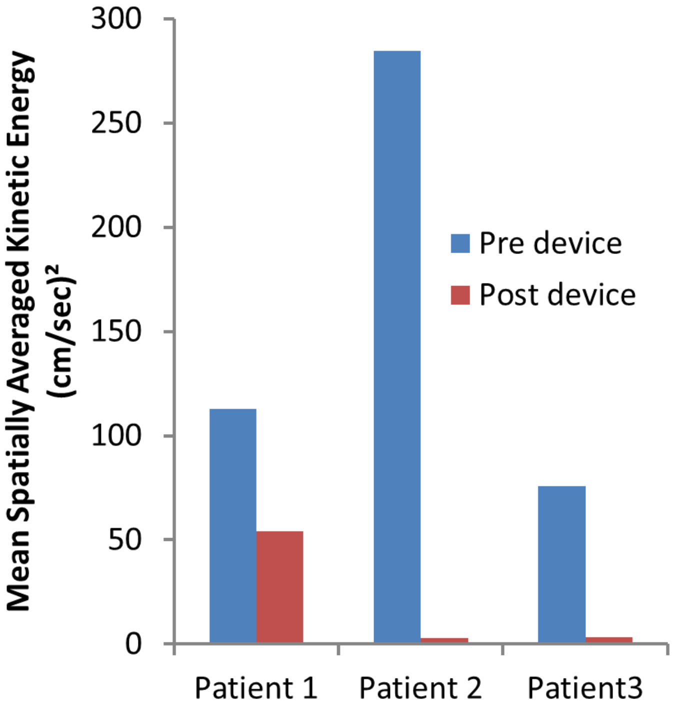

Figure 76: Mean spatially averaged kinetic energy results pre and post flow diverter implantation for the three patients derived from CFD simulations.

The reduction in mean intra-aneurysmal kinetic energy was highest for Patient 2 at 98.95% followed by Patient 3 who had 95.7% reduction. Patient 1 had the lowest percentage reduction at 52% (Figure 77).

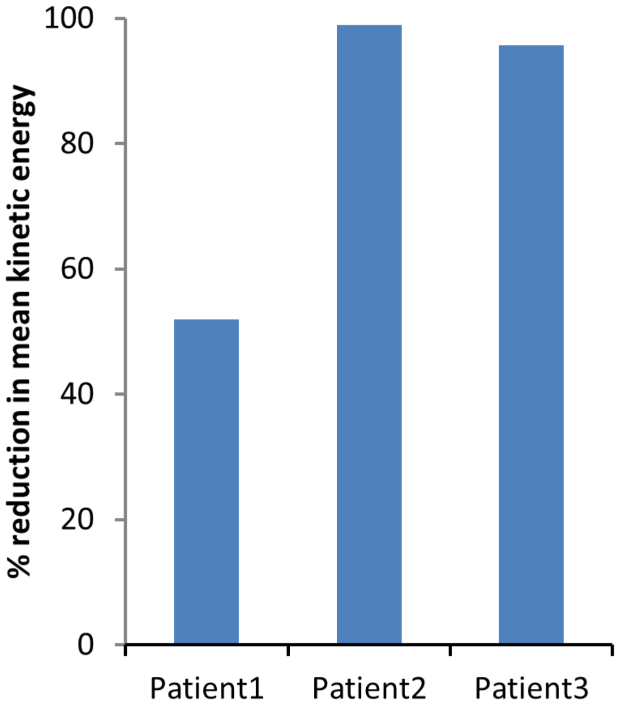

Figure 77: Percentage reduction in mean spatially averaged kinetic energy post flow diverter implantation for the three patients

DISCUSSION

The clinical flow simulations on two patients produced very similar reduction in the beat averaged kinetic to those obtain in the *in vitro* experiments on sidewall aneurysms described in chapter 3. The *in vitro* study on Pipeline and FRED demonstrated a 97-98% reduction of kinetic energy inside the aneurysm post device implantation. These values are comparable to the results for Patients 2 and 3. Not surprisingly, the flow diversion effect in these cases gets augmented through telescoping of multiple Pipeline devices to ensure sufficient flow reduction.

Following flow diverter deployment a reversal in flow pattern was observed in Chapters 2 and 3 where CFD simulations were performed on the sidewall aneurysm model. Tortuosity of the parent artery and the location of the aneurysms immediately after a sharp bend was responsible for head on entry of flow into the aneurysm and hence the flow patterns never reversed inside these patient aneurysms during the cardiac cycle.

In our simulations a flow waveform obtained from the literature was used as inflow boundary condition since flow data was not acquired in the patients during the procedure. The outlet flow distribution was unknown as well therefore we used zero pressure as outlet boundary condition. A more physiological outflow boundary condition can be applied by using a 3-element Windkessel model, however, this approach is more beneficial when some flow information is obtained directly from the patient such as flow distribution and pressure data for the patients. Another simplification used in the present calculations is the assumption of rigid walls. Using deformable walls as boundaries can help in improving the physiologically relevant details of the flow field such as near wall phenomena which can be used to calculate variables such as shear stresses or near wall residence time of cellular elements. However, for calculations of bulk variables such as kinetic energy in the aneurysm simplifications as used here are justified. Our study used a cropped version of the flow diverter to increase the computational efficiency and reduce grid generation complications due to distorted elements particularly around the device filaments when multiple devices (>2-3) are used. Telescoping of devices may affect the flow in the parent artery and the aneurysm mostly during the initial days post device implantation before a neointima is established. The lack of modeling of multiple devices on the flow field both in the parent artery and at the neck of the aneurysm is a potential source of some errors. For example, FRED (MicroVention), which has been described in detail in Chapter 3, is a dual layered flow diverter composed of an outer thick wire braided device and an inner fine wire braided flow diverter. Hence the entire length of the device along the circumference of the artery should be modeled to minimize potential errors.

Clinical CFD and correlation with angiographic contrast washout:

As part of this study CFD simulations were compared to high speed angiograms that were obtained in the patients before and immediately after flow diversion to establish a correlation between data obtainable clinically vs calculations that need to be executed off line. Apart from the convection decay time constants, the average slopes of the washout curves during the wash-in and wash-out phases[106, 113] are plotted alongside the kinetic energy in Figures 78-80. For the three patients both wash-in and wash-out slopes reduced post device implantation in concert with reduction in kinetic energy. For Patient 2 the reductions in kinetic energy, wash-in slope, and wash-out slope were more prominent than for Patient 1 and Patient 3. The convection time constant, related to the wash-out, was inversely related to kinetic energy. The convection time constant signifies the time of contrast transport through the aneurysm and is expected to increase post device implantation. Change in the convection time constant is more pronounced for Patient 2 as reflected in the slopes of wash-in and wash-out as well.

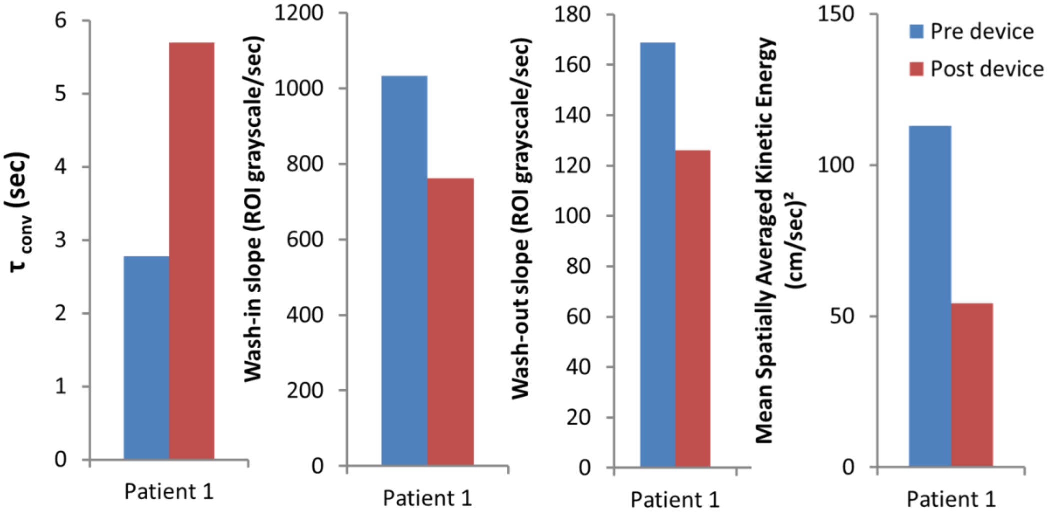

Figure 78: Angiographic parameters and kinetic energy results for Patient 1.

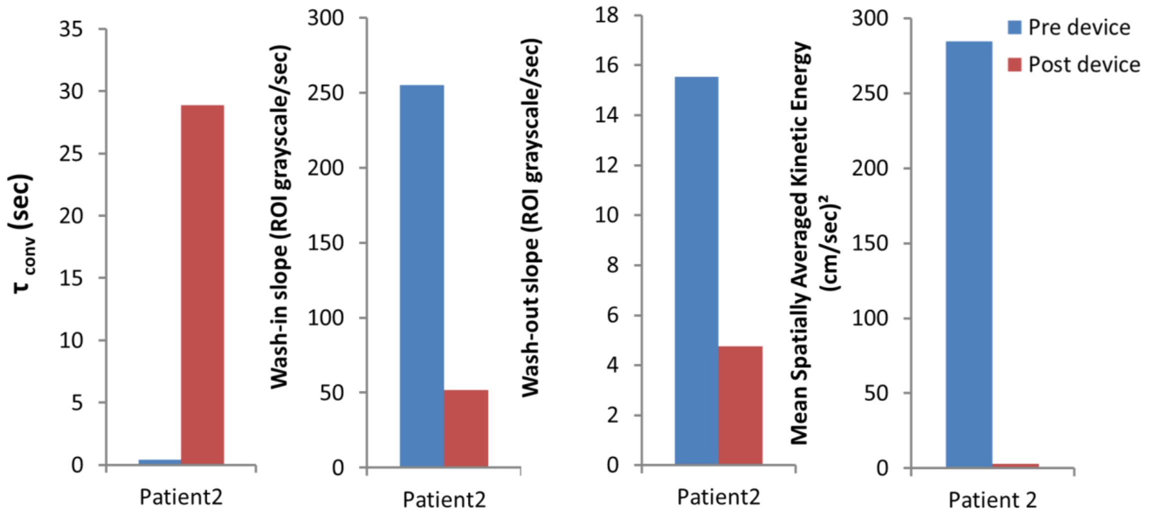

Figure 79: Angiographic parameters and kinetic energy results for Patient 2.

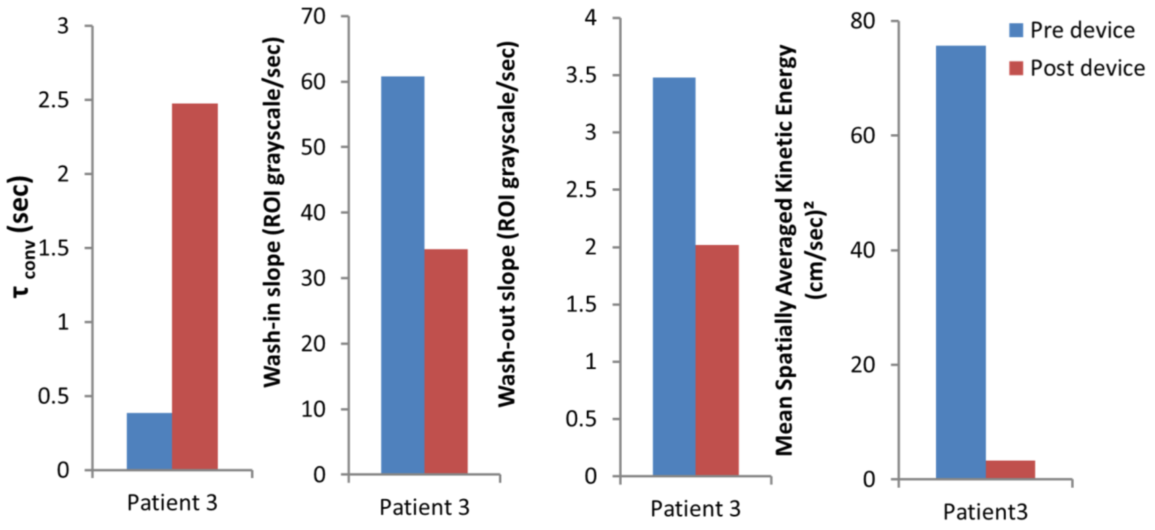

Figure 80: Angiographic parameters and kinetic energy results for Patient 3.

Since only three patients were analyzed it is too small of a sample size to draw statistical conclusions. However, a trend can be observed when correlating angiographic parameters to mean percentage change in kinetic energy post flow diversion (Figures 81-83). Convective decay time constant relates weakly to kinetic energy for this set of three patients. Change in the angiographic concentration time curve during the wash-out phase quantified by the average slope was more prominent than the wash-in phase and seemed to correlate better with the respective kinetic energy data (Figure 82). Additional data is needed to draw any conclusions regarding the relationship between washout parameters and the CFD derived kinetic energy inside the aneurysm.

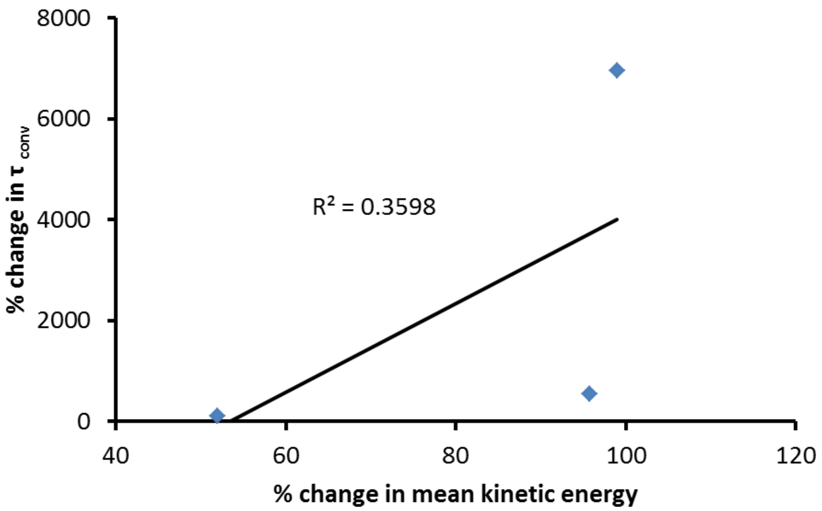

Figure 81: Percentage change in the convective decay time constant vs percentage change in mean kinetic energy with a trendline indicating weak correlation (p=0.54).

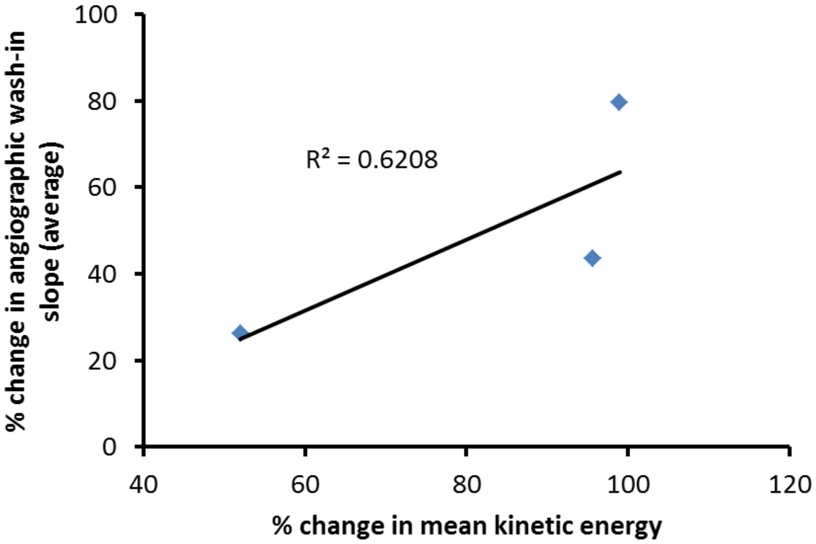

Figure 82: Percentage change in the average slope of angiographic wash-in vs percentage change in mean kinetic energy with a trendline indicating weak correlation (p=0.423).

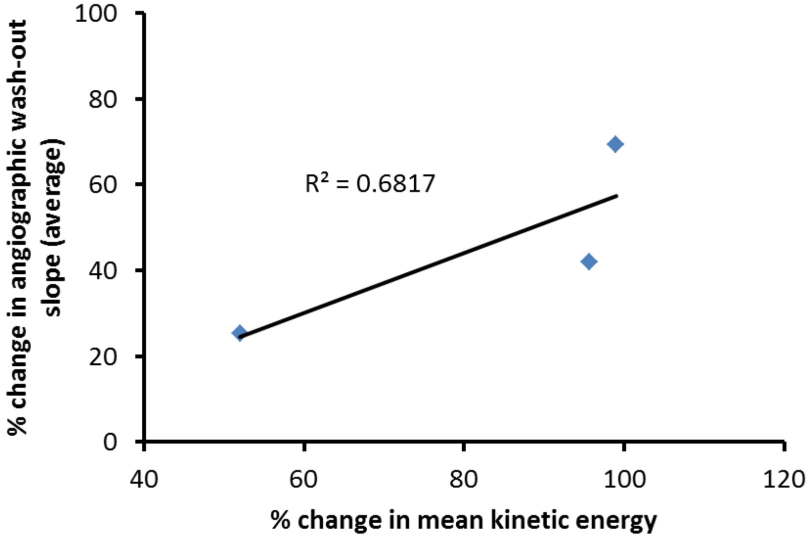

Figure 83: Percentage change in the average slope of angiographic wash-out vs percentage change in mean kinetic energy with a trend line indicating weak correlation (p=0.382).

These preliminary results testing the correlation between experimental angiographic data and flow results from CFD simulations appear promising. Data from CFD analysis on models from a few more patients can possibly establish a correlation with statistical significance. The level of agreement between contrast transport mechanics (rate of change in intensity and stagnation) and the CFD velocity derived kinetic energy results provide validation for the CFD simulations. Understanding of intra-aneurysmal hemodynamics post flow diversion in clinical patient models thus seems feasible through CFD analysis.

CHAPTER 7: CONCLUSION AND RECOMMENDATIONS

This work was based upon the hypothesis that angiographic and computational fluid dynamics parameters can predict the long-term outcome of flow diversion treatment for cerebral aneurysms. To test the hypothesis, this work evaluated flow diversion treatment of cerebral aneurysms via *in-silico, in-vitro, in vivo,* as well as clinical studies. This is the first study to apply combined angiographic and numerical analysis of intra-aneurysmal hemodynamics in various experimental and computational models for evaluation of flow diversion performance.

This is the first study to compare five commercial neurovascular devices in a bench-top experimental set up as well as computational flow simulations based on the exact experimental device geometry obtained using microCT. The bench top experiments and CFD simulations between neurovascular devices in a sidewall aneurysm delineated differences in the capacity to alter intra-aneurysmal flow between high porosity stents and low porosity flow diverters. Significant differences noted in the experiments between the Pipeline and FRED flow diverters were not observed in the CFD simulations. This could be due to alterations in the Pipeline wire configuration, which is sensitive to deployment technique and flow rig forces, between simulation and experiment. For a more robust comparison, multiple samples of the same device must be compared with microCT imaging/CFD simulation and experiments. Future comparison studies for the neurovascular devices evaluated in this work can be performed in a patient specific aneurysm geometry. The aneurysm position and orientation within the experimental setup must be maintained constant to obtain consistent mixing of contrast and reduce experimental variability.

Overall, however, this work confirms that experimental high speed angiographic image analysis can be applied to evaluate stent/flow diverter designs and CFD simulations can complement the experimental data adding value to the development process. Additionally this work provides valuable data to neurointerventionalists on the comparative performance of the evaluated devices.

The image-to-fluid domain mesh construction process used in this study, whether experimental microCT to CAD or patient rotational angiography to CAD, involved multiple laborious steps and is not suitable for simulating the large sample sizes required for statistical conclusions. An image to mesh technique (I2M) currently being developed to obtain finite element grids directly from segmented medical imaging data has the potential to overcome the time deficit of generating solid models[118-120]. The meshes obtained from the I2M technique may be validated against the results obtained in the current study prior to future application. Once validated and verified, I2M techniques may offer a more efficient pathway to simulation and replace the current model construction process. Apart from being unable to handle Boolean operations of tortuous/complex geometries, ADINA has the additional drawback of mesh generation via Delaunay triangulation which introduces slivers in the finite element meshes when discretizing complex geometries involving a huge transition in edge sizes. The I2M technique steps away from the freeform Delaunay triangulation algorithms and offers a body centered cubic lattice based structured grid that can produce highly anisotropic meshes with a smooth transition in size of the elements to avoid any simulation instabilities.

The intra-aneurysmal concentration-time curves recorded in both the rabbit model and in patients were well quantified by the mathematical model used here and the angiographic analysis showed significant differences in contrast transport due to flow diverter deployment. However, due to low sample sizes (n~10 per group) in both studies, only trends could be noted between aneurysm occluded and non-occluded groups. The rabbit study noted near statistically significant differences in the washout coefficient values between the occluded and non-occluded groups. This could be attributed to the sample size of n=9 for each group, which was lower than the target sample size of n=10 for each group. The washout coefficient, a single term based on the parameters obtained from angiographic analysis captured the intra-aneurysmal contrast mechanics differences between the occluded and the non-occluded groups. With respect to the rabbit elastase induced model, the washout coefficient value could function as a diagnostic tool to predict treatment efficacy. Based on the data from this work, the washout coefficient is expected to increase for the occluded groups and hence a threshold defining the minimum value of the washout coefficient could serve as the diagnostic test of flow diversion efficacy. Since, the parameter is based on diffusive components of contrast transport obtained from the mathematical model; the washout coefficient for clinical patients could not be obtained due to the dominant convective contrast transport. The power of especially the clinical study to predict aneurysm occlusion was low considering the sample size of n~10 per group in the analysis while the total enrollment was 40 patients. The patient data was affected by the heterogeneous nature of aneurysm shape, size and morphology for the cohort of patients analyzed. The occlusion rates were lowest for the fusiform geometries. In case of clinical patients the current definition of the washout coefficient is not valid since no diffusive transport is observed in most of the cases. The washout coefficient should be defined based on the convective contrast transport parameters instead and tested for differences between the occluded and non-occluded groups. Individually the convective decay time constant did not differ significantly between the occluded and non-occluded groups but trends of differences could be noted. These trends can be confirmed following collection and analysis of data from more patients added to the current cohort. Provided a large pool of data from clinical patients is available, the patient data-sets may then be stratified based on their aneurysm morphologies or locations and then tested for differences within those subgroups.

In the rabbits, 55% of the un-occluded aneurysms presented with minimal residual filling and it can be speculated that given a longer follow up time, these aneurysms might have completely occluded. Future studies should potentially involve a longer follow up of up to 1 year. Alternately, near complete occlusion (≥95% of the aneurysm occluded) could be used as a measure of treatment success instead of complete occlusion (100% of aneurysm occluded) used here. These values are justified and have been included in clinical studies[43, 103].

In patients with small (under-4mm) aneurysms, the effect of flow diversion was not detectable through angiographic analysis (concentration-time curves were nearly the same pre- and post-flow diversion). Almost all these aneurysms completely occluded at follow-up and thus, conducting angiographic analysis to predict flow diversion outcome in small aneurysms may be unnecessary.

The rabbit model produces homogenous aneurysm morphologies with similar contrast transport behavior resulting in lower variance between the samples. In contrast, the cohort of patients in the clinical study demonstrated heterogeneous morphologies, thus exhibiting higher variance in contrast transport behavior. The analysis, thus, may need to be conducted in a larger group of patients, potentially via multi-center collaborations, to overcome the intra-group variances and obtain statistical significance between the occluded and non-occluded groups. In order to mitigate radiation exposure to the patients from high speed angiography, angiographic data can be acquired utilizing a VFR protocol at the lowest possible frame rate that successfully resolves contrast transport mechanics. The overall results indicate that angiographic analysis can help determine a predictive or diagnostic tool for flow diversion efficacy.

Although based on a small sample, the patient-specific CFD modeling with flow diverter implantation was complemented by the clinical angiographic analysis. This portion of the study indicates potential applicability of CFD in aneurysm treatment planning through virtual flow diverter implantation and assessment of long-term treatment efficacy prior to treating the patient. Future patient geometry based simulations may apply FSI instead of CFD to incorporate the compliance of blood vessels in the models. Whenever flow information in the form of phase contrast MR data is available, the outlet flow may be modeled accordingly. The outlet boundary conditions may include the proximal as well as distal capillary bed resistance. Availability of patient’s blood pressure values will also be crucial towards implementation of accurate physiologic boundary conditions.

REFERENCES:

1. Lieber BB, Livescu V, Hopkins LN, Wakhloo AK. Particle image velocimetry assessment of stent design influence on intra-aneurysmal flow. *Ann Biomed Eng*. 2002;30:768-777

2. Go AS, Mozaffarian D, Roger VL, Benjamin EJ, Berry JD, Blaha MJ, Dai S, Ford ES, Fox CS, Franco S, Fullerton HJ, Gillespie C, Hailpern SM, Heit JA, Howard VJ, Huffman MD, Judd SE, Kissela BM, Kittner SJ, Lackland DT, Lichtman JH, Lisabeth LD, Mackey RH, Magid DJ, Marcus GM, Marelli A, Matchar DB, McGuire DK, Mohler ER, Moy CS, Mussolino ME, Neumar RW, Nichol G, Pandey DK, Paynter NP, Reeves MJ, Sorlie PD, Stein J, Towfighi A, Turan TN, Virani SS, Wong ND, Woo D, Turner MB. Heart disease and stroke statistics—2014 update: A report from the american heart association. *Circulation*. 2013

3. Juvela S, Porras M, Poussa K. Natural history of unruptured intracranial aneurysms: Probability of and risk factors for aneurysm rupture. *J Neurosurg*. 2000;93:379-387

4. Deshaies EM, Eddleman CS, Boulos AS. *Handbook of neuroendovascular surgery*. New York: Thieme; 2012.

5. Ferro JM, Canhao P, Peralta R. Update on subarachnoid haemorrhage. *J Neurol*. 2008;255:465-479

6. Suarez JI, Tarr RW, Selman WR. Aneurysmal subarachnoid hemorrhage. *N Engl J Med*. 2006;354:387-396

7. Mayberg MR, Batjer HH, Dacey R, Diringer M, Haley EC, Heros RC, Sternau LL, Torner J, Adams HP, Jr., Feinberg W, et al. Guidelines for the management of aneurysmal subarachnoid hemorrhage. A statement for healthcare professionals from a special writing group of the stroke council, american heart association. *Circulation*. 1994;90:2592-2605

8. Linn FH, Rinkel GJ, Algra A, van Gijn J. Incidence of subarachnoid hemorrhage: Role of region, year, and rate of computed tomography: A meta-analysis. *Stroke*. 1996;27:625-629

9. Rhoton AL, Jr. Aneurysms. *Neurosurgery*. 2002;51:S121-158

10. Schievink WI. Intracranial aneurysms. *N Engl J Med*. 1997;336:28-40

11. Kayembe KN, Sasahara M, Hazama F. Cerebral aneurysms and variations in the circle of willis. *Stroke*. 1984;15:846-850

12. Ferguson GG. The pathogenesis of intracranial saccular aneurysms. *Int Anesthesiol Clin*. 1982;20:19-24

13. Crompton MR. The natural history of cerebral berry aneurysms. *Am Heart J*. 1967;73:567-569

14. Crompton MR. Mechanism of growth and rupture in cerebral berry aneurysms. *Br Med J*. 1966;1:1138-1142

15. Crompton MR. The comparative pathology of cerebral aneurysms. *Brain*. 1966;89:789-796

16. Crompton MR. The pathogenesis of cerebral aneurysms. *Brain*. 1966;89:797-814

17. Crompton MR. The pathogenesis of cerebral infarction following the rupture of cerebral berry aneurysms. *Brain*. 1964;87:491-510

18. Crawford T. Some observations on the pathogenesis and natural history of intracranial aneurysms. *J Neurol Neurosurg Psychiatry*. 1959;22:259-266

19. Wijdicks EF, Kallmes DF, Manno EM, Fulgham JR, Piepgras DG. Subarachnoid hemorrhage: Neurointensive care and aneurysm repair. *Mayo Clin Proc*. 2005;80:550-559

20. Brisman JL, Song JK, Newell DW. Cerebral aneurysms. *N Engl J Med*. 2006;355:928-939

21. Rinkel GJ, Djibuti M, Algra A, van Gijn J. Prevalence and risk of rupture of intracranial aneurysms: A systematic review. *Stroke*. 1998;29:251-256

22. Kayembe KN, Kataoka H, Hazama F. Early changes in cerebral aneurysms in the internal carotid artery/posterior communicating artery junction. *Acta Pathol Jpn*. 1987;37:1891-1901

23. Jeong YG, Jung YT, Kim MS, Eun CK, Jang SH. Size and location of ruptured intracranial aneurysms. *J Korean Neurosurg Soc*. 2009;45:11-15

24. Forget TR, Jr., Benitez R, Veznedaroglu E, Sharan A, Mitchell W, Silva M, Rosenwasser RH. A review of size and location of ruptured intracranial aneurysms. *Neurosurgery*. 2001;49:1322-1325; discussion 1325-1326

25. Rhoton AL, Jr., Saeki N, Perlmutter D, Zeal A. Microsurgical anatomy of common aneurysm sites. *Clin Neurosurg*. 1979;26:248-306

26. Rhoton AL, Jr. Anatomy of saccular aneurysms. *Surg Neurol*. 1980;14:59-66

27. Ogilvy CS. Neurosurgical clipping versus endovascular coiling of patients with ruptured intracranial aneurysms. *Stroke*. 2003;34:2540-2542

28. Kassell NF, Torner JC. Aneurysmal rebleeding: A preliminary report from the cooperative aneurysm study. *Neurosurgery*. 1983;13:479-481

29. Jane JA, Winn HR, Richardson AE. The natural history of intracranial aneurysms: Rebleeding rates during the acute and long term period and implication for surgical management. *Clin Neurosurg*. 1977;24:176-184

30. Roy D, Milot G, Raymond J. Endovascular treatment of unruptured aneurysms. *Stroke*. 2001;32:1998-2004

31. Phatouros CC, Higashida RT, Halbach VV. New methods of treatment for cerebral aneurysms. *West J Med*. 1998;169:286-287

32. Fernandez Zubillaga A, Guglielmi G, Vinuela F, Duckwiler GR. Endovascular occlusion of intracranial aneurysms with electrically detachable coils: Correlation of aneurysm neck size and treatment results. *AJNR. American journal of neuroradiology*. 1994;15:815-820

33. Brilstra EH, Rinkel GJ, van der Graaf Y, van Rooij WJ, Algra A. Treatment of intracranial aneurysms by embolization with coils: A systematic review. *Stroke*. 1999;30:470-476

34. Debrun GM, Aletich VA, Kehrli P, Misra M, Ausman JI, Charbel F. Selection of cerebral aneurysms for treatment using guglielmi detachable coils: The preliminary university of illinois at chicago experience. *Neurosurgery*. 1998;43:1281-1295; discussion 1296-1287

35. Kawanabe Y, Sadato A, Taki W, Hashimoto N. Endovascular occlusion of intracranial aneurysms with guglielmi detachable coils: Correlation between coil packing density and coil compaction. *Acta neurochirurgica*. 2001;143:451-455

36. Kai Y, Hamada J, Morioka M, Yano S, Kuratsu J. Evaluation of the stability of small ruptured aneurysms with a small neck after embolization with guglielmi detachable coils: Correlation between coil packing ratio and coil compaction. *Neurosurgery*. 2005;56:785-792; discussion 785-792

37. Hayakawa M, Murayama Y, Duckwiler GR, Gobin YP, Guglielmi G, Vinuela F. Natural history of the neck remnant of a cerebral aneurysm treated with the guglielmi detachable coil system. *J Neurosurg*. 2000;93:561-568

38. Ferns SP, Sprengers ME, van Rooij WJ, Rinkel GJ, van Rijn JC, Bipat S, Sluzewski M, Majoie CB. Coiling of intracranial aneurysms: A systematic review on initial occlusion and reopening and retreatment rates. *Stroke*. 2009;40:e523-529

39. Lylyk P, Miranda C, Ceratto R, Ferrario A, Scrivano E, Luna HR, Berez AL, Tran Q, Nelson PK, Fiorella D. Curative endovascular reconstruction of cerebral aneurysms with the pipeline embolization device: The buenos aires experience. *Neurosurgery*. 2009;64:632-642; discussion 642-633; quiz N636

40. Wakhloo AK, Tio FO, Lieber BB, Schellhammer F, Graf M, Hopkins LN. Self-expanding nitinol stents in canine vertebral arteries: Hemodynamics and tissue response. *AJNR. American journal of neuroradiology*. 1995;16:1043-1051

41. Wakhloo AK, Lanzino G, Lieber BB, Hopkins LN. Stents for intracranial aneurysms: The beginning of a new endovascular era? *Neurosurgery*. 1998;43:377-379

42. Nelson PK, Lylyk P, Szikora I, Wetzel SG, Wanke I, Fiorella D. The pipeline embolization device for the intracranial treatment of aneurysms trial. *AJNR. American journal of neuroradiology*. 2011;32:34-40

43. Fiorella D, Woo HH, Albuquerque FC, Nelson PK. Definitive reconstruction of circumferential, fusiform intracranial aneurysms with the pipeline embolization device. *Neurosurgery*. 2008;62:1115-1120; discussion 1120-1111

44. Fiorella D, Kelly ME, Albuquerque FC, Nelson PK. Curative reconstruction of a giant midbasilar trunk aneurysm with the pipeline embolization device. *Neurosurgery*. 2009;64:212-217; discussion 217

45. Becske T, Kallmes DF, Saatci I, McDougall CG, Szikora I, Lanzino G, Moran CJ, Woo HH, Lopes DK, Berez AL, Cher DJ, Siddiqui AH, Levy EI, Albuquerque FC, Fiorella DJ, Berentei Z, Marosfoi M, Cekirge SH, Nelson PK. Pipeline for uncoilable or failed aneurysms: Results from a multicenter clinical trial. *Radiology*. 2013;267:858-868

46. Lieber BB, Sadasivan C. Endoluminal scaffolds for vascular reconstruction and exclusion of aneurysms from the cerebral circulation. *Stroke*. 2010;41:S21-25

47. Lieber BB, Stancampiano AP, Wakhloo AK. Alteration of hemodynamics in aneurysm models by stenting: Influence of stent porosity. *Ann Biomed Eng*. 1997;25:460-469

48. Lieber BB, Gounis MJ. The physics of endoluminal stenting in the treatment of cerebrovascular aneurysms. *Neurol Res*. 2002;24 Suppl 1:S33-42

49. Aenis M, Stancampiano AP, Wakhloo AK, Lieber BB. Modeling of flow in a straight stented and nonstented side wall aneurysm model. *Journal of biomechanical engineering*. 1997;119:206-212

50. Trager AL, Sadasivan C, Seong J, Lieber BB. Correlation between angiographic and particle image velocimetry quantifications of flow diverters in an in vitro model of elastase-induced rabbit aneurysms. *Journal of biomechanical engineering*. 2009;131:034506

51. Trager AL, Sadasivan C, Lieber BB. Comparison of the in vitro hemodynamic performance of new flow diverters for bypass of brain aneurysms. *Journal of biomechanical engineering*. 2012;134:084505

52. Seong J, Wakhloo AK, Lieber BB. In vitro evaluation of flow divertors in an elastase-induced saccular aneurysm model in rabbit. *Journal of biomechanical engineering*. 2007;129:863-872

53. Sadasivan C, Lieber BB, Cesar L, Miskolczi L, Seong J, Wakhloo AK. Angiographic assessment of the performance of flow divertors to treat cerebral aneurysms. *Conf Proc IEEE Eng Med Biol Soc*. 2006;1:3210-3213

54. Sadasivan C, Cesar L, Seong J, Rakian A, Hao Q, Tio FO, Wakhloo AK, Lieber BB. An original flow diversion device for the treatment of intracranial aneurysms: Evaluation in the rabbit elastase-induced model. *Stroke*. 2009;40:952-958

55. Bassingthwaighte JB. Dispersion of indicator in the circulation. *Proceedings. IBM Medical Symposium*. 1963:57-76

56. Lieber BB, Sadasivan C, Gounis MJ, Seong J, Miskolczi L, Wakhloo AK. Functional angiography. *Crit Rev Biomed Eng*. 2005;33:1-102

57. Sadasivan C, Cesar L, Seong J, Wakhloo AK, Lieber BB. Treatment of rabbit elastase-induced aneurysm models by flow diverters: Development of quantifiable indexes of device performance using digital subtraction angiography. *IEEE Trans Med Imaging*. 2009;28:1117-1125

58. Onizuka M, Miskolczi L, Gounis MJ, Seong J, Lieber BB, Wakhloo AK. Elastase-induced aneurysms in rabbits: Effect of postconstruction geometry on final size. *AJNR. American journal of neuroradiology*. 2006;27:1129-1131

59. Kallmes DF, Fujiwara NH, Berr SS, Helm GA, Cloft HJ. Elastase-induced saccular aneurysms in rabbits: A dose-escalation study. *AJNR. American journal of neuroradiology*. 2002;23:295-298

60. Hoh BL, Rabinov JD, Pryor JC, Ogilvy CS. A modified technique for using elastase to create saccular aneurysms in animals that histologically and hemodynamically resemble aneurysms in human. *Acta neurochirurgica*. 2004;146:705-711

61. Ding YH, Danielson MA, Kadirvel R, Dai D, Lewis DA, Cloft HJ, Kallmes DF. Modified technique to create morphologically reproducible elastase-induced aneurysms in rabbits. *Neuroradiology*. 2006;48:528-532

62. Ding YH, Dai D, Lewis DA, Danielson MA, Kadirvel R, Mandrekar JN, Cloft HJ, Kallmes DF. Can neck size in elastase-induced aneurysms be controlled? A prospective study. *AJNR. American journal of neuroradiology*. 2005;26:2364-2367

63. Ding YH, Dai D, Danielson MA, Kadirvel R, Lewis DA, Cloft HJ, Kallmes DF. Control of aneurysm volume by adjusting the position of ligation during creation of elastase-induced aneurysms: A prospective study. *AJNR. American journal of neuroradiology*. 2007;28:857-859

64. Cesar L, Miskolczi L, Lieber BB, Sadasivan C, Gounis MJ, Wakhloo AK. Neurological deficits associated with the elastase-induced aneurysm model in rabbits. *Neurological research*. 2009;31:414-419

65. Altes TA, Cloft HJ, Short JG, DeGast A, Do HM, Helm GA, Kallmes DF. 1999 arrs executive council award. Creation of saccular aneurysms in the rabbit: A model suitable for testing endovascular devices. American roentgen ray society. *AJR Am J Roentgenol*. 2000;174:349-354

66. Sadasivan C, Lieber BB, Gounis MJ, Lopes DK, Hopkins LN. Angiographic quantification of contrast medium washout from cerebral aneurysms after stent placement. *AJNR. American journal of neuroradiology*. 2002;23:1214-1221

67. Sadasivan C, Fiorella DJ, Woo HH, Lieber BB. Physical factors effecting cerebral aneurysm pathophysiology. *Ann Biomed Eng*. 2013;41:1347-1365

68. Watton PN, Ventikos Y, Holzapfel GA. Modelling the growth and stabilization of cerebral aneurysms. *Math Med Biol*. 2009;26:133-164

69. Ventikos Y, Holland EC, Bowker TJ, Watton PN, Kakalis NM, Megahed M, Zhu F, Summers PE, Byrne JV. Computational modelling for cerebral aneurysms: Risk evaluation and interventional planning. *Br J Radiol*. 2009;82 Spec No 1:S62-71

70. Valencia A, Morales H, Rivera R, Bravo E, Galvez M. Blood flow dynamics in patient-specific cerebral aneurysm models: The relationship between wall shear stress and aneurysm area index. *Med Eng Phys*. 2008;30:329-340

71. Torii R, Oshima M, Kobayashi T, Takagi K, Tezduyar TE. Fluid-structure interaction modeling of blood flow and cerebral aneurysm: Significance of artery and aneurysm shapes. *Computer Methods in Applied Mechanics and Engineering*. 2009;198:3613-3621

72. Tateshima S, Chien A, Sayre J, Cebral J, Vinuela F. The effect of aneurysm geometry on the intra-aneurysmal flow condition. *Neuroradiology*. 2010;52:1135-1141

73. Stuhne GR, Steinman DA. Finite-element modeling of the hemodynamics of stented aneurysms. *Journal of biomechanical engineering*. 2004;126:382-387

74. Steinman DA, Milner JS, Norley CJ, Lownie SP, Holdsworth DW. Image-based computational simulation of flow dynamics in a giant intracranial aneurysm. *AJNR. American journal of neuroradiology*. 2003;24:559-566

75. Steinman DA. Image-based computational fluid dynamics modeling in realistic arterial geometries. *Ann Biomed Eng*. 2002;30:483-497

76. Karmonik C, Klucznik R, Benndorf G. Blood flow in cerebral aneurysms: Comparison of phase contrast magnetic resonance and computational fluid dynamics--preliminary experience. *Rofo*. 2008;180:209-215

77. Humphrey JD, Taylor CA. Intracranial and abdominal aortic aneurysms: Similarities, differences, and need for a new class of computational models. *Annual review of biomedical engineering*. 2008;10:221-246

78. Dempere-Marco L, Oubel E, Castro M, Putman C, Frangi A, Cebral J. Cfd analysis incorporating the influence of wall motion: Application to intracranial aneurysms. *Med Image Comput Comput Assist Interv*. 2006;9:438-445

79. Cebral JR, Pergolizzi RS, Jr., Putman CM. Computational fluid dynamics modeling of intracranial aneurysms: Qualitative comparison with cerebral angiography. *Acad Radiol*. 2007;14:804-813

80. Cebral JR, Mut F, Raschi M, Scrivano E, Ceratto R, Lylyk P, Putman CM. Aneurysm rupture following treatment with flow-diverting stents: Computational hemodynamics analysis of treatment. *AJNR. American journal of neuroradiology*. 2011;32:27-33

81. Cebral JR, Lohner R. Efficient simulation of blood flow past complex endovascular devices using an adaptive embedding technique. *IEEE Trans Med Imaging*. 2005;24:468-476

82. Augsburger L, Reymond P, Rufenacht DA, Stergiopulos N. Intracranial stents being modeled as a porous medium: Flow simulation in stented cerebral aneurysms. *Ann Biomed Eng*. 2011;39:850-863

83. Stewart SC, Paterson E, Burgreen G, Hariharan P, Giarra M, Reddy V, Day S, Manning K, Deutsch S, Berman M, Myers M, Malinauskas R. Assessment of cfd performance in simulations of an idealized medical device: Results of fda’s first computational interlaboratory study. *Cardiovasc Eng Tech*. 2012;3:139-160

84. Hariharan P, D'Souza G, Horner M, Malinauskas RA, Myers MR. Verification benchmarks to assess the implementation of computational fluid dynamics based hemolysis prediction models. *Journal of biomechanical engineering*. 2015;137

85. Trias M, Arbona A, Masso J, Minano B, Bona C. Fda's nozzle numerical simulation challenge: Non-newtonian fluid effects and blood damage. *PloS one*. 2014;9:e92638

86. Steinman DA, Hoi Y, Fahy P, Morris L, Walsh MT, Aristokleous N, Anayiotos AS, Papaharilaou Y, Arzani A, Shadden SC, Berg P, Janiga G, Bols J, Segers P, Bressloff NW, Cibis M, Gijsen FH, Cito S, Pallares J, Browne LD, Costelloe JA, Lynch AG, Degroote J, Vierendeels J, Fu W, Qiao A, Hodis S, Kallmes DF, Kalsi H, Long Q, Kheyfets VO, Finol EA, Kono K, Malek AM, Lauric A, Menon PG, Pekkan K, Esmaily Moghadam M, Marsden AL, Oshima M, Katagiri K, Peiffer V, Mohamied Y, Sherwin SJ, Schaller J, Goubergrits L, Usera G, Mendina M, Valen-Sendstad K, Habets DF, Xiang J, Meng H, Yu Y, Karniadakis GE, Shaffer N, Loth F. Variability of computational fluid dynamics solutions for pressure and flow in a giant aneurysm: The asme 2012 summer bioengineering conference cfd challenge. *Journal of biomechanical engineering*. 2013;135:021016

87. Berg P, Roloff C, Beuing O, Voss S, Sugiyama SI, Aristokleous N, Anayiotos AS, Ashton N, Revell A, Bressloff NW, Brown AG, Chung BJ, Cebral JR, Copelli G, Fu W, Qiao A, Geers AJ, Hodis S, Dragomir-Daescu D, Nordahl E, Suzen YB, Khan MO, Valen-Sendstad K, Kono K, Menon PG, Albal PG, Mierka O, Munster R, Morales HG, Bonnefous O, Osman J, Goubergrits L, Pallares J, Cito S, Passalacqua A, Piskin S, Pekkan K, Ramalho S, Marques N, Sanchi S, Schumacher KR, Sturgeon J, Svihlova H, Hron J, Usera G, Mendina M, Xiang J, Meng H, Steinman DA, Janiga G. The computational fluid dynamics rupture challenge 2013 - phase ii: Variability of hemodynamic simulations in two intracranial aneurysms. *Journal of biomechanical engineering*. 2015

88. Xu J, Deng B, Fang Y, Yu Y, Cheng J, Wang S, Wang K, Liu JM, Huang Q. Hemodynamic changes caused by flow diverters in rabbit aneurysm models: Comparison of virtual and realistic fd deployments based on micro-ct reconstruction. *PloS one*. 2013;8:e66072

89. Lieber BB, Sadasivan C, Hao Q, Seong J, Cesar L. The mixability of angiographic contrast with arterial blood. *Med Phys*. 2009;36:5064-5078

90. Dennis KD, Rossman TL, Kallmes DF, Dragomir-Daescu D. Intra-aneurysmal flow rates are reduced by two flow diverters: An experiment using tomographic particle image velocimetry in an aneurysm model. *Journal of neurointerventional surgery*. 2014

91. Bertin JJ, Smith ML. *Aerodynamics for engineers*. Englewood Cliffs, N.J.: Prentice Hall; 1989.

92. Bathe K-J, Bathe K-J. *Finite element procedures*. Englewood Cliffs, N.J.: Prentice Hall; 1996.

93. Westerhof N, Stergiopulos N, Noble MIM. Snapshots of hemodynamics an aid for clinical research and graduate education. 2010

94. Zamir M. *The physics of pulsatile flow*. New York: AIP Press : Springer; 2000.

95. Nichols WW, O'Rourke MF, Vlachopoulos C. Mcdonald's blood flow in arteries : Theoretical, experimental and clinical principles. 2011

96. Milnor WR, Bertram CD. The relation between arterial viscoelasticity and wave propagation in the canine femoral artery in vivo. *Circ Res*. 1978;43:870-879

97. Womersley JR. Method for the calculation of velocity, rate of flow and viscous drag in arteries when the pressure gradient is known. *The Journal of Physiology*. 1955;127:553-563

98. Gundert TJ, Shadden SC, Williams AR, Koo BK, Feinstein JA, Ladisa JF, Jr. A rapid and computationally inexpensive method to virtually implant current and next-generation stents into subject-specific computational fluid dynamics models. *Ann Biomed Eng*. 2011;39:1423-1437

99. Seong J, Sadasivan C, Onizuka M, Gounis MJ, Christian F, Miskolczi L, Wakhloo AK, Lieber BB. Morphology of elastase-induced cerebral aneurysm model in rabbit and rapid prototyping of elastomeric transparent replicas. *Biorheology*. 2005;42:345-361

100. Patel NV, Gounis MJ, Wakhloo AK, Noordhoek N, Blijd J, Babic D, Takhtani D, Lee SK, Norbash A. Contrast-enhanced angiographic cone-beam ct of cerebrovascular stents: Experimental optimization and clinical application. *AJNR. American journal of neuroradiology*. 2011;32:137-144

101. Raymond J, Darsaut TE, Bing F, Makoyeva A, Kotowski M, Gevry G, Salazkin I. Stent-assisted coiling of bifurcation aneurysms may improve endovascular treatment: A critical evaluation in an experimental model. *AJNR. American journal of neuroradiology*. 2013;34:570-576

102. Gwilliam MN, Hoggard N, Capener D, Singh P, Marzo A, Verma PK, Wilkinson ID. Mr derived volumetric flow rate waveforms at locations within the common carotid, internal carotid, and basilar arteries. *J Cereb Blood Flow Metab*. 2009;29:1975-1982

103. Fiorella D, Arthur A, Boulos A, Diaz O, Jabbour P, Pride L, Turk AS, Woo HH, Derdeyn C, Millar J, Clifton A. Final results of the us humanitarian device exemption study of the low-profile visualized intraluminal support (lvis) device. *Journal of neurointerventional surgery*. 2015

104. Kallmes DF, Ding YH, Dai D, Kadirvel R, Lewis DA, Cloft HJ. A new endoluminal, flow-disrupting device for treatment of saccular aneurysms. *Stroke*. 2007;38:2346-2352

105. Kallmes DF, Ding YH, Dai D, Kadirvel R, Lewis DA, Cloft HJ. A second-generation, endoluminal, flow-disrupting device for treatment of saccular aneurysms. *AJNR. American journal of neuroradiology*. 2009;30:1153-1158

106. Struffert T, Ott S, Kowarschik M, Bender F, Adamek E, Engelhorn T, Golitz P, Lang S, Strother CM, Doerfler A. Measurement of quantifiable parameters by time-density curves in the elastase-induced aneurysm model: First results in the comparison of a flow diverter and a conventional aneurysm stent. *European radiology*. 2013;23:521-527

107. Flahault A, Cadilhac M, Thomas G. Sample size calculation should be performed for design accuracy in diagnostic test studies. *J Clin Epidemiol*. 2005;58:859-862

108. Agresti A, Coull BA. Approximate is better than "exact" for interval estimation of binomial proportions. *The American Statistician*. 1998;52:119-126

109. Massoud TF, Guglielmi G, Ji C, Vinuela F, Duckwiler GR. Experimental saccular aneurysms. I. Review of surgically-constructed models and their laboratory applications. *Neuroradiology*. 1994;36:537-546

110. O'Kelly C J, Krings T, Fiorella D, Marotta TR. A novel grading scale for the angiographic assessment of intracranial aneurysms treated using flow diverting stents. *Interventional neuroradiology : journal of peritherapeutic neuroradiology, surgical procedures and related neurosciences*. 2010;16:133-137

111. Grunwald IQ, Kamran M, Corkill RA, Kuhn AL, Choi IS, Turnbull S, Dobson D, Fassbender K, Watson D, Gounis MJ. Simple measurement of aneurysm residual after treatment: The smart scale for evaluation of intracranial aneurysms treated with flow diverters. *Acta neurochirurgica*. 2012;154:21-26; discussion 26

112. Tenjin H, Asakura F, Nakahara Y, Matsumoto K, Matsuo T, Urano F, Ueda S. Evaluation of intraaneurysmal blood velocity by time-density curve analysis and digital subtraction angiography. *AJNR. American journal of neuroradiology*. 1998;19:1303-1307

113. Golitz P, Struffert T, Rosch J, Ganslandt O, Knossalla F, Doerfler A. Cerebral aneurysm treatment using flow-diverting stents: In-vivo visualization of flow alterations by parametric colour coding to predict aneurysmal occlusion: Preliminary results. *European radiology*. 2015;25:428-435

114. Pereira VM, Bonnefous O, Ouared R, Brina O, Stawiaski J, Aerts H, Ruijters D, Narata AP, Bijlenga P, Schaller K, Lovblad KO. A dsa-based method using contrast-motion estimation for the assessment of the intra-aneurysmal flow changes induced by flow-diverter stents. *AJNR. American journal of neuroradiology*. 2013;34:808-815

115. Ladisa Jr JF, Dholakia RJ, Figueroa CA, Vignon-Clementel IE, Chan FP, Samyn MM, Cava JR, Taylor CA, Feinstein JA. Computational simulations demonstrate altered wall shear stress in aortic coarctation patients treated by resection with end-to-end anastomosis. *Congenit Heart Dis*. 2011

116. Taylor CA, Figueroa CA. Patient-specific modeling of cardiovascular mechanics. *Annual review of biomedical engineering*. 2009;11:109-134

117. Sadasivan C, Lieber BB, Fiorella D, Woo H. System and method for simulating deployment configuration of an expandable device. 2012

118. Chernikov JXaA. Quality meshing of 2d images with guarantees derived by a computer-assisted proof. *VMASC 2014 Capstone Conference*. 2014

119. Chrisochoides PFaN. High quality real-time image-to-mesh conversion for finite element simulations. *27th ACM International Conference on Supercomputing (ICS'13)*. 2013:233-242

120. Foteinos PA, Chrisochoides NP. High quality real-time image-to-mesh conversion for finite element simulations. *Journal of Parallel and Distributed Computing*. 2014;74:2123-2140

APPENDIX A: Rabbit data

Angiograms and washout curve analysis data for 15 rabbits are presented below. In general, pre-treatment, post-treatment, and follow-up angiograms are shown left to right in the top row. The bottom panels show the mathematical model fit to the washout curve data. Both the convective and diffusive components of the model are also shown. For each curve, the red color indicates the raw normalized angiographic washout curve. The blue color indicates the mathematical model fitted to the data. The cyan indicates the diffusive component of the model and the green indicates the convective component.

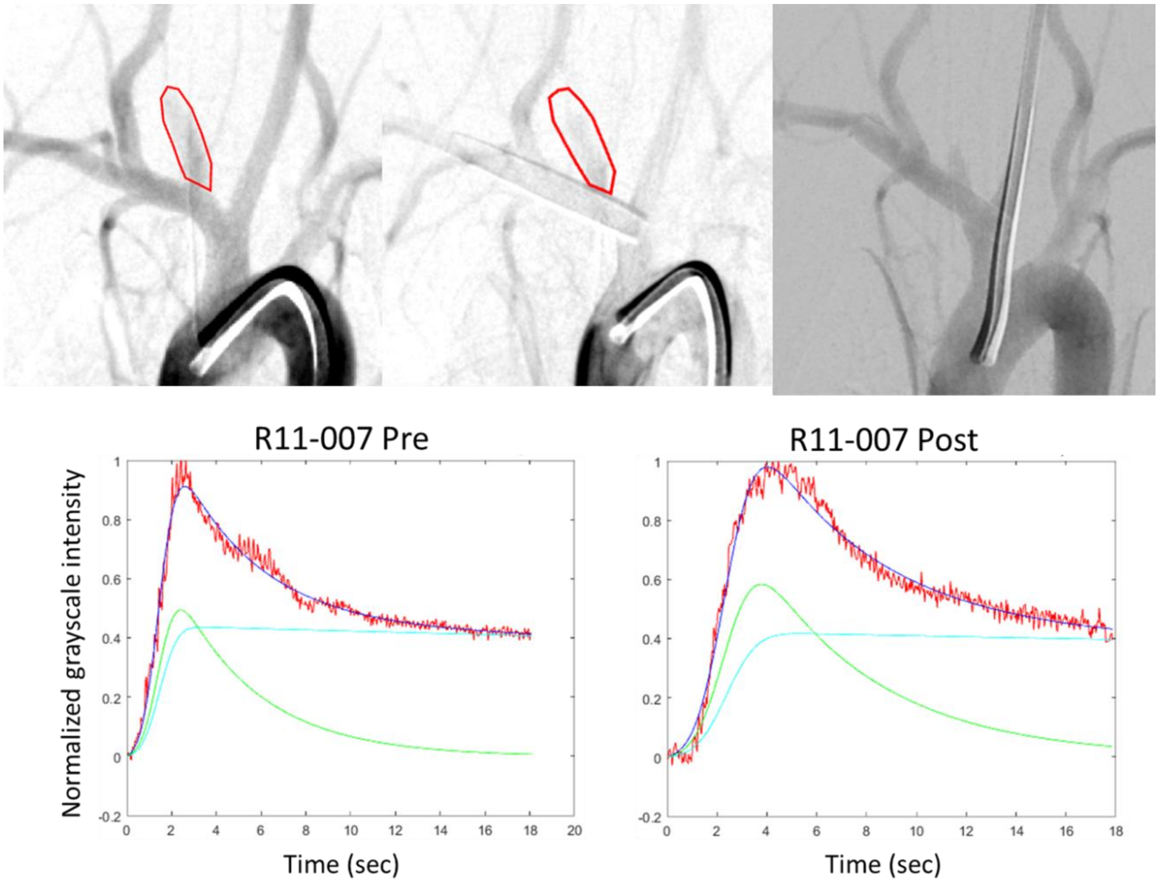

Figure 84: Angiographic image analysis and washout curve mathematical modeling for Rabbit R11-007

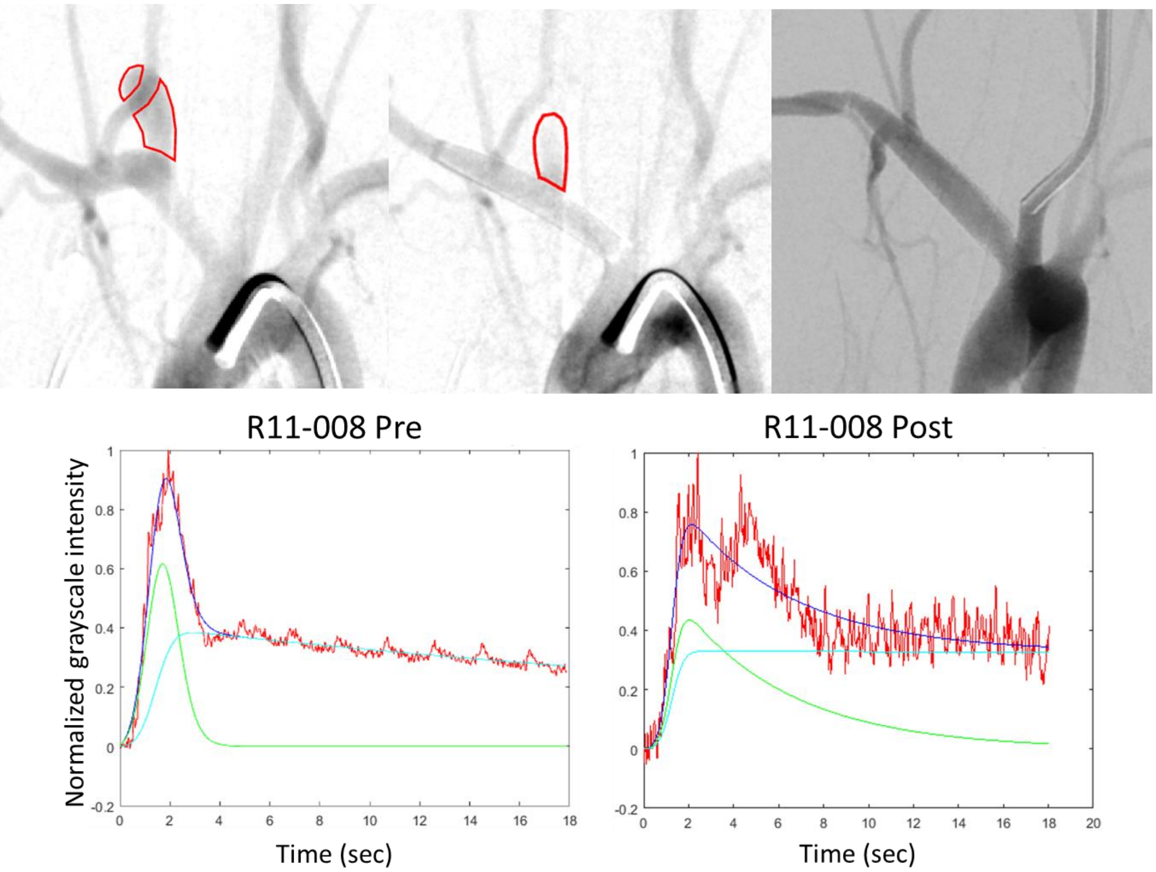

Figure 85: Angiographic image analysis and washout curve mathematical modeling for Rabbit R11-008

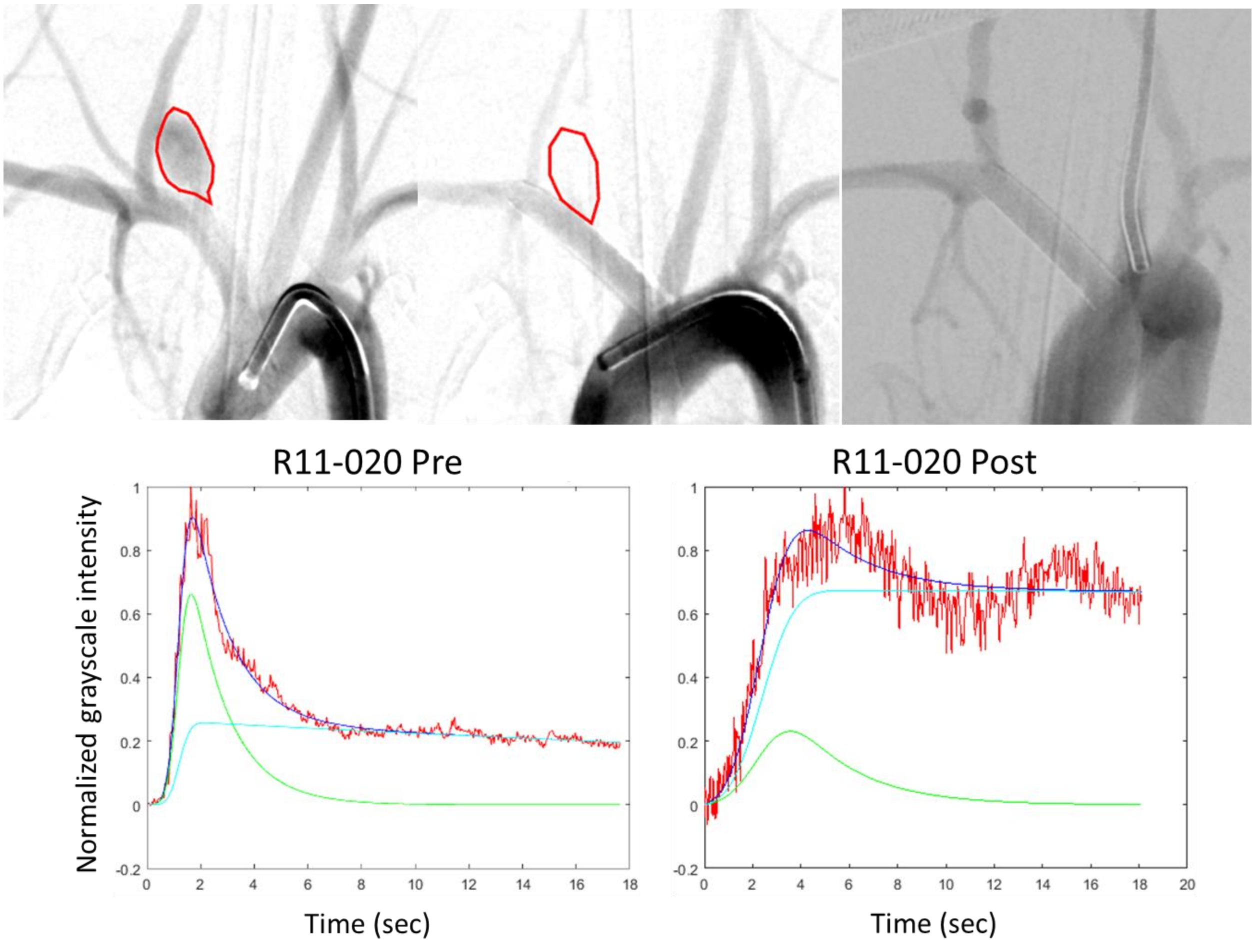

Figure 86: Angiographic image analysis and washout curve mathematical modeling for Rabbit R11-020

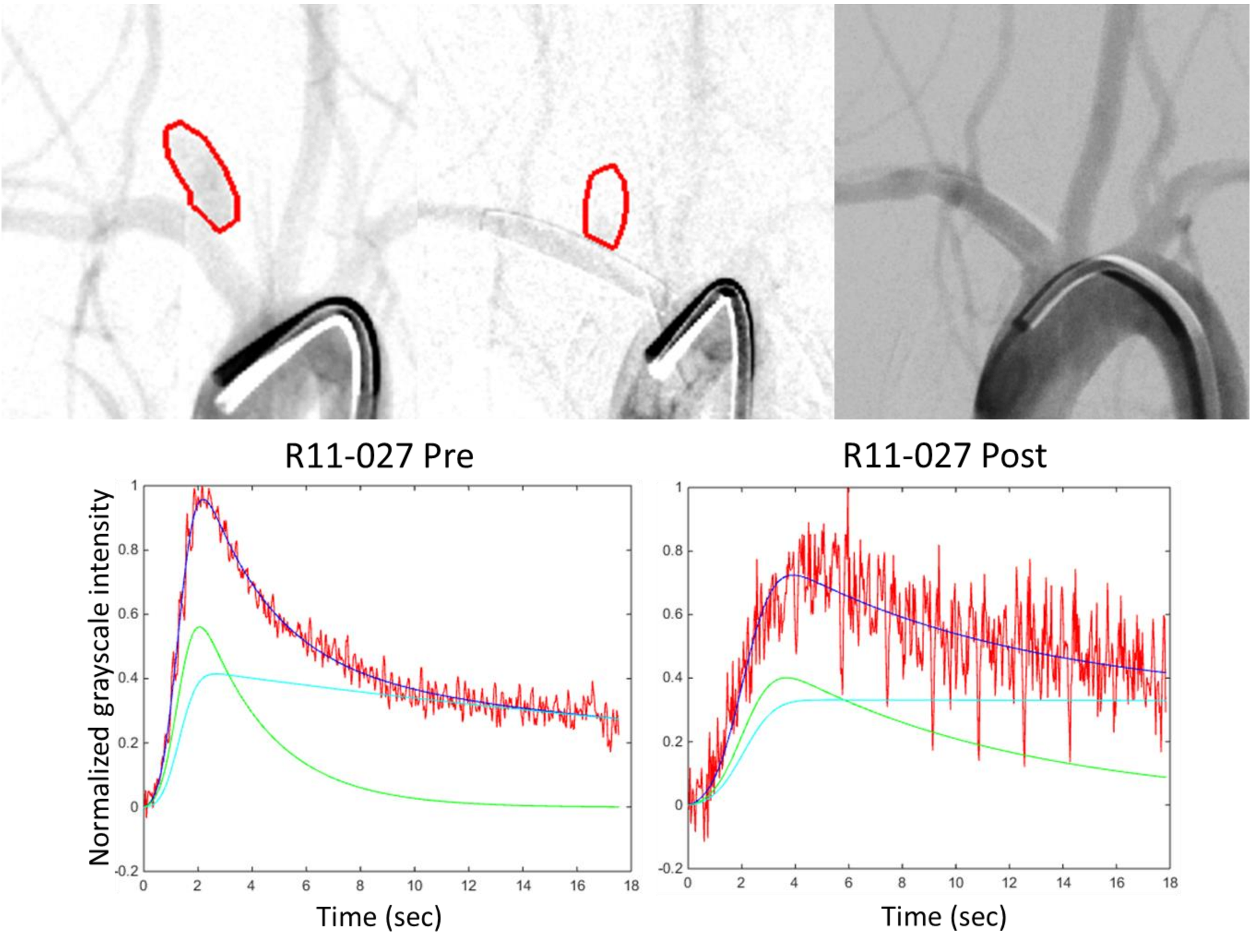

Figure 87: Angiographic image analysis and washout curve mathematical modeling for Rabbit R11-027

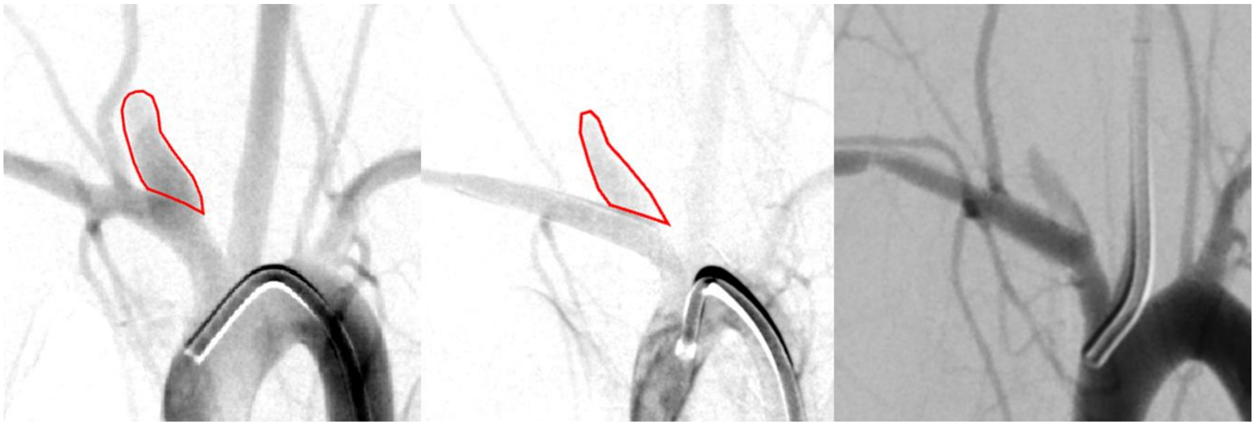

R11-028 Pre

R11-028 Post

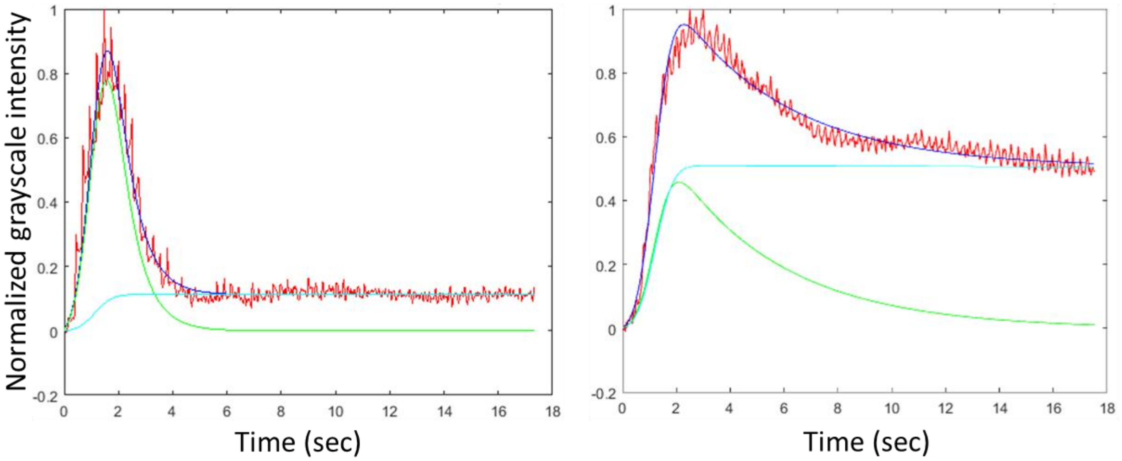

Figure 88: Angiographic image analysis and washout curve mathematical modeling for Rabbit R11-028

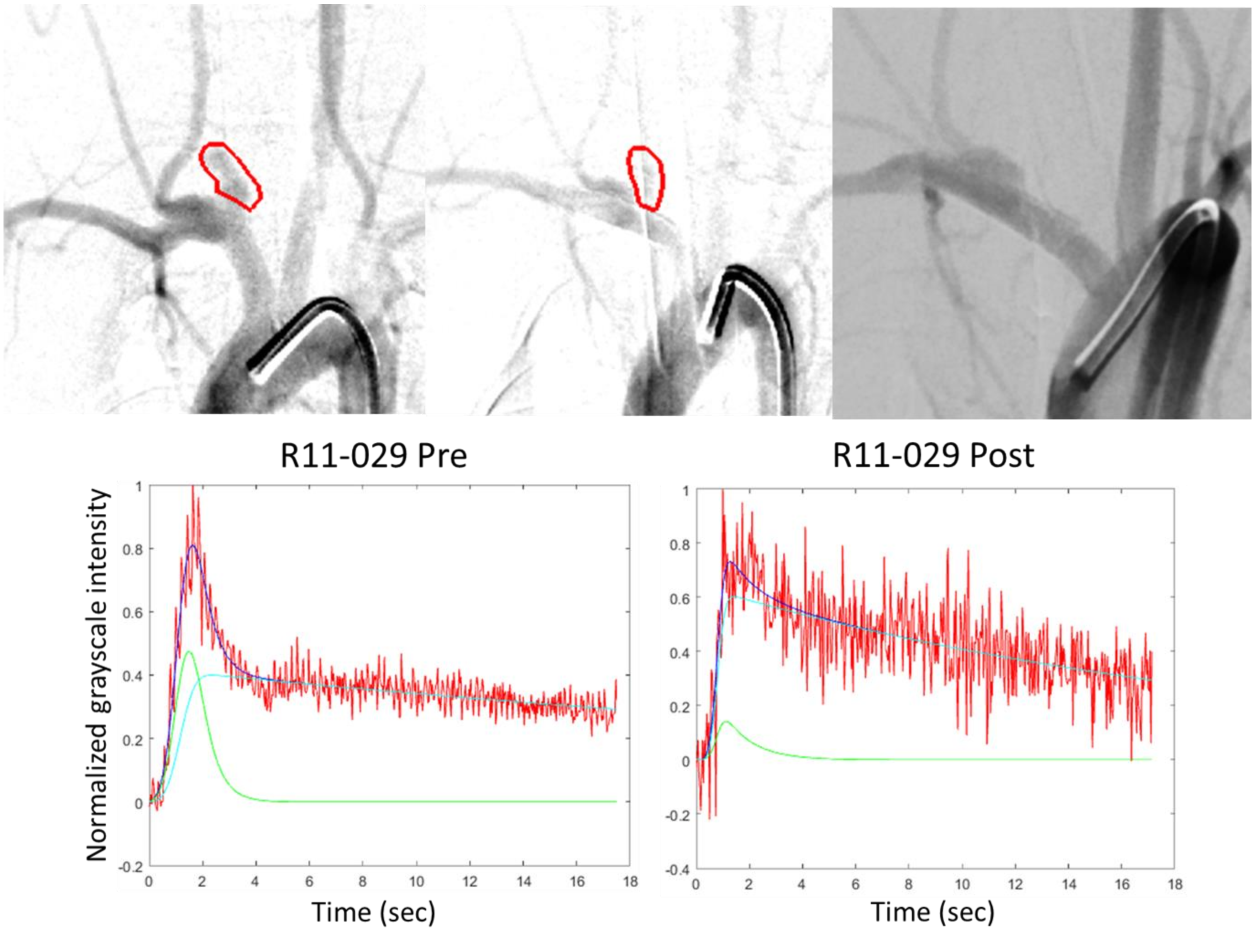

Figure 89: Angiographic image analysis and washout curve mathematical modeling for Rabbit R11-029

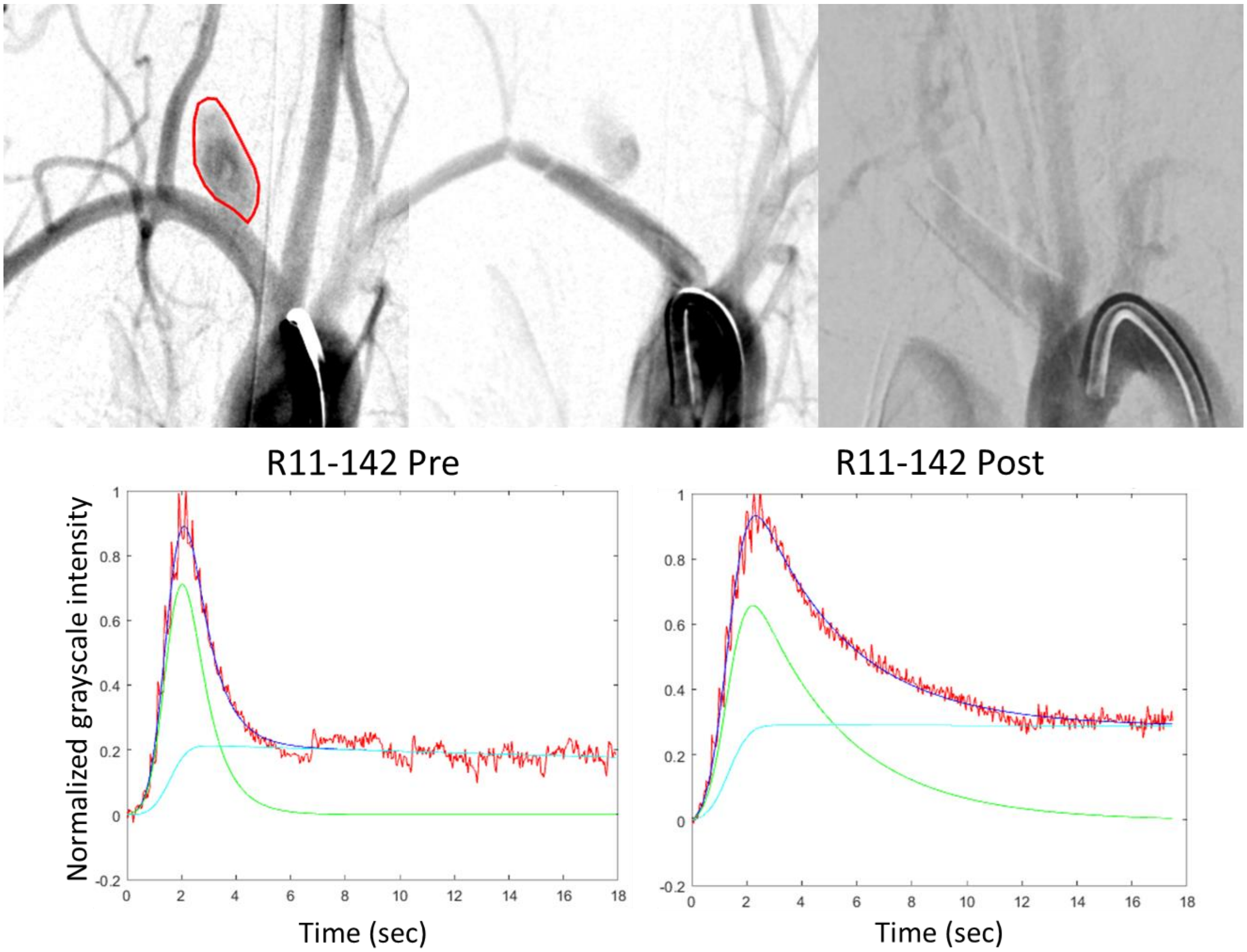

Figure 90: Angiographic image analysis and washout curve mathematical modeling for Rabbit R11-142

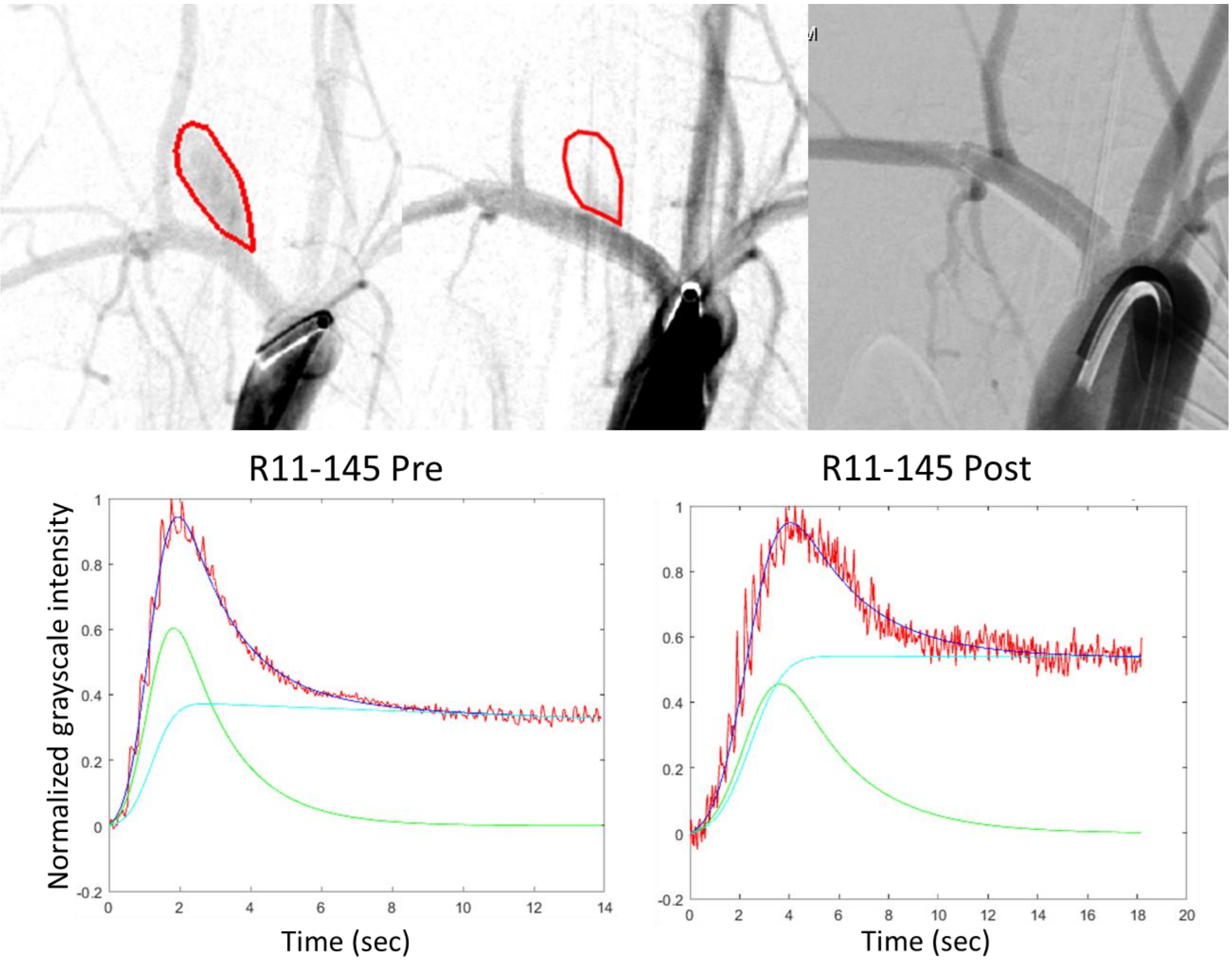

Figure 91: Angiographic image analysis and washout curve mathematical modeling for Rabbit R11-145

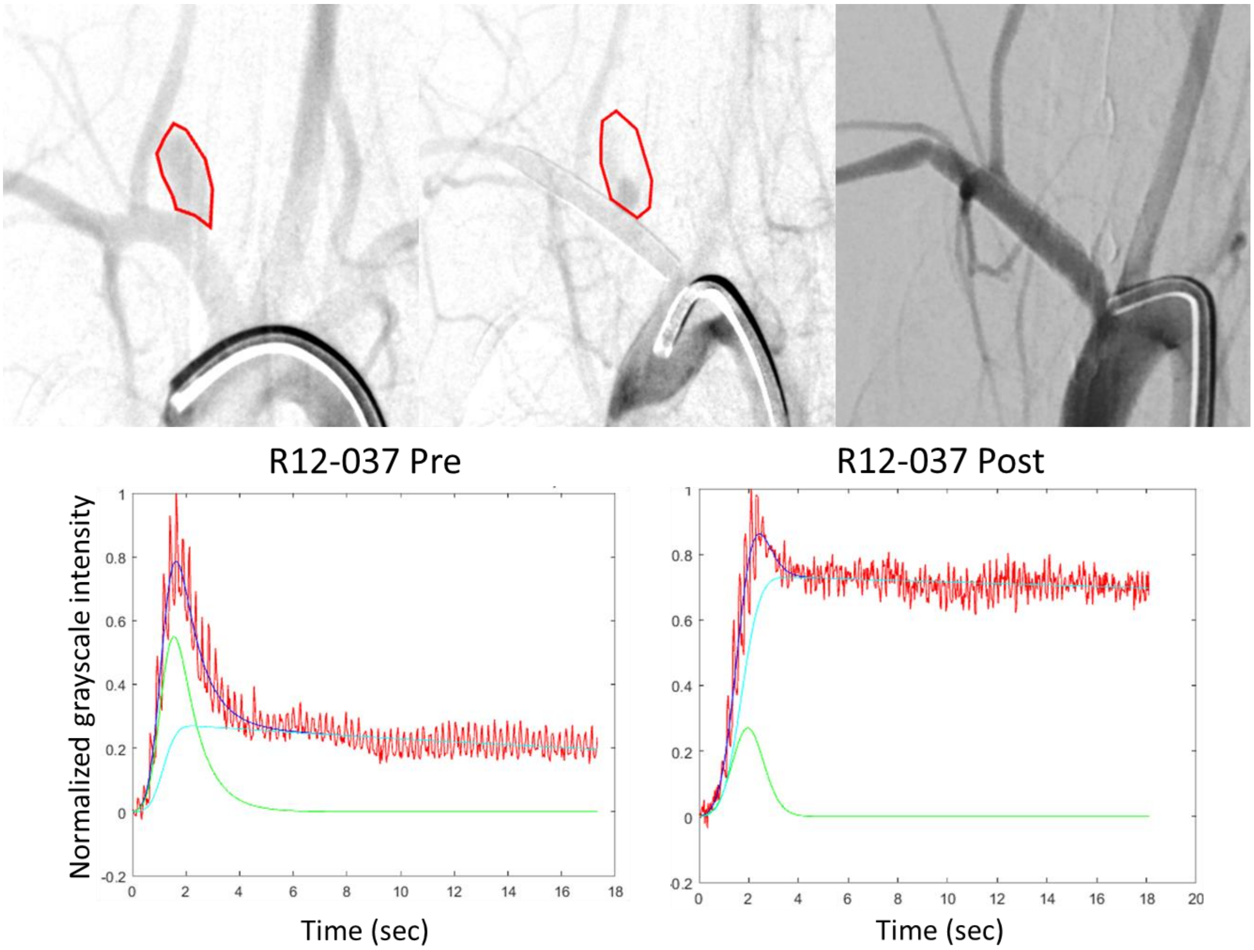

Figure 92: Angiographic image analysis and washout curve mathematical modeling for Rabbit R12-037

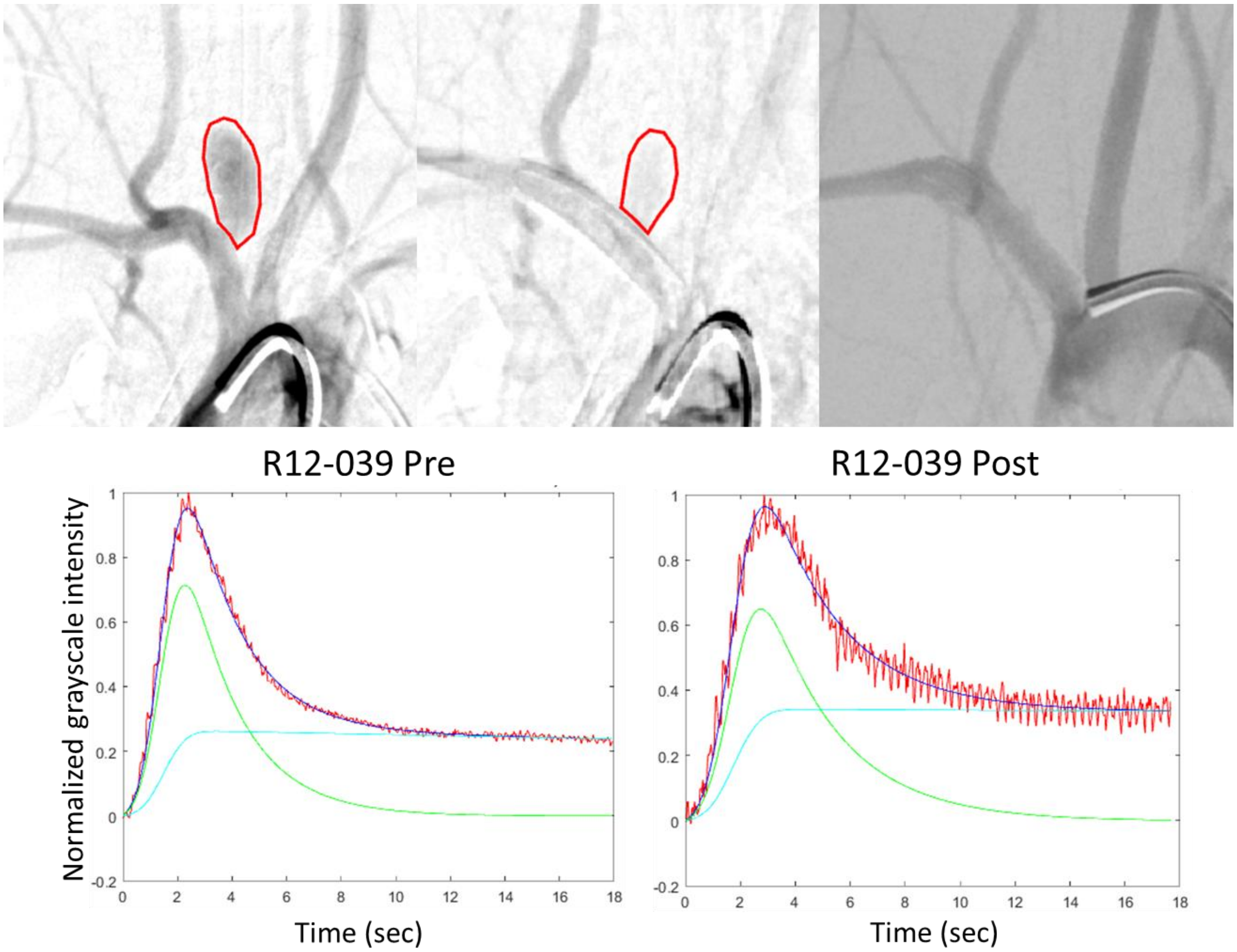

Figure 93: Angiographic image analysis and washout curve mathematical modeling for Rabbit R12-039

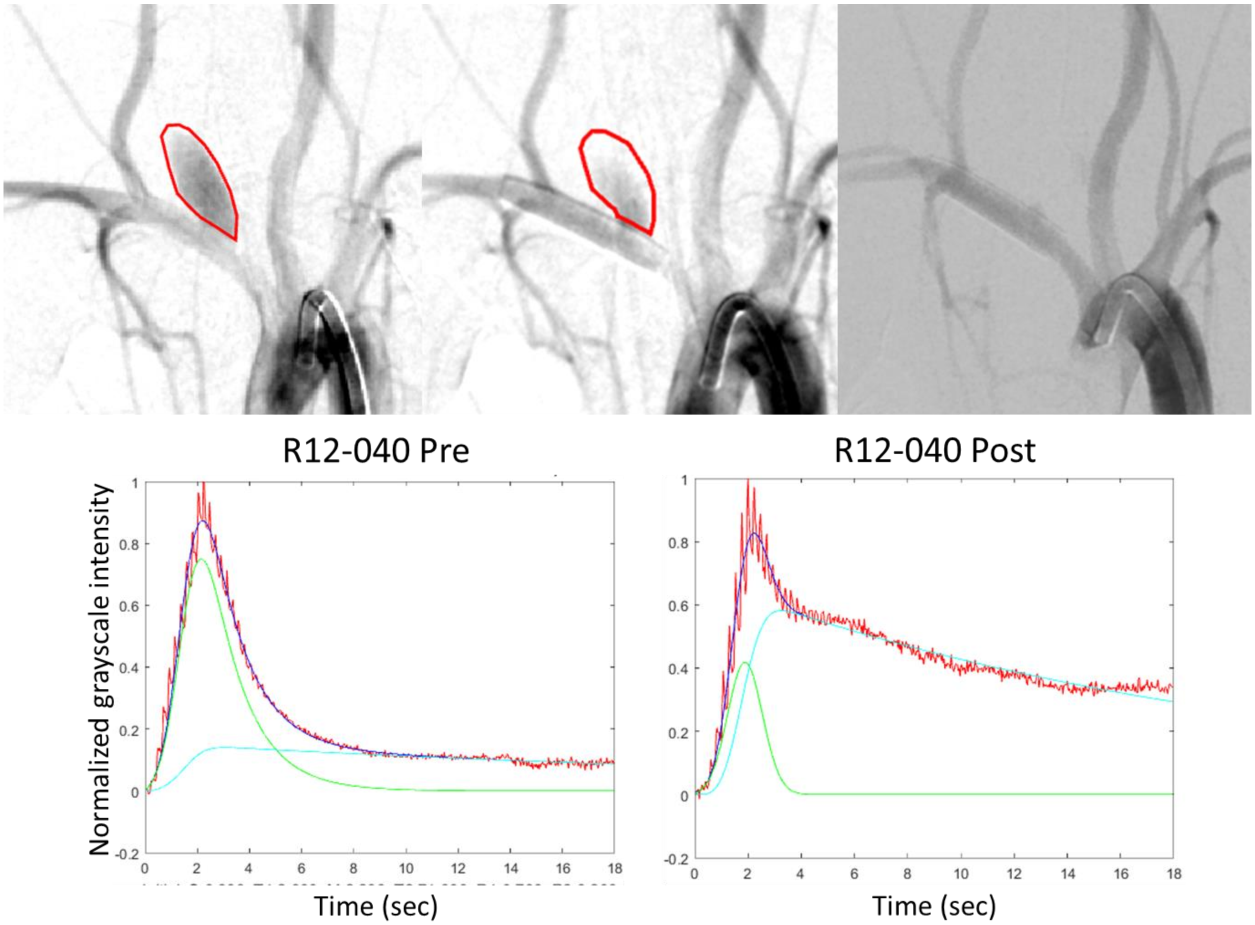

Figure 94: Angiographic image analysis and washout curve mathematical modeling for Rabbit R13-197

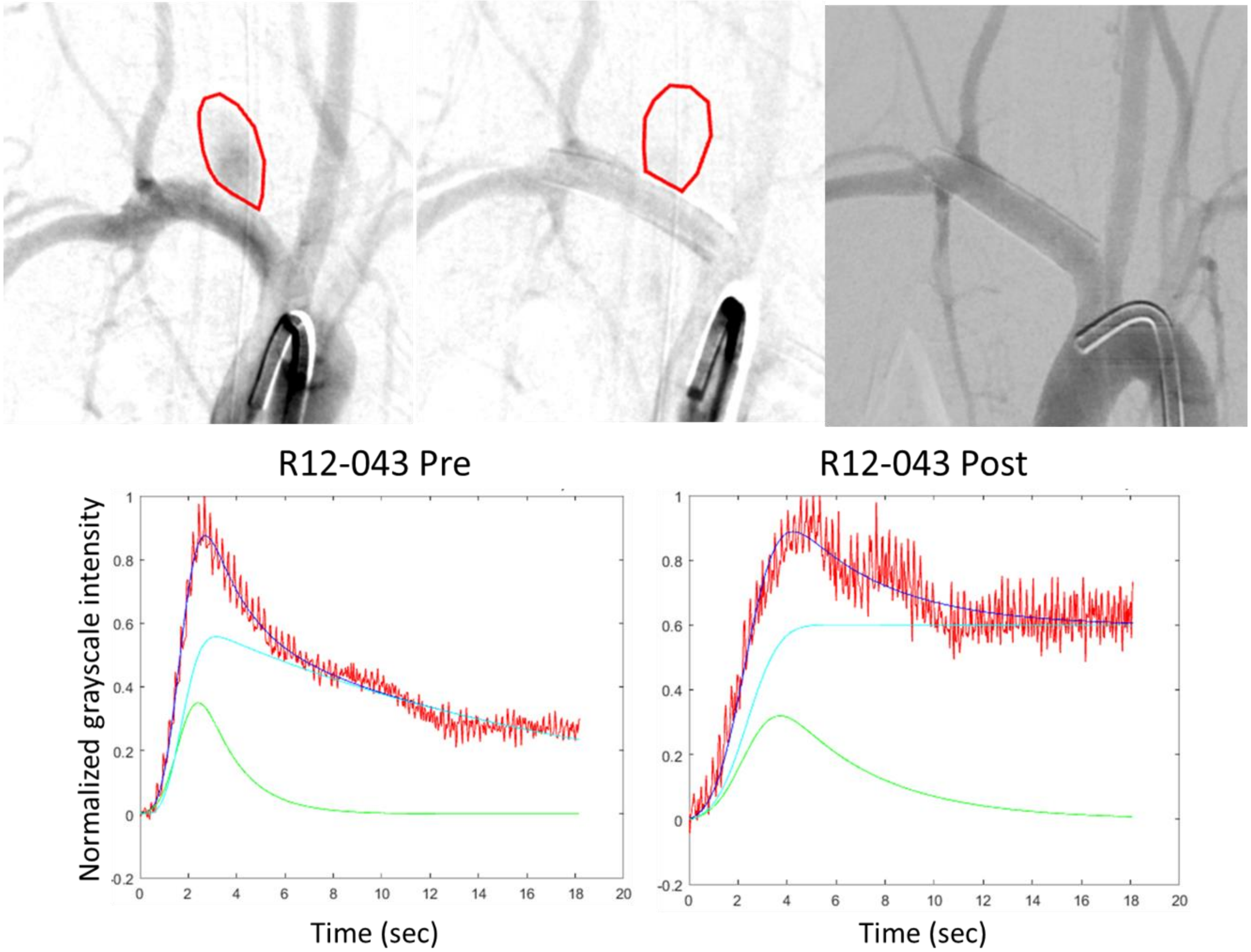

Figure 95: Angiographic image analysis and washout curve mathematical modeling for Rabbit R12-043

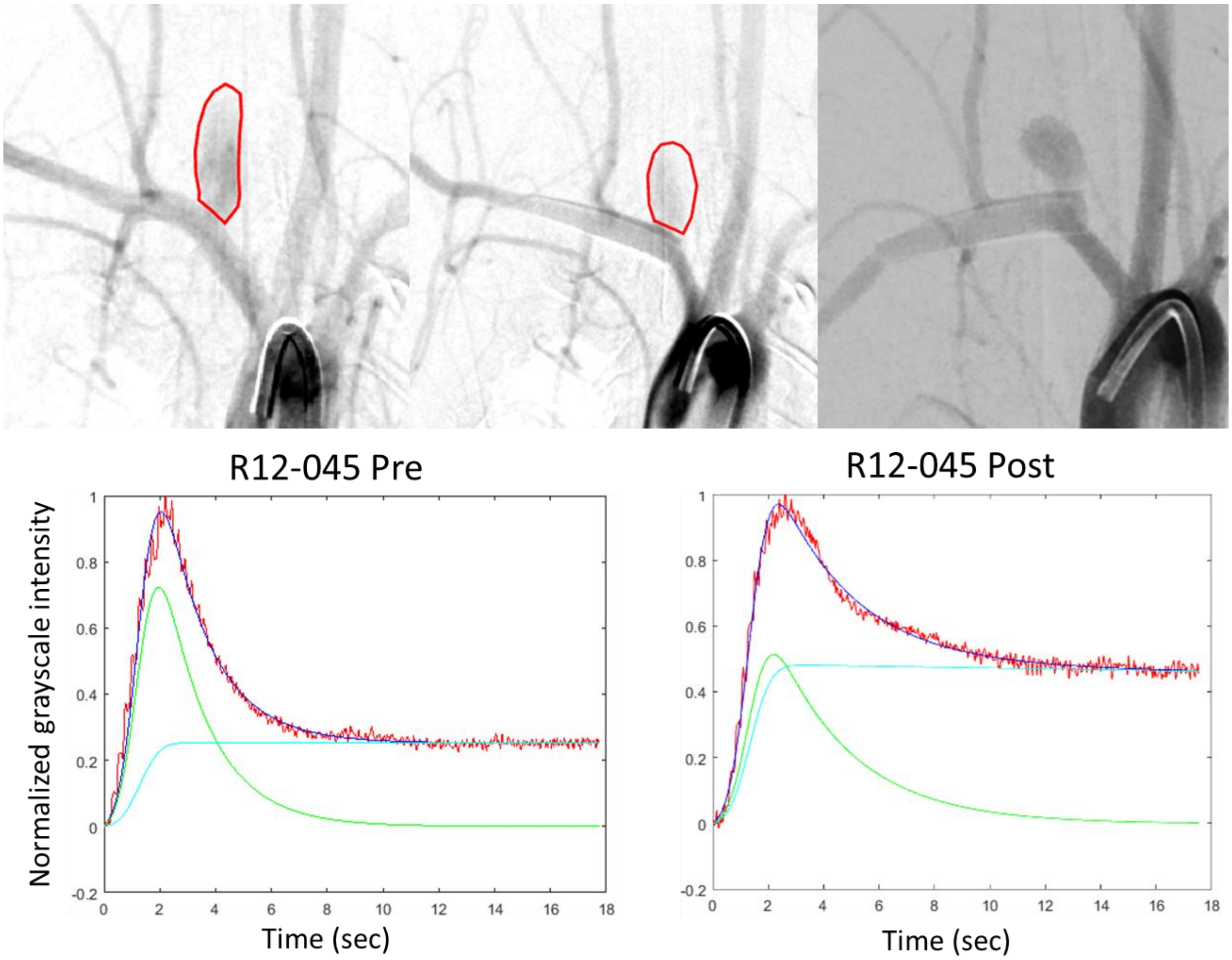

Figure 96: Angiographic image analysis and washout curve mathematical modeling for Rabbit R12-045

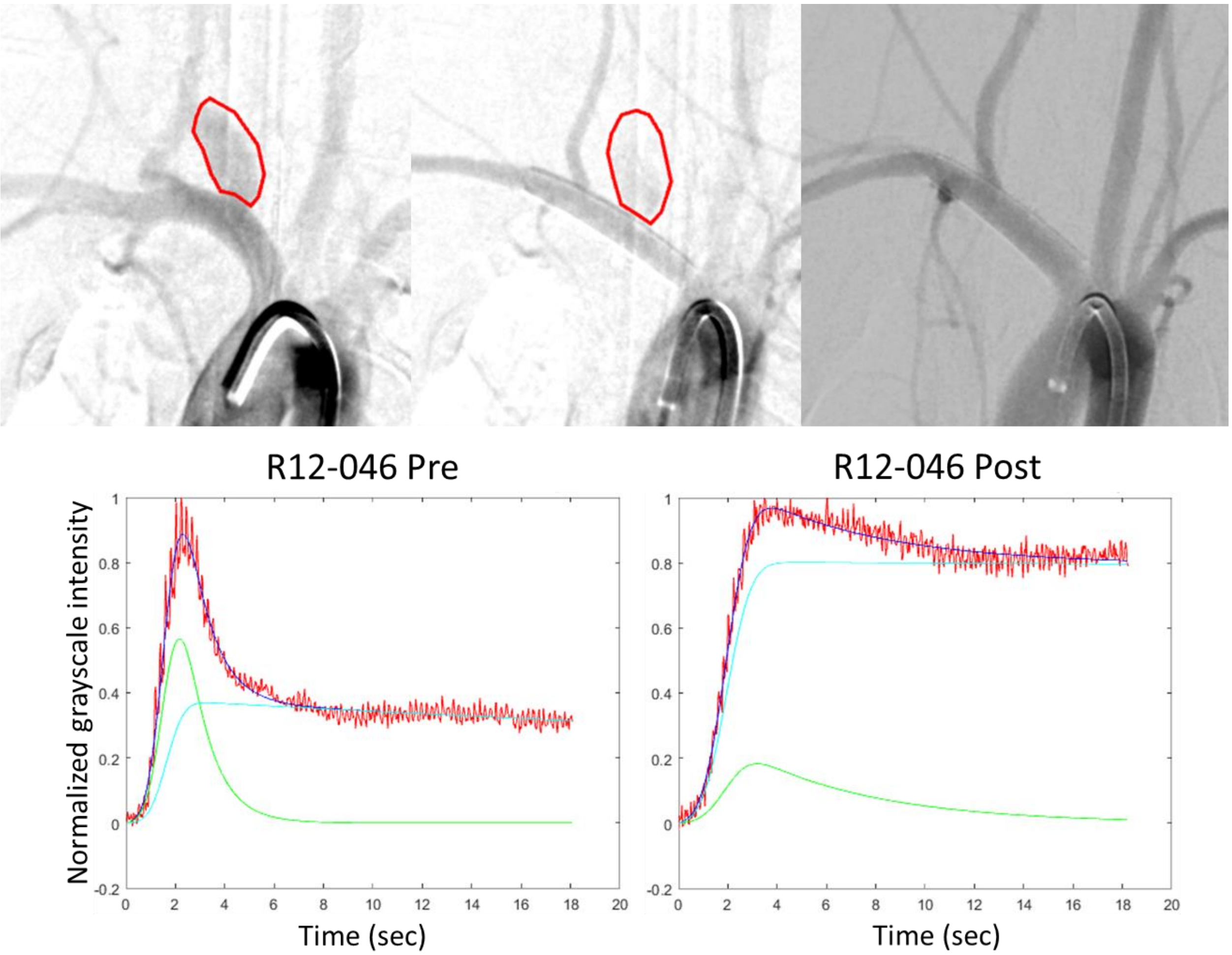

Figure 97: Angiographic image analysis and washout curve mathematical modeling for Rabbit R12-046

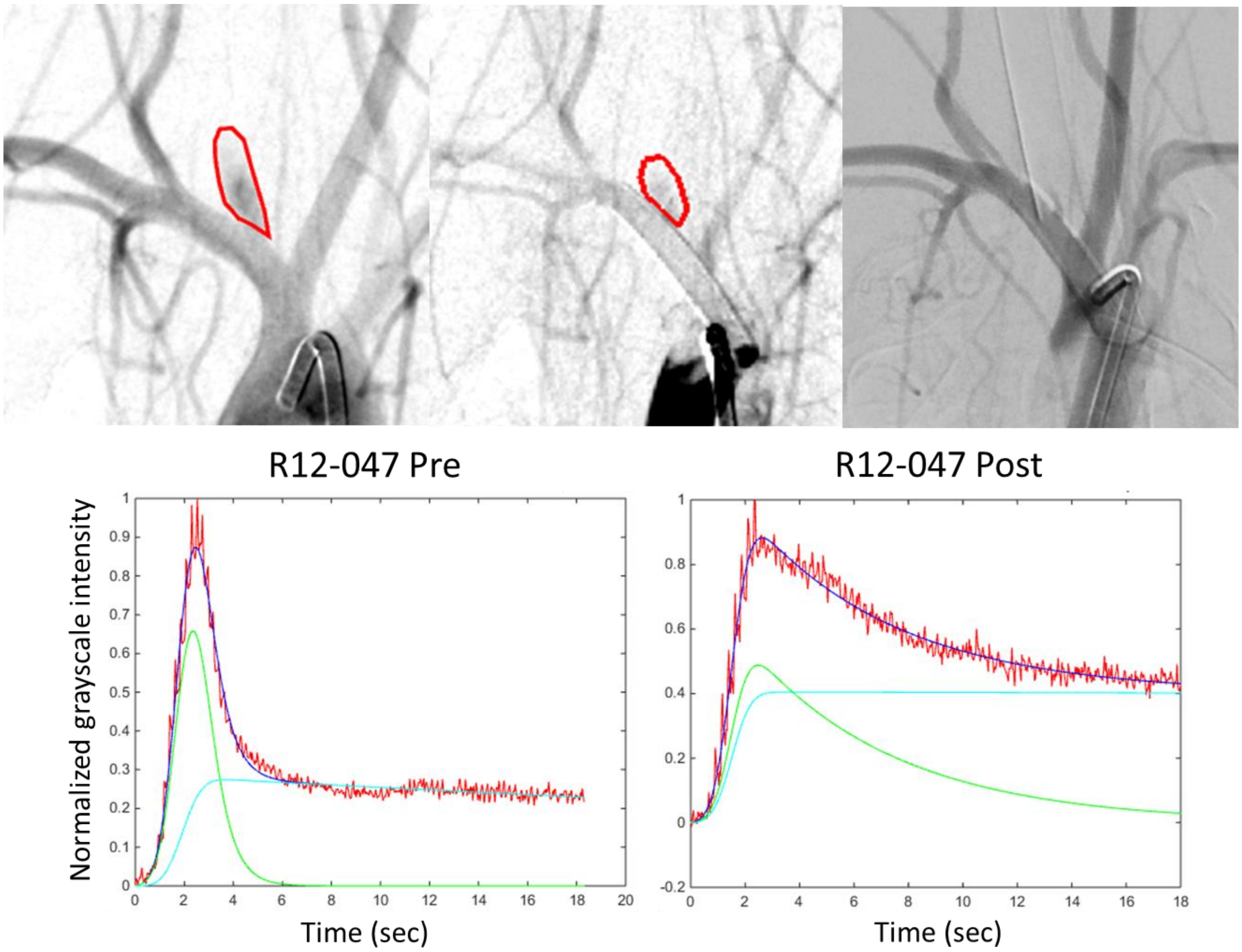

Figure 98: Angiographic image analysis and washout curve mathematical modeling for Rabbit R12-047

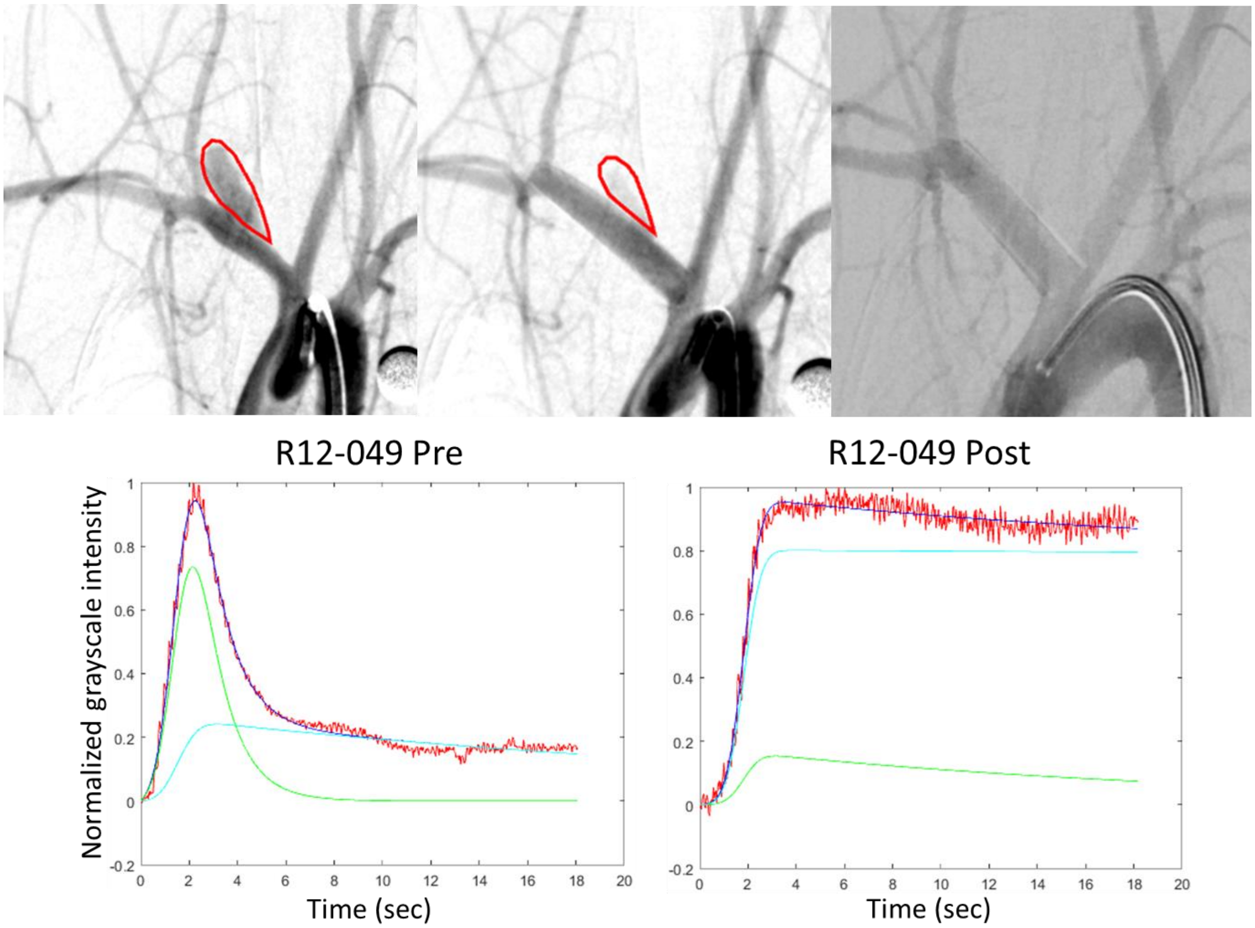

Figure 99: Angiographic image analysis and washout curve mathematical modeling for Rabbit R12-049

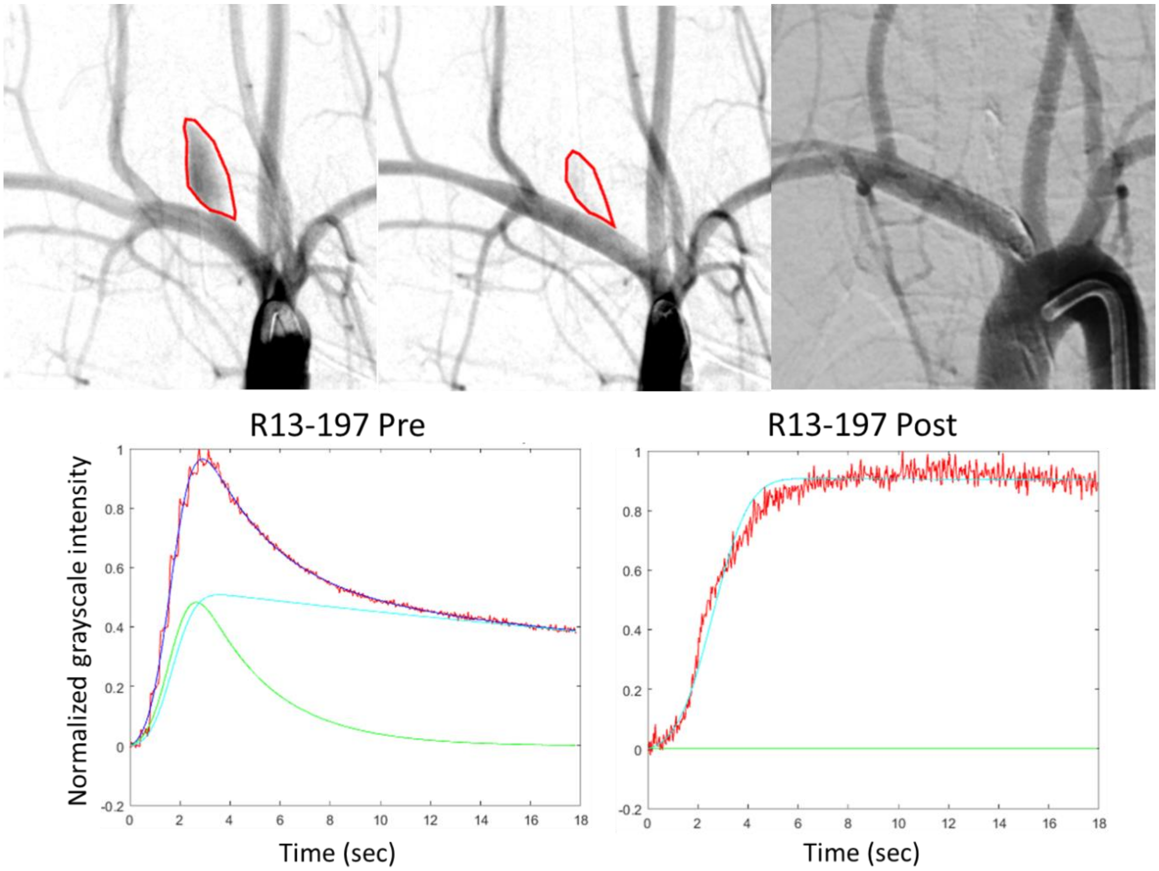

Figure 100: Angiographic image analysis and washout curve mathematical modeling for Rabbit R13-197

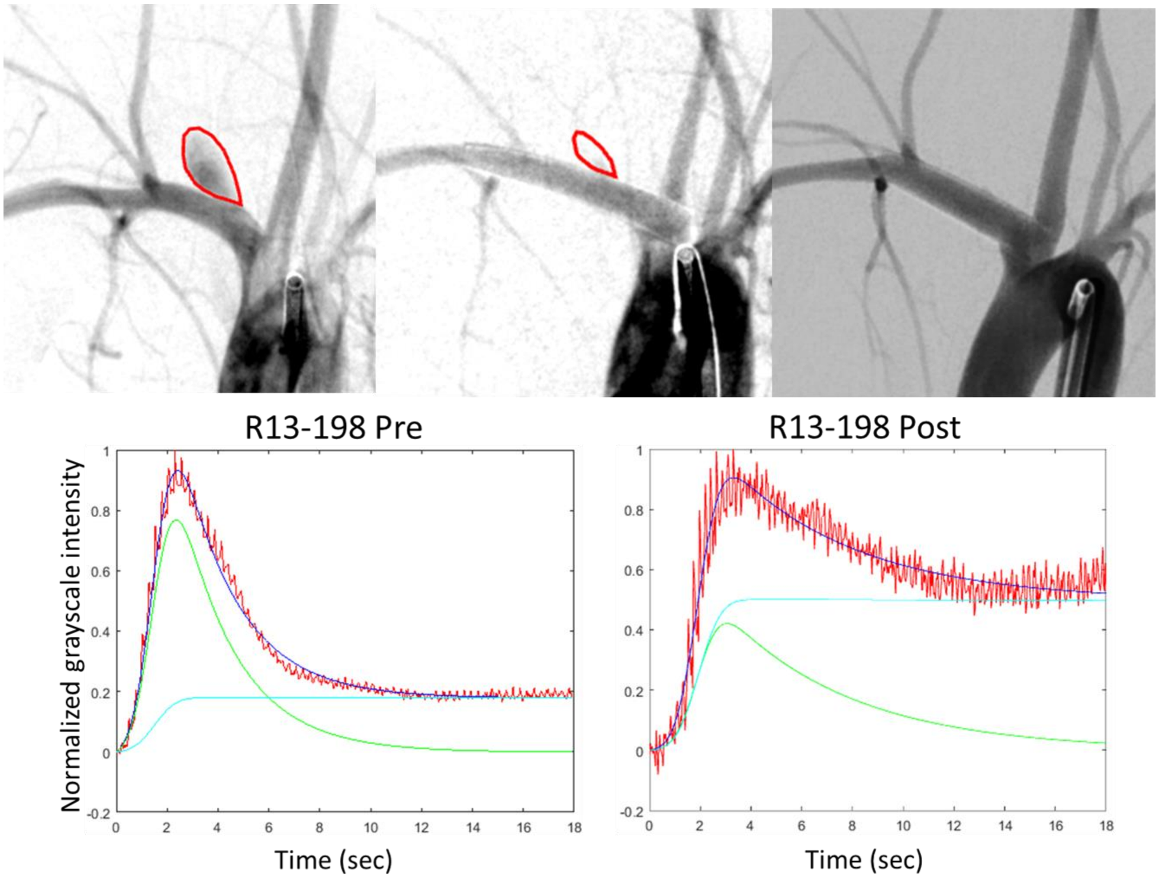

Figure 101: Angiographic image analysis and washout curve mathematical modeling for Rabbit R13-198

Appendix B: Clinical data

Patient1: Patient presented with a giant partially thrombosed mid-basilar fusiform aneurysm. The patient was enrolled for the washout study. The patient was treated with 3 Pipeline devices. At 6 month follow up the patient presented with filling of the aneurysm and was treated with additional 4.5x20 mm Pipeline device. The angiographic images of the patient at treatment, 6 month follow up, and repeat treatment are included.

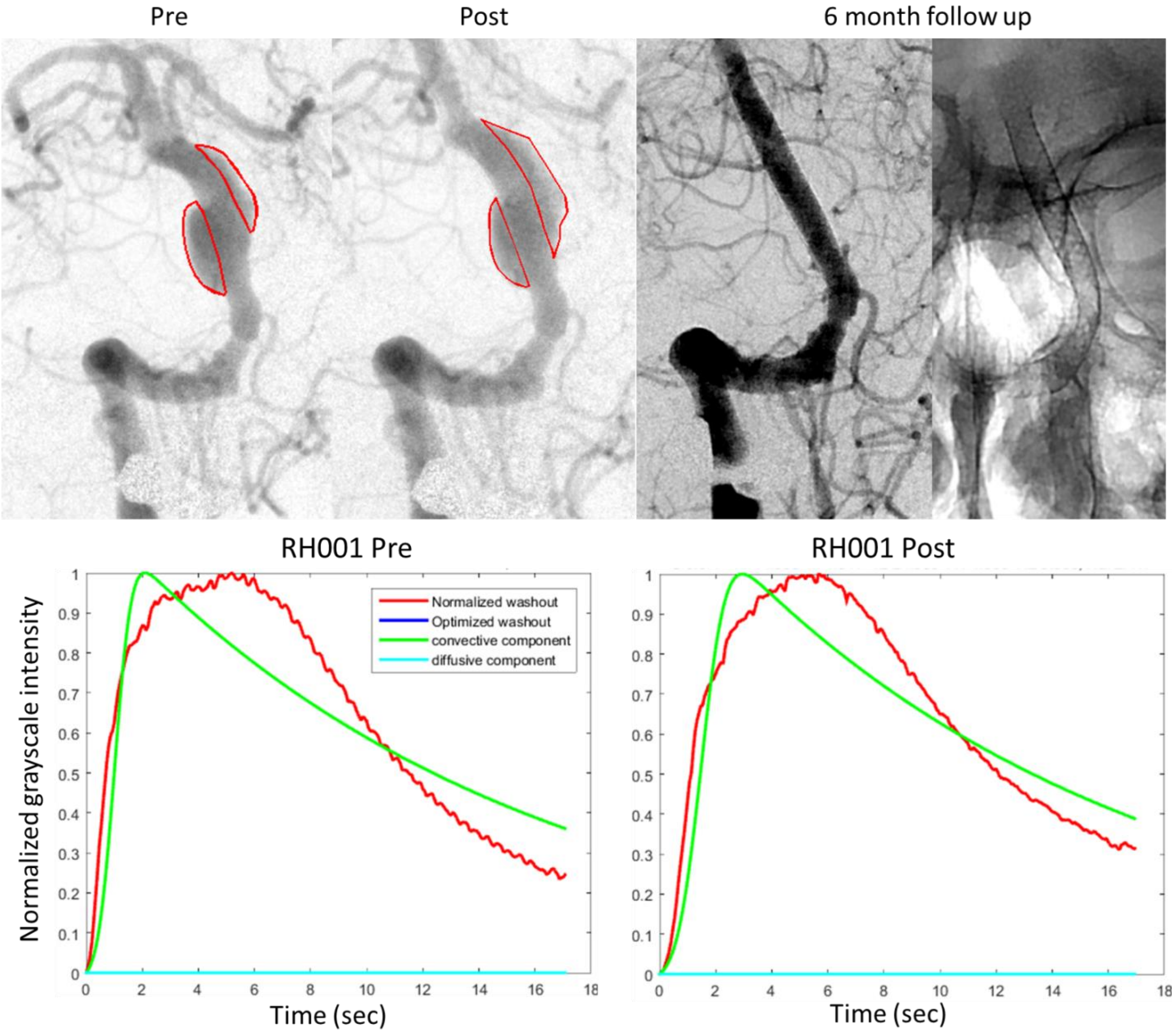

Figure 102: Angiographic image analysis and follow up data and the washout curve mathematical modeling for Patient RH001

Patient 2: Patient presented with giant cavernous RICA aneurysm. The patient underwent treatment through flow diversion through deployment of 5 Pipeline devices. At 6 month follow up the patient presented with minimal residual filling of the aneurysm from the proximal aspect of the Pipeline construct as seen in figure. The patient was then followed up at 12 months and the residual filling persisted and hence the patient was brought in for repeat aneurysm treatment done through deployment of 3 additional Pipeline devices telescoping inside the proximal aspect of the previous construct: PED1-5x20m, PED2-5x12 mm, PED3-5x16mm. A follow up at 6 months from this repeat treatment procedure demonstrated again the persistent minimal residual filling from the proximal aspect and a third treatment procedure was conducted through deployment of 2 PEDs: PED1-5x20mm, PED2-5x20mm. At the next 6 month follow up the patient demonstrated minimal residual filling from approximately the spot. The patient has in all 10 Pipeline devices deployed to embolize and occlude the giant cavernous RICA aneurysm.

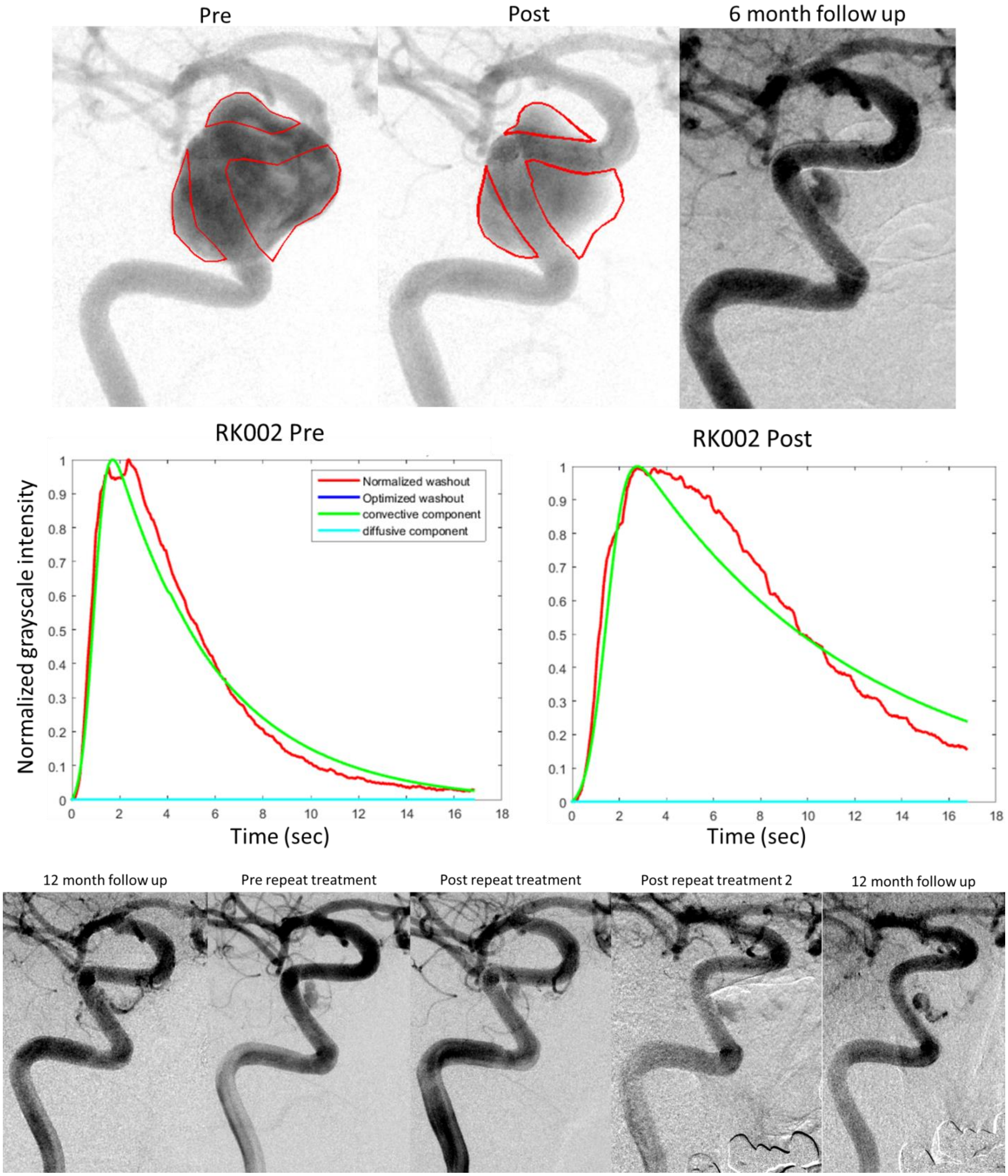

Figure 103: Angiographic image analysis (top) and follow up data (bottom) and the washout curve mathematical modeling (center) for Patient RK002

Patient 3 LP004: 51 year old female patient with left ophthalmic segment ICA aneurysm was treated with 3 Pipeline devices. Follow up at 6 month recorded complete occlusion of the aneurysm as seen in the angiogram.

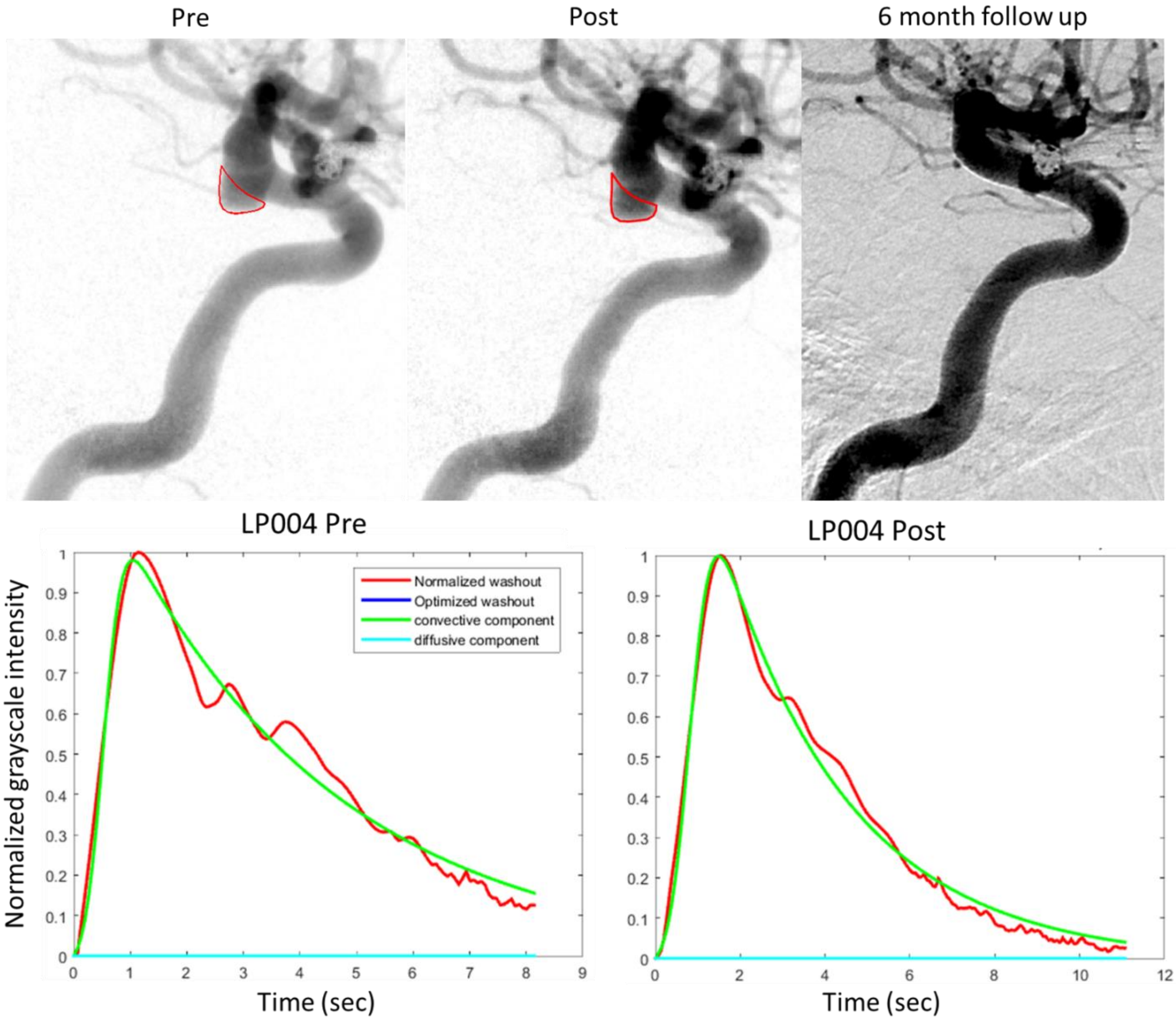

Figure 104: Angiographic image analysis and follow up data (top) and the washout curve mathematical modeling (bottom) for Patient LP004

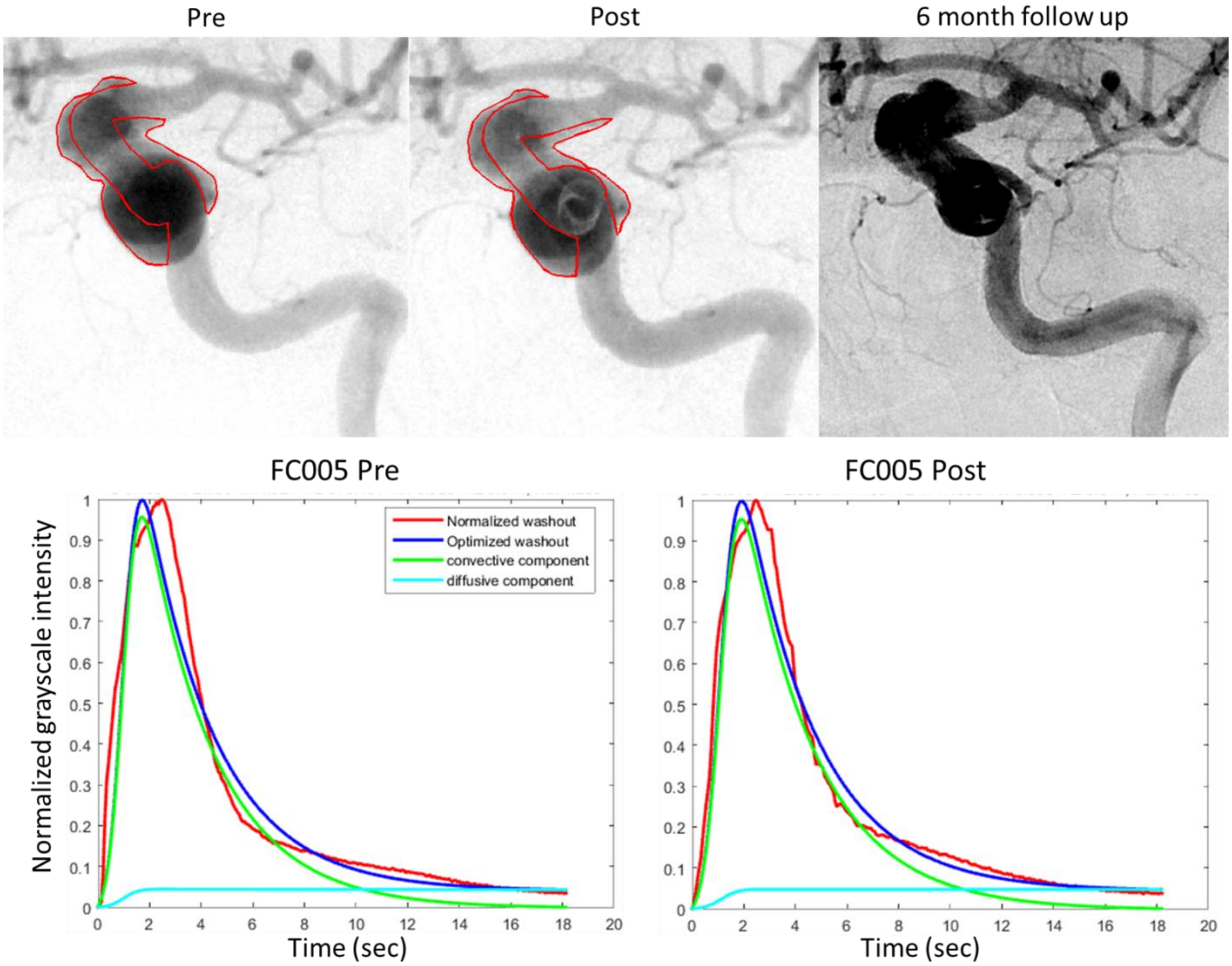

Figure 105: Angiographic image analysis and follow up data (top) and the washout curve mathematical modeling (bottom) for Patient FC005

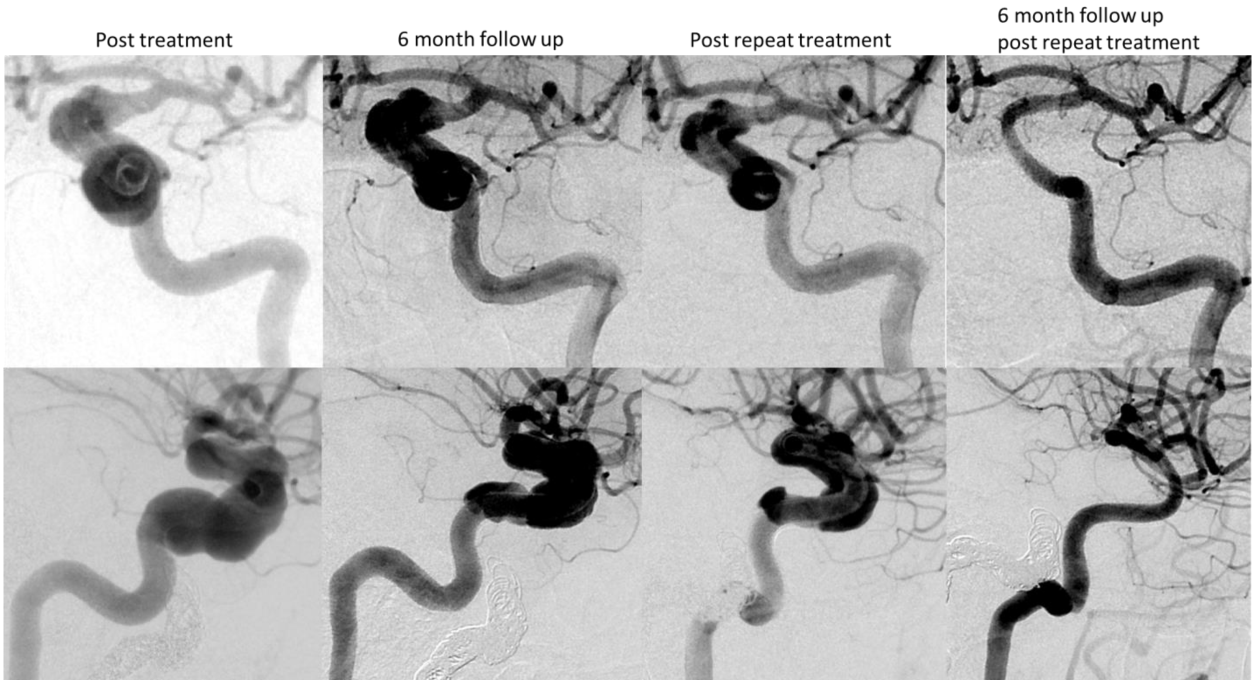

Figure 106: Follow up data for Patient FC005 in biplane A(top) and biplane B(bottom)

Patient 4 FC005: 52 year old female patient presented with giant bilateral cavernous internal carotid artery aneurysms. The RICA cavernous region aneurysm was treated by coiling the internal carotid artery and sacrificing the RICA. The giant LICA fusiform cavernous aneurysm measured longest at 9.6 cm and supraclinoid segment of 3.5 cm. The patient was treated through deployment of 7 Pipeline devices (specifications in table). The aneurysm was persistently filling at 6 months with some reduction in size. Retreatment of the giant cavernous fusiform LICA aneurysm was conducted through implantation of another 7 PEDs to create a denser construct and reduce flow inside the aneurysm. At 6 months following repeat treatment (12 month to original treatment date), the aneurysm was completely occluded. Angiographic snapshots from biplane A(antero-posterior) and biplane B(lateral) views are included to demonstrate the shape and size of the aneurysm.

Patient 5 LC006: Patient with left ICA terminus aneurysm was treated with 1 Pipeline device. Complete occlusion of the aneurysm as seen in the angiogram was recorded at 6 month follow up to treatment.

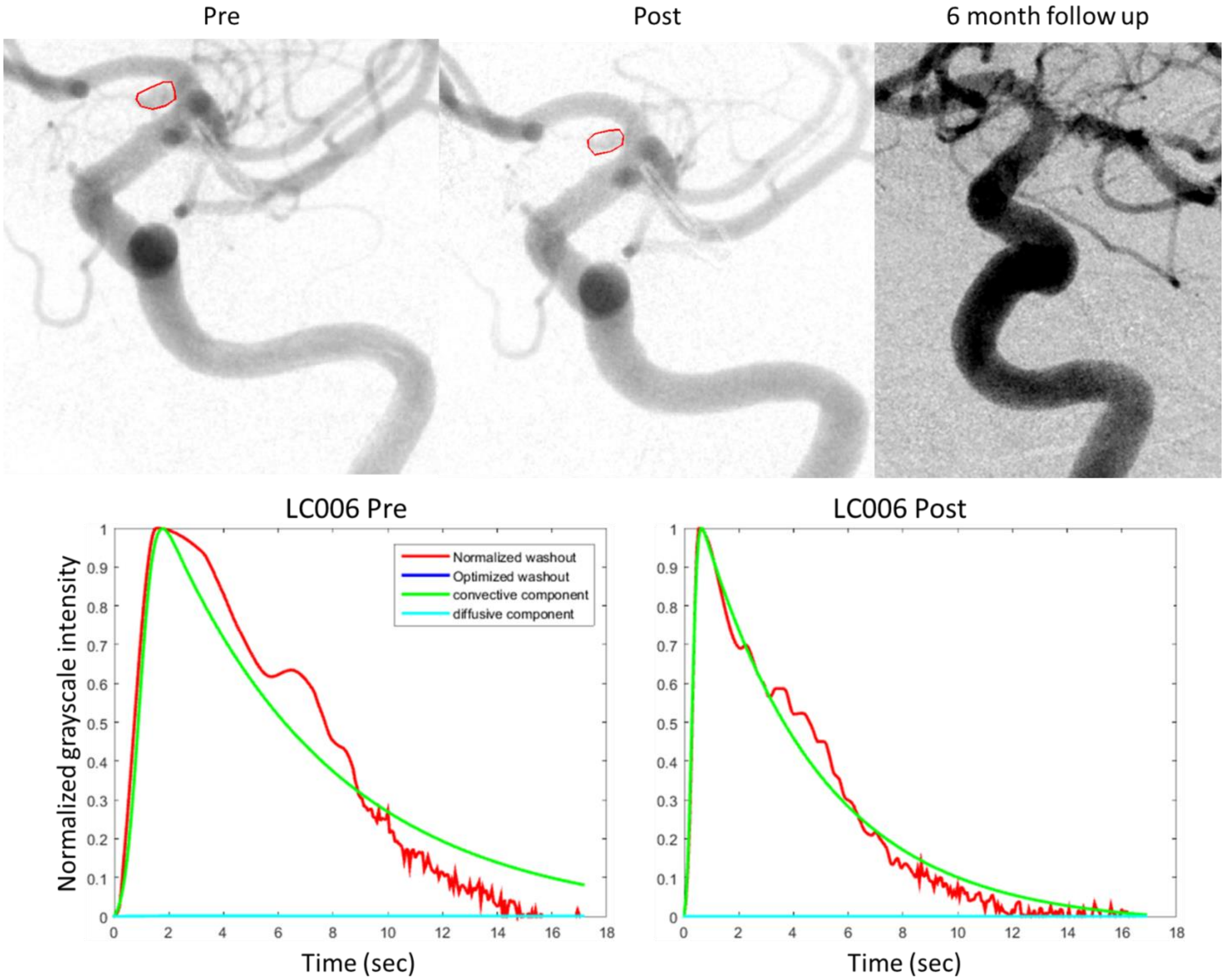

Figure 107: Angiographic image analysis and follow up data (top) and the washout curve mathematical modeling (bottom) for Patient LC006

Patient 6 RH008: Patient with left ophthalmic segment internal carotid artery aneurysm was treated through deployment of 3 Pipeline devices. Follow up to treatment at 6 months demonstrated complete occlusion of the aneurysm as seen in the angiogram

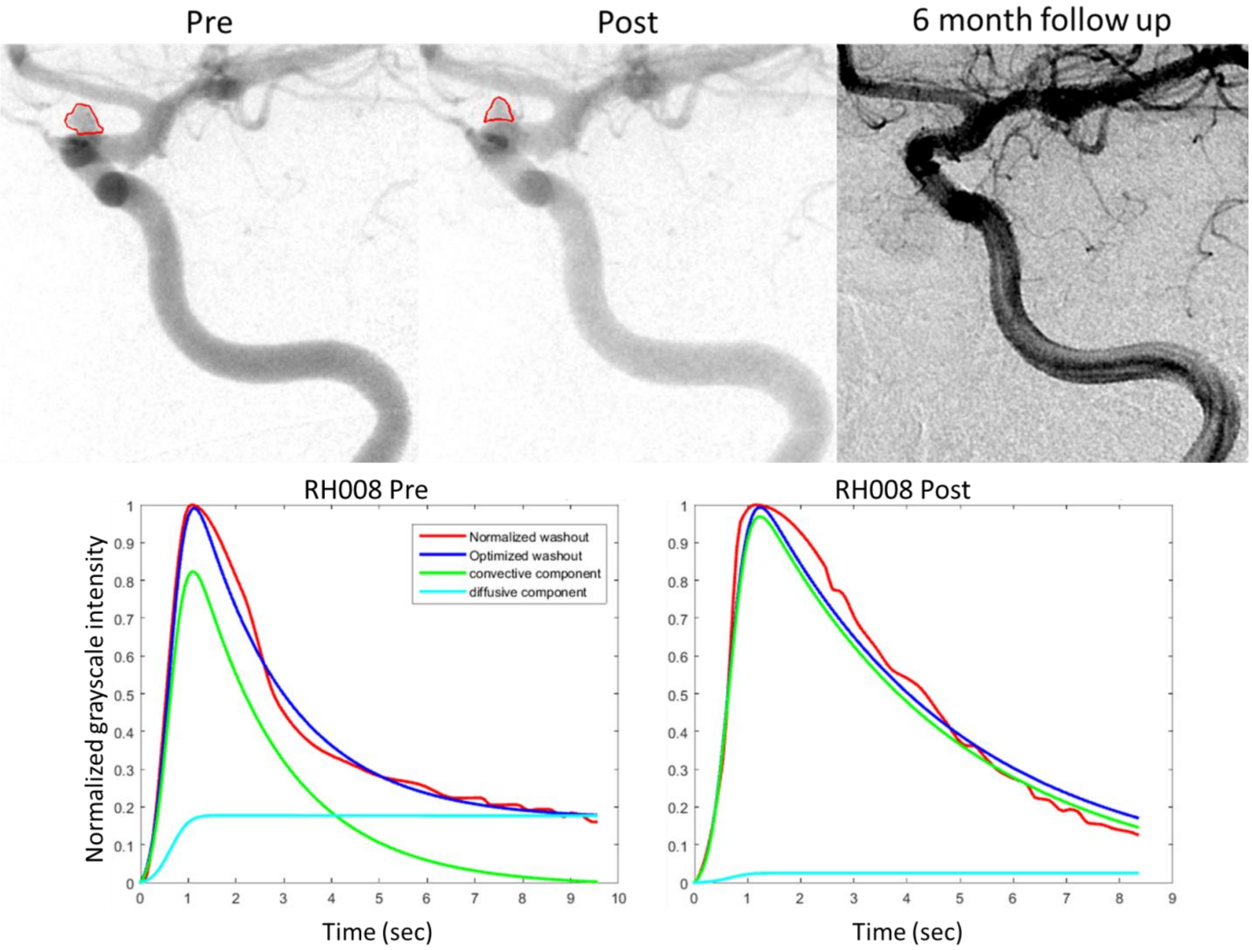

Figure 108: Angiographic image analysis and follow up data (top) and the washout curve mathematical modeling (bottom) for Patient RH008

Patient 7 AA010: 47 year old male patient with a large fusiform left vertebral artery aneurysm was treated through deployment of 4 Pipeline devices to create a parent vessel construct. Complete occlusion of the fusiform aneurysm was recorded at 6 month follow up to treatment.

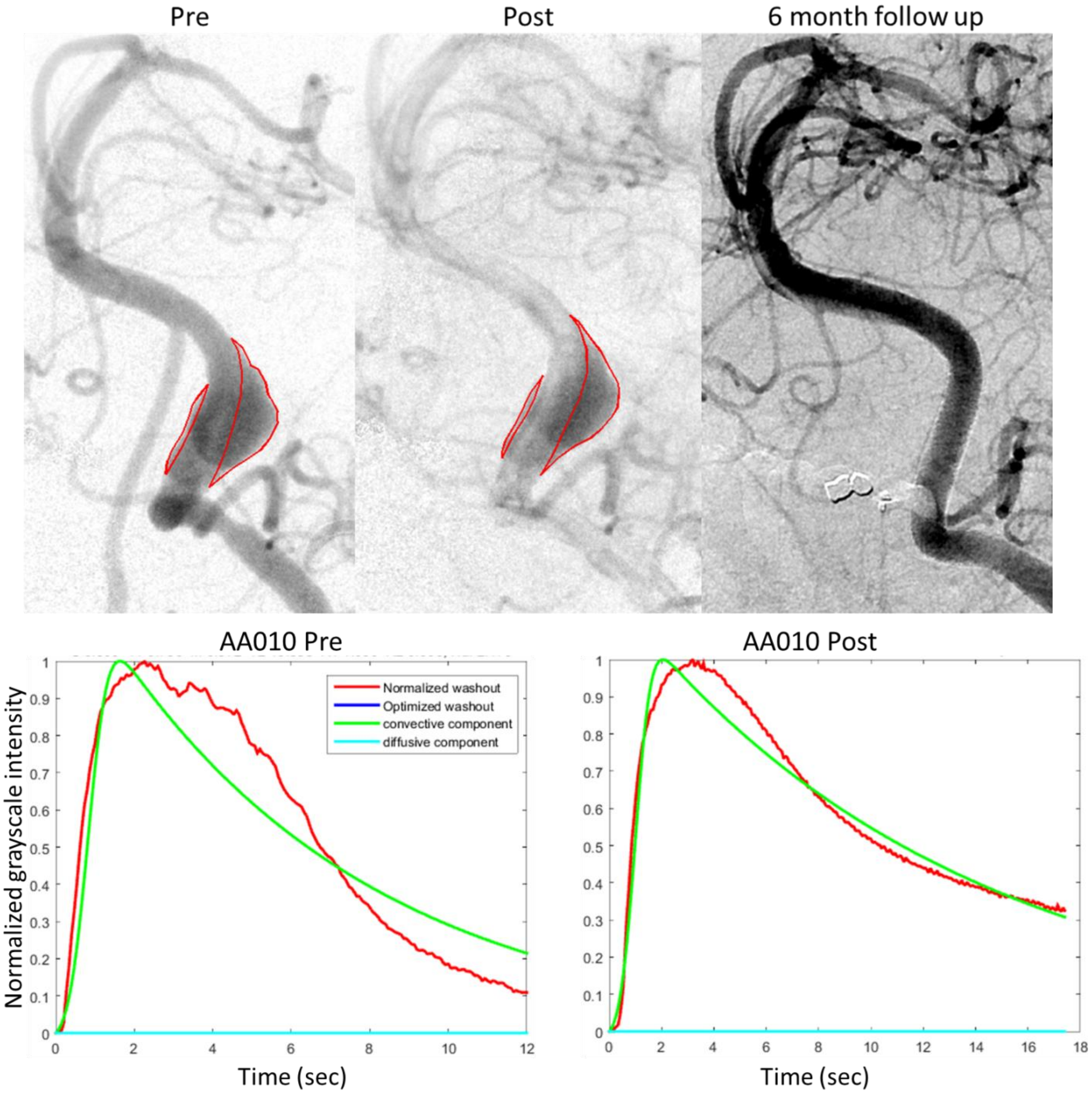

Figure 109: Angiographic image analysis and follow up data (top) and the washout curve mathematical modeling (bottom) for Patient AA010

Patient 8 EAM011: Patient with aneurysm in the posterior communicating artery (PCOM) segment of left ICA was treated through deployment of 3 Pipeline devices across the aneurysm. Residual filling of the aneurysm was recorded at 6 month follow up angiogram upon which the

Plavix regimen for the patient was modified and aneurysm occlusion was confirmed through MRA done 75 days from procedure.

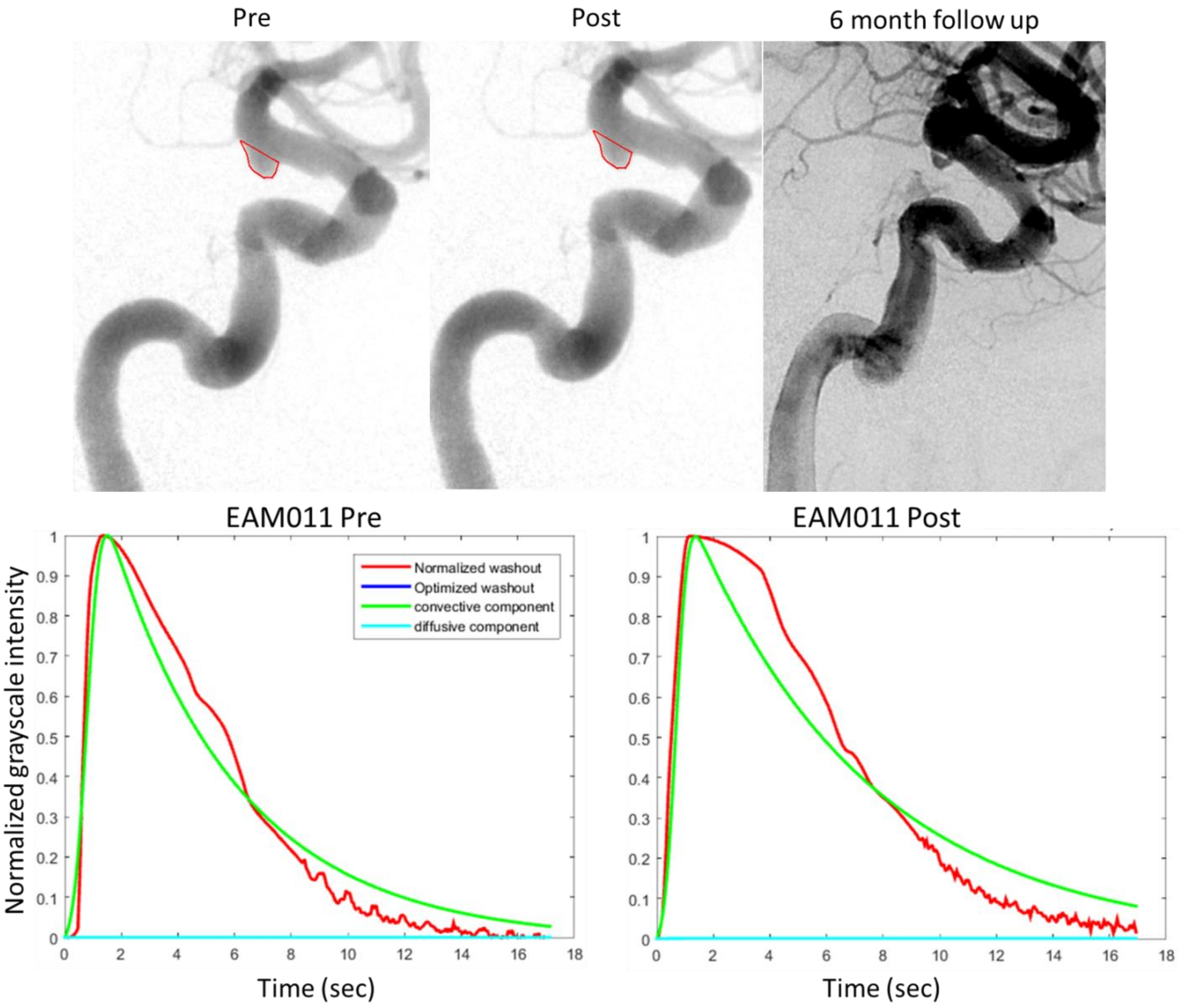

Figure 110: Angiographic image analysis and follow up data (top) and the washout curve mathematical modeling (bottom) for Patient EAM011

Patient 9 DT012: 17 year old male patient with giant bilateral cavernous region fusiform ICA aneurysms with a multi systemic smooth muscle dysfunction syndrome was treated for the right

ICA aneurysm through deployment of 12 Pipeline devices to create a construct for remodeling of parent artery. The aneurysm measured more than 4 cm long from the cavernous to petrous segments. Segmented angiograms marking ROI are demonstrated long with the 12 Pipeline construct. The patient did not return for 6 month follow up angiogram.

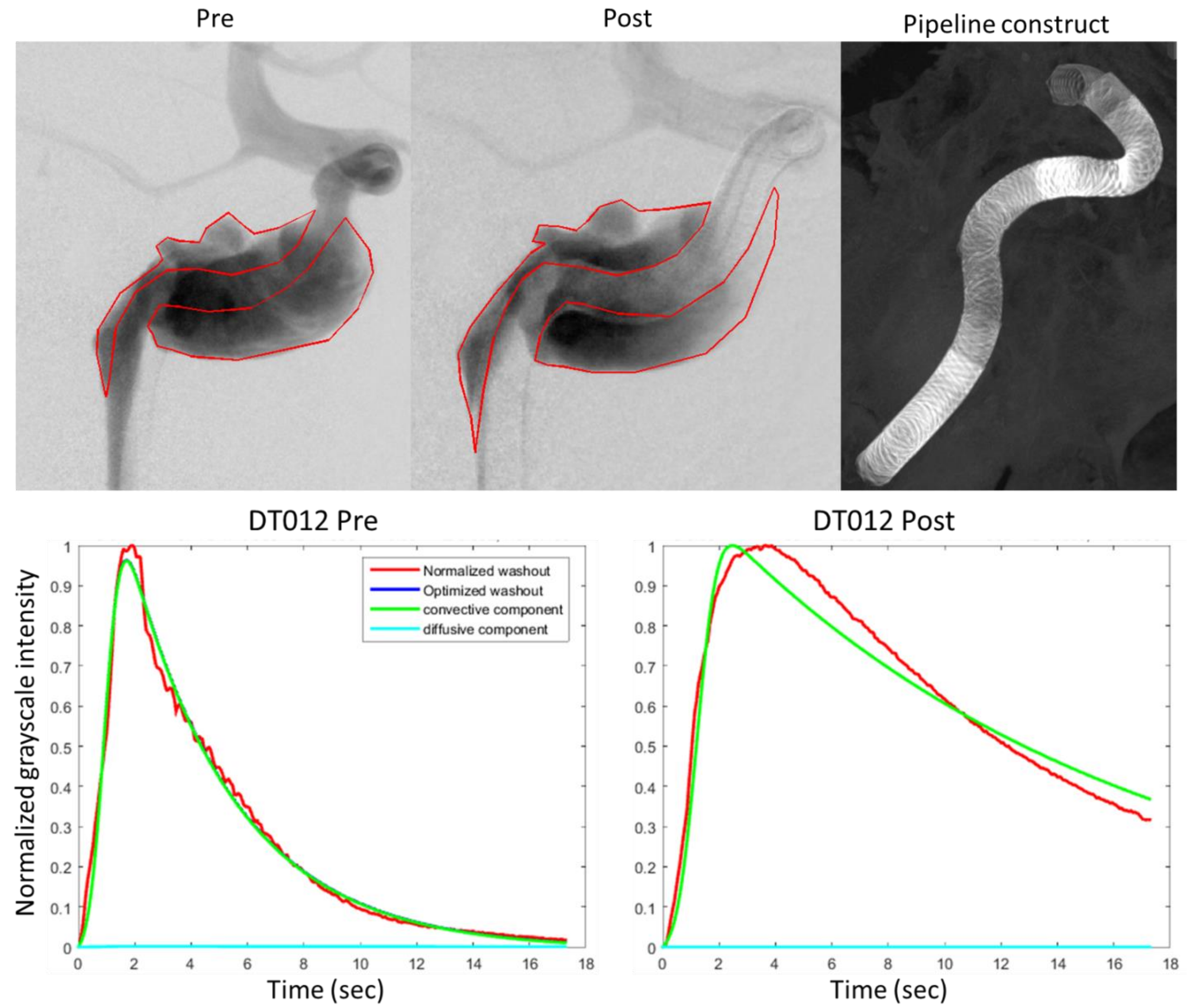

Figure 111: Angiographic image analysis (top) and the washout curve mathematical modeling (bottom) for Patient DT012 (excluded from study because no follow up available)

Patient 10 MN015: 66 year old female patient with large ophthalmic segment right ICA aneurysm was treated through deployment of 2 Pipeline devices. Follow up at 6 months demonstrated residual filling of the aneurysm along the posterior aspect of the fundus. The anterior aspect was noted to have remodeled along the parent artery. Minimal residual filling with reduction observed from previous follow up was observed at 15 month follow up angiogram. Follow at 34 months demonstrated slight remnant.

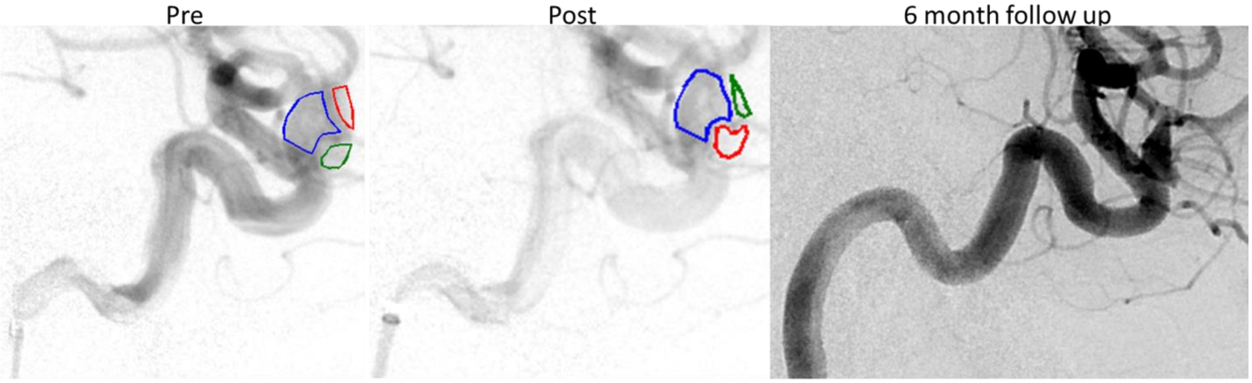

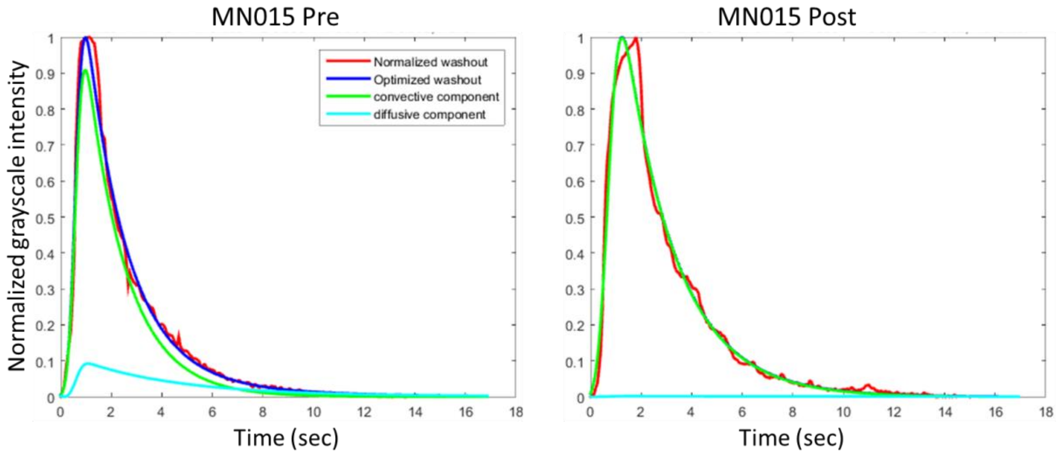

Figure 112: Angiographic image analysis and follow up data (top) and the washout curve mathematical modeling (middle) and further follow up (bottom) for Patient MN015

Patient 11 PC016: 67 year old female patient with a 13 mm large ophthalmic segment right ICA aneurysm was treated with 2 Pipeline devices. The treated aneurysm was completely occluded as seen during 6 month follow up to treatment.

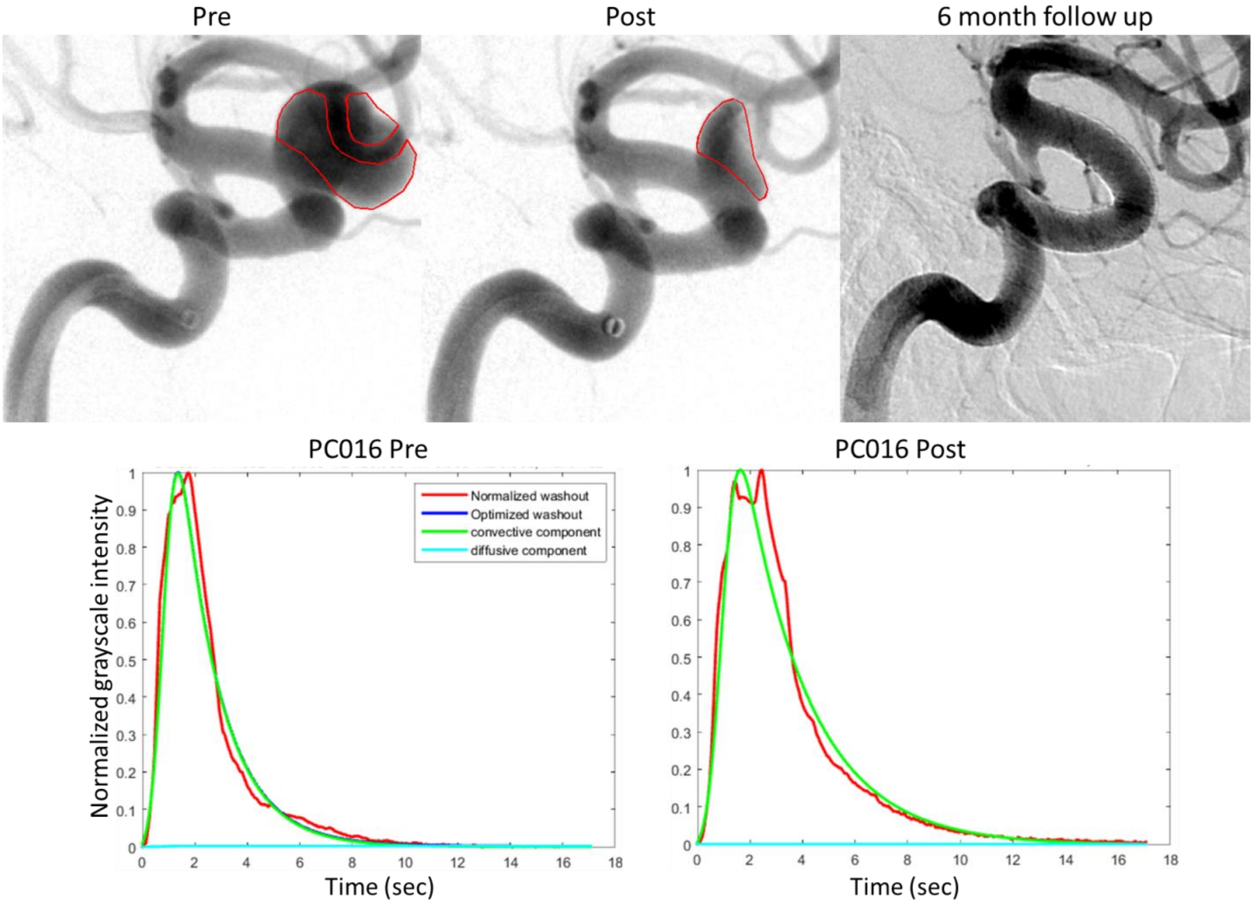

Figure 113: Angiographic image analysis and follow up data (top) and the washout curve mathematical modeling (bottom) for Patient PC016

Patient 12 LT018: 68 year old female with large ophthalmic segment left ICA aneurysm was treated through implantation of 2 Pipeline devices. Complete occlusion of the treated aneurysm was observed during the 6 month follow up to treatment.

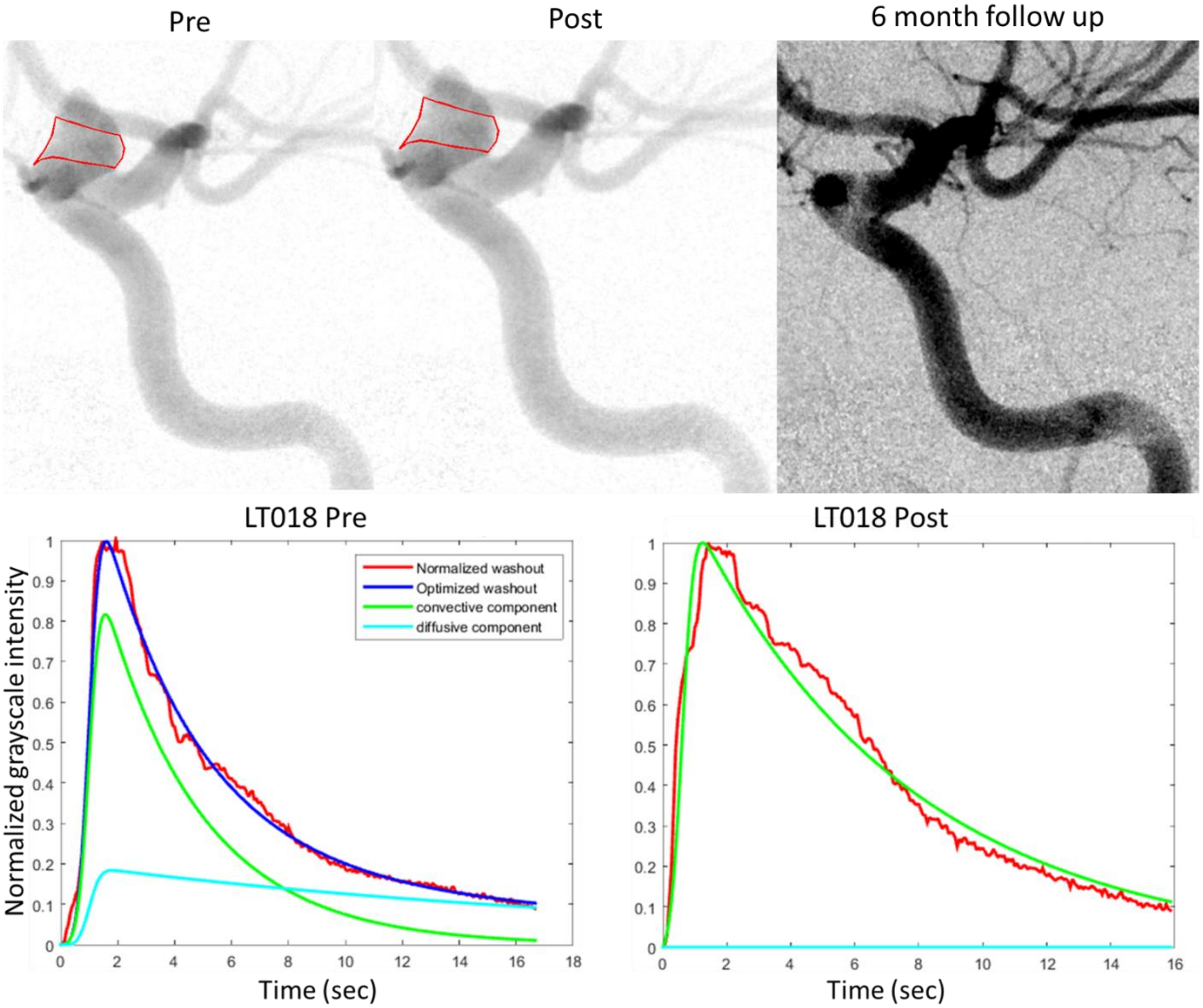

Figure 114: Angiographic image analysis and follow up data (top) and the washout curve mathematical modeling (bottom) for Patient LT018

Patient 13 MZ019: 71 year old female patient with large ophthalmic segment right ICA aneurysm was treated through implantation of 1 Pipeline device across the aneurysm. Complete occlusion of the aneurysm was recorded at 6 month follow up as seen in the angiogram.

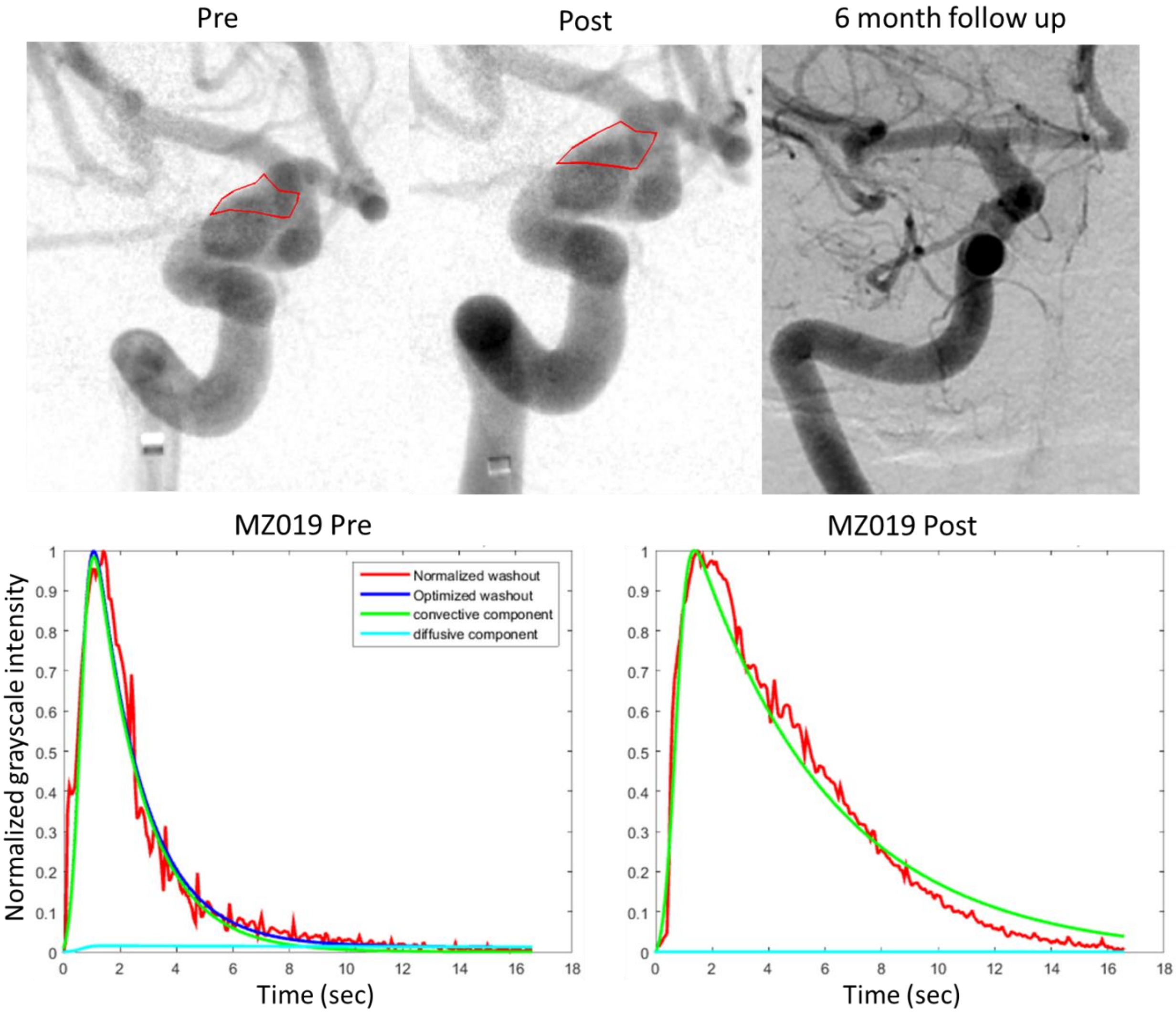

Figure 115: Angiographic image analysis and follow up data (top) and the washout curve mathematical modeling (bottom) for Patient MZ019

Patient 14 KD020: 66 year old female patient with ophthalmic segment right ICA aneurysm was treated through implantation of 2 Pipeline devices. 6 month follow up presented diminished aneurysm with minimal residual filling and complete occlusion was observed at 12 month follow up.

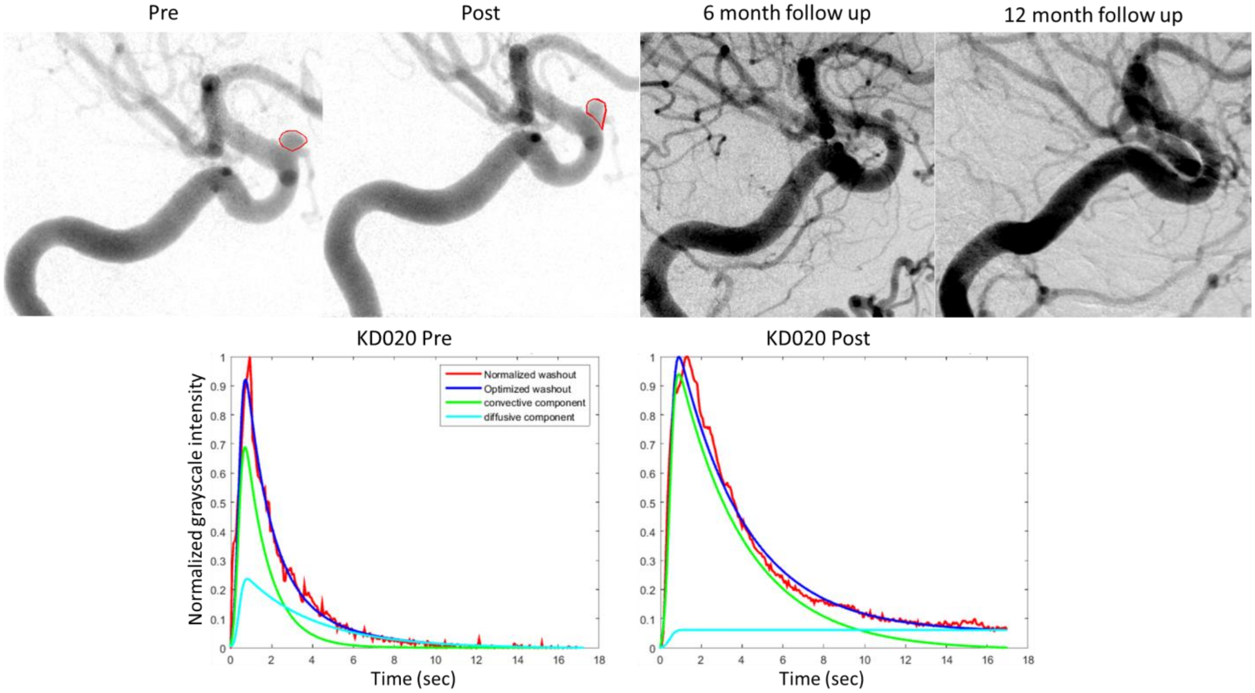

Figure 116: Angiographic image analysis and follow up data (top) and the washout curve mathematical modeling (bottom) for Patient KD020

Patient 15 CM021: 73 year old female patient with large cavernous segment right ICA aneurysm was treated through deployment of 1 Pipeline device. Near complete occlusion was observed at 6 month follow up with a small neck remnant in the posterior genu of the cavernous segment of the aneurysm. The patient is expected for a second follow up. Patient data was used for CFD modeling.

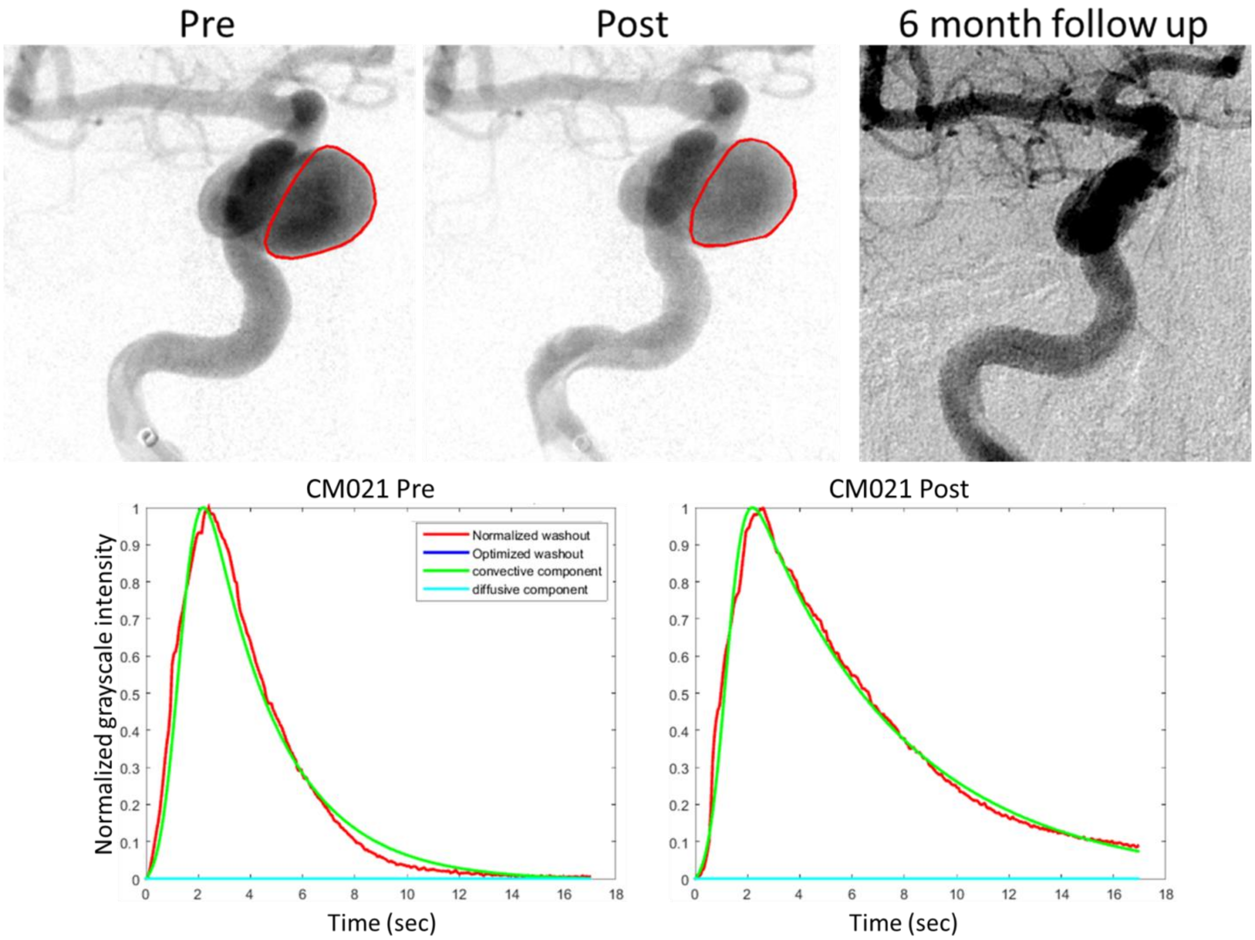

Figure 117: Angiographic image analysis and follow up data (top) and the washout curve mathematical modeling (bottom) for Patient CM021

Patient 16 RG022: 50 year old female patient with ophthalmic segment right ICA aneurysm was treated through deployment of 2 Pipeline devices. 6 month follow up demonstrated complete occlusion of the aneurysm. Patient data was used for CFD modeling.

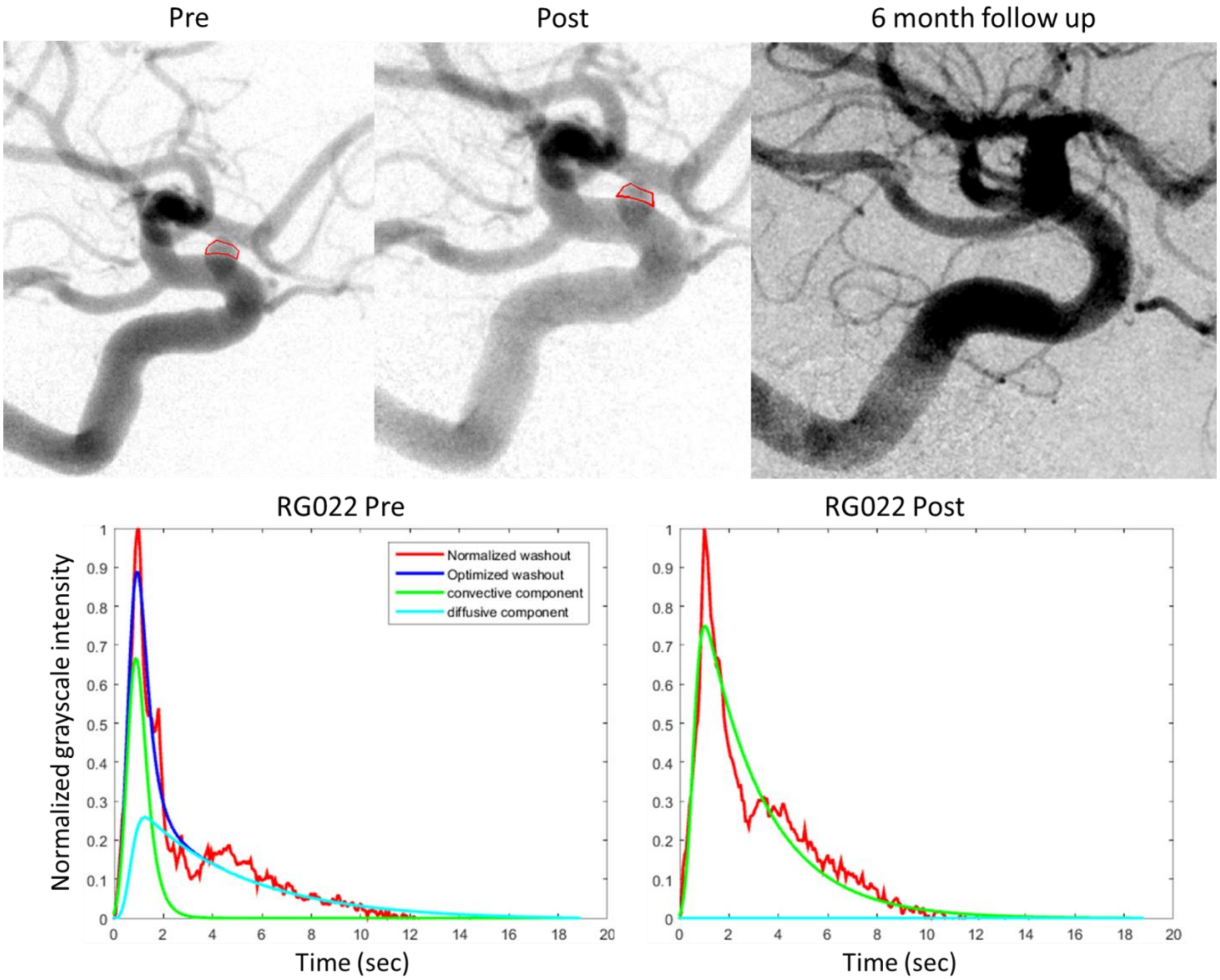

Figure 118: Angiographic image analysis and follow up data (top) and the washout curve mathematical modeling (bottom) for Patient RG022

Patient 17 DF023: 75 year old female patient presented with a giant LICA partially thrombosed cavernous aneurysm. The patient was treated with 2 Pipeline devices. Follow up at 6month presented persistent residual filling in the proximal aspect of the Pipeline construct. Repeat treatment was performed with 3 additional Pipeline devices: PED1-4.75x20mm, PED2-4.75x18mm, and PED3-4.75x16mm. Follow up at 6 months from repeat treatment demonstrated minimal residual filling to effect of near complete occlusion of the aneurysm. Patient data was used for construction of CFD model.

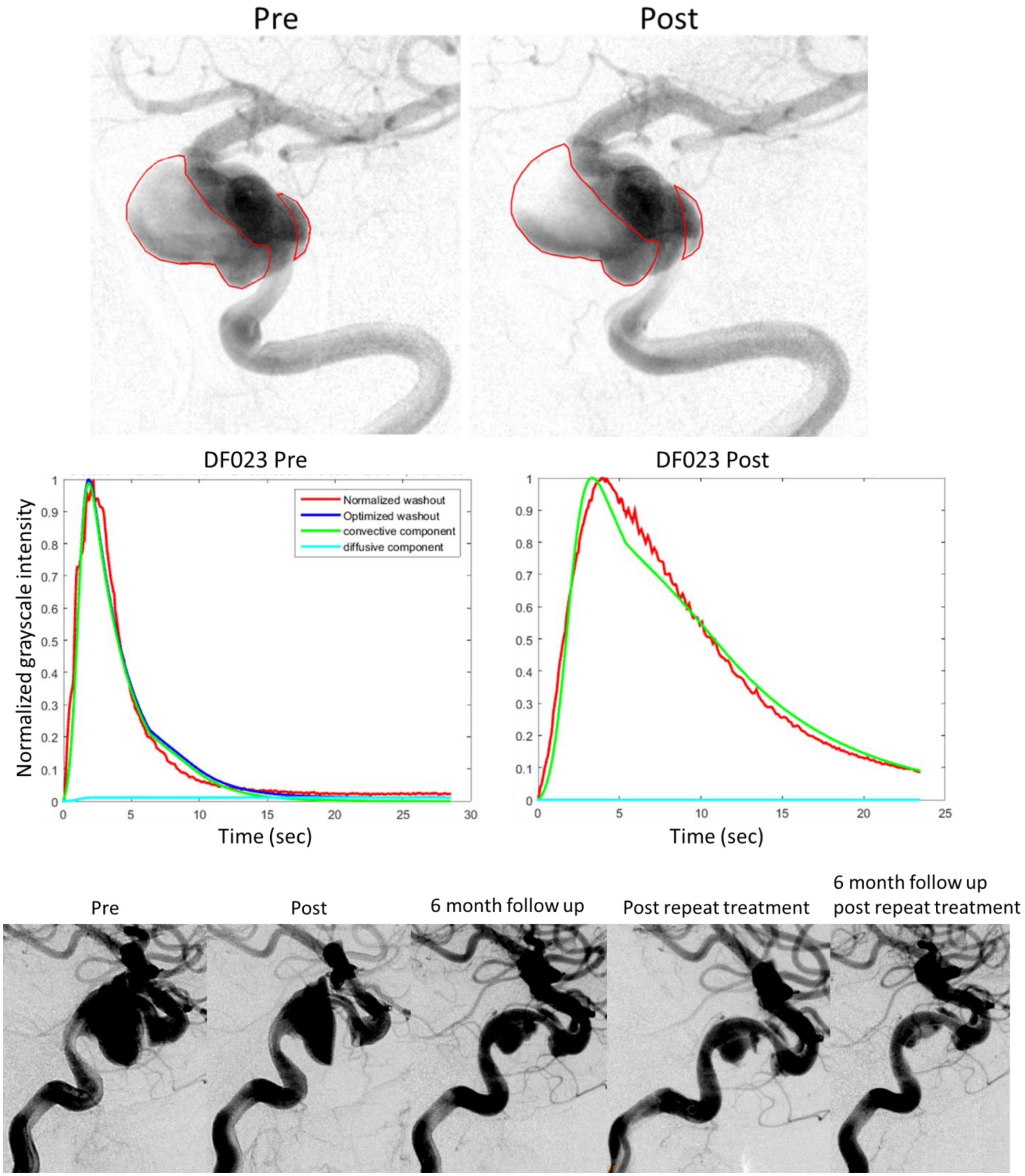

Figure 119: Angiographic image analysis (top) and the washout curve mathematical modeling (middle) and follow up images (bottom) for Patient DF023

Patient 18 LM025: 50 year old female patient with superior hypophyseal right ICA aneurysm was treated through deployment of 3 Pipeline devices across the aneurysm. The aneurysm was completely occluded at 6 months follow up angiogram. Patient data was used for CFD modeling.

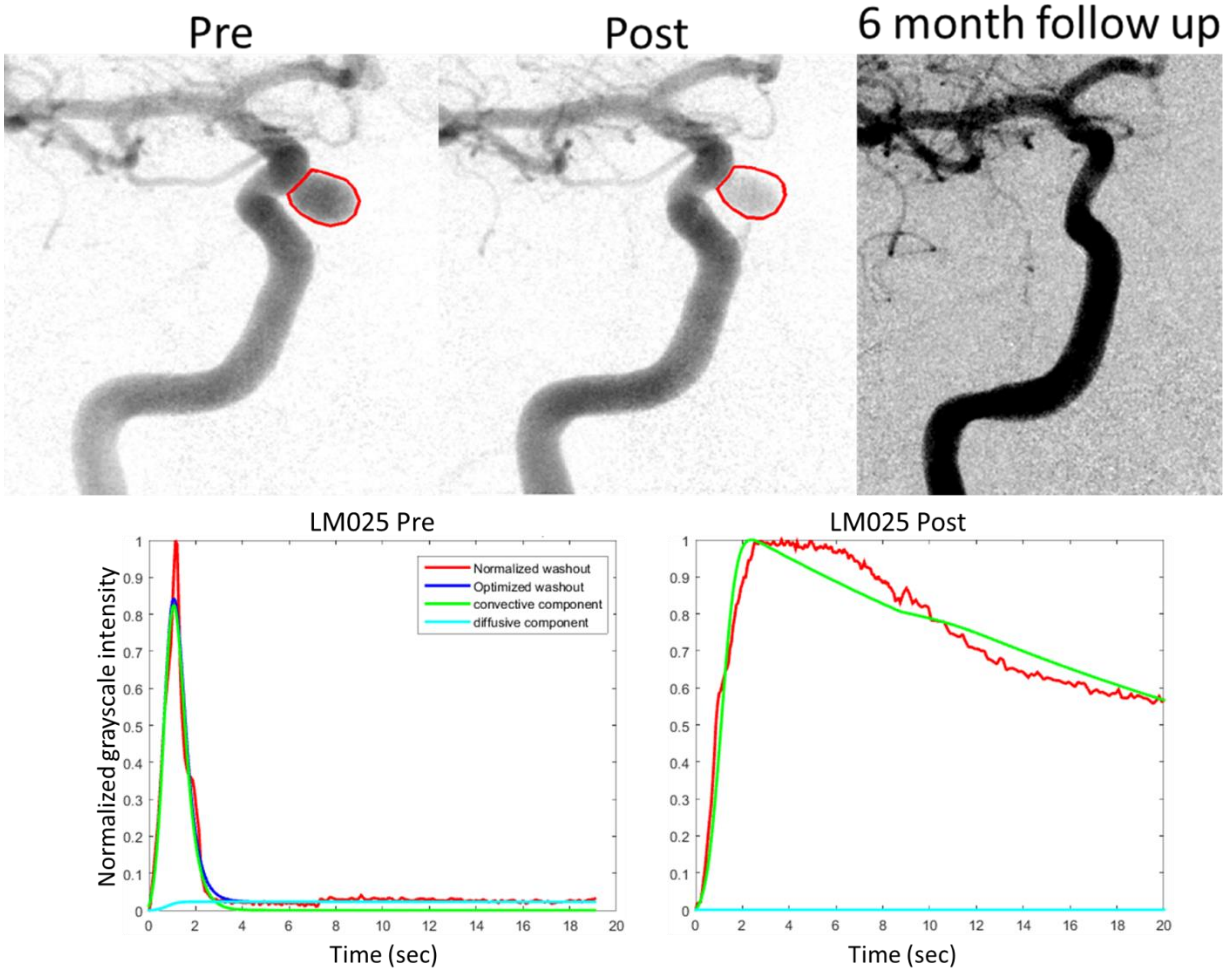

Figure 120: Angiographic image analysis and follow up data (top) and the washout curve mathematical modeling (bottom) for Patient LM025

Patient 19 DL026: 56 year old female superior hypophyseal right ICA aneurysm was treated through deployment of 2 Pipeline devices. Complete occlusion of the aneurysm was recorded at 6 month follow up angiogram.

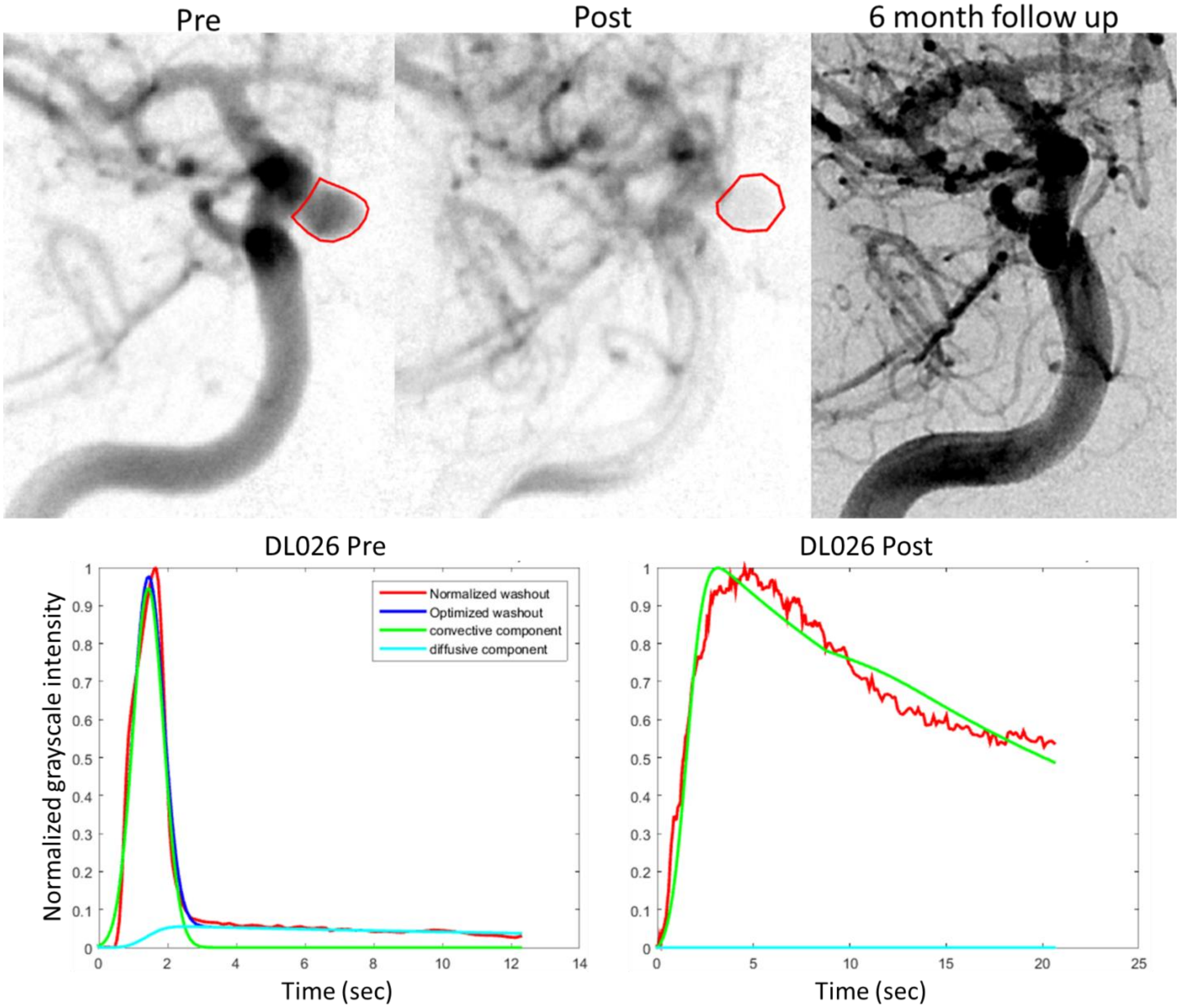

Figure 121: Angiographic image analysis and follow up data (top) and the washout curve mathematical modeling (bottom) for Patient DL026

Patient 20 MN027: 84 year old female patient with wide necked posterior communicating artery segment right ICA aneurysm was treated through deployment of 1 Pipeline device. Follow up angiography to treatment expected in September 2015.

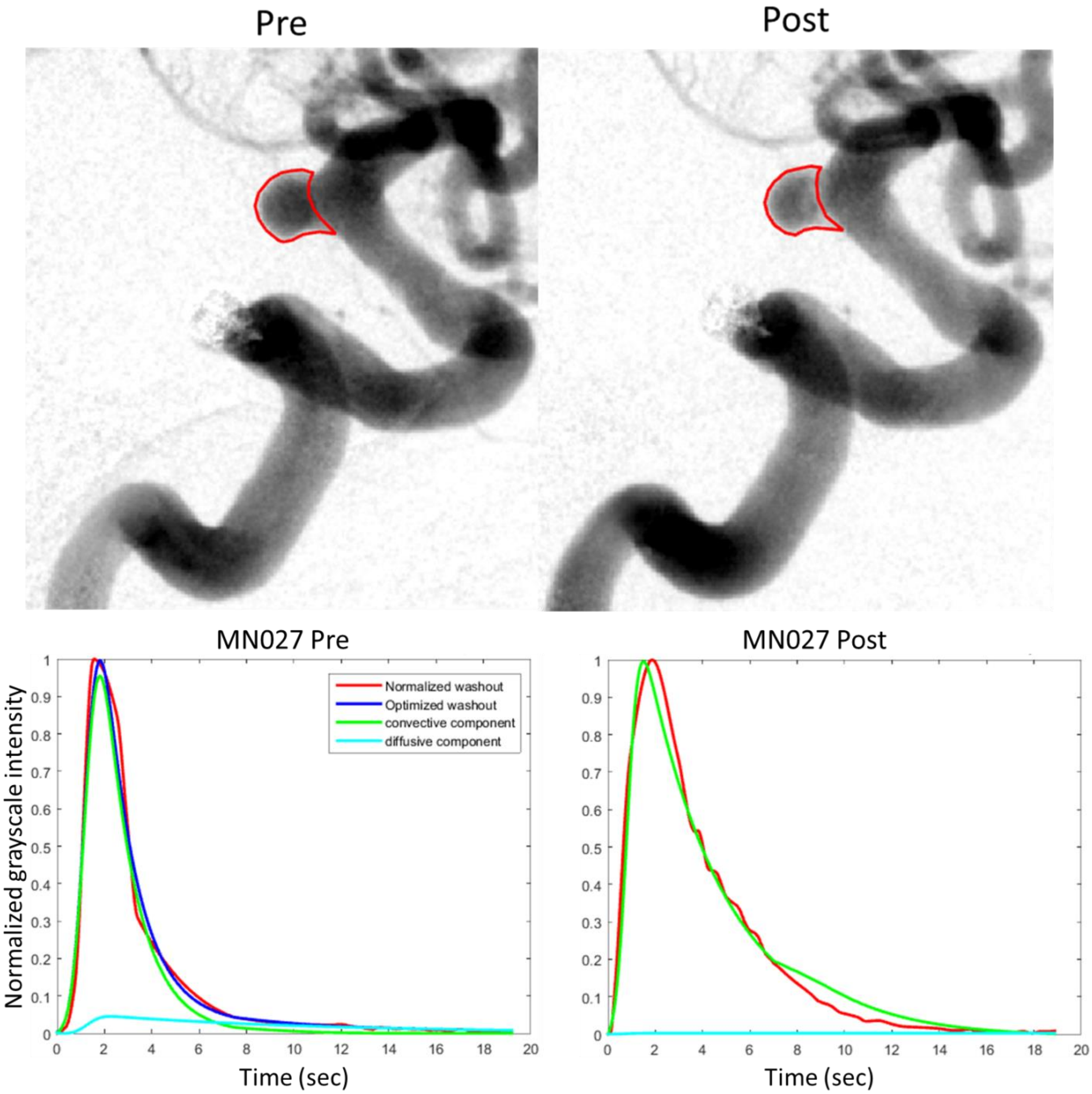

Figure 122: Angiographic image analysis (top) and the washout curve mathematical modeling (bottom) for Patient MN027

Patient 21 VK028: 39 year old female with superior hypophyseal left ICA aneurysm was treated through deployment of 1 Pipeline across the aneurysm. Complete occlusion of the aneurysm was reported at the 6 month follow up angiogram to treatment.

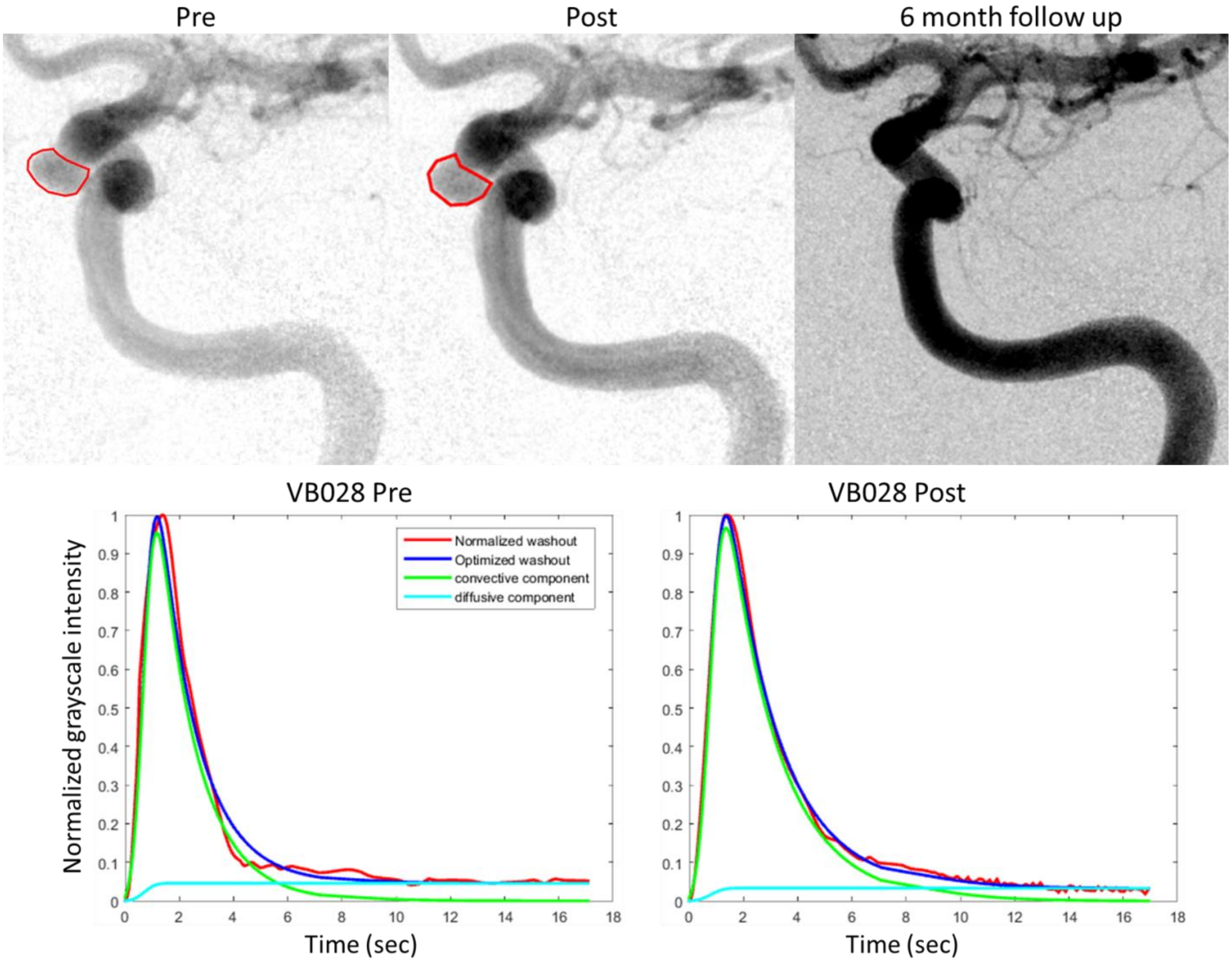

Figure 123: Angiographic image analysis and follow up data (top) and the washout curve mathematical modeling (bottom) for Patient VB028

Patient 22 VK029: 50 year old female patient with wide necked ophthalmic segment left ICA aneurysm was treated through deployment of 1 Pipeline device. 6 month follow up expected in September 2015.

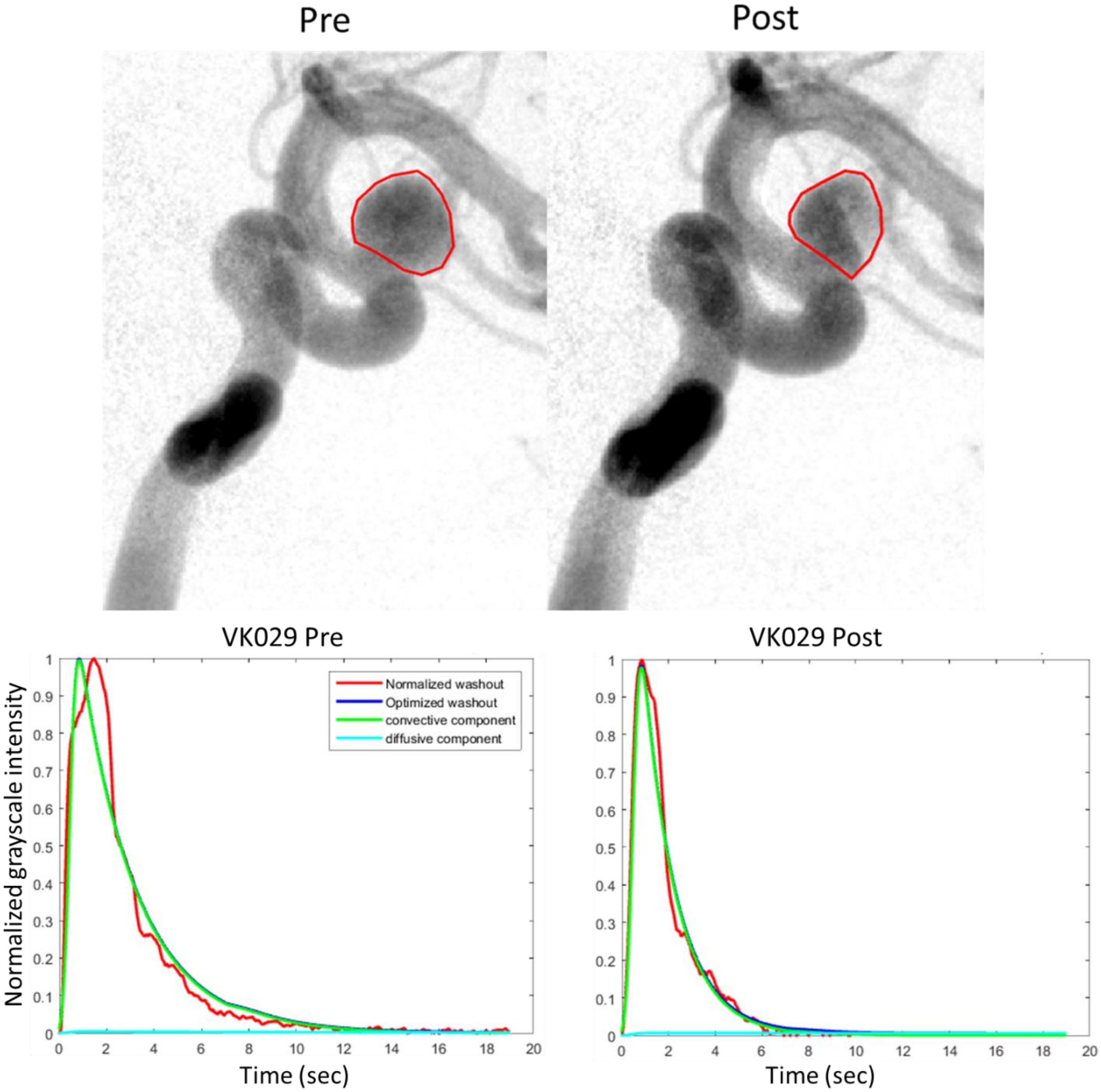

Figure 124: Angiographic image analysis (top) and the washout curve mathematical modeling (bottom) for Patient VK029

Patient 23 MA031: 43 year old female patient with posterior communicating artery left ICA wide necked aneurysm was treated through deployment of 3 Pipeline devices. Follow up angiogram is expected in January 2016.

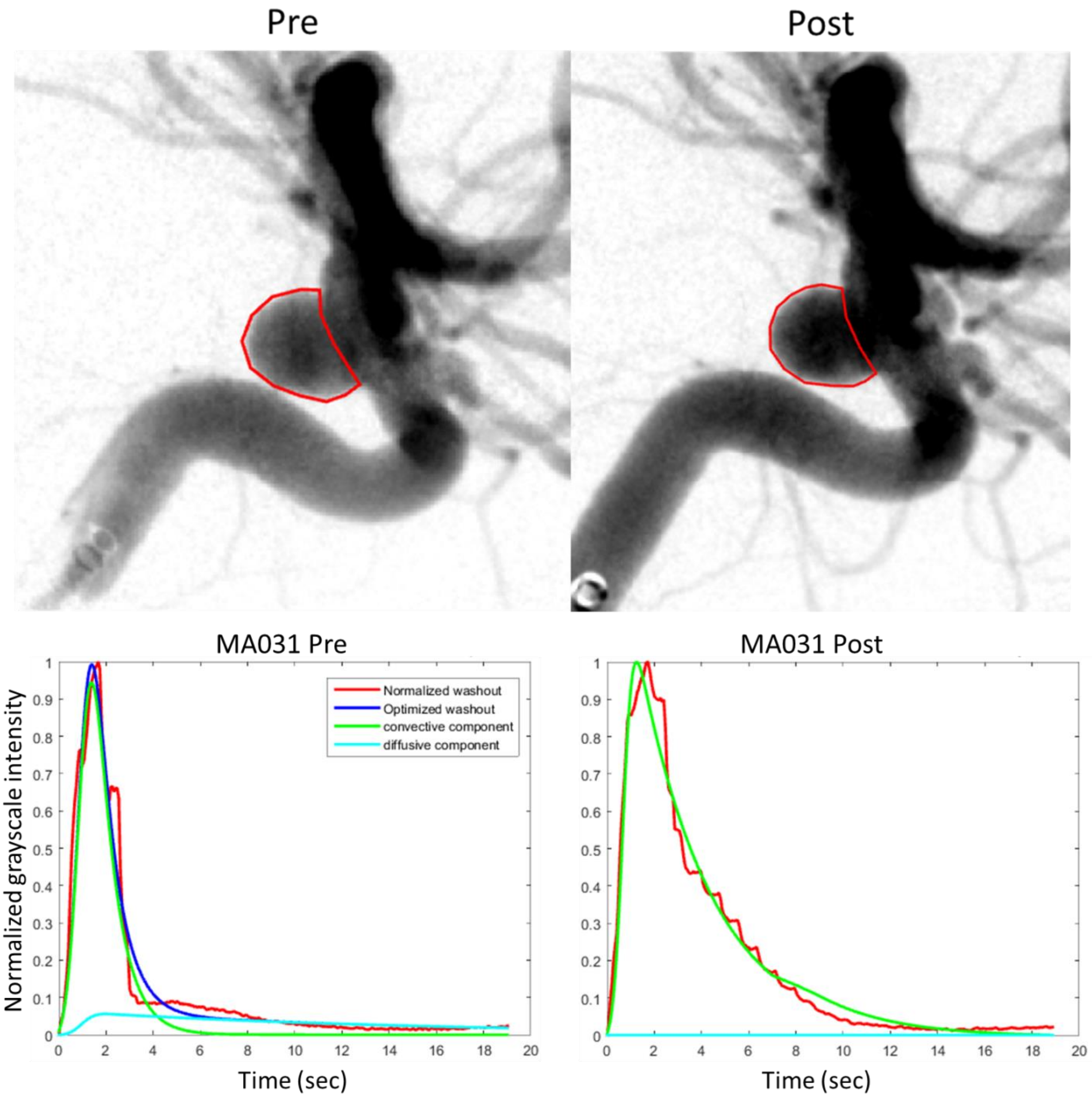

Figure 125: Angiographic image analysis (top) and the washout curve mathematical modeling (bottom) for Patient MA031

Patient 24 DW032: 69 year old male patient with large fusiform middle cerebral artery (MCA) aneurysm sized 1.2 cm x 1.57 cm was treated through deployment of 2 Pipeline devices. Follow up angiogram is expected in January 2016.

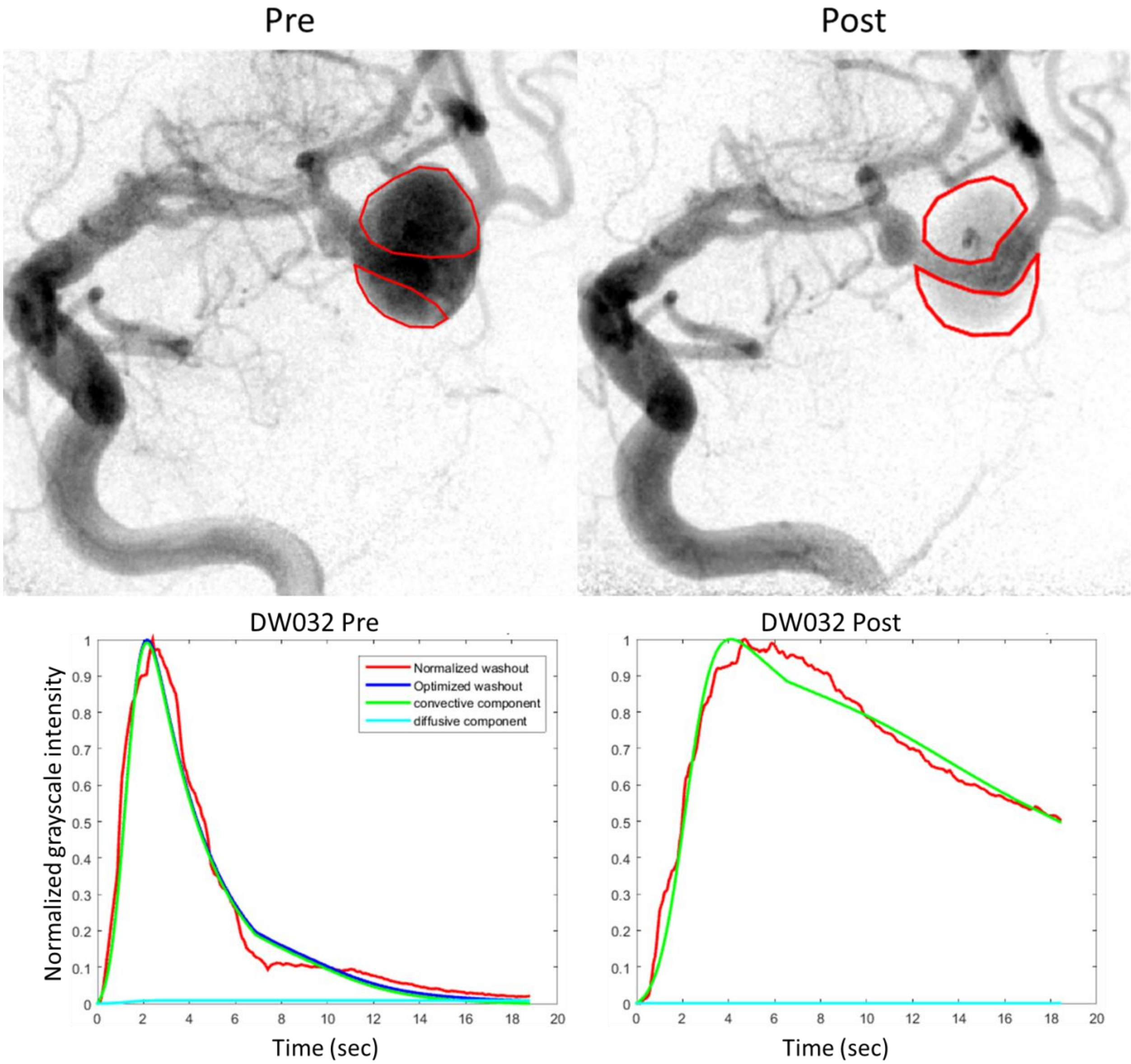

Figure 126: Angiographic image analysis (top) and the washout curve mathematical modeling (bottom) for Patient DW032